

Synthesis and Stability: Metal-Organic Frameworks Exposure to Water, Sulfur Dioxide, and Hydrogen Sulfide

A Dissertation
Presented to
The Academic Faculty

by

Julian Hungerford

In Partial Fulfillment
of the Requirements for the Degree
Doctor of Philosophy in the
School of Chemical and Biomolecular Engineering

Georgia Institute of Technology
August, 2019

Copyright © Julian Hungerford 2019

Synthesis and Stability: Metal-Organic Frameworks Exposure to Water, Sulfur Dioxide, and Hydrogen Sulfide

Approved by:

Dr. Krista S. Walton, Advisor
School of Chemical &
Biomolecular Engineering
*Georgia Institute of
Technology*

Dr. David S. Sholl
School of Chemical &
Biomolecular Engineering
*Georgia Institute of
Technology*

Dr. Sankar Nair
School of Chemical &
Biomolecular Engineering
*Georgia Institute of
Technology*

Dr. Ryan Lively
School of Chemical &
Biomolecular Engineering
*Georgia Institute of
Technology*

Dr. Angus P. Wilkinson
School of Chemistry and
Biochemistry
*Georgia Institute of
Technology*

Date Approved April 22, 2019

ACKNOWLEDGEMENTS

First I would like to thank my mother: Kathy Bodzick, my father: Tom Hungerford, and my sister: Emilie Hungerford for all of their love and support over the years. Without their support I would not be where I am today. I am especially grateful for their understanding of my pursuit of this Ph.D. so far from home in tiny Indian River, Michigan, and am truly grateful for all of their visits to Atlanta, GA.

I would like to thank the Walton group members both past and present: Dr. Karen Tulig, Dr. Nick Burtch, Dr. Bogna Grabicka, Dr. Ian Walton, Dr. Bart Marszalek, Dr. Xiao Jiang, Dr. Michael Mangarella, Dr. Chris Murdock, Dr. Lalit Darunte, Dr. William Mounfield III, Dr. Michael Dutzer, Dr. Cody Morelock, Carmen Chen, Yutao Gong, Rohan Murty, Brandon Bout, Danny Shade, Chengzhai Wang, and Tania Evans for their friendship and support during my time at Georgia Tech. Particularly I would like to thank my 2014 entering class at Georgia Tech Dr. Colton Moran, Jay Joshi, and Jake Deneff for being true friends and helping make graduate school fun and assisting me in achieving my research goals. I would also like to thank my officemate and pun enthusiast Eli Carter.

I would also like to thank the Costco crew members Thomas Kwok and Greg Chipman for many adventures after seminar on Wednesdays.

I would like to thank three members of Dr. Sholl's research group: Dr. Ross Verploegh, Dr. Rebecca Han, and Jack Findley.

I would like to thank the Center for Understanding and Control of Acid Gas-Induced Evolution of Materials for Energy (UNCAGE-ME) an Energy Frontier Research Center

funded by the U.S. Department of Energy, Office of Science, Basic Energy Sciences for supporting this work.

I would also like to thank my committee members: Dr. Sankar Nair, Dr. David Sholl, Dr. Angus Wilkinson, and Dr. Ryan Lively. I would also like to thank my Ph.D. advisor, Dr. Krista Walton for being the best advisor at Georgia Tech and providing me with support and advice throughout my Ph.D.

TABLE OF CONTENTS

ACKNOWLEDGEMENTS	iii
LIST OF TABLES.....	xi
LIST OF FIGURES.....	xiii
SUMMARY	1
CHAPTER 1: INTRODUCTION	5
1.1 Metal-Organic Frameworks	5
1.2 Synthesis of MOFs at Room Temperature	10
1.3 Defects in MOFs.....	12
1.4 Water and Acid Gas Stability of MOFs.....	13
1.5 Dissertation Scope	14
1.6 References.....	15
CHAPTER 2: EXPERIMENTAL MATERIALS AND METHODS	21
2.1 MOF Materials.....	21
2.1.1 DMOF as a Platform Material.....	21
2.1.2 UiO-66.....	24
2.1.3 ZIF-8.....	27
2.1.4 Cu-BTC	28
2.2 Experimental Methods.....	30
2.2.1 Limitations of MOFs	30
2.2.2 Limitations of Experimental Techniques	32
2.3 Conclusion	33
2.4 References.....	34

**CHAPTER 3: ROOM TEMPERATURE SYNTHESIS OF METAL-ORGANIC
FRAMEWORK ISOMERS IN THE TETRAGONAL AND KAGOME CRYSTAL
STRUCTURE40**

3.1	Introduction.....	40
3.2	Experimental.....	42
3.2.1	Materials.....	42
3.2.2	Characterization.....	44
3.3	Results and Discussion	45
3.3.1	Solvent effects in the synthesis of ZnBD and DMOF-1	45
3.3.2	CO ₂ and Water Adsorption: Topological Differences in ZnBD MOF and DMOF-1	51
3.3.3	Room temperature synthesis of Zn ₂ (X) ₂ (DABCO).....	53
3.4	Conclusions.....	55
3.5	References.....	56

**CHAPTER 4: DMOF-1 AS A REPRESENTATIVE MOF FOR SO₂ ADSORPTION
IN BOTH HUMID AND DRY CONDITIONS.....58**

4.1	Introduction.....	58
4.2	Experimental.....	60
4.2.1	Materials.....	60
4.2.2	Characterization.....	62
4.3	Results and Discussion	65
4.3.1	Effects of Water Adsorption.....	65
4.3.2	Dry SO ₂ Adsorption and FTIR.....	68
4.3.3	Humid SO ₂ Exposure	73
4.4	Conclusions.....	76
4.5	References.....	77

**CHAPTER 5: THE FEASIBILITY OF CU-BTC AS AN ADSORBENT FOR ACID
GASES: H₂S, SO₂, AND NO₂80**

5.1	Introduction.....	80
5.2	Results and Discussion	81
5.3	Conclusions.....	89

5.4	References.....	89
-----	-----------------	----

**CHAPTER 6: IMPACT OF METAL-ORGANIC FRAMEWORK SYNTHESIS
PROCEDURE ON ADSORPTION PERFORMANCE: ROOM TEMPERATURE
VERSUS SOLVOTHERMAL.....91**

6.1	Introduction.....	91
6.2	Experimental.....	92
6.2.1	Materials	92
6.2.2	Characterization.....	95
6.3	Results and Discussion	98
6.3.1	Characterization of Materials	98
6.3.2	Water Adsorption Experiments	103
6.3.3	CO ₂ Adsorption Experiments	105
6.3.4	SO ₂ Pressure Decay	106
6.3.5	Acid Gas Breakthrough	108
6.4	Conclusions.....	113
6.5	References.....	115

**CHAPTER 7: COMPREHENSIVE STUDY OF SO₂ ADSORPTION IN A SERIES
OF METAL-ORGANIC FRAMEWORKS118**

7.1	Introduction.....	118
7.2	Materials and Methods	120
7.2.1	MOF and ZIF Materials	120
7.2.2	MIL-53(Al) Synthesis Procedure	121
7.2.3	Dry SO ₂ Pressure Decay and Stability Determination	121
7.3	Results and Discussion	121
7.4	Conclusions.....	124
7.5	References.....	124

CHAPTER 8: CONCLUSIONS AND RECOMMENDATIONS127

8.1	Dissertations Conclusions.....	127
8.2	Recommendations and Future Work	130

APPENDIX A: MOF SYNTHESIS PROCEDURES.....132

A.1	Solvothermal Synthesis Procedures for M-DMOF-L.....	132
A.1.1	Solvothermal Synthesis of Parent DMOF	132
A.1.2	Solvothermal Synthesis of DMOF-TM	133
A.1.3	Solvothermal Synthesis of DMOF-DM	133
A.1.4	Solvothermal Synthesis of DMOF-NDC	133
A.1.5	Solvothermal Synthesis of DMOF-ADC	133
A.2	Room Temperature Synthesis Procedures for M-DMOF-L	134
A.2.1	Room Temperature Synthesis of Zn-DMOF	134
A.3	Room Temperature Synthesis Procedure of MBD	135
A.3.1	Room Temperature Synthesis of ZnBD	135
A.4	Solvothermal Synthesis of UiO-66	136
A.5	Room Temperature Synthesis of UiO-66	136
A.6	Solvothermal Synthesis of ZIF-8.....	137
A.7	Room Temperature Synthesis of ZIF-8	137
A.8	References.....	138

APPENDIX B: CHARACTERIZATION AND EXPERIMENTAL TECHNIQUES139

B.1	Powder X-ray Diffraction	139
B.2	Nitrogen Physisorption Analysis	139
B.3	Thermogravimetric Analysis (TGA)	140
B.4	Scanning Electron Microscope (SEM)	140
B.5	X-ray Photoelectron Spectroscopy (XPS)	140
B.6	Infrared Spectroscopy	141
B.7	Water Vapor Adsorption Isotherms	141
B.8	Dry CO ₂ Adsorption Isotherms	141
B.9	Dry SO ₂ Pressure Decay and Stability Determination	142
B.10	Humid SO ₂ Exposure.....	143
B.11	In-Situ SO ₂ Exposure Infrared Spectroscopy	144
B.12	Breakthrough Acid Gas Experiments	145
B.13	References.....	146

APPENDIX C: WATER ADSORPTION IN DMOF147

C.1	Introduction.....	147
C.2	Ligand Functionalization in DMOF	148
C.3	Metal Substitution in DMOF	150
C.4	Experiments at Argonne National Lab	154
C.4.1	Powder X-ray Diffraction Experiments at Argonne National Lab.....	154
C.4.2	Single Crystal X-ray Diffraction Experiments at Argonne National Lab ..	156
C.5	Conclusion	158
C.6	References.....	159

**APPENDIX D: SUPPLEMENTAL INFORMATION FOR ROOM
TEMPERATURE SYNTHESIS OF METAL-ORGANIC FRAMEWORK
ISOMERS IN THE TETRAGONAL AND KAGOME CRYSTAL STRUCTURE .161**

D.1	Materials and Crystal Structure	161
D.2	Brunauer-Emmett-Teller (BET) Surface Area Analysis	163
D.3	CO ₂ Adsorption Comparison	165
D.4	Zn-DMOF-TM Stability	165
D.5	Metal Substitution Room Temperature Synthesis	167
D.6	Investigation of Zinc Precursors in the Room Temperature Synthesis Procedure	169
D.7	References.....	172

**APPENDIX E: SUPPLEMENTAL INFORMATION FOR DMOF-1 AS A
REPRESENTATIVE MOF FOR SO₂ ADSORPTION IN BOTH HUMID AND DRY
CONDITIONS174**

E.1	Materials	174
E.2	Humid SO ₂ Exposure Unit.....	175
E.3	Thermal Gravimetric Analysis (TGA).....	176
E.4	In Situ FTIR Difference Spectra.....	177
E.5	Powder X-ray Diffraction Data (PXRD)	180
E.6	Scanning Electron Microscopy (SEM) and Photographs of Samples	183
E.7	Cobalt XPS Data.....	186
E.8	Nitrogen Physisorption Data.....	187

E.9	Previous Water and SO ₂ Adsorption Studies.....	191
E.10	References	191

APPENDIX F: THE FEASIBILITY OF CU-BTC AS AN ADSORBENT FOR ACID GASES: H₂S, SO₂, AND NO₂193

F.1	Materials and Crystal Structure	193
F.2	Brunauer-Emmett-Teller (BET) Surface Area Analysis	193
F.3	Breakthrough Experiment.....	194
F.4	X-ray Photoelectron Spectroscopy (XPS)	195
F.5	References.....	199

APPENDIX G: IMPACT OF METAL-ORGANIC FRAMEWORK SYNTHESIS PROCEDURE ON ADSORPTION PERFORMANCE: ROOM TEMPERATURE VERSUS SOLVOTHERMAL.....200

G.1	Materials and Crystal Structure	200
G.2	Brunauer-Emmett-Teller (BET) Surface Area Analysis	201
G.3	Powder X-ray Diffraction (PXRD).....	205
G.4	Infrared Spectroscopy (IR)	206
G.5	Thermogravimetric Analysis (TGA)	211
G.6	H ₂ S Breakthrough.....	212
G.7	SO ₂ Breakthrough.....	220
G.8	SO ₂ Pressure Decay Apparatus.....	226
G.8	Acid Gas Breakthrough Apparatus	227
G.9	References.....	228

APPENDIX H: SUPPLEMENTAL INFORMATION FOR COMPREHENSIVE STUDY OF SO₂ ADSORPTION IN A SERIES OF METAL-ORGANIC FRAMEWORKS230

H.1	SO ₂ Adsorption Isotherms	230
-----	--	-----

LIST OF TABLES

Table 3.1: BET surface area analysis for DMOF and ZnBD room temperature synthesis. BA refers to benzoic acid which was used as a modulator in the synthesis. Zn-DMOF-X-RT (X = TM, ADC, NH ₂ , or DM) (RT = room temperature).....	47
Table 4.1: BET Surface Area Measurements of Zn-DMOF-X (X = TM, DM, NDC, and ADC)	66
Table 4.2: BET Surface Area Measurements of M-DMOF-TM (M = Zn, Cu, Ni, and Co)	67
Table 5.1: BET surface area results of nitrogen physisorption analysis for Cu-BTC exposed to H ₂ S, SO ₂ , and NO ₂ as well as after SO ₂ breakthrough and adsorption experiments	83
Table 6.1: BET surface areas of UiO-66, DMOF-TM, and ZIF-8 synthesized via room temperature (RT) and solvothermal (Solvo) methods	102
Table 6.2: H ₂ S (5000 ppm in nitrogen) and SO ₂ (1000 ppm in nitrogen) breakthrough capacities (mmol/g) for UiO-66, DMOF-TM, and ZIF-8 synthesized solvothermally and at room temperature.....	111
Table 7.1: Surface areas and pore volumes for select MOF materials	119
Table C.1: BET surface areas before and after water adsorption in functionalized DMOF. “Reproduced from 1 and 2. Copyright 2012, American Chemical Society.”	150
Table D.1: Solvent Properties. ^{6,7,8}	162
Table D.2: BET SA, pore volume, and pore sizes for the DMOF-1 and ZnBD MOFs. ¹⁻⁵	163
Table D.3: BET surface area and pore volume of Zn-DMOF-TM-RT over time.	166
Table D.4: BET surface area and pore volume of M ₂ (BDC) ₂ (DABCO) where M = Zn, Co, Ni, Cu synthesized solvothermally in DMF.....	169
Table D.5: BET surface area and pore volume of Zn ₂ (BDC) ₂ (DABCO) synthesized from different metal precursors (Zn(NO ₃) ₂ ·6H ₂ O, ZnCl ₂ , and Zn(CH ₃ CO ₂) ₂ ·2H ₂ O) using methanol and DMF as solvents.....	171

Table G.1: BET surface areas and pore volumes of UiO-66, DMOF-TM, and ZIF-8 synthesized solvothermally and at room temperature for samples after SO ₂ pressure decay, SO ₂ breakthrough, and H ₂ S breakthrough analysis.	203
Table G.2: H ₂ S (5000 ppm in nitrogen) and SO ₂ (1000 ppm in nitrogen) breakthrough capacities (mmol/g) for UiO-66, DMOF-TM, and ZIF-8 synthesized solvothermally and at room temperature.	213
Table H.1: SO ₂ adsorption isothermal points	232

LIST OF FIGURES

Figure 1.1: Schematic of MOF Formation	6
Figure 2.1: Structures of DMOF (left) and ZnBD (right) viewing down the AB-plane (BDC). “Reproduced from 12. Copyright 2017, Elsevier.”	24
Figure 2.2: Structures of UiO-66 (left), ZIF-8 (middle), and CuBTC (right) (viewing AC-plane).....	27
Figure 3.1: Crystal structure of A) DMOF and B) ZnBD, viewed down the c-axis. “Crystallographic information from 2 (ZnBD) and 3 (DMOF).”	41
Figure 3.2: PXRD patterns of the fast, room temperature $Zn_2(X)_2(DABCO)$ synthesis comparing: A) materials produced from DMF, methanol, and DMF:methanol mixed solvents, and B) materials synthesized in DMSO, DMF, acetonitrile, DEF, acetone, ethanol, and methanol. PXRD patterns from crystalization information files 2 (ZnBD) and 3 (DMOF) are also provided.	46
Figure 3.3: PXRD patters of materials synthesized via a fast, room temperature $Zn_2(X)_2(DABCO)$ synthesis using: A) acidic and B) basic modulators and DMF as solvent unless otherwise stated.....	50
Figure 3.4: A) CO_2 adsorption isotherms at 25 °C for ZnBD-DMF, Zn-DMOF-Methanol-RT, and Zn-DMOF synthesized solvothermally “Reproduced from 18. Copyright 2010, <i>Elsevier</i> ” B) CO_2 adsorption isotherms of ZnBD-DMF at 10 °C, 25 °C, and 40 °C.	52
Figure 3.5: A) Water adsorption isotherms of ZnBD-DMF increased stepwise from 20 – 50% RH. B) PXRD patterns of ZnBD-DMF before and after exposure to 50% RH.	53
Figure 3.6: PXRD patterns of $Zn_2(X)_2(DABCO)$ materials produced using a 4 hour room temperature synthesis. The structures were produced using the “ZnBD” synthesis method, but led to the tetragonal DMOF topology rather than the Kagome ZnBD structure.	54
Figure 4.1: Water adsorption isotherms for: A) M-DMOF-TM and B) Zn-DMOF-X, where closed and open symbols represent adsorption and desorption, respectively.....	68
Figure 4.2: Dry SO_2 adsorption measurements for: A) M-DMOF-TM and B) Zn-DMOF-X	69
Figure 4.3: FTIR difference spectra of: A) M-DMOF-TM and B) Zn-DMOF-X upon exposure to 260 ppm SO_2 in helium flow	70

Figure 4.4: PXRD patterns of: A) Zn-DMOF-TM, B) Cu-DMOF-TM, C) Ni-DMOF-TM, and D) Co-DMOF-TM, for as synthesized, after water adsorption, after dry SO ₂ adsorption, and after humid SO ₂ exposure for 1 day (85% RH and 50 ppm SO ₂)	72
Figure 5.1: PXRD patterns of Cu-BTC exposed to H ₂ S, SO ₂ , and NO ₂ , and patterns after SO ₂ breakthrough and adsorption experiments.....	82
Figure 5.2: Observable color change during the H ₂ S, SO ₂ , and NO ₂ exposure experiments	84
Figure 5.3: SO ₂ adsorption isotherms from 0 – 2.5 bar for Cu-BTC	87
Figure 5.4: A) In Situ IR data collected under 1000 ppm SO ₂ in helium flow. B) In Situ IR data collected under 5000 ppm H ₂ S in helium flow	88
Figure 6.1: SEM images of A) DMOF-TM, B) ZIF-8, and C) UiO-66. Capital letters are material synthesized solvothermally and lower case letters are materials synthesized at room temperature	100
Figure 6.2: PXRD patterns of UiO-66, DMOF-TM, and ZIF-8 synthesized solvothermally (Solvo) and at room temperature (RT)	103
Figure 6.3: Water adsorption isotherms for UiO-66, DMOF-TM, and ZIF-8 synthesized solvothermally (Solvo) and at room temperature (RT)	105
Figure 6.4: CO ₂ adsorption isotherms for UiO-66, DMOF-TM, and ZIF-8 synthesized solvothermally (Solvo) and at room temperature (RT)	106
Figure 6.5: SO ₂ pressured decay isotherms for UiO-66, ZIF-8, and DMOF-TM synthesized solvothermally (Solvo) and at room temperature (RT)	108
Figure 6.6: H ₂ S breakthrough curves for solvothermally (upper case) and room temperature (lower case) synthesized A) UiO-66, B) DMOF-TM, and C) ZIF-8. Breakthrough was conducted using a flowrate of 50 mL/min and an H ₂ S concentration of 5000 ppm in nitrogen.	109
Figure 6.7: SO ₂ breakthrough curves for solvothermally (upper case) and room temperature (lower case) synthesized A) UiO-66, B) DMOF-TM, and C) ZIF-8. Breakthrough was conducted using a flowrate of 50 mL/min and concentration of 1000 ppm in nitrogen.	112
Figure 7.1: SO ₂ adsorption isotherms of a variety of MOF materials.....	122
Figure B.1 Diagram of humid exposure unit.....	143
Figure B.2: Typical breakthrough curve. (Cu-BTC breakthrough curve for 1000 ppm SO ₂ in nitrogen (Capacity: 0.45 mmol/g MOF)).....	145

Figure C.1: Ligand functionalization of BDC. (Top left to right) BDC-NO₂, BDC-OH, BDC-Br. (Middle left to right) DM, TM. (Bottom left to right) NDC, ADC.

.....148

Figure C.2: (Left) Water vapor adsorption/desorption isotherms at 298 K for DMOF-NO₂, DMOF-Br, DMOF-Cl₂, and DMOF-OH. “Reproduced from 1. Copyright 2012, American Chemical Society.” (Right) Water vapor adsorption/desorption isotherms at 298 K for DMOF-TM (Labeled as DMOF-TM2) and DMOF-DM. “Reproduced from 1. Copyright 2012, American Chemical Society.”150

Figure C.3: Schematic illustration of decomposition pathway of M(bdc)(ted)_{0.5} (M = Cu, Zn, Ni, Co) reactions with water. “Reproduced from 3. Copyright 2012, American Chemical Society.”151

Figure C.4: PXRD pattern of hydrated MOF materials after exposing to 9.5 Torr D₂O vapor and pristine MOF samples. “Reproduced from 3. Copyright 2012, American Chemical Society.”152

Figure C.5: Raman spectra of activated and hydrated MOF samples after exposure to 9.5 Torr water vapor pressure. “Reproduced from 3. Copyright 2012, American Chemical Society.”153

Figure C.6: A) Change in the (1 1 0) and (0 0 1) Bragg peaks collected at Argonne National Lab. B) DMOF-TM water adsorption isotherm in the humidity range from 0 to 80% RH, i – iv correspond to the four humidity levels that we used in the in situ PXRD experiment. “Reproduced from 4. Copyright 2019, Nature Research.”155

Figure C.7: a) Asymmetric unit of DMOF-TM obtained from SCXRD measurements. b) Expanded structure of DMOF-TM. Proposed c) cis and d) trans defect formation in upon water adsorption in DMOF-TM. “Reproduced from 4. Copyright 2019, Nature Research.”157

Figure C.8: (Top) Water loading in DMOF-TM corresponding to the 3 regimes identified during PXRD measurements. (Bottom) SCXRD measurements showing the location of water molecules at increasing levels of water loading within the structure. “Reproduced from 4. Copyright 2019, Nature Research.”158

Figure D.1: Ligands in DMOF and ZnBD Room Temperature Synthesis.....161

Figure D.2: Crystal structure of DMOF-1 (left) and ZnBD (right). “Reproduced from 5. Copyright 2017, *Elsevier*.”162

Figure D.3: Nitrogen physisorption isotherms for ZnBD and DMOF samples synthesized using a variety of solvents (DMF = N,N-dimethylformamide, DMSO = dimethyl sulfoxide, methanol, ethyl acetate, DEF = N,N-diethylformamide, acetone, ethanol, acetonitrile, 50/50 methanol/DMF)163

Figure D.4: Nitrogen physisorption isotherms for ZnBD samples synthesized using a variety of acid and base modulators (1:1 Benzoic acid/BDC, 5:1 Benzoic acid/BDC, Sodium terephthalate, diisopropyl-ethylamine)	164
Figure D.5: Nitrogen physisorption isotherms for Zn-DMOF-X samples synthesized at room temperature in DMF. (DM = 2,5-dimethylterephthalic acid, NH ₂ = 2-aminoterephthalic acid, TM = 2,3,5,6-tetramethylterephthalic acid, and ADC = 9,10-anthracenedicarboxylic acid).....	164
Figure D.6: Comparison of the CO ₂ adsorption isotherms for ZnBD-DMF, Zn-DMOF-Methanol-RT, Zn-DMOF-Ethanol-RT, and Zn-DMOF-Solvothermal. “Reproduced from 9. Copyright 2010, <i>Elsevier</i> .”	165
Figure D.7: Zn-DMOF-TM PXRD patterns showing degradation after 1 month in air.....	166
Figure D.8: Nitrogen physisorption isotherms for Zn-DMOF-TM-RT over time	167
Figure D.9: PXRD patterns of M ₂ (BDC) ₂ (DABCO) where M = Zn, Co, Ni, Cu all synthesized at room temperature in DMF.	168
Figure D.10: Nitrogen physisorption isotherms for ZnBD-DMF, CoBD-DMF, and Cu-DMOF-DMF synthesized at room temperature.	169
Figure D.11: PXRD patterns of Zn ₂ (BDC) ₂ (DABCO) synthesized from different metal precursors (zinc nitrate = Zn(NO ₃) ₂ ·6H ₂ O, zinc chloride = ZnCl ₂ , and zinc acetate = Zn(CH ₃ CO ₂) ₂ ·2H ₂ O (AC ₂)) using methanol and DMF as solvents.....	171
Figure D.12: Nitrogen physisorption isotherms of Zn ₂ (BDC) ₂ (DABCO) synthesized from different metal precursors (Zn(NO ₃) ₂ ·6H ₂ O, ZnCl ₂ , and Zn(CH ₃ CO ₂) ₂ ·2H ₂ O) using methanol and DMF as solvents. Closed circles correspond to adsorption and open circles correspond to desorption.	172
Figure E.1: DMOF substituting ligands (BDC, DM, NDC, TM, and ADC)	174
Figure E.2: Structure of DMOF (hydrogen atoms omitted).....	175
Figure E.3: Diagram of humid exposure unit setup	176
Figure E.4: TGA curves for M-DMOF-TM conducted from room temperature to 700 °C using a ramp rate of 5 °C/min	176
Figure E.5: Complete FTIR difference spectra of M-DMOF-TM and Zn-DMOF-ADC at 260 ppm SO ₂ concentration	178
Figure E.6: Complete FTIR difference spectra of M-DMOF-TM and Zn- DMOF-ADC at A) 50 ppm SO ₂ concentration and B) 150 ppm SO ₂ concentration in helium carrier gas	178

Figure E.7: FTIR difference spectra variation with exposure time for: A) Zn-DMOF-TM B) Cu-DMOF-TM C) Ni-DMOF-TM D) Co-DMOF-TM E) Zn-DMOF-ADC	179
Figure E.8: FTIR Difference Spectra for Desorption Profile of: A) Zn-DMOF-TM B) Cu-DMOF-TM C) Ni-DMOF-TM D) Co-DMOF-TM E) Zn-DMOF-ADC ...	180
Figure E.9: PXRD patterns of: A) Zn-DMOF-TM B) Zn-DMOF-DM C) Zn-DMOF-NDC D) Zn-DMOF-ADC, for as synthesized, after water adsorption, after dry SO ₂ adsorption, and after 250 ppm-days humid SO ₂ exposure (when applicable) (50ppm SO ₂ and 85% RH)	181
Figure E.10: PXRD Patterns of humid SO ₂ exposed samples for 100 and 250 ppm-days, after in situ FTIR, and as synthesized materials for: A) Zn-DMOF-TM B) Cu-DMOF-TM C) Ni-DMOF-TM D) Co-DMOF-TM	182
Figure E.11: SEM images of M-DMOF-TM materials taken before and after exposure to humid SO ₂ . A) Zn-DMOF-TM before a) after B) Cu-DMOF-TM before b) after C) Ni-DMOF-TM before c) after D) Co-DMOF-TM before d) after	184
Figure E.12: SEM images of Zn-DMOF-X materials taken before and after exposure to humid SO ₂ . A) Zn-DMOF-TM before a) after B) Zn-DMOF-ADC before b) after	185
Figure E.13: Pictures of Pre Exposed, Post Exposed, and Post Exposure Reactivated Samples of M-DMOF-TM for Humid SO ₂ Exposure. Samples are Co, Zn, Ni, Cu from Left to Right.	186
Figure E.14: XPS survey scan of Co-DMOF-TM after 5-day humid SO ₂ exposure	186
Figure E.15: Nitrogen Physisorption Isotherm of Zn-DMOF-TM collected for as synthesized, water adsorbed, SO ₂ pressure decay, FTIR, and 50, 100, and 250 ppm-days humid SO ₂ exposed samples.....	187
Figure E.16: Nitrogen Physisorption Isotherm of Co-DMOF-TM collected for as synthesized, water adsorbed, SO ₂ pressure decay, FTIR, and 50, 100, and 250 ppm-days humid SO ₂ exposed samples.....	188
Figure E.17: Nitrogen Physisorption Isotherm of Cu-DMOF-TM collected for as synthesized, water adsorbed, SO ₂ pressure decay, FTIR, and 50, 100, and 250 ppm-days humid SO ₂ exposed samples.....	188
Figure E.18: Nitrogen Physisorption Isotherm of Ni-DMOF-TM collected for as synthesized, water adsorbed, SO ₂ pressure decay, FTIR, and 50, 100, and 250 ppm-days humid SO ₂ exposed samples.....	189

Figure E.19: Nitrogen Physisorption Isotherm of Zn-DMOF-DM collected for as synthesized and water adsorbed samples	189
Figure E.20: Nitrogen Physisorption Isotherm of Zn-DMOF-NDC collected for as synthesized, water adsorbed, and SO ₂ pressure decay samples	190
Figure E.21: Nitrogen Physisorption Isotherm of Zn-DMOF-ADC collected for as synthesized, water adsorbed, SO ₂ pressure decay, FTIR, and 250 ppm-days humid SO ₂ exposed samples.....	190
Figure E.22: A) Water adsorption data for DMOF. (Reproduced from 2. Copyright 2012 American Chemical Society) B) SO ₂ adsorption data for Ni-DMOF and Zn-DMOF. (Reproduced from 3. Copyright 2013 American Chemical Society)	191
Figure F.1: Crystal structure of Cu-BTC (Left) and Trimesic acid (right)	193
Figure F.2: Nitrogen physisorption isotherms of Cu-BTC samples after acid gas testing	194
Figure F.3: Cu-BTC breakthrough curve for 1000 ppm SO ₂ in nitrogen (Capacity: 0.45 mmol/g MOF).....	195
Figure F.4: XPS of Pristine Cu-BTC. A) survey scan B) Cu2p scan C) S2p scan D) N1s scan	196
Figure F.5: XPS of SO ₂ exposed Cu-BTC. A) survey scan B) Cu2p scan C) S2p scan D) N1s scan	197
Figure F.6: XPS of NO ₂ exposed Cu-BTC. A) survey scan B) Cu2p scan C) S2p scan D) N1s scan	198
Figure F.7: XPS of H ₂ S exposed Cu-BTC. A) survey scan B) Cu2p scan C) S2p scan D) N1s scan	199
Figure G.1: Ligands used in MOF synthesis from left to right: BDC, TMBC, DABCO, 2-methylimidazole.....	200
Figure G.2: Structures of UiO-66 (left), ¹ DMOF-TM (center), ² and ZIF-8 (right) ³	201
Figure G.3: Nitrogen physisorption isotherms of UiO-66, DMOF-TM, and ZIF-8 synthesized solvothermally and at room temperature corresponding to the BET surface areas reported in the main text.....	202
Figure G.4: Nitrogen physisorption isotherms of UiO-66 synthesized solvothermally and at room temperature after SO ₂ pressure decay, SO ₂ breakthrough, H ₂ S breakthrough, and H ₂ O adsorption experiments.....	204

Figure G.5: Nitrogen physisorption isotherms of DMOF-TM synthesized solvothermally and at room temperature after SO ₂ pressure decay, SO ₂ breakthrough, H ₂ S breakthrough, and H ₂ O adsorption experiments.....	204
Figure G.6: Nitrogen physisorption isotherms of ZIF-8 synthesized solvothermally and at room temperature after SO ₂ pressure decay, SO ₂ breakthrough, H ₂ S breakthrough, and H ₂ O adsorption experiments.	205
Figure G.7: PXRD patterns of UiO-66 synthesized A) solvothermally and B) at room temperature (right) after SO ₂ pressure decay, SO ₂ breakthrough, and H ₂ S breakthrough experiments.	205
Figure F.8: PXRD patterns of DMOF-TM synthesized A) solvothermally and B) at room temperature after SO ₂ pressure decay, SO ₂ breakthrough, and H ₂ S breakthrough experiments.	206
Figure G.9: PXRD patterns of ZIF-8 synthesized A) solvothermally and B) at room temperature after SO ₂ pressure decay, SO ₂ breakthrough, and H ₂ S breakthrough experiments.	206
Figure G.10: IR spectra of UiO-66 synthesized solvothermally and at room temperature	207
Figure G.11: IR spectra of DMOF-TM synthesized solvothermally and at room temperature	208
Figure G.12: IR drifts spectra of DMOF-TM synthesized solvothermally and at room temperature focusing on 1000 – 2000 cm ⁻¹	209
Figure G.13: IR spectra of ZIF-8 synthesized solvothermally and at room temperature	210
Figure G.14: TGA data for UiO-66 synthesized A) solvothermally and B) at room temperature	211
Figure G.15: TGA data for DMOF-TM synthesized A) solvothermally and B) at room temperature	212
Figure G.16: TGA data for ZIF-8 synthesized A) solvothermally and B) at room temperature	212
Figure G.17: H ₂ S breakthrough curves for solvothermally (upper case) and room temperature (lower case) synthesized UiO-66 A) Run 1 B) Run 2 C) Run 3. Solid orange line corresponds to H ₂ S concentration (C/C ₀) and dotted blue line corresponds to the nitrogen concentration (C/C ₀).	214

Figure G.18: H ₂ S breakthrough curves for solvothermally (upper case) and room temperature (lower case) synthesized DMOF-TM A) Run 1 B) Run 2 C) Run 3. Solid orange line corresponds to H ₂ S concentration (C/C ₀) and dotted blue line corresponds to the nitrogen concentration (C/C ₀).	215
Figure G.19: H ₂ S breakthrough curves for solvothermally (upper case) and room temperature (lower case) synthesized ZIF-8 A) Run 1 B) Run 2 C) Run 3. Solid orange line corresponds to H ₂ S concentration (C/C ₀) and dotted blue line corresponds to the nitrogen concentration (C/C ₀).	216
Figure G.20: Complete H ₂ S breakthrough curve for A) solvothermally and B) room synthesized UiO-66.....	217
Figure G.21: Complete H ₂ S breakthrough curve for A) solvothermally and B) room synthesized DMOF-TM	218
Figure G.22: Complete H ₂ S breakthrough curve for A) solvothermally and B) room synthesized ZIF-8.....	219
Figure G.23: SO ₂ breakthrough curves for solvothermally (upper case) and room temperature (lower case) synthesized UiO-66 A) Run 1 B) Run 2 C) Run 3	221
Figure G.24: SO ₂ breakthrough curves for solvothermally (upper case) and room temperature (lower case) synthesized DMOF-TM A) Run 1 B) Run 2 C) Run 3	222
Figure G.25: SO ₂ breakthrough curves for solvothermally (upper case) and room temperature (lower case) synthesized ZIF-8 A) Run 1 B) Run 2 C) Run 3	223
Figure G.26: Complete SO ₂ breakthrough curve for A) solvothermally and B) room synthesized UiO-66.....	224
Figure G.27: Complete SO ₂ breakthrough curve for A) solvothermally and B) room synthesized DMOF-TM	225
Figure G.28: Complete SO ₂ breakthrough curve for A) solvothermally and B) room synthesized ZIF-8.....	226
Figure G.29: (left) SO ₂ pressure decay apparatus. (right) Close-up of reference cell and sample cell.	227
Figure G.30: Photograph of acid gas breakthrough apparatus	228
Figure H.1: (Left) SO ₂ pressure decay apparatus (Right) Reference and sample cells.....	231

NOMENCLATURE

Abbreviations

MOF	Metal-Organic Framework	BTC	Benzene-1,3,5-tricarboxylic Acid
SBU	Secondary Building Unit	a.u.	Arbitrary Units
CUS	Coordinatively Unsaturated Sites	Å	Angstrom
HKUST	Hong Kong University of Science and Technology	m	Meter
UiO	University of Oslo	nm	Nanometer
MIL	Materials Institute	m ²	Square Meters
Lavoisier		cm ³	Cubic Centimeter
ZIF	Zeolitic Imidazolate Framework	g	Gram
BDC	1,4-Benzenedicarboxylic Acid	mg	Milligram
ADC	9,10-Anthracenedicarboxylic Acid	L	Liter
NDC	1,4-Naphthalenedicarboxylic Acid	mL	Milliliter
TM	2,3,5,6-Tetramethylterephthalic Acid	mol	Mole
		mmol	Millimole
		h	Hour
		min	Minute
		s	Second
		K	Kelvin
		°C	Degrees Celsius
		CO ₂	Carbon Dioxide
		SO ₂	Sulfur Dioxide
		NO ₂	Nitrogen Dioxide

H ₂ S	Hydrogen Sulfide
N ₂	Nitrogen
He	Helium
DMF	N,N'- Dimethylformamide
MeOH	Methanol
EtOH	Ethanol
IPA	Isopropanol
BET	Bruanauer, Emmet, and Teller
IGA	Intelligent Gravimetric Adsorption
MFC	Mass Flow Controller
NMR	Nuclear Magnetic Resonance
PXRD	Powder X-ray Diffraction
TGA	Thermogravimetric Analysis
PD	Pressure Decay
Solvo	Solvothermal
RT	Room Temperature

SUMMARY

The overall goal of this work is to explore the impact of water and acid gas exposure (SO_2 and H_2S) on the degradation and adsorption properties of metal-organic frameworks (MOFs). MOFs are a class of materials that have shown potential for a variety of applications including separation, catalysis, drug delivery, and gas storage. However, little is known regarding their interactions with acid gases, specifically SO_2 and H_2S , which are constituents commonly found in flue gas, sour natural gas, and in other industrial processes. Better understanding of these interactions is an important step in creating MOFs for industrial applications and is the focus of this dissertation.

DMOF (DABCO MOF) is a pillared MOF that contains two ligands, DABCO (1,4-diazabicyclo[2.2.2]octane) and BDC (benzene-1,4-dicarboxylic acid), as well as a M^{2+} ($\text{M} = \text{Co}, \text{Ni}, \text{Cu}, \text{Zn}$) metal center. DMOF is highly tailorable through both metal substitution and ligand substitution, making it an excellent platform material candidate. Chapter 2 will discuss DMOF as a platform material and its feasibility for adsorption-based separations. In chapter 3, the role that synthesis conditions have on MOF structure and topology will be discussed using DMOF, the platform material. DMOF was synthesized at room temperature using a variety of solvents including: DMF (N,N-dimethylformamide), DEF (N,N-diethylformamide), DMSO (dimethylsulfoxide), methanol, ethanol, acetonitrile, ethyl acetate, and acetone. In the room temperature synthesis, a base is added to deprotonate the carboxylic acid group of the BDC ligand, which facilitates fast growth of the MOF. This differs from traditional solvothermal synthesis, as DMF degradation to dimethyl amine is no longer necessary for deprotonation of BDC. Solvent choice was found

to play a vital role in the resulting MOF topology. Methanol, ethanol, acetonitrile, ethyl acetate, acetone, and DEF were found to produce the DMOF crystal structure while DMF and DMSO resulted in the formation of ZnBD, an isomer of DMOF.

In chapter 4, ligand functionalization and metal substitution were assessed in the platform DMOF material to develop structure property relationships for dry and humid SO₂ exposed materials. DMOF was found to be most stable towards dry SO₂ when TM (2,3,5,6-tetramethylterephthalic acid) or ADC (9,10-anthracene dicarboxylic acid) ligands were used in place of the BDC ligand. Humid SO₂ experiments showed that the bulkiest ADC ligand provided additional stability over TM. Metal node was also found to have a significant role in the stability of these materials. Metal substitutions in DMOF-TM showed that the material's stability towards humid SO₂ followed the Irving-Williams stability order: Co < Ni < Cu > Zn.

Chapter 5 explores the acid gas stability of a copper-based MOF, Cu-BTC, towards SO₂, H₂S, and NO₂ in dry conditions. Cu-BTC was exposed to SO₂ (1000 ppm in nitrogen), H₂S (5000 ppm in nitrogen), and NO₂ (1000 ppm in nitrogen) using a flow through breakthrough setup. Post exposed samples were then characterized by surface area analysis and PXRD to assess the stability of Cu-BTC towards these gases. Cu-BTC degraded rapidly when exposed to H₂S and NO₂ degrading into copper sulfide and copper nitrate respectively. Cu-BTC did not degrade when exposed to SO₂ and we calculated a breakthrough capacity of 0.45 mmol/g at an SO₂ concentration of 1000 ppm in nitrogen. SO₂ pressure decay measurements were also collected and Cu-BTC reached a capacity of 13 mmol/g at 2.5 bar pure SO₂ and showed only a slight drop in capacity following

subsequent trials. Cu-BTC was found to be an effective adsorbent for SO₂ at both high and low pressures where water and other acid gases, such as H₂S and NO₂ are not present.

Chapter 6 combines what was learned in Chapters 2 and 4, and applies those principals to other MOFs. UiO-66, DMOF-TM, and ZIF-8 were synthesized via traditional solvothermal methods, as well as room temperature synthesis methods. The materials' stability and adsorption properties were then assessed upon exposure to humidity, SO₂, and H₂S. We believed that room temperature MOF synthesis would result in the formation of defective structures and could potentially lead to changes in the adsorption behavior and stability of these materials upon exposure to acid gases. All materials displayed a decrease in H₂S breakthrough capacity across subsequent runs such that none of the MOFs tested can be recommended for H₂S adsorption. SO₂ breakthrough studies showed that UiO-66 and ZIF-8 make poor adsorbents at low concentrations (1000 ppm in nitrogen). However, DMOF-TM displayed an excellent SO₂ breakthrough capacity of 0.90 mmol/g and was successfully regenerated using mild activation conditions. This breakthrough capacity is among the highest reported for any MOF at a concentration of 1000 ppm SO₂ in nitrogen.

In chapter 7, a series of MOFs were selected, and adsorption isotherms were collected using pure SO₂ to assess the material properties that would correlate with strong SO₂ adsorption. MIL-101(Cr) was identified as the best performing MOF at high pressure, reaching an SO₂ adsorption of over 20 mmol/g-MOF at 2.5 bar total pressure. Cu-BTC and DMOF-TM had the highest low-pressure adsorption of the MOFs tested. Two important trends were identified in this study. First, SO₂ adsorption capacity at high pressure (> 1 bar) is primarily dominated by the pore volume of the MOF such that MOFs with large pore volumes have high SO₂ capacity. Second, low pressure SO₂ adsorption is dominated

by open-metal site MOFs, such as Cu-BTC, or MOFs with pore diameters similar in size to the kinetic diameter of SO₂, such as DMOF-TM.

Lastly, chapter 8 will discuss the overall conclusions of this dissertation work as well as offer recommendations to further explore acid gas interactions in MOFs.

CHAPTER 1: INTRODUCTION

Chapter one of this dissertation will begin by introducing metal-organic frameworks (MOFs) and their potential applications in separations, catalysis, drug delivery, and gas storage. The next section will discuss traditional MOF synthesis methods and the need to explore new novel approaches for MOF formation. This thesis will specifically focus on room temperature synthesis methods. The third section will examine how defects are introduced into MOF structure during the synthesis process. The fourth section will detail how water vapor and acid gas stability are crucial towards realizing MOFs for potential applications. Lastly, the scope of this dissertation will be presented.

1.1 Metal-Organic Frameworks

Metal-organic frameworks (MOFs) are a novel class of porous materials that contain metal nodes connected by organic linkers. MOFs are typically formed solvothermally by combining a metal salt and organic linker in a solvent such as N,N-dimethylformamide (DMF). A solvothermal synthesis entails the mixture of metal salt, organic linker, and solvent being heated for many hours to days. During this time, the DMF degrades to dimethyl amine, causing the subsequent deprotonation of the organic linkers. The MOF then forms a porous network of metal clusters bridged by organic linkers trapping solvent molecules within the pore space of the MOF.¹ After the synthesis is complete, the resulting MOF crystal powders are typically collected via filtration or centrifuge, and then washed with DMF or methanol to remove any excess reactants. The

final step in the MOF synthesis process is activation. Activation involves heating the MOF under vacuum, this process removes the solvent trapped within the pores of the MOF such that the pore space becomes accessible. A schematic of MOF formation is shown in Figure 1.1.

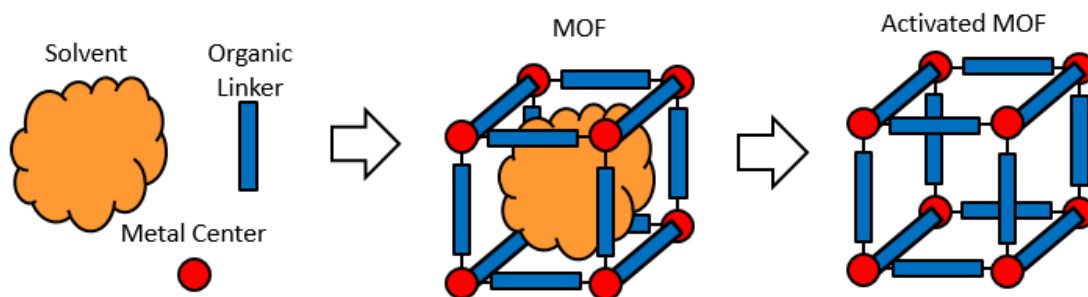


Figure 1.1: Schematic of MOF Formation

MOFs are highly tunable porous materials; both the metal nodes and organic linkers can be interchanged allowing for the formation of many different structures. To date thousands of MOFs have been synthesized in the lab and tens of thousands of MOFs have been realized through computational methods.² These combinations allow for the immense tailoring of MOF properties including: pore size, active sites, and surface area.³⁻⁷ For these reasons, MOFs have attracted attention for use in a large swathe of applications including: separations, catalysis, drug delivery, and gas storage.⁸⁻¹⁹ This section will provide a brief overview of the current progress that has been made in the utilization of MOFs for these applications.

One of the advantages that MOFs offer over other porous materials, such as zeolites, is their tailorability through the wide variety of structures possible through ligand substitution. The industrial availability of various ligands allows for the fine control over

MOF pore sizes, making them ideal candidates for separation applications. MOFs also have the potential to be used as molecular sieves. In fact, MOFs have been used as molecular sieves to separate ethane from ethylene. Current methods for ethane/ethylene separations are extremely costly because of the similarity in boiling points and molecular size of ethane and ethylene. The current industrial method for separating ethane and ethylene is cryogenic distillation, which utilizes extremely large distillation columns consisting of hundreds of trays. Additionally, operating a distillation column at cryogenic temperatures is very energy intensive and MOFs could potentially replace distillation as a means of separation for this difficult process. Martin-Calvo et. al.²⁰ used a series of IRMOFs (Iso Reticular MOFs) for the separation of ethane and ethylene. In this study, IRMOF-11 and IRMOF-13 were the most selective MOFs for ethane over ethylene adsorption, achieving an adsorption selectivity of ~2 over a concentration range of 10 - 90% ethane in ethylene. This study found that ethane selectivity was enhanced in this series of IRMOFs due to interpenetration of the MOF structures. The authors also found that IRMOF-16 was more selective to ethylene, due to its large pore cavities. While MOFs are promising materials for separation applications, they are not without their downfalls. Unlike zeolites which tend to be very rigid materials, MOFs are flexible, due to their organic ligands.²¹ MOF flexibility provides difficulty in some separations as molecules larger than their pore apertures can then diffuse through the pore space of the MOF. Zhang et. al.²² showed that molecules with a molecular diameter of 4.0 Å were able to diffuse into the structure of ZIF-8, however the XRD-derived pore aperture was only 3.4 Å. While flexible ligands may negatively affect the separation performance for some applications, they can also provide some advantages. He et. al.²³ partially replaced the biphenyl-4,4'-dicarboxylic acid linker with the flexible 1,3-

bis(4-pyridyl)propane using solvent assisted ligand exchange (SALE) and observed an enhancement in the material's CO_2/N_2 and CH_4/N_2 separation performance. In conclusion, if MOFs are to be used for separation-based applications, more research needs to be conducted to understand what factors are most important to achieve high selectivity as well as obtaining more efficient synthesis methods for scale-up and mass production.

MOFs have also garnered attention for applications in catalysis due to their large surface areas and numerous active sites. For example, Farha et. al.²⁴ used a zirconium MOF, UiO-66, as a catalyst for the degradation of chemical warfare agents. In this study, UiO-66 was used to catalytically hydrolyze the nerve agent dimethyl 4-nitrophenyl phosphate (DMNP). The authors concluded that the Zr-OH-Zr active site mimics the Lewis acid site found in enzymes.

MOF linkers can be substituted to contain additional functional groups to improve catalytic performance as well as increase the number of active sites.²⁵ In addition to ligand functional groups, nanoparticles can also be incorporated into a MOF structure to increase the available active sites in MOFs for catalysis applications. The typical routes for incorporation of nanoparticles is either through impregnation, in which a MOF is soaked in a solution of nanoparticles that diffuse into the MOF pore space, or insertion, a process where MOF is grown around the nanoparticles. Chen et. al.²⁶ was able to successfully incorporate gold nanoparticles into HKUST-1 (Hong Kong University of Science and Technology) for carbon monoxide oxidation. MOFs allow for the incorporation of a variety of different active sites due to the tailorability of both the metal node and linkers, as well as the incorporation of nanoparticles.

MOFs have also been considered as support materials for drug delivery applications. MOFs have large surface areas and pore volumes, making them potential carriers for medicine. Typically, when medicine is ingested, it is delivered at high dosages over short periods of time. MOFs may be tailored, such that they slowly degrade within the body, and release medicine continuously over an extended period. Panahi et. al.²⁷ loaded ibuprofen into DMOF (DABCO MOF) with an efficiency of roughly 50% and the MOF was able to steadily release the drug over the course of one day. While MOFs have shown promise as agents for drug delivery, more research is necessary to better understand the toxicity of ingesting MOFs and any long-term consequences caused by their consumption.²⁸

Due to the high surface areas and pore volumes of MOFs, they have also been considered for gas storage applications. Hydrogen storage has been extensively studied in the literature.²⁹⁻³¹ Ferey et. al.³² showed the potential for hydrogen storage in the MOFs: MIL-100 and MIL-101(Cr). MIL-101(Cr) has an exceptionally high surface area of 5500 m²/g and showed an uptake of 6.1 weight percent at 60 bar. The Department of Energy (DOE) has set a target of 6.5 weight percent hydrogen uptake for adsorbent materials and although current MOF technology has been unable to meet this standard, their performance has been steadily improving over the past few years.³³ Soon, MOFs may reach the DOE's target for hydrogen storage.

This dissertation will focus on MOFs for applications in separation processes, with particular interest on the interactions of MOFs when exposed to water vapor and acid gases such as H₂S and SO₂. Acid gases are common in a variety of industrial streams including natural gas, syn gas, and flue gas capture from power plants. H₂S and SO₂ must be removed

from these processes before processing steps or release into the atmosphere as they are highly corrosive and could damage process equipment; additionally, they are all highly toxic to the environment and contribute to acid rain. Current technology to remove SO_2 and H_2S acid gases from process streams typically involve liquid absorbent materials that strongly bind these acid gases.³⁴ Alkaline solutions are typically used to scrub sulfur containing species from flue gas streams and collect elemental sulfur for further processing. Carbon dioxide is another acid gas that is known to contribute to global warming. In response to the rising carbon dioxide emissions, some countries have imposed carbon taxes. Monoethanolamine (MEA) is the most commonly used absorbent to remove CO_2 from point sources. Regeneration costs for MEA (CO_2 capture) and alkaline solutions (SO_2 and H_2S capture) are expensive due to their strong adsorbent-adsorbate interactions. Therefore, new materials must be explored to perform these expensive separations. MOFs could potentially replace these costly materials as they are highly tailorable,^{35,36} and generally store gases via physisorption interactions.³⁷ Such interactions would cut down on the regeneration costs of these processes.

1.2 Synthesis of MOFs at Room Temperature

MOFs are traditionally synthesized via solvothermal methods, requiring heating for many days in solvents such as DMF, DMSO, or water. MOFs have also been formed using mechanosynthesis, sonication, microwave, and room temperature synthesis methods (the focus of this section).³⁸⁻⁴¹ These methods have advantages over solvothermal methods as they require less heat, solvent, or time, all of which have made scale-up of MOFs difficult and a topic of ongoing research.⁴² Room temperature synthesis methods are particularly

advantageous due to their simplicity and low energy costs. Instead of the long heating periods seen with traditional solvothermal synthesis, room temperature synthesis methods usually only require stirring or centrifuge to collect the MOF product. Additionally, many room temperature synthesis methods are fast and could potentially be used in continuous stirred reactors (CSTR) instead of the typical batch MOF processes. For these reasons, there has been a recent push in the literature towards alternative synthesis methods, including room temperature synthesis, which has shown to be feasible in: DMOF-1, ZnBD, UiO-66, ZIF-8, MIL-53(Al), and MIL-100.⁴³⁻⁴⁸ One concern that has not been addressed in the literature is whether these room temperature synthesis methods will produce MOFs of the same quality as those achieved from solvothermal methods. DeStefano et. al.⁴⁶ showed that the room temperature synthesis of UiO-66 resulted in a MOF with more defects than would typically be present when conducting a traditional solvothermal synthesis. The authors, however, did not confirm the water or chemical stability of the UiO-66 material made using their room temperature synthesis method. UiO-66 has been shown to be highly stable towards water, both liquid and vapor, and acidic solutions. UiO-66 is stable in water for two months, and stable when exposed to a pH 4 solution of HCl for two months. Most MOFs will degrade upon exposure to similar conditions.⁴⁹ Therefore, more work needs to be done when synthesizing MOFs using new methods to ensure that the materials formed meet the same stability and adsorption criteria as materials that were synthesized using traditional methods.

1.3 Defects in MOFs

MOFs are typically described as pristine ordered porous materials. However, in many cases, MOFs may contain defects. These defects may be deliberately incorporated into the MOF or a result of unavoidable imperfections that occur during synthesis. Point defects, such as missing cluster and missing linker, have been the primary mode of defects discussed in the literature.⁵⁰ Defects in UiO-66 have been generated using acidic modulators such as acetic acid and trifluoroacetic acid, which coordinate the metal sites that linkers would typically occupy. In UiO-66, these point defects have been identified as missing clusters and missing linkers. Currently however, it is difficult to quantify the exact number and types of defects experimentally. Researchers have been able to estimate the defects using computational modeling, where they compare the experimental and theoretical calculated surface areas.⁵⁰ Both missing cluster and missing linker defects will cause the measured MOF BET surface area per unit mass to deviate from the ideal. This is due to missing clusters lowering the sample weight, and missing linkers reducing the available surface sites for adsorption. Defects have been shown to improve the adsorption characteristics of MOFs towards a variety of adsorbates.^{51,52} While defects in UiO-66 have been studied at great length, the role of defects in other MOFs is not well understood.⁵³⁻⁵⁵ This dissertation seeks to identify the defect structures in other MOFs, and determine their role in MOF stability and adsorption performance.

In addition to point defects, MOFs have been studied through computational means to assess the feasibility and effects that extended defects may have on their structure. Han et. al.⁵⁶ characterized the impact that stacking faults in ZIF-8 have on the MOF structure. The authors found that these extended defects may impact the diffusion of adsorbates into

the MOF structure, effectively causing a change in the MOF's transport properties. This could have consequences on the separation performance of ZIF-8 in potential applications. De Vos et. al.⁵⁷ examined the electronics of defects in UiO-66(Ti,Hf) for applications in photocatalytic purposes. They found that the nodes of the UiO-66 defect structure with the strongest local distortions alter the electronic structure the most. Computational methods have been a vital part of MOF research and will likely continue to play a greater role as data science and big data moves to the forefront of academic research.

1.4 Water and Acid Gas Stability of MOFs

MOFs are a novel class of materials, and in the previous sections, several possible applications have been discussed. This section will focus on one of the pitfalls that many MOFs face, which is their instability towards water and acid gases, both of which are present in a variety of industrial streams. For example, MOF-74 has shown exceptional CO₂ adsorption capacity due to strong interactions with CO₂ at its open-metal sites, however the MOF degrades upon exposure to humidity in the air.^{58,59} Many other MOFs also degrade when exposed to humidity in the air. This instability raises concerns about the industrial viability of MOFs, which upon degradation, lose their desirable properties and cannot be reused or regenerated. One MOF that is known to be extremely stable is UiO-66. Even after being boiled in water or submerged in highly corrosive sulfuric acid for a week, UiO-66 maintained its crystallinity and BET surface area.^{58,60} To fully realize MOFs for industrial applications where humidity and water vapor are present, additional work needs to be done to identify and synthesize water stable MOFs.

Water stability of MOFs has been discussed extensively in the literature, however data for acid gas stability of MOF materials is not as well characterized. Tan et. al.⁶¹ collected SO₂ adsorption isotherms for DMOF containing nickel and zinc metal centers. The authors identified that the materials degraded due to the SO₂ exposure. Bhattacharyya et. al.⁶² investigated the stability of a series of ZIF materials when exposed to dry SO₂, humid SO₂, and sulfuric acid, and found stability relationships as well as degradation rates for these materials. The authors identified ZIF-71 as the only material stable towards all exposure environments, and they attributed this stability to the combination of low linker pK_a and the inherent hydrophobicity of the framework. Other hazardous gases, such as H₂S and NO₂, have been shown to degrade these same materials that are stable towards dry SO₂.⁶²⁻⁶⁴ While the initial work at UNCAGE-ME (a DOE EFRC research center) has focused primarily on MOF interactions with SO₂, the center's research will now shift towards the less well-studied H₂S and NO₂.

1.5 Dissertation Scope

This dissertation seeks to assess the stability of MOFs towards acid gases, such as SO₂ and H₂S, and water, as well as address the role that defects in MOF structure have on their stability and adsorption properties. This goal was achieved by researching the following three objectives: 1) select a platform MOF material to investigate how metal site and ligand functional groups can impact the material's stability and adsorption properties towards acid gases, 2) induce defects into the platform material through novel room temperature synthesis methods, 3) explore other MOFs interactions with acid gases and the

role that synthesis and defects play in the materials stability and adsorption properties. Further details regarding these objectives will be defined in the chapters that follow.

1.6 References

- [1] Li, H.; Eddaoudi, M.; O’Keeffe, M.; Yaghi, O. Design and Synthesis of an Exceptionally Stable and Highly Porous Metal–Organic Framework. *Nature*. **1999**, 402, 276-279.
- [2] Cambridge Structural Database. Data Update – May 2017. <https://www.ccdc.cam.ac.uk/support-and-resources/ccdcresources/csd-2017-updates/>. (Accessed 8/1/2017)
- [3] Wang, L.; Deng, H.; Furukawa, H.; Gandara, F.; Cordova, K.; Peri, D.; Yaghi, O. Synthesis and Characterization of Metal–Organic Framework-74 Containing 2, 4, 6, 8, and 10 Different Metals. *Inorg. Chem.* **2014**, 53, 5881-5883.
- [4] Diaz-Garcia, M.; Sanchez-Sanchez, M. Synthesis and Characterization of a New Cd-based Metal–Organic Framework Isostructural with MOF-74/CPO-27 Materials. *Microporous Mesoporous Mater.* **2014**, 190, 248-254.
- [5] Yuan, S.; Lu, W.; Chen, Y.; Zhang, Q.; Liu, T.; Feng, D.; Wang, X.; Qin, J.; Zhou, H. Sequential Linker Installation: Precise Placement of Functional Groups in Multivariate Metal–Organic Frameworks. *J. Am. Chem. Soc.* **2015**, 137, 3177-3180.
- [6] Dau, P.; Kim, M.; Garibay, S.; Munch, F.; Moore, C.; Cohen, S. Single-Atom Ligand Changes Affect Breathing in an Extended Metal–Organic Framework. *Inorg. Chem.* **2012**, 51, 5671-5676.
- [7] Cmarik, G.; Kim, M.; Cohen, S.; Walton, K. Tuning the Adsorption Properties of UiO-66 via Ligand Functionalization. *Langmuir*. **2012**, 28, 15606-15613.
- [8] Millward, A.; Yaghi, O. Metal–Organic Frameworks with Exceptionally High Capacity for Storage of Carbon Dioxide at Room Temperature. *J. Am. Chem. Soc.* **2005**, 127, 17998-17999
- [9] Burtch, N.; Jasuja, H.; Dubbeldam, D.; Walton, K. Molecular-level Insight into Unusual Low Pressure CO₂ Affinity in Pillared Metal–Organic Frameworks. *J. Am. Chem. Soc.* **2013**, 135, 7172-7180.
- [10] Chun, H.; Dybtsev, D.; Kim, H.; Kim, K. Synthesis, X-ray Crystal Structures, and Gas Sorption Properties of Pillared Square Grid Nets Based on Paddle-Wheel Motifs: Implications for Hydrogen Storage in Porous Materials. *Chem. Eur. J.* **2005**, 11, 3521-3529.

- [11] Chen, Y.; Lee, J.; Babarao, R.; Li, J.; Jiang, J. A Highly Hydrophobic Metal–Organic Framework Zn(BDC)(TED)_{0.5} for Adsorption and Separation of CH₃OH/H₂O and CO₂/CH₄: An Integrated Experimental and Simulation Study. *J. Phys. Chem. C*. **2010**, 114, 6602-6609.
- [12] Dau, P.; Cohen, S. Cyclometalated Metal–Organic Frameworks as Stable and Reusable Heterogeneous Catalysts for Allylic N-alkylation of Amines. *Chem. Commun.* **2013**, 49, 6128-6130.
- [13] Li, Z.; Peters, A.; Bernales, V.; Ortuno, M.; Schweitzer, N.; DeStefano, M.; Gallington, L.; Platero-Prats, A.; Chapman, K.; Cramer, C.; Gagliardi, L.; Hupp, J.; Farha, O. Metal–Organic Framework Supported Cobalt Catalysts for the Oxidative Dehydrogenation of Propane at Low Temperature. *ACS Central Science*. **2016**, 3, 31-38.
- [14] Tu, T.; Nguyen, K.; Nguyen, T.; Truong, T.; Phan, N. New Topological Co₂(BDC)₂(DABCO) as a Highly Active Heterogeneous Catalyst for the Amination of Oxazoles via Oxidative C–H/N–H Couplings. *Catal. Sci. Technol.* **2016**, 6, 1384-1392.
- [15] Lee, J.; Farha, O.; Roberts, J.; Scheidt, K.; Nguyen, S.; Hupp, T. Metal–Organic Framework Materials as Catalysts. *Chem. Soc. Rev.* **2009**, 38, 1450-1459.
- [16] Vasconcelos, I.; Wanderley, K.; Rodrigues, N.; Costa, N.; Freire, R.; Junior, S. Host-guest Interaction of ZnBDC-MOF þ Doxorubicin: A Theoretical and Experimental Study. *Journal of Molecular Structure*. **2017**, 1131, 36-42.
- [17] Yang, R.; Li, Y. Gas Adsorption and Storage in Metal-Organic Framework MOF-177. *Langmuir*. **2007**, 23, 12937-12944.
- [18] Rowsell, J.; Yaghi, O. Strategies for Hydrogen Storage in Metal–Organic Frameworks. *Angew. Chem. Int. Ed.* **2005**, 44, 4670-4679.
- [19] Latroche, M.; Surble, S.; Serre, C.; Mellot-Draznieks, C.; Llewellyn, P.; Lee, J.; Chang, J.; Jhung, S.; Ferey, G. Hydrogen Storage in the Giant-Pore Metal–Organic Frameworks MIL-100 and MIL-101. *Angew. Chem.* **2006**, 118, 8407-8411.
- [20] Lahoz-Martin, F.; Calero, S.; Gutierrez-Sevillano, J.; Martin-Calvo, A. Adsorptive Separation of Ethane and Ethylene using IsoReticular Metal-Organic Frameworks. *Microporous Mesoporous Mater.* **2017**, 248, 40-45.
- [21] Zhang, K.; Lively, R.; Zhang, C.; Chance, R.; Koros, W.; Sholl, D.; Nair, S. Exploring the Framework Hydrophobicity and Flexibility of ZIF-8: From Biofuel Recovery to Hydrocarbon Separations. *J. Phys. Chem. Lett.* **2013**, 4, 3618-3622.
- [22] Zhang, C.; Lively, R.; Zhang, K.; Johnson, J.; Karvan, O.; Koros, W. Unexpected Molecular Sieving Properties of Zeolitic Imidazolate Framework-8. *J. Phys. Chem. Lett.* **2012**, 3, 2130-2134.

- [23] He, Y.; Shang, J.; Gu, Q.; Li, G.; Li, J.; Singh, R.; Xiao, P.; Webley, P. Converting 3D Rigid Metal-Organic Frameworks (MOFs) to 2D Flexible Networks via Ligand Exchange for Enhanced CO₂/N₂ and CH₄/N₂ Separation. *Chem. Commun.* **2015**, 51, 14716-14719.
- [24] Mondloch, J.; Katz, M.; Isley III, W.; Ghosh, P.; Liao, P.; Bury, W.; Wagner, G.; Hall, M.; DeCoste, J.; Peterson, G.; Snurr, R.; Cramer, C.; Hupp, J.; Farha, O. Destruction of Chemical Warfare Agents using Metal-Organic Frameworks. *Nature Materials*. **2015**. 14, 512-516.
- [25] Joshi, J.; Garcia-Gutierrez, E.; Moran, C.; Deneff, J.; Walton, K. Engineering Copper Carboxylate Functionalities on Water Stable Metal-Organic Frameworks for Enhancement of Ammonia Removal Capacities. *J. Phys. Chem. C*. **2017**, 121, 3310-3319.
- [26] Liu, Y.; Zhang, J.; Song, L.; Xu, W.; Guo, Z.; Yang, X.; Wu, X.; Chen, X. Au-HKUST-1 Composite Nanocapsules: Synthesis with a Coordination Replication Strategy and Catalysis on CO Oxidation. *ACS Appl. Mater. Interfaces*. **2016**. 8, 22745-22750.
- [27] Nadizadeh, Z.; Naimi-Jamal, M.; Panahi, L. Mechanochemical Solvent-Free In Situ Synthesis of Drug-Loaded {Cu₂(1,4-BDC)₂(DABCO)}_n MOFs for Controlled Drug Delivery. *Journal of Solid State Chemistry*. **2018**. 259, 35-42.
- [28] Horcajada, P.; Serre, C.; Vallet-Regi, M.; Sebban, M.; Taulelle, F.; Gericq, G. Metal-organic Frameworks as Efficient Materials for Drug Delivery. *Angew. Chem.* **2006**, 118, 6120-6124.
- [29] Suh, M.; Park, H.; Prasad, T.; Lim, D. Hydrogen Storage in Metal-Organic Frameworks. *Chemical Reviews*. **2012**, 112, 782-835.
- [30] Rowsell, J.; Yaghi, O. Strategies for Hydrogen Storage in Metal-Organic Frameworks. *Angew. Chem. Int. Ed.* **2005**, 44, 4670-4679.
- [31] Murray, L.; Dinca, M.; Long, J. Hydrogen Storage in Metal-Organic Frameworks. *Chem. Soc. Rev.* **2009**, 38, 1294-1314.
- [32] Latroche, M.; Surble, S.; Serre, C.; Mellot-Draznieks, C.; Llewellyn, P.; Lee, J.; Chang, J.; Jung, S.; Ferey, G. Hydrogen Storage in the Giant-Pore Metal-Organic Frameworks MIL-100 and MIL-101. *Angew. Chem.* **2006**. 118, 8407-8411.
- [33] Department of Energy Office of Energy Efficiency & Renewable Energy. <https://www.energy.gov/eere/fuelcells/doe-technical-targets-onboard-hydrogen-storage-light-duty-vehicles>. (Accessed 5/1/2018)
- [34] Nolan, P. Flue Gas Desulfurization Technologies for Coal-Fired Power Plants. The Babcock & Wilcox Company. 2000.

- [35] Queen, W.; Hudson, M.; Bloch, E.; Mason, J.; Gonzalez, M.; Lee, J.; Gygi, D.; Howe, J.; Lee, K.; Darwish, T.; James, M.; Peterson, V.; Teat, S.; Smit, B.; Neaton, J.; Long, J.; Brown, C. Comprehensive Study of Carbon Dioxide Adsorption in Metal-Organic Frameworks $M_2(\text{DOBDC})$ ($M=\text{Mg, Mn, Fe, Co, Ni, Cu, Zn}$). *Chem. Sci.* **2014**, 5, 4569-4581.
- [36] Jasuja, H.; Huang, Y.; Walton, K. Adjusting the Stability of Metal-Organic Frameworks Under Humid Conditions by Ligand Functionalization. *Langmuir*. **2012**, 29, 633-642.
- [37] Sumida, K.; Rogow, D.; Mason, J.; McDonald, T.; Cloch, E.; Herm, Z.; Bae, T.; Long, J. Carbon Dioxide Capture in Metal-Organic Frameworks. *Chem. Rev.* **2012**, 112, 724-781.
- [38] Katsenis, A.; Puskaric, A.; Strukil, V.; Mottillo, C.; Julien, P.; Uzarevic, K.; Pham, M.; Do, T.; Kimber, S.; Lazic, P.; Magdysyuk, O.; Dinnebier, R.; Halasz, I.; Friscic, T. In Situ X-ray Diffraction Monitoring of a Mechanochemical Reaction Reveals a Unique Topology Metal-Organic Framework. *Nature Communications*. **2015**, 6, 1-8.
- [39] Cabello, C.; Arean, C.; Parra, J.; Ania, C.; Rumori, P.; Palomino, G. A Rapid Microwave-assisted Synthesis of a Sodium-Cadmium Metal-Organic Framework having Improved Performance as a CO_2 Adsorbent for CCS. *Dalton Transactions*. **2015**, 44, 9955-9963.
- [40] Tranchemontagne, D.; Hunt, J.; Yaghi, O. Room Temperature Synthesis of Metal-Organic Frameworks: MOF-5, MOF-74, MOF-177, MOF-199, and IRMOF-0. *Tetrahedron*. **2008**, 64, 8553-8557.
- [41] Stock, N.; Biswas, S. Synthesis of Metal-Organic Frameworks (MOFs): Routes to Various MOF Topologies, Morphologies, and Composites. *Chem. Rev.* **2012**, 112, 933-969.
- [42] Kim, S.; Lee, Y.; Hong, S.; Jang, M.; Ahn, W. Pilot-scale Synthesis of a Zirconium Benzenedicarboxylate UiO-66 for CO_2 Adsorption and Catalysis. *Catalysis Today*. **2015**, 245, 54-60.
- [43] Hungerford, J.; Walton, K. Room Temperature Synthesis of Metal-organic Framework Isomers in the Tetragonal and Kagome Crystal Structure. *Inorganic Chemistry*. Submitted.
- [44] Duan, C.; Li, F.; Xiao, J.; Liu, Z.; Li, C.; Xi, H. Rapid Room-Temperature Synthesis of Hierarchical Porous Zeolitic Imidazolate Frameworks with High Space-time Yield. *Sci. China Mater.* **2017**, 60, 1205-1214.
- [45] Pan, Y.; Liu, Y.; Zeng, G.; Zhao, L.; Lai, Z. Rapid Synthesis of Zeolitic Imidazolate Framework-8 (ZIF-8) Nanocrystals in an Aqueous System. *Chem. Commun.* **2011**, 47, 2071-2073.

- [46] DeStefano, M.; Islamoglu, T.; Garibay, S.; Hupp, J.; Farha, O. Room-Temperature Synthesis of UiO-66 and Thermal Modulation of Densities of Defect Sites. *Chem. Mater.* **2017**, 29, 1357-1361.
- [47] Guesh, K.; Caiuby, C.; Mayoral, A.; Diaz-Garcia, M.; Diaz, I.; Sanchez-Sanchez, M. Sustainable Preparation of MIL-100(Fe) and its Photocatalytic Behavior in the Degradation of Methyl Orange in Water. *Cryst. Growth Des.* **2017**, 17, 1806-1813.
- [48] Zhou, K.; Chaemchuen, S.; Wu, Z.; Verpoort, F. Rapid Room Temperature Synthesis Forming Pillared Metal-Organic Frameworks with Kagome Net Topology. *Microporous Mesoporous Mater.* **2017**, 239, 28-33.
- [49] Leus, K.; Bogaerts, T.; Decker, J.; Depauw, H.; Hendrickx, K.; Vrielinck, H.; Speybroeck, V.; Voort, P. Systematic Study of the Chemical and Hydrothermal Stability of Selected “Stable” Metal-Organic Frameworks. *Microporous Mesoporous Mater.* **2016**, 226, 110-116.
- [50] Cliffe, M.; Wan, W.; Zou, X.; Chater, P.; Kleppe, A.; Tucker, M.; Wilhelm, H.; Funnell, N.; Coudert, F.; Goodwin, A. Correlated Defect Nanoregions in a Metal-Organic Framework. *Nature Communications.* **2014**, 5(4176).
- [51] Liang, W.; Coghlan, C.; Ragon, F.; Rubio-Martinez, M.; D'Alessandro, D.; Babarao, R. Defect Engineering of UiO-66 for CO₂ and H₂O Uptake - a Combined Experimental and Simulation Study. *Dalton Transactions.* **2016**, 45, 4496-4500.
- [52] Shearer, G.; Chavan, S.; Bordiga, S.; Svelle, S.; Olsbye, U.; Lillerud, K. Defect Engineering: Tuning the Porosity and Composition of the Metal-Organic Framework UiO-66 via Modulated Synthesis. *Chem. Mater.* **2016**, 28, 3749-3761.
- [53] Wu, D.; Yan, W.; Xu, H.; Zhang, E.; Li, Q. Defect Engineering of Mn-based MOFs with Rod-shaped Building Units by Organic Linker Fragmentation. *Inorganica Chimica Acta.* **2017**, 460, 93-98.
- [54] Fang, Z.; Bueken, B.; De Vos, D.; Fischer, R. Defect-engineered Metal-organic Frameworks. *Angew. Chem. Int. Ed.* **2015**, 54, 7234-7254.
- [55] Zhang, W.; Kauer, M.; Guo, P.; Kunze, S.; Cwik, S.; Muhler, M.; Wang, Y.; Epp, K.; Kieslich, G.; Fischer, R. Impact of Synthesis Parameters on the Formation of Defects in HKUST-1. *Eur. J. Inorg. Chem.* **2017**, 925-931.
- [56] Han, R.; Sholl, D. Computational Model and Characterization of Stacking Faults in ZIF-8 Polymorphs. *J. Phys. Chem. C.* **2016**, 120, 27380-27388.
- [57] De Vos, A.; Hendrickx, K.; Van Der Voort, P.; Van Speybroeck, V.; Lejaeghere, K. Missing Linkers: An Alternative Pathway to UiO-66 Electronic Structure Engineering. *Cham. Mater.* **2017**, 29, 3006-3019.

- [58] Burch, N.; Jasuja, H.; Walton, K. Water Stability and Adsorption in Metal-organic Frameworks. *Chem. Rev.* **2014**, 114, 10575-10612.
- [59] Peng, X.; Lin, L.; Sun, W.; Smit, B. Water Adsorption in Metal-organic Frameworks with Open-metal Sites. *AIChE Journal*. **2015**, 61, 677-687.
- [60] Cavka, J.; Jakobsen, S.; Olsbye, U.; Guillou, N.; Lamberti, C.; Bordiga, S.; Lillerud, K. A New Zirconium Inorganic Building Brick Forming Metal-organic Frameworks with Exceptional Stability. *J. Am. Chem. Soc.* **2008**, 130, 13850-13851.
- [61] Tan, K.; Canepa, P.; Gong, Q.; Liu, J.; Johnson, D.; Dyevoich, A.; Thallapally, P.; Thonhauser, T.; Li, J.; Chabal, Y. Mechanism of Preferential Adsorption of SO₂ into Two Microporous Paddle Wheel Frameworks M(bdc)(ted)_{0.5}. *Chem. Mater.* **2013**, 25, 4653-4662.
- [62] Bhattacharyya, S.; Han, R.; Kim, W.; Chiang, Y.; Jayachandrababu, K.; Hungerford, J.; Dutzer, M.; Ma, C.; Walton, K.; Sholl, D.; Nair, S. Acid Gas Stability of Zeolitic Imidazolate Frameworks: Generalized Kinetic and Thermodynamic Characteristics. *Chem. Mater.* **2018**, 30, 4089-4101.
- [63] Hungerford, J.; Bhattacharyya, S.; Tumuluri, U.; Nair, S.; Wu, Z.; Walton, K.; DMOF-1 as a Representative MOF for SO₂ Adsorption in Both Humid and Dry Conditions. *J. Phys. Chem. C*. **2018**, 122, 23493-23500.
- [64] Liu, J.; Wei, Y.; Li, P.; Zhao, Y.; Zou, R. Selective H₂S/CO₂ Separation by Metal-organic Frameworks Based on Chemical-physical Adsorption. *J. Phys. Chem. C*. **2017**, 121, 13249-13255.

CHAPTER 2: EXPERIMENTAL MATERIALS AND METHODS

Chapter two of this dissertation will discuss the materials and methods that were utilized to conduct synthesis and investigate water, CO₂, and acid gas adsorption and exposure experiments in MOFs. This chapter contains two sections: 1) a background on the previous research involving the platform material, DMOF, as well as UiO-66, ZIF-8, and Cu-BTC, three MOFs which will be utilized throughout this dissertation. 2) A section describing the experimental methodologies that were used in conducting this dissertation work as well as the limitation of experimental techniques and the limitations of MOFs for applications in adsorption-based separations.

2.1 MOF Materials

2.1.1 *DMOF as a Platform Material*

DMOF, also known as DABCO MOF, is a pillared MOF. Pillared MOFs contain two different ligands, one ligand forms sheets in the AB-plane that are connected by the pillaring ligand to extend the MOF into the C-direction. DMOF contains terephthalic acid (BDC) ligands connecting metal nodes and the pillared ligand 1,4-diazabicyclo[2.2.2]octane (DABCO), see Figure 2.1 for a diagram of DMOF.¹ DMOF synthesizes in the P4/mmm space group and has tetragonal symmetry, it contains a 7.5 x 7.5 Å pore window in the AB-plane (BDC-BDC) and a 7.5 x 5.0 Å pore window in the AC and BC-planes (BDC-DABCO). DMOF can be easily tailored by both metal substitution (M = Zn, Ni, Co, or Cu) and ligand substitution (L = terephthalic acid (BDC), 2,3,5,6-

tetramethylterephthalic acid (TM), 2,5-dimethylterephthalic acid (DM), 2-aminoterephthalic acid (BDC-NH₂), 9,10-anthracenedicarboxylic acid (ADC)). The metal used to synthesize DMOF generally consists of a nitrate-based metal salt which can be used for all the available metal substitutions presented above. From here on DMOF containing BDC ligands will be referred to as parent DMOF and all ligand and metal functionalities will be referred to as M-DMOF-L. The tailorability of DMOF makes it an excellent candidate to study water and acid gas stability as well as adsorption characteristics and is the primary reason it was selected as the platform material for this dissertation.

Parent DMOF typically contains the zinc metal node, however it has also been synthesized with nickel, cobalt, and copper metal nodes.^{2,3} Tailoring DMOF through metal substitutions has been shown by Tan et. al.³ to impact the water adsorption and degradation mechanisms in parent DMOF. The authors showed that the preferred pathway for water degradation in DMOF varied across the metal centers. Co and Zn-DMOF both degraded via bond breaking at the metal-oxygen coordination bond whereas Cu-DMOF degraded due to bond breakage at the copper-nitrogen bond. Ni-DMOF simulations showed a more complex degradation mechanisms requiring more energy than what was required to break the bonds in the Co and Zn-DMOF simulations.³ (Appendix C of this dissertation provides a thorough overview of previous water adsorption studies involving the platform DMOF material.) Metal substitution has also been shown to play a role in the stability of M-DMOF-TM when exposed to humid SO₂.⁴ In this work the authors showed that the material stability followed the Irving Williams series: Co < Ni < Cu > Zn,^{5,6} which predicts metal-ligand bond strength based on three criteria: 1) metal atom size, 2) ligand field stabilization energy, and 3) Jahn-Teller distortion.⁷ While DMOF does not contain open metal sites, the

metal center has been shown to affect the stability of the material when exposed to water (parent DMOF) and acid gases (M-DMOF-TM) and metal node should be a consideration when designing stable MOFs for applications where water and acid gases are present.

Instability towards humidity and liquid water is a common concern shared among many MOFs in the literature.⁸ Parent DMOF has been shown to be unstable in air above 50% relative humidity (RH) and is completely unstable in liquid water. DMOF is a hydrophobic MOF and adsorbs very little water from 0 – 40% RH, between 40 and 50% RH its water adsorption isotherm undergoes a step change in quantity adsorbed followed by degradation at 50% RH. Ligand substitutions, however, have been shown to drastically improve DMOF's humid stability. Jasuja et. al.⁹ showed that by substituting BDC with either TM or ADC resulted in a framework isomer exhibiting complete stability upon exposure to 90% RH. The improved stability of Zn-DMOF-TM has been attributed to the steric effects of the four methyl groups on the TMBDC ligand, which inhibit the attack of water molecules on the metal nodes.¹⁰ Additionally parent DMOF and DMOF-TM have small structural differences as a result of the bulky methyl groups, the BDC linkers in DMOF are parallel to the AB-plane. The TMBDC linkers in DMOF-TM are at slight angles to account for the bulkiness of the linkers, this results in increased hydrophobicity of the metal node and improves the humid stability of DMOF-TM. Burtch et. al.¹¹ utilized high intensity PXRD to develop an electron density envelop and determine where water vapor lies within the MOF structure at different humidity concentrations between 0 – 80% RH in Zn-DMOF-TM. Ligand functionalization in DMOF has been shown to allow tuning of the water stability, however the impacts of acid gas stability have not been completely characterized.

In addition to metal and ligand substitutions, DMOF also shares the same precursors ($\text{Zn}(\text{NO}_3)_2 \cdot 6\text{H}_2\text{O}$, BDC, and DABCO) as another MOF, ZnBD, see Figure 2.1.^{12,13} ZnBD differs from DMOF by topology. While DMOF forms in the tetragonal crystal structure, ZnBD forms a Kagome lattice in the BDC plane which are connected by DABCO in the C-direction similarly to DMOF. ZnBD forms two 1-D channels, a large 15 Å hexagonal pore and a smaller 4.5 Å triangular pore, both are in the AB-plane (BDC). While DMOF stability has been well characterized in the literature, ZnBD has not. For these reasons, DMOF was selected as a platform material for studying acid gas and water interactions, and ZnBD was also used to compare to DMOF as they contain the same linkers and metal centers but differ in structure.

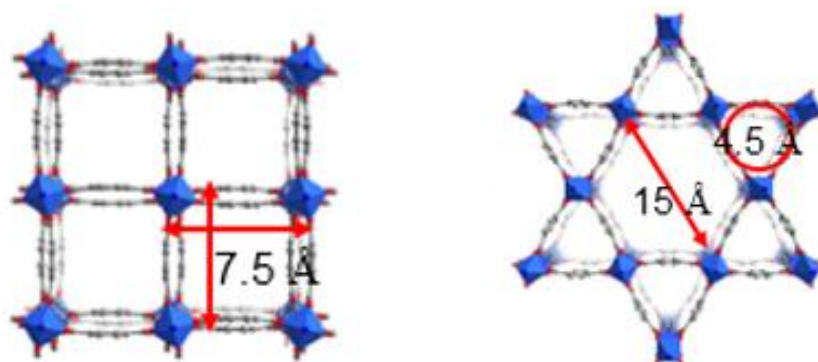


Figure 2.1: Structures of DMOF (left) and ZnBD (right) viewing down the AB-plane (BDC). “Reproduced from 12. Copyright 2017, Elsevier.”

2.1.2 UiO-66

In the previous section, DMOF was discussed as a platform material. One shortcoming of DMOF that was discussed is its instability towards humidity and liquid water. UiO-66 (UiO = University of Oslo) is a highly coordinated MOF, coordination

number of 12, that typically contains a zirconium metal center connected by BDC linkers (see Figure 2.2). Unlike DMOF, UiO-66 is highly stable towards humidity, boiling water, and is even stable when submerged in acids.¹⁴ Due to its tremendous stability, UiO-66 has been investigated for a variety of applications where water or acid gases may be present, these applications include: hydrogenation of CO₂ to methanol, toxic chemical removal of dimethyl 4-nitrophenylphosphate, and water based separations.¹⁵⁻¹⁷

UiO-66 has shown the successful incorporation of nanoparticles into the structure for a variety of applications in catalysis. Tulig et. al.^{18,19} encapsulated gold nanoparticles in UiO-66 to catalytically oxidize CO to CO₂. The authors achieved nearly a 100% conversion of CO at 448 K after calcination of the samples to remove the capping ligand used in the synthesis of the MOF-nanoparticle composite. Joshi et. al.²⁰ investigated incorporating copper into the structure of UiO-66 containing carboxylic acid functionalized ligands through two methods: 1) encapsulation of copper nanoparticles and 2) insertion of copper onto the carboxylic acid groups of the functionalized ligand. The incorporation of copper sites into the UiO-66 framework was to improve ammonia adsorption capacity. The authors found that the incorporation of two carboxylic acid functional groups onto the ligands of UiO-66 produced the highest adsorptive uptake for ammonia, reaching a capacity of 6.38 mmol/g in dry conditions and 6.84 mmol/g in wet conditions. UiO-66 has not only shown extreme stability, but also tailorability through ligand functionalization and the incorporation of catalytically active nanoparticles.

While MOFs are typically described as perfect porous structures, in practice they often contain many structure defects.²¹ UiO-66 has proven to be an ideal candidate to study defect interactions in MOFs due to its coordination environment and exceptional stability

towards water and acidic conditions. Liang et. al.²² has shown that incorporation of acidic modulators into the synthesis of UiO-66 leads to an increase in the number of missing linker defects without detriment to the material's water stability. This increase in the number of defect sites in UiO-66 coincides with an increase in the MOF's surface area as well as its adsorptive properties for target gas species. Jiao et. al.²³ observed a 20% increase in the SO₂ adsorption of UiO-66 upon incorporation of defects into the structure. Wu. et. al.²⁴ showed that even without the use of acid modulator, defects arise in UiO-66 at a surprising high rate of roughly 10 % suggesting that defects are an inherent quality of MOFs. Defects in UiO-66 should be further explored to better understand the breaking point between defect concentration and material stability, as well as determine whether defect knowledge gained by studying UiO-66 can be transferred to other MOF systems.

UiO-66 was selected as a complementary material to DMOF for studying acid gas interactions for three primary reasons. First, it is a highly studied material that has been investigated for a variety of applications and is highly tunable through incorporation of linker functional groups, nanoparticles, and defective sites, making it a potential candidate for adsorption-based separations.²⁵⁻²⁸ Also it has shown extreme stability, a trait that is rather unusual among MOF materials.⁸ Lastly, UiO-66 and DMOF share BDC as a linker material and allow for investigations into coordination number and topology and how they affect MOF stability.

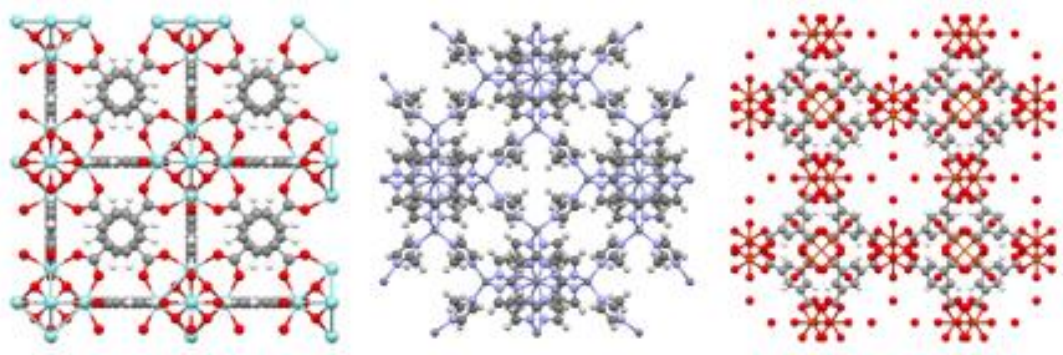


Figure 2.2: Structures of UiO-66 (left), ZIF-8 (middle), and CuBTC (right)^{14,29} (viewing AC-plane)

2.1.3 ZIF-8

ZIF-8 is a Zeolitic Imidazolate Framework (ZIF) containing a zinc metal node connected by 2-methylimidazole linkers, see Figure 2.2. ZIFs are a subsection of MOFs that share topologies with zeolites,³⁰ which are a class of porous aluminum-silicate materials. ZIF-8 forms in the sodalite topology (zeolite-type structure) with a cubic I-43m space group and contains large pores 11.6 Å in diameter which are accessible through 3.4 Å windows.³¹ Unlike many MOFs, ZIF-8 is very stable towards water; ZIF-8 maintains its structure even after being submerged for 7 days in boiling water.²⁹ The combination of excellent chemical stability and a small pore windows has made ZIF-8 an attractive material for gas-based separations. Additionally, ZIF-8 has been successfully incorporated into a variety of MOF-polymer composite membranes, showing potential for further processing and applications.^{32,33}

ZIF-8 has been shown to be a viable candidate for several difficult and energy intensive gas separations. Venna et. al.³¹ showed the effectiveness of ZIF-8 membranes for CO₂/CH₄ separation. The authors incorporated ZIF-8 into an α -alumina support while

maintaining a surface area of 1072 m²/g and micropore volume of 0.53 cm³/g. This membrane displayed excellent CO₂ permeance of 2.4 x 10⁻⁵ mol/m²·s·Pa (0.0072 GPU) and proved to be selective for CO₂ achieving a selectivity of 7 for CO₂/CH₄ separations. In addition to CO₂/CH₄ selectivity, a ZIF-8 analog has also been utilized for hydrocarbon/alkene separations. Mondal et. al.³⁴ showed the efficacy of using partially fluorinated ZIF-8 in ethane/ethylene separations and Ramu et. al.³⁵ achieved a propylene/propane separation factor of 105 in ZIF-8 membranes. The selectivity of ZIF-8 towards these molecules has primarily been attributed to its small pore window resulting in a molecular sieving effect for separation applications.

ZIF-8 was selected as a complementary material for studying acid gas interactions for the following reasons. First, it has shown potential in a variety of separation processes as a result of its small pore window and molecular sieving effect.³⁶⁻³⁸ Also, it has been successfully incorporated into membrane materials showing that it has excellent processability.³⁹ Additionally, ZIF-8 is stable in humidity and has shown stability when submerged in boiling water.³³ Lastly, ZIF-8 is in the class of MOFs that contain imidazolate linkers (aromatic heterocycle with non-adjacent nitrogen atoms), which offers some similarity to DMOF, which also contains nitrogen groups in its pillared DABCO linker.

2.1.4 Cu-BTC

Cu-BTC, also known as HKUST-1 (Hong Kong University of Science and Technology), is an open-metal site MOF which contains copper nodes connected by trimesic acid linkers (BTC), see Figure 2.2. Open-metal site MOFs contain uncoordinated metal sites which allow for strong adsorbent-adsorbate interactions. Cu-BTC forms in the space group Fm and has a pore diameter of 10.7 Å.⁴⁰ Unlike UiO-66 and ZIF-8, Cu-BTC is not stable towards water. Once activated Cu-BTC will adsorb water from the air at its

open-metal site which will lead to framework degradation.⁴¹ Therefore, Cu-BTC is not suitable for applications where humidity or liquid water are present.

Cu-BTC has shown potential as an adsorbent for CO₂ capture. While Cu-BTC has poor water stability several authors have found methods to improve the material's water stability while not negatively impacting the materials CO₂ adsorption capacity. Wu et. al.⁴² grafted glycine onto the open-metal site of Cu-BTC which not only led to increased CO₂ adsorption capacity, but also inhibited degradation by blocking water molecules from coordinating to the open-metal site. Cu-BTC grafted with glycine displayed a 12% increase in CO₂ adsorption reaching a capacity of 5.4 mmol/g at 1 bar of CO₂. The material was also selective for CO₂ over CH₄ and N₂ having selectivities of 8.5 and 59.4 respectively. Lin et. al.⁴³ similarly grafted acetonitrile onto the open-metal site which once again led to increased water stability and CO₂ adsorption. The authors reported a CO₂ capacity of 4.3 mmol/g at 1 bar of CO₂.

Cu-BTC was selected as a complementary material to study acid gas interactions for the following reasons. Unlike UiO-66, DMOF, and ZIF-8, Cu-BTC contains open-metal sites and has shown to be an attractive material for CO₂ adsorption and separations. While the stability of the material towards water and acid gases is poor, others have shown that the water stability of the material can be improved by grafting acetonitrile or glycine onto the open-metal site.^{42,43} Additionally, copper was found to be the most stable metal center in DMOF-TM (see chapter 4) upon exposure to humid SO₂ and further investigating copper-based MOFs was desirable. SO₂ interactions with copper-based MOFs is an area of ongoing research as there is uncertainty in the MOF community as to whether SO₂ coordinates strongly to copper open-metal sites.^{44,45}

2.2 Experimental Methods

This section will discuss some of the limitations of MOFs, as well as the limitations of the experimental techniques that have been employed to study MOF materials. Appendix A contains the solvothermal and room temperature synthesis methods for DMOF-TM, UiO-66, and ZIF-8 which were used throughout this dissertation. Appendix B provides a thorough description of the characterization techniques and adsorption experiments that were used in this dissertation. I direct the reader to these appendices for any clarifications regarding synthesis methods (APPENDIX A: MOF SYNTHESIS PROCEDURES), characterization techniques, and adsorption experiments (APPENDIX B: CHARACTERIZATION AND EXPERIMENTAL TECHNIQUES).

2.2.1 *Limitations of MOFs*

In chapter 1 the general instability of MOF materials towards water vapor was discussed in detail and will not be expanded further in this section. This section will focus on two other limitations of MOFs: 1) process scale-up and 2) the expense of starting materials. MOFs have not gained widespread use in industry; however, a few startups have emerged in recent years using MOFs for specialty applications. MOF Technologies is a UK based company founded in 2014 that uses a MOF to slowly release the chemical compound 1-methylcyclopropene.⁴⁶ 1-methylcyclopropene is a synthetic plant growth regulator that slows the ripening process of fruits and vegetables, allowing them to stay fresh longer. NuMat Technologies was founded in 2012 and is based outside of Chicago.⁴⁷ NuMat uses a MOF material to deliver dopant gases electronically, this process takes advantage of the lower binding energies in MOFs compared to traditional materials. In the

near future it is likely that new startups will continue to use MOFs for niche applications that can best take advantage of their chemical diversity.

Traditional lab scale MOF syntheses utilize batch reactors and generally produce MOFs with low (milligram) yields. Kim et. al.⁴⁸ constructed a pilot scale synthesis of UiO-66 using a 5 L vessel and was able to produce a material with similar surface area and PXRD patterns as would be produced in a lab-bench scale synthesis. Recent work has also begun to expand to new synthesis routes that allow for process scale-up and increased yield. Crawford et. al.⁴⁹ synthesized Cu-BTC and ZIF-8 mechanochemically using an extrusion process. Using this technique, the authors were able to produce ZIF-8 at a rate of 4 kg/h while using minimal solvent. Further experimentation needs to be conducted in order to develop and better understand new MOF synthesis methods that can be easily scaled, as well as understand how the properties of the produced MOFs are impacted by synthesis procedures.

In addition to MOF scale-up, the expense of linkers and solvent is a limitation that MOFs have faced in becoming industrially viable. MOFs synthesized using batch processes generally require large quantities of solvent relative to the yield. Common MOF solvents, such as DMF, are hazardous and degrade during solvothermal synthesis such that they cannot be recovered post synthesis. New synthesis techniques that use less solvent, use more environmentally friendly solvents, and allow for solvents to be recovered must be discovered. In addition to solvent cost, specialty linkers used in MOF synthesis can cost in excess of \$500 per gram and the economies of scale that would be involved in producing certain MOFs at massive scales is unknown.⁵⁰ Zhan et. al.⁵¹ wrote an excellent review article discussing MOF synthesis from solid matter and economic synthesis strategies for

large-scale industrial manufacturing. In conclusion, MOFs will likely continue to find niche applications, but largescale commercialization will likely require overcoming many of the limitations that described throughout this section and in chapter 1.

2.2.2 Limitations of Experimental Techniques

Experimental and computational methods involving MOFs have advanced extensively since they were first discovered in the late 1990s. This section will outline the advances in experimental techniques over the past 20 years as well as areas where further improvement is needed. Additionally, the limitations of computational techniques will also be discussed.

Typical experimental characterization techniques involving MOFs include: PXRD, nitrogen physisorption, adsorption isotherms, NMR, TGA, and IR spectroscopy. Walton et. al.⁵² showed the applicability of the Brunauer-Emmett-Teller (BET) method for calculating the surface areas of MOFs. Techniques for calculating pore size distribution, however, are not accurate. The current models are only applicable for rigid structures, such as activated carbons, whereas MOFs typically are highly flexible.^{53,54} For this reason, pore size distributions can only be compared qualitatively among MOF materials and not quantitatively. MOFs have been considered as adsorbents for numerous adsorbates over the past 20 years, however for many applications multiple adsorbates must be considered. Multicomponent adsorption isotherms are still uncommon in the literature and further experimentation needs to be performed to compare to those that have been computationally determined.⁵⁵ Taylor et. al.⁵⁶ collected multicomponent adsorption isotherms for the Co(bdp) framework and achieved a large CO₂/CH₄ selectivity of 61. While a few studies

probing multicomponent adsorption do exist, they have primarily been limited in scope and are not consistent with conditions that would be found in real world applications.

Computation research involving MOFs has been instrumental in directing experimental synthesis and identifying material interactions with adsorbent molecules. In the previous paragraph, the limitations of experimental multicomponent adsorption isotherms were discussed. Computational MOF research has been a valuable aid in developing models to predict multicomponent adsorption when experimental results are not available. Additionally, computational modeling can predict the results of toxic gas adsorption and identify the best MOFs for such applications. This limits the number of experiments that are run using these dangerous gases such as H₂S and allows for more refined and carefully planned experimental testing.^{57,58} In addition to molecular simulations, machine learning is an emerging field with the potential to screen and identify ligand functionalities and metal sites in MOFs that are best suited for a target application. Qiao et. al.⁵⁹ used machine learning to identify the best linker functional groups in MOFs for separation of H₂S and CO₂ from natural gas. In conclusion better computation models and experimental techniques and practices will allow for better designed experiments that mimic the conditions that would be present in industrial applications.

2.3 Conclusions

In this chapter DMOF was introduced as the platform material for this dissertation research. UiO-66, ZIF-8, and Cu-BTC were also discussed due to the potential that they have shown for a variety of applications. DMOF was selected as a platform material due to its tailorability through both linker and metal substitutions, M-DMOF-L (M = Zn, Ni,

Co, Cu) (L = BDC, DM, NDC, TMBDC, ADC). The limitations of MOFs were also discussed in this chapter and concerns were raised regarding MOF water stability, scale-up and processability, as well as expense due to specialty linkers and solvents. Lastly, the limitations of MOF experimental and computation techniques were discussed as well as areas where future research should be directed.

2.4 References

- [1] Dybtsev, D.; Chun, H.; Kim, K. Rigid and Flexible: A Highly Porous Metal-Organic Framework with Unusual Guest-Dependent Dynamic Behavior. *Angew. Chem. Int. Ed.* **2004**, 116, 2858-2861.
- [2] Chun, H.; Dybtsev, D.; Kim, H.; Kim, K. Synthesis, X-ray Crystal Structures, and Gas Sorption Properties of Pillared Square Grid Nets Based on Paddle-Wheel Motifs: Implications for Hydrogen Storage in Porous Materials. *Chemistry*. **2005**, 11, 3521-3529.
- [3] Tan, K.; Nijem, N.; Canepa, P.; Gong, Q.; Li, J.; Thonhauser, T.; Chabal, Y. Stability and Hydrolyzation of Metal-Organic Frameworks with Paddle Wheel SBUs upon Hydration. *Chem. Mater.* **2012**, 24, 3153-3167.
- [4] Hungerford, J.; Bhattacharyya, S.; Tumuluri, U.; Nair, S.; Wu, Z.; Walton, K. DMOF-1 as a Representative MOF for SO₂ Adsorption in Both Humid and Dry Conditions. *J. Phys. Chem. C*. **2018**, 122, 23493-23500.
- [5] Griffith, J.; Orgel, L. Ligand-Field Theory. *Quarterly Reviews, Chemical Society*. **1957**, 11, 381-393.
- [6] Figgis, B. Ligand Field Theory. In *Comprehensive Coordination Chemistry*. Upton: NY, **1987**, pp. 214-276.
- [7] Irving, H.; Williams, R. The Stability of Transition-Metal Complexes. *Journal of the Chemical Society*. **1953**, 3192-3210.
- [8] Burtch, N.; Jasuja, H.; Walton, K. Water Stability and Adsorption in Metal-organic Frameworks. *Chemical Reviews*. **2014**, 114, 10575-10612.
- [9] Jasuja, H.; Huang, Y.; Walton, K. Adjusting the Stability of Metal-Organic Frameworks under Humid Conditions by Ligand Functionalization. *Langmuir*. **2012**, 29, 633-642.

- [10] Jasuja, H.; Burtch, N.; Huang, Y.; Cai, Y.; Walton, K. Kinetic Water Stability of an Isostructural Family of Zinc-Based Pillared Metal-Organic Frameworks. *J. Am. Chem. Soc.* **2013**, 135, 7172-7180.
- [11] Burtch, N.; Walton, I.; Hungerford, J.; Morelock, C.; Jiao, Y.; Heinen, J.; Chen, Y.; Yakovenko, A.; Xu, W.; Dubbeldam, D.; Walton, K. In Situ Visualization of Loading-dependent Water Effects in a Stable Metal-Organic Framework. *Submitted*.
- [12] Zhou, K.; Chaemchuen, S.; Wu, Z.; Verpoort, F. Rapid Room Temperature Synthesis Forming Pillared Metal-Organic Frameworks with Kagome Net Topology. *Microporous Mesoporous Mater.* **2017**, 239, 28-33.
- [13] Chun, H.; Moon, J. Discovery, Synthesis, and Characterization of an Isomeric Coordination Polymer with Pillared Kagome Net Topology. *Inorg. Chem.* **2007**, 46, 4371-4373.
- [14] Cavka, J.; Jakobsen, S.; Olsbye, U.; Guillou, N.; Lamberti, C.; Bordiga, S.; Lillerud, K. A New Zirconium Inorganic Building Brick Forming Metal-Organic Frameworks with Exceptional Stability. *J. Am. Chem. Soc.* **2008**, 130, 13850-13851.
- [15] Rungtaweeworanit, B.; Baek, J.; Araujo, J.; Archanjo, B.; Choi, K.; Yaghi, O.; Somorjai, G. Copper Nanocrystals Encapsulated in Zr-based Metal-organic Frameworks for Highly Selective CO₂ Hydrogenation to Methanol. *Nano Letters.* **2016**, 16, 7645-7649.
- [16] Peterson, G.; Destefano, M.; Garibay, S.; Ploskonka, A.; McEntee, M.; Hall, M.; Karwacki, C.; Hupp, J.; Farha, O. Optimizing Toxic Chemical Removal through Defect-induced UiO-66-NH₂ Metal-organic Framework. *Chem. Eur. J.* **2017**, 23, 15913-15916.
- [17] Wang, N.; Zhang, G.; Wang, L.; Li, J.; An, Q.; Ji, S. Pervaporation Dehydration of Acetic Acid using NH₂-UiO-66/PEI Mixed Matrix Membranes. *Separation and Purification Technology.* **2017**, 186, 20-27.
- [18] Tulig, K.; Walton, K. An Alternative UiO-66 Synthesis for HCl-sensitive Nanoparticle Encapsulation. *RSC Adv.* **2014**, 51080-51083.
- [19] Tulig, K. "Encapsulation of Nanoparticles in Metal-organic Frameworks for Air Purification." Copyright 2016.
- [20] Joshi, J.; Garcia-Gutierrez, E.; Moran, C.; Deneff, J.; Walton, K. Engineering Copper Carboxylate Functionalities on Water Stable Metal-organic Frameworks for Enhancement of Ammonia Removal Capacities. *J. Phys. Chem. C.* **2017**, 121, 3310-3319.

- [21] Fang, Z.; Bueken, B.; De Vos, D.; Fischer, R. Defect-Engineered Metal-Organic Frameworks. *Angew. Chem. Int. Ed.* **2015**, 54, 7234-7254.
- [22] Liang, W.; Coghlan, C.; Ragon, F.; Rubio-Martinez, M.; D'Alessandro, D.; Babarao, R. Defect Engineering of UiO-66 for CO₂ and H₂O Uptake - A Combined Experimental and Simulation Study. *Dalton Transactions.* **2016**, 45, 4496-4500.
- [23] Jiao, Y.; Liu, Y.; Zhu, G.; Hungerford, J.; Bhattacharyya, S.; Lively, R.; Sholl, D.; Walton, K. Heat-Treatment of Defective UiO-66 from Modulated Synthesis: Adsorption and Stability Studies. *J. Phys. Chem. C.* **2017**, 121, 23471-23479.
- [24] Wu, H.; Chua, Y.; Krungleviciute, V.; Tyagi, M.; Chen, P.; Yildirim, T.; Zhou, W. Unusual and Highly Tunable Missing-linker Defects in Zirconium MOF UiO-66 and Their Important Effects on Gas Adsorption. *J. Am. Chem. Soc.* **2013**, 135, 10525-10532.
- [25] Li, L.; Liao, P.; He, C.; Wei, Y.; Zhou, H.; Lin, J.; Li, X.; Zhang, J. Grafting Alkylamine in UiO-66 by Charge-assisted Coordination Bonds for Carbon Dioxide Capture from High-humidity Flue Gas. *J. Mater. Chem. A.* **2015**, 3, 21849-21855.
- [26] DeCoste, J.; Demasky, T.; Katz, M.; Farha, O.; Hupp, J. A UiO-66 Analogue with Uncoordinated Carboxylic Acids for the Broad-spectrum Removal of Toxic Chemicals. *New J. Chem.* **2015**, 39, 2396-2399.
- [27] Schaate, A.; Roy, P.; Godt, A.; Lippke, J.; Waltz, F.; Wiebcke, M.; Behrens, P. Modulated Synthesis of Zr-Based Metal-Organic Frameworks: From Nano to Single Crystals. *Chem. Eur. J.* **2011**, 17, 6643-6651.
- [28] Bueken, B.; Velthoven, N.; Krajnc, A.; Smolders, S.; Taulelle, F.; Mellot-Draznieks, C.; Mali, G.; Bennett, T.; De Vos, D. Tackling the Defect Conundrum in UiO-66: A Mixed-Linker Approach to Engineering Missing Linker Defects. *Chem. Mater.* **2017**, 29, 10478-10486.
- [29] Park, K.; Ni, Z.; Cote, A.; Choi, J.; Huang, R.; Uribe-Romo, F.; Chae, H.; O'Keeffe, M.; Yaghi, O. Exceptional Chemical and Thermal Stability of Zeolitic Imidazolate Frameworks. *PNAS.* **2006**, 103, 10186-10191.
- [30] Baerlocher, C.; McCusker, L.; Olson, D. *Atlas of Zeolite Framework Types.* Elsevier, 2007.
- [31] Venna, S.; Carreon, M. Highly Permeable Zeolite Imidazolate Framework-8 Membranes for CO₂/CH₄ Separation. *J. Am. Chem. Soc.* **2010**, 132, 76-78.
- [32] Huang, Z.; Dong, P.; Zhang, Y.; Nie, X.; Wang, X.; Zhang, X. A ZIF-8 Decorated TiO₂ Grid-like Film with High CO₂ Adsorption for CO₂ Photoreduction. *Journal of CO₂ Utilization.* **2018**, 24, 369-375.

- [33] Ramu, G.; Lee, M.; Jeong, H. Effects of Zinc Salts on the Microstructure and Performance of Zeolitic Imidazolate Framework ZIF-8 Membranes for Propylene/Propane Separation. *Microporous Mesoporous Mater.* **2018**, 259, 155-162.
- [34] Mondal, S.; Hovestadt, M.; Dey, S.; Paula, C.; Glomb, S.; Kelling, A.; Schilde, U.; Janiak, C.; Hartmann, M.; Holdt, H. Synthesis of a Partially Fluorinated ZIF-8 Analog for Ethane/Ethene Separation. *Cryst. Eng. Comm.* **2017**, 19, 5882-5891.
- [35] Ramu, G.; Lee, M.; Jeong, H. Effects of Zinc Salts on the Microstructure and Performance of Zeolitic-Imidazolate Framework ZIF-8 Membranes for Propylene/Propane Separation. *Microporous Mesoporous Mater.* **2018**, 259, 155-162.
- [36] Lahoz-Martin, F.; Martin-Calvo, A.; Gutierrez-Sevillano J.; Calero, S. Effect of Light Gases in the Ethane/Ethylene Separation Using Zeolitic Imidazolate Frameworks. *J. Phys. Chem. C* **2018**, 122, 8637-8646.
- [37] Ramu, G.; Lee, M.; Jeong, H. Effects of Zinc Salts on the Microstructure and Performance of Zeolitic-Imidazolate Framework ZIF-8 Membranes for Propylene/Propane Separation. *Microporous Mesoporous Mater.* **2018**, 259, 155-162.
- [38] Zhang, X.; Xiao, P.; Zhan, C.; Liu, B.; Zhong, R.; Yang, L.; Sun, C.; Liu, H.; Pan, Y.; Chen, G.; Li, N. Separation of Methane/Ethylene Gas Mixtures Using Wet ZIF-8. *Ind. Eng. Chem. Res.* **2015**, 54, 7890-7898.
- [39] Shahid, S.; Nijmeijer, K. Matrimid(R)/Polysulfone Blend Mixed Matrix Membrane Containing ZIF-8 Nanoparticles for High Pressure Stability in Natural Gas Separation. *Separation and Purification Technology*. **2017**, 189, 90-100.
- [40] Schlichte, K.; Kratzke, T.; Kaskel, S. Improved Synthesis, Thermal Stability and Catalytic Properties of the Metal-Organic Framework Compound Cu₃(BTC)₂. *Microporous Mesoporous Mater.* **2004**, 73, 81-88.
- [41] Al-Janabi, N.; Alfutimie, A.; Siperstein, F.; Fan, X. Underlying Mechanism of the Hydrothermal Instability of Cu₃(BTC)₂ Metal-organic Framework. *Front. Chem. Sci. Eng.* **2016**, 10, 103-107.
- [42] Wu, Y.; Lv, Z.; Zhou, X.; Peng, J.; Tang, Y.; Li, Z. Tuning Secondary Building Unit of Cu-BTC to Simultaneously Enhance its CO₂ Selective Adsorption and Stability Under Moisture. *Chemical Engineering Journal*. **2019**, 355, 815-821.
- [43] Lin, Z.; Lv, Z.; Zhou, X.; Xiao, H.; Wu, J.; Li, Z. Postsynthetic Strategy to Prepare ACN@Cu-BTCs with Enhanced Water Vapor Stability and CO₂/CH₄ Separation Selectivity. *Ind. Eng. Chem. Res.* **2018**, 57, 3765-3772.

- [44] Yu, J.; Ma, Y.; Balbuena, P. Evaluation of the Impact of H₂O, O₂, and SO₂ on Postcombustion CO₂ Capture in Metal-Organic Frameworks. *Langmuir*, **2012**, 28, 8064-8071.
- [45] Peterson, G.; Rossin, J.; DeCoste, J.; Killops, K.; Browe, M.; Valdes, E.; Jones, P. Zirconium Hydroxide Metal-organic Framework Composites for Toxic Chemical Removal. *Ind. Eng. Chem. Res.* **2013**, 52, 5462-5469.
- [46] Urquhart, J. World's First Commercial MOF Keeps Fruit Fresh. *Chemistry World*. **2016**. Accessed online at: <https://www.chemistryworld.com/news/worlds-first-commercial-mof-keeps-fruit-fresh/1017469.article>
- [47] NuMat Technologies. Ret: 1/2/2019. <https://www.numat-tech.com/our-process/>
- [48] Kim, S.; Lee, Y.; Hong, S.; Jang, M.; Ahn, W. Pilot-scale Synthesis of a Zirconium-benzenedicarboxylate UiO-66 for CO₂ Adsorption and Catalysis. *Catalysis Today*. **2015**, 245, 54-60.
- [49] Crawford, D.; Casaban, J.; Haydon, R.; Giri, N.; McNally, T.; James, S. Synthesis by Extrusion: Continuous, Large-scale Preparation of MOFs using Little or No Solvent. *Chem. Sci.* **2015**, 6, 1645-1649.
- [50] Sigma-Aldrich. Ret: 1/2/2019. <https://www.sigmaaldrich.com/materials-science/material-science-products.html?TablePage=103996379>
- [51] Zhan, G.; Zeng, H. Alternative Synthetic Approaches for Metal-organic Frameworks: Transformation from Solid Matters. *Chem. Commun.* **2017**, 53, 72-81.
- [52] Walton, K.; Snurr, R. Applicability of the BET Method for Determining Surface Areas of Microporous Metal-Organic Frameworks. *J. Am. Chem. Soc.* **2007**, 129, 8552-8556.
- [53] Neimark, A.; Lin, Y.; Ravikovitch, P.; Thommes, M. Quenched Solid Density Functional Theory and Pore Size Analysis of Micro-mesoporous Carbons. *Carbon*. **2009**, 47, 1617-1628.
- [54] Azo Materials. Quenched Solid State Functional Theory (QSDFT) for Pore Size Analysis of Disordered Carbon. <https://www.azom.com/article.aspx?ArticleID=5191>. (Accessed March 20, 2019)
- [55] Sircar, S. Basic Research Needs for Design of Adsorptive Gas Separation Processes. *Ind. Eng. Chem. Res.* **2006**, 45, 5435-5446.
- [56] Taylor, M.; Runcevski, T.; Oktawiec, J.; Bachman, J.; Siegelman, R.; Jiang, H.; Mason, J.; Tarver, J.; Long, J. Near-perfect CO₂/CH₄ Selectivity Achieved through Reversible Guest Templating in the Flexible Metal-organic Framework Co(bdp). *J. Am. Chem. Soc.* **2018**, 140, 10324-10331.

- [57] Han, C.; Verploegh, R.; Sholl, D. Assessing the Impact of Point Defects on Molecular Diffusion in ZIF-8 using Molecular Simulations. *J. Phys. Chem. Lett.* **2018**, 9, 4037-4044.
- [58] Al-Jadir, T.; Siperstein, F. The Influence of the Pore Size in Metal-organic Frameworks in Adsorption and Separation of Hydrogen Sulphide: A Molecular Simulation Study. *Microporous Mesoporous Mater.* **2018**, 160-168.
- [59] Qiao, Z.; Xu, Q.; Jiang, J. Computational Screening of Hydrophobic Metal-organic Frameworks for the Separation of H₂S and CO₂ from Natural Gas. *J. Mater. Chem. A.* **2018**, 6, 18898-18905.

CHAPTER 3: ROOM TEMPERATURE SYNTHESIS OF METAL-ORGANIC FRAMEWORK ISOMERS IN THE TETRAGONAL AND KAGOME CRYSTAL STRUCTURE

This chapter was reproduced from Hungerford, J.; Walton, K., “Room Temperature Synthesis of Metal-Organic Framework Isomers in the Tetragonal and Kagome Crystal Structure” *Inorganic Chemistry*, Submitted.

3.1 Introduction

Chapter 1 introduced MOFs and discussed typical solvothermal synthesis of these materials as well as alternative routes of MOF synthesis including, room temperature synthesis, which will be the focus of this chapter. Chapter 2 introduced DMOF as a platform material that will be used throughout this dissertation work for exploring water and acid gas stability and adsorption in MOF materials. This chapter will further explore DMOF and ZnBD, an isomer of DMOF, and discuss how synthesis solvent directs the formation of one MOF topology over another.

DMOF and ZnBD provide an interesting system to explore adsorption and stability characteristics as these materials contain the same metal centers and linkers and only differ by topology (see Figure 1 for material crystal structures). Chapter 2 discussed how incorporation of bulky linkers such as: 2,3,5,6-tetramethylterephthalic acid (TM) and 9,10-anthracenedicarboxylic acid (ADC), resulted in improved humid stability for parent DMOF. In this chapter we attempted to incorporate a variety of functionalized BDC linkers into the ZnBD framework. Additionally, we assessed whether MOFs synthesized via

different methods and with different solvents will result in materials of similar quality. Previous room temperature synthesis experiments involving UiO-66 showed that the resulting framework contained a large number of defects within the structure.¹ This led to an increase in the material's surface area and pore volume, however the authors did not rigorously test whether the stability of UiO-66 was negatively impacted by room temperature induced defects. The impact that defects may have on MOF stability towards acid gases and the affect that defects have on their adsorption properties towards these acid gases has only been explored sparingly in the literature.

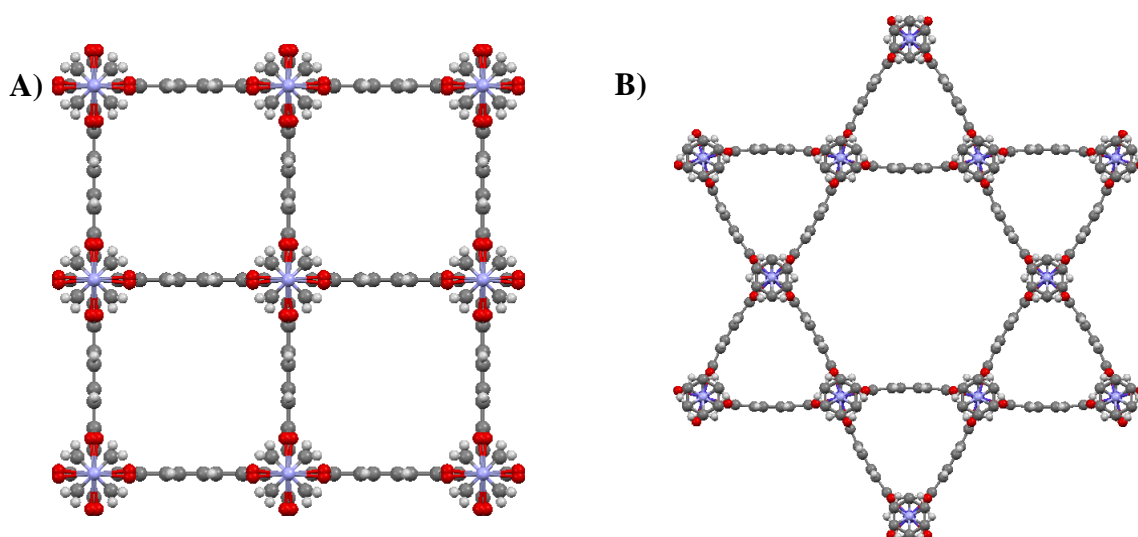


Figure 3.1: Crystal structure of A) DMOF and B) ZnBD, viewed down the c-axis.
 “Crystallographic information from 2 (ZnBD) and 3 (DMOF).”

In this chapter we synthesized the framework isomers DMOF and ZnBD by expanding on the synthesis procedures previously reported by Zhou et. al.⁴ to include different solvents: methanol, ethanol, dimethyl sulfoxide (DMSO), acetone, acetonitrile, and N,N-diethylformamide (DEF). To the authors knowledge this is the first time that a

room temperature synthesis has been reported for functionalized Zn-DMOF-L (L = TM, DM, NH₂, ADC). Additionally, CO₂ adsorption isotherms of these two materials were compared, as well as an assessment of the material's stability in humid conditions. Overall, this study provides a probe into the structural differences in MOFs as well as solvent directing effects, which have only been discussed sparsely in the literature.⁵⁻⁷ This study also sets the groundwork for future chapters to examine the acid gas stability and adsorption properties of the platform material. Lastly, this chapter also introduces the concept of defect incorporation through room temperature synthesis and how synthesis conditions may affect MOF stability and adsorption properties.

3.2 Experimental

3.2.1 Materials

All of the chemicals in this study were used as received without further purification from the following sources: zinc (II) nitrate hexahydrate (Zn(NO₃)₂·6H₂O), benzene-1,4-dicarboxylic acid (BDC), 2-aminoterephthalic acid (NH₂), 1,4-diazabicyclo[2.2.2]octane (DABCO), 9,10-anthracenedicarboxylic acid (ADC), 2,5-dimethylterephthalic acid (DM), trimethylamine, dimethyl sulfoxide (DMSO), acetonitrile, and diisopropyl-ethylamine from Sigma Aldrich; N,N-dimethylformamide (DMF), methanol, ethanol, acetone, and N,N-diethylformamide (DEF) from VWR; 2,3,5,6-tetramethylterephthalic acid (TM) from TCI America. A diagram of the following linkers: BDC, DM, NH₂, TM, and ADC, can be found in the supplemental information Figure D.1.

3.2.1.1 General Synthetic Procedure

The synthetic procedures for all synthesized materials were identical, except for substitution of DMF with the following solvents: DEF, DMSO, acetonitrile, methanol, ethanol, acetone, and ethyl acetate. Additionally, for some samples trimethylamine was substituted for diisopropyl-ethylamine, and the volume added was adjusted to ensure a consistent molar ratio of diisopropyl-ethylamine to BDC. Prepared samples will all be referred to as ZnBD-xxx, where xxx is the solvent name or abbreviation as was stated above. The basis for the synthesis procedures can be found in the literature.⁴ See Figure D.1 and D.2 in the supplemental information for a schematic of the DMOF and ZnBD structures and ligands.

General Procedure: Two separate solvent solutions of 15 mL of DMF were first prepared. To the first solution $\text{Zn}(\text{NO}_3)_2 \cdot 6\text{H}_2\text{O}$ (0.436 g, 1.5 mmol) and BDC (0.249 g, 1.5 mmol) were added, and to the second solution DABCO (0.140 g, 1.25 mmol) and 350 μL of triethylamine (or diisopropyl-ethylamine) were added. The solutions were then separately mixed at room temperature until a uniform solution appeared. (For solution 1 only in the DEF, DMF, DMSO solvent systems did BDC dissolve completely. DABCO dissolved in solution 2 for all solvent systems after the addition of triethylamine.) Solution 1 and 2 were then mixed and stirred on a stir plate at 200 rpm at room temperature for 4 hours. (Solvent was added as needed to maintain the solution level for methanol, ethanol, acetone, acetonitrile, and ethyl acetate as they evaporated rapidly) The mixture was then poured into a vial and centrifuged until solid samples were observed at the bottom of the vial. The solvent was then exchanged 3 times with DMF to remove any excess starting materials and

then 3 times with methanol. Prior to characterization the samples were all activated under vacuum at 150 °C for 18 hours.

3.2.2 Characterization

3.2.2.1 Powder X-ray Diffraction

A PANalytical X'Pert X-ray diffractometer containing an X'Celerator detector was used to collect powder X-ray diffraction (PXRD) patterns utilizing Cu K α ($\lambda = 1.5418 \text{ \AA}$) radiation. Patterns were collected from 2θ 2 – 50°. The results were then compared to patterns found in the literature to confirm that the expected materials had been properly synthesized.⁸⁻¹⁰

3.2.2.2 Surface Area Analysis

Surface areas and pore volumes were determined via nitrogen physisorption measurements on a Quadrasorb from Quantichrome Instruments operating at 77K. The Brunauer-Emmett-Teller (BET) surface areas were measured over the pressure range of $0.003 \leq P/P_0 \leq 0.05$.¹¹ Prior to experimentation the materials were outgassed at 150 °C for 18 hours under vacuum using a FloVac Degasser also from Quantichrome.

3.2.2.3 Water Vapor Adsorption Isotherms

A 3Flex Surface Characterization Analyzer from Micromeritics was used to collect room temperature water vapor adsorption isotherms. Samples were activated on a Micromeritics Smart VacPrep at an activation temperature of 150°C for 18 hours under vacuum prior to testing. Sample measurements were collected over a relative pressure range of $P/P_0 = 0 - 0.80$.

3.2.2.4 Dry CO₂ Adsorption Isotherms

An Intelligent Gravimetric Adsorption (IGA-1) instrument from Hiden Isochema was used to collect CO₂ adsorption measurements up to 20 bar. Prior to testing, samples were activated in situ under vacuum at 150 °C.

3.3 Results and Discussion

3.3.1 Solvent effects in the synthesis of ZnBD and DMOF-1

Solvent effects were assessed to better understand the formation of one isomer over another (Kagome vs. tetragonal) in the Zn₂(BDC)₂(DABCO) MOFs using the following solvents: DMF, DEF, acetonitrile, methanol, acetone, ethanol, and DMSO. These solvents were selected for two primary reasons 1) they have similar properties to DMF (DEF, acetonitrile, DMSO) and 2) they are less hazardous/more environmentally friendly than DMF (methanol, acetone, ethanol). Table D.1 provides a list of properties for the solvents used in this study. With the exception of changing the solvent, the synthesis procedures remained unchanged for all materials as described in the experimental section. Powder X-ray diffraction patterns were collected for the as-synthesized materials and are shown in Figure 3.2. Nitrogen physisorption isotherms were measured to determine the BET surface areas of the materials, and the results of these experiments are given in Table 3.1. Room temperature synthesis was also conducted for metal substituted samples including: nickel, copper, and cobalt and the PXRD patterns (Figure D.9) and BET surface area measurements (Table D.4) can be found in the supplemental information.

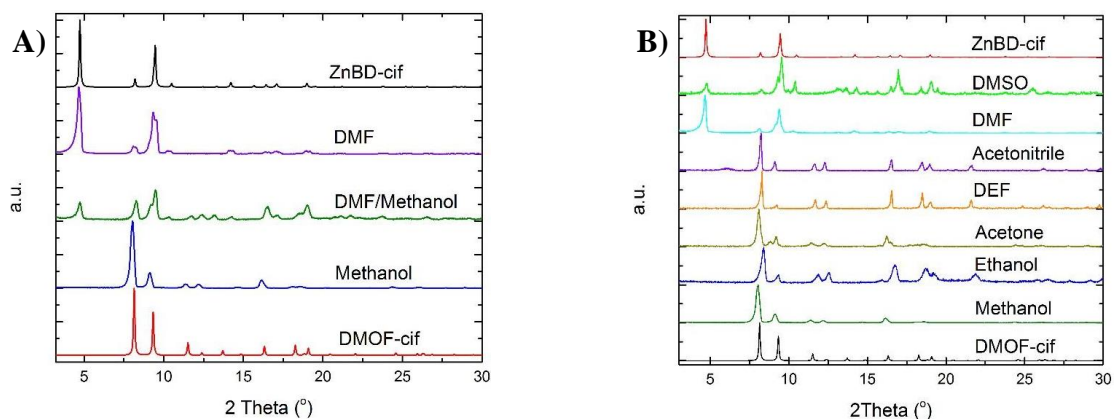


Figure 3.2: PXRD patterns of the fast, room temperature $\text{Zn}_2(\text{X})_2(\text{DABCO})$ synthesis comparing: A) materials produced from DMF, methanol, and DMF:methanol mixed solvents, and B) materials synthesized in DMSO, DMF, acetonitrile, DEF, acetone, ethanol, and methanol. PXRD patterns from crystalization information files 2 (ZnBD) and 3 (DMOF) are also provided.

Figure 3.2 shows the PXRD patterns for the $\text{Zn}_2(\text{BDC})_2(\text{DABCO})$ materials. Only when using DMSO or DMF as solvents does the ZnBD framework form in the room temperature synthesis procedure.¹² All other solvents resulted in the formation of DMOF-1. Additionally, while both DMF and DMSO formed the ZnBD crystal structure, there were many phase impurities in ZnBD-DMSO. The other solvents that were used in the synthesis procedure, acetonitrile, DEF, ethanol, acetone, and methanol all resulted in the formation of DMOF-1. The purity and crystallinity of the resultant materials were best when the synthesis was performed in either methanol, acetonitrile, or DEF. When acetone or ethanol were used in the synthesis, the resultant PXRD patterns indicate the presence of many phase impurities that may have been caused by adsorbed water in the solvents. Since DMOF-1 is unstable in liquid water it is likely that this may have caused some degradation of the sample even if water is in low concentration in the solution. DMF proved to be the

best solvent for room temperature synthesis of ZnBD whereas methanol and DEF were the best solvents for the formation of DMOF-1 based on the results of PXRD patterns and BET surface area analysis (Table 3.1). Nitrogen physisorption isotherms can be found in the supplemental information, Figures D.3 – D.5.

Table 3.1: BET surface area analysis for DMOF and ZnBD room temperature synthesis. BA refers to benzoic acid which was used as a modulator in the synthesis. Zn-DMOF-X-RT (X = TM, ADC, NH₂, or DM) (RT = room temperature)

MOF	BET SA (m ² /g)	Pore Volume (cm ³ /g)
Solvent Effects		
ZnBD-DMF	2104	0.80
ZnBD-DMSO	1046	0.43
Zn-DMOF-Methanol	2113	0.78
Zn-DMOF-DEF	2080	0.79
Zn-DMOF-EthylAcetate	2222	0.70
Zn-DMOF-Acetone	1757	0.66
Zn-DMOF-Ethanol	1230	0.49
Zn-DMOF-Acetonitrile	2119	0.70
Zn-DMOF-Methanol/DMF	1452	0.54
Modulators		
ZnBD-1:1BA ^a	1747	0.66
ZnBD-5:1BA	1237	0.50
ZnBD-Diisopropyl-ethylamine	2151	0.84
ZnBD-Na ₂ BDC	1728	0.66
Zn-DMOF-X-RT^b		
Zn-DMOF-TM-RT	950	0.43
Zn-DMOF-ADC-RT	732	0.32
Zn-DMOF-NH ₂ -RT	1287	0.55
Zn-DMOF-DM-RT	1272	0.70

a BA = Benzoic Acid (used as a modulator for BDC linker)

b Zn-DMOF-X-RT (X = TM, ADC, NH₂, or DM) (RT = room temperature)

The solubility of the starting materials in the solvents varies drastically. The DABCO linker readily dissolved in all solvents after the addition of the trimethylamine base, and Zn(NO₃)₂·6H₂O also dissolved in all tested solvents. BDC, however, only readily

dissolved in DMSO, DEF, and DMF. While low solubility does not necessarily hinder MOF growth, e.g., methanol produced high purity DMOF-1, all of the solvents with low solubility formed preferentially the DMOF-1 framework over ZnBD. DMOF has previously been determined to be the thermodynamically favored structure, however formation of the triangular oligomer structures has been shown to be favored in DMF solution over the square oligomer, which may explain the preferential synthesis of ZnBD in DMF.¹³ DEF is the outlier in this study as it readily dissolves BDC and yet did not form ZnBD. From these results, we hypothesize that solubility is not the primary factor contributing to the formation of one structure over another. Follow-up experiments using insoluble linkers will be discussed in the following paragraphs to test this hypothesis. Table D.1, shows a list of solvent properties for the solvents used in this study and the resultant MOF that formed from the synthesis. We speculate that intermediate formation is a pivotal component of MOF formation, however we cannot state at this time what intermediate in the solution may be causing the selective formation of ZnBD versus DMOF-1. Further experimentation is required to better understand MOF topology control and synthesis formation mechanisms. We observed, however, that all syntheses containing pure solvent systems produced pure phases of either ZnBD or DMOF-1, with the exception of ZnBD-DMSO. ZnBD-DMSO contains additional peaks that correspond to a partially degraded sample similar to those that will be shown after water adsorption (See Figure 3.5).

In addition to exploring a variety of solvents in the synthesis procedure, adding heat to the system was also tested. Similar to the general room temperature synthesis procedure stated in the experimental section, two separate solutions of 15 mL of DMF were prepared. To the first solution $\text{Zn}(\text{NO}_3)_2 \cdot 6\text{H}_2\text{O}$ and BDC were added, and to the second solution

DABCO and 350 μ L of triethylamine were added. The two solutions were mixed separately until all solids had completely dissolved. The solutions were then combined and immediately poured into a Teflon lined autoclave and placed into a programmable oven at 120 °C for 48 as was done in the traditional DMOF-1 synthesis.^{3,14} The resultant material was the DMOF-1 structure which suggests that ZnBD is a kinetically favored state at room temperature and adding energy to the system will instead result in the formation of DMOF-1.

A mixed solvent system consisting of a 50:50 ratio of DMF:methanol was also tested and the resulting synthesis produced a material of mixed phases consisting of both the tetragonal DMOF-1 and Kagome ZnBD. We conclude DMOF-1 preferentially forms around DMF solvent molecules, whereas ZnBD forms around methanol solvent molecules as long as no additional energy is added to the system, which would preferentially promote growth of the DMOF-1 tetragonal crystal structure. Figure 3.2A shows the PXRD patterns of the DMF:methanol produced material as well as the presence of the two separate phases.

After investigating solvent effects on the $\text{Zn}_2(\text{X})_2(\text{DABCO})$ synthesis, the effects of basic and acidic modulators were also explored. Benzoic acid was used as a modulator in a 5:1 Benzoic acid:BDC ligand and 1:1 ratio in DMF in the synthesis of ZnBD, and it was found to have little impact on the final structure (see PXRD Figure 3.3A). Additionally, a 1:1 ratio of benzoic acid was also used in the synthesis of $\text{Zn}_2(\text{X})_2(\text{DABCO})$ using methanol as a solvent, and it resulted in the formation of DMOF-1. These results are consistent with what has been seen in the prior experiments and show that the addition of a benzoic acid modulator does not significantly impact the final material.

The final investigation into the room temperature synthesis of $\text{Zn}_2(\text{X})_2(\text{DABCO})$ involved changing the triethylamine base. Diisopropyl-ethylamine was utilized as a similar tertiary amine in the synthesis, and it resulted in the formation of ZnBD similar to what was also obtained when using trimethylamine as a base (see PXRD Figure 3.3B). Lastly, the amine base was eliminated from the synthesis completely and BDC was replaced with sodium terephthalate as was prepared by Kaduk et. al.¹⁵ While sodium terephthalate does not readily dissolve in DMF, it was still able to produce a single MOF phase of ZnBD in solution after stirring for 4 hours, see PXRD data in Figure 3.3B. Previously it was discussed that BDC did not readily dissolve in methanol, ethanol, acetone, or ethyl acetate and the material formed DMOF-1. Therefore, we can hypothesize that DMF/DMSO is the primary factor contributing to the topology of the final material and is important in the room temperature synthesis of ZnBD over DMOF-1.

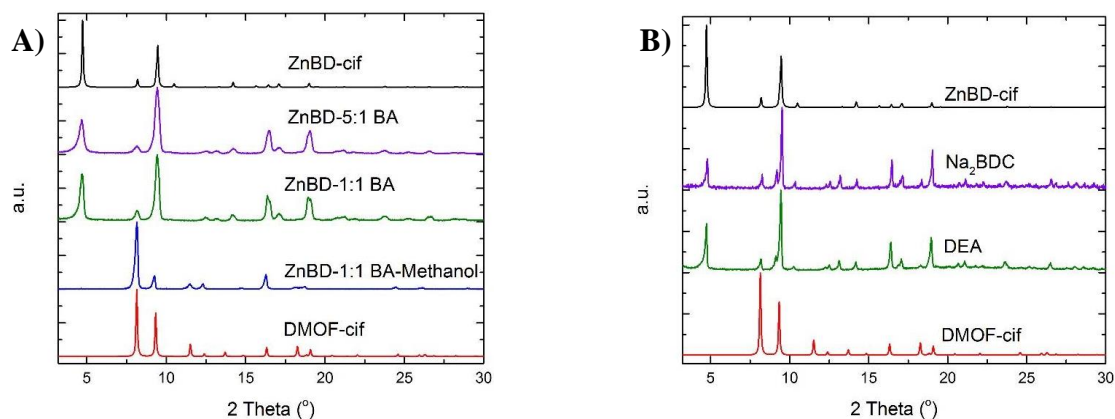


Figure 3.3: PXRD patterns of materials synthesized via a fast, room temperature $\text{Zn}_2(\text{X})_2(\text{DABCO})$ synthesis using: A) acidic and B) basic modulators and DMF as solvent unless otherwise stated

3.3.2 CO₂ and Water Adsorption: Topological Differences in ZnBD MOF and DMOF-1

ZnBD and Zn-DMOF-1 were both synthesized using the procedures discussed previously from the same starting materials: BDC, DABCO, and Zn(NO₃)₂·6H₂O. CO₂ adsorption isotherms for ZnBD-DMF and DMOF-1 synthesized both solvothermally and at room temperature are shown in Figure 3.4. The adsorption isotherms show that ZnBD adsorbs much less CO₂ in the low-pressure range (0 – 10 bar) compared to DMOF-1. ZnBD contains larger pores than DMOF-1 (15 Å pore vs 7.5 Å pore) such that it can be expected to have weaker binding interactions with CO₂ compared to the parent DMOF-1 structure (only physisorption is expected in these materials).⁶ At zero coverage the heat of CO₂ adsorption on ZnBD was calculated to be 22 kJ/mol, which is slightly higher than the value reported by Zhao et. al. for DMOF-1 at 19.8 – 20.3 kJ/mol.¹⁶ Similarly shaped isotherms have been observed in the MIL-101 series of MOFs, which also have large pore sizes on the order of 12 Å and 16 Å and exhibit weak CO₂ adsorption interactions.¹⁷ At 20 bar, however, DMOF-1 and ZnBD adsorb roughly the same amount of CO₂ reaching a capacity of 14 mmol/g. One would expect ZnBD and DMOF-1 to reach similar maximum uptakes of CO₂ adsorption because they have similar pore volumes, and neither material contains open metal sites where strong interactions between CO₂ and the MOF would be likely to occur. This suggests that the affinity for CO₂ is likely due to favorable adsorption potentials within the pores of the two MOFs.

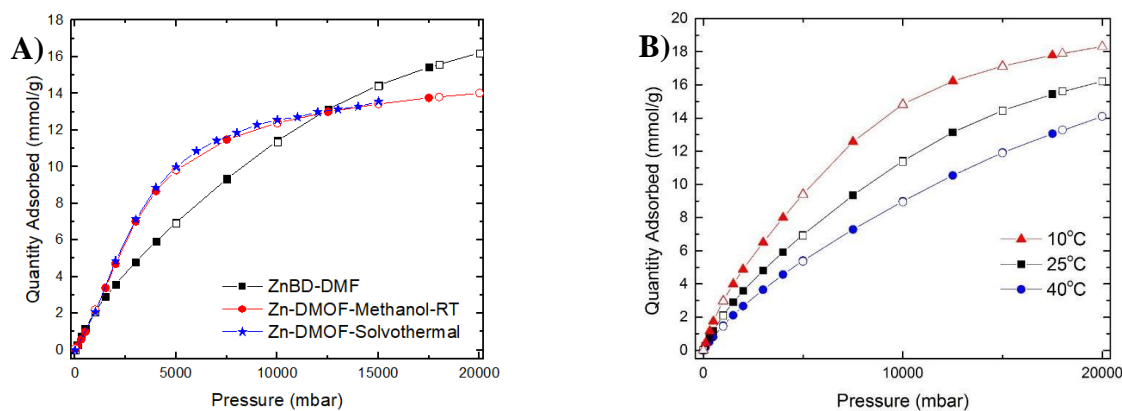


Figure 3.4: A) CO₂ adsorption isotherms at 25 °C for ZnBD-DMF, Zn-DMOF-Methanol-RT, and Zn-DMOF synthesized solvothermally “Reproduced from 18. Copyright 2010, Elsevier” B) CO₂ adsorption isotherms of ZnBD-DMF at 10 °C, 25 °C, and 40 °C.

Water adsorption isotherms of the ZnBD MOF were collected over $P/P_0 = 0 - 0.5$ in subsequent exposures on the same sample beginning at $P/P_0 = 0.2$ and increasing in 0.1 increments. Figure 3.5A shows that ZnBD adsorbs very little water over the range $P/P_0 = 0 - 0.4$, but it exhibits a sharp uptake of water up to 8 mmol/g over the relative pressure range 0.4 – 0.5. The desorption step following exposure to $P/P_0 = 0.5$ shows that the adsorbed water cannot be completely desorbed as the structure has likely degraded. This was later confirmed via PXRD (Figure 3.5B). Previously, it has been shown in the literature by Liang et. al. that DMOF-1 is stable up to humidity exposures of 40% RH and then begins to degrade if the humidity is further increased.¹⁸ This trend matches what has been observed in ZnBD proving that the materials have similar framework stability towards water vapor as well as similar water adsorption characteristics, in spite of the topological differences.^{8,9}

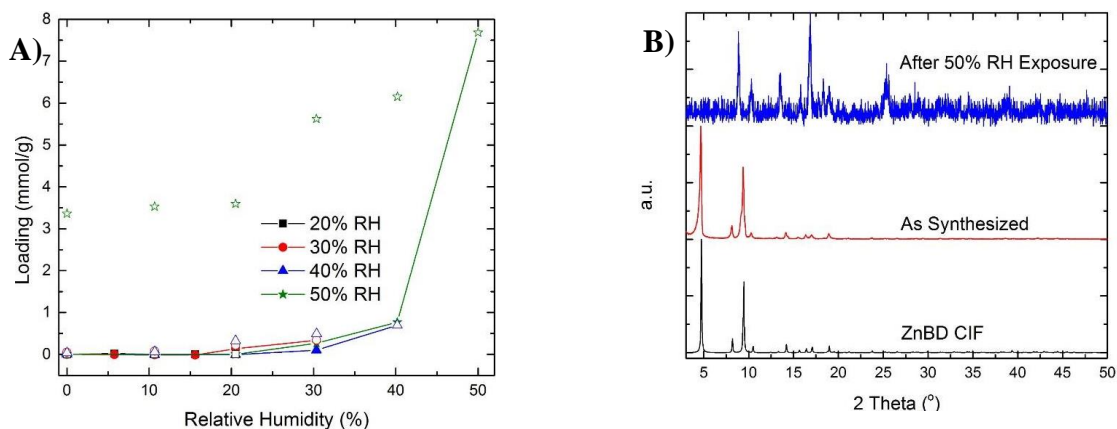


Figure 3.5: A) Water adsorption isotherms of ZnBD-DMF increased stepwise from 20 – 50% RH. B) PXRD patterns of ZnBD-DMF before and after exposure to 50% RH.

3.3.3 Room temperature synthesis of $\text{Zn}_2(\text{X})_2(\text{DABCO})$

In the previous section it was shown that ZnBD degrades when exposed to water at concentrations greater than $P/P_o = 0.4$, which is similar to the behavior of DMOF-1. DMOF-1, however, has been shown to be stable up to 0.9 P/P_o water exposure by incorporating 2,3,5,6-tetramethylterephthalic acid (TM) or anthracene dicarboxylic acid (ADC) ligands in the place of the parent BDC ligand. A similar approach was attempted in which the BDC linker was substituted for a variety of other ligands including DM, NH_2 , ADC, and TM, while all other synthesis conditions remained the same as previously reported. It was found that while the ZnBD Kagome topology was present when conducting synthesis with the BDC ligand, any synthesis utilizing functionalized BDC ligands resulted in the formation of the tetragonal crystal structure of DMOF-1. These results are shown in the PXRD patterns in Figure 3.6. To the authors' knowledge, this is the first time that these materials have been synthesized using a room temperature 4-hour synthesis, and it provides a much simpler approach for the formation of functionalized DMOF-1 material compared

to what has been previously reported in the literature. Table D.2 in the supplemental information shows the BET surface area and pore volumes for the materials synthesized using the room temperature synthesis method, and these results are comparable to those obtained using traditional solvothermal synthesis methods.

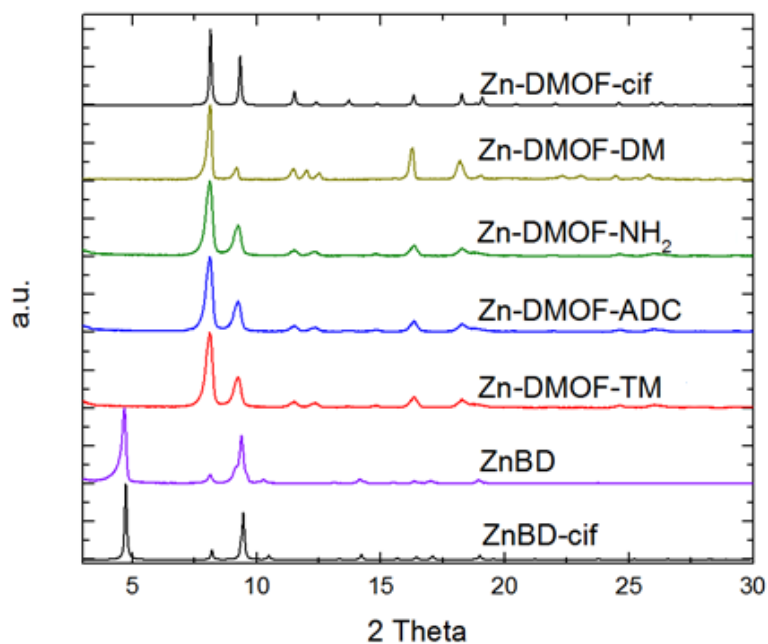


Figure 3.6: PXRD patterns of $\text{Zn}_2(\text{X})_2(\text{DABCO})$ materials produced using a 4 hour room temperature synthesis. The structures were produced using the “ZnBD” synthesis method, but led to the tetragonal DMOF topology rather than the Kagome ZnBD structure.

All attempts at creating a functionalized ZnBD material have been unsuccessful and two explanations will be proposed to explain this phenomenon. First, the additional bulk that the functionalized ligands (NH_2 , TM, ADC, DM) impose may prevent the formation of the Kagome lattice. The small triangular pores in ZnBD would allow for a sphere of diameter 4.2 \AA to reside within them. When functionalized ligands are used in the synthesis it is possible that electrostatic interactions between the functional groups may

be too great to accommodate the Kagome topology. Similar effects are also observed in the DMOF-1 framework when it is functionalized with TM or ADC: both materials see a large decrease in the pore window in their structures due to the addition of these bulky side groups.^{19,20} Additionally the ligands in both DMOF-TM and DMOF-ADC are rotated out of plane when compared to the parent structure. Henke et. al. also reported the topology direction of of pillar-layered MOFs due to impose steric effects.^{21,22} Second, by functionalizing the BDC ligand, the pKa and electronic properties of the ligand are changed, which may inhibit the formation of the Kagome structure. This also explains why a pure tetragonal phase is observed in the PXRD patterns for the functionalized materials for all of the ligand functionalities that were chosen.

3.4 Conclusions

In conclusion, we have shown that a fast, room temperature synthesis method exists for the formation of $\text{Zn}_2(\text{X})_2(\text{DABCO})$ using a variety of solvents and acidic and basic modulators. The synthesis is structure directed by the solvent molecule and can form either ZnBD, using DMF or DMSO as a solvent, or DMOF-1, using methanol, ethanol, ethyl acetate, and DEF as solvents. While DMOF-1 can be easily functionalized, it has proven difficult to use functionalized BDC ligands in the ZnBD synthesis due to suspected steric effects. For the first time CO_2 adsorption behavior and water stability of ZnBD were assessed. While the water stability was similar to DMOF-1, its CO_2 adsorption isotherms show slightly weaker adsorption at low pressures as a result of the larger main pore but similar high pressure capacity at roughly 20 bar due to similar pore volumes.

3.5 References

- [1] DeStefano, M.; Islamoglu, T.; Garibay, S.; Hupp, J.; Farha, O. Room-Temperature Synthesis of UiO-66 and Thermal Modulation of Densities of Defect Sites. *Chem. Mater.* **2017**, 29, 1357-1361.
- [2] Chun, H.; Moon, J. Discovery, Synthesis, and Characterization of an Isomeric Coordination Polymer with Pillared Kagome Net Topology. *Inorg. Chem.* **2007**, 46, 4371-4373.
- [3] Dybtsev, D.; Chun, H.; Kim, K. Rigid and Flexible: A Highly Porous Metal–Organic Framework with Unusual Guest-Dependent Dynamic Behavior. *Angew. Chem.* **2004**, 116, 5143-5146.
- [4] Zhou, K.; Chaemchuen, S.; Wu, Z.; Verpoort, F. Rapid Room Temperature Synthesis Forming Pillared Metal–Organic Frameworks with Kagome Net Topology. *Microporous Mesoporous Mater.* **2017**, 239, 28-33.
- [5] Natarajan, S.; Mahata, P. Metal–Organic Framework Structures – How Closely are they Related to Classical Inorganic Structures? *Chem. Soc. Rev.* **2009**, 38, 2304-2318.
- [6] Stock, N.; Biswas, S. Synthesis of Metal–Organic Frameworks (MOFs): Routes to Various MOF Topologies, Morphologies, and Composites. *Chem. Rev.* **2012**, 112, 933-969.
- [7] Seetharaj, R.; Vandana, P.; Arya, P.; Mathew, S. Dependence of Solvents, pH, Molar Ratio and Temperature in Tuning Metal–Organic Framework Architecture. *Arabian Journal of Chemistry.* 2016, <http://dx.doi.org/10.1016/j.arabjc.2016.01.003>.
- [8] Jasuja, H.; Burtch, N.; Huang, Y.; Cai, Y.; Walton, K. Kinetic Water Stability of an Isostructural Family of Zinc-Based Pillared Metal–Organic Frameworks. *Langmuir.* **2012**, 29, 633-642.
- [9] Jasuja, H.; Huang, Y.; Walton, K. Adjusting the Stability of Metal–Organic Frameworks under Humid Conditions by Ligand Functionalization. *Langmuir.* **2012**, 28, 16874-16880.
- [10] Lee, J.; Olson, D.; Pan, L.; Emge, T.; Li, J. Microporous Metal–Organic Frameworks with High Gas Sorption and Separation Capacity. *Adv. Funct. Mater.* **2007**, 17, 1255-1262.
- [11] Walton, K.; Snurr, R. Applicability of the BET Method for Determining Surface Areas of Microporous Metal–Organic Frameworks. *J. Am. Chem. Soc.* **2007**, 129, 8552-8556.

- [12] Li, L.; Wang, S.; Chen, T.; Sun, Z.; Luo, J.; Hong, M. Solvent-Dependent Formation of Cd(II) Coordination Polymers Based on a C₂-Symmetric Tricarboxylate Linker. *Cryst. Growth Des.* **2012**, 12, 4109-4115.
- [13] Kondo, M.; Takashima, Y.; Seo, J.; Kitagawa, S.; Furukawa, S. Control Over the Nucleation Process Determines the Framework Topology of Porous Coordination Polymers. *CrystEngComm.* **2010**, 12, 2350-2353.
- [14] Chun, H.; Dybtsev, D.; Kim, H.; Kim, K. Synthesis, X-ray Crystal Structures, and Gas Sorption Properties of Pillared Square Grid Nets Based on Paddle-Wheel Motifs: Implications for Hydrogen Storage in Porous Materials. *Chem. Eur. J.* **2005**, 11, 3521-3529.
- [15] Kaduk, J. Terephthalate Salts: Salts of Monopositive Cations. *Acta. Cryst.* **2000**, 56, 474-485.
- [16] Zhao, Y.; Wu, H.; Emge, T.; Gong, Q.; Nijem, N.; Chabal, Y.; Kong, L.; Langreth, D.; Liu, H.; Zeng, H.; Li, J. Enhancing Gas Adsorption and Separation Capacity through Ligand Functionalization of Microporous Metal–Organic Framework Structures. *Chem. Eur. J.* **2011**, 17, 5101-5109.
- [17] Llewellyn, P.; Bourrelly, S.; Serre, C.; Vimont, A.; Daturi, M.; Hamon, L.; Weireld, G.; Chang, J.; Hong, D.; Hwang, Y.; Jung, S.; Ferey, G. High Uptakes of CO₂ and CH₄ in Mesoporous Metal-Organic Frameworks MIL-100 and MIL-101. *Langmuir.* **2008**, 24, 7245-7250.
- [18] Liang, Z.; Marshall, M.; Chaffee, A. CO₂ Adsorption, Selectivity and Water Tolerance of Pillared-layer Metal-Organic Frameworks. *Microporous Mesoporous Mater.* **2010**, 132, 305-310.
- [19] Chun, H.; Dybtsev, D.; Kim, H.; Kim, K. Synthesis, X-ray Crystal Structures, and Gas Sorption Properties of Pillared Square Grid Nets Based on Paddle-Wheel Motifs: Implications for Hydrogen Storage in Porous Materials. *Chem. Eur. J.* **2005**, 11, 3521-3529.
- [20] Tanaka, D.; Horike, S.; Kitagawa, S.; Ohba, M.; Hasegawa, M.; Ozawa, Y.; Toriumi, K. Anthracene array-type porous coordination polymer with host–guest charge transfer interactions in excited states. *Chem. Commun.* **2007**, 0, 3142-3144.
- [21] Henke, S.; Fischer, R. Gated Channels in a Honeycomb-like Zinc-Dicarboxylate-Bipyridine Framework with Flexible Alkyl Ether Side Chains. *J. Am. Chem. Soc.* **2011**, 133, 2064-2067.
- [22] Henke, S.; Schneemann, A.; Wutscher, A.; Fischer, R. Directing the Breathing Behavior of Pillared-Layered Metal-Organic Frameworks via a Systematic Library of Functionalized Linkers Bearing Flexible Substituents. *J. Am. Chem. Soc.* **2012**, 134, 9464-9474.

CHAPTER 4: DMOF-1 AS A REPRESENTATIVE MOF FOR SO₂ ADSORPTION IN BOTH HUMID AND DRY CONDITIONS

This chapter was partially reproduced from a previous manuscript. “Reprinted with permission from Hungerford, J.; Bhattacharyya, S.; Tumuluri, U.; Nair, Z.; Wu, Z.; Walton, K. DMOF-1 as a Representative MOF for SO₂ Adsorption in Both Humid and Dry Conditions. *J. Phys. Chem. C*. 2018, 122, 23493 – 23500. Copyright 2018 American Chemical Society.”

4.1 Introduction

In the previous chapters, DMOF was discussed as a platform material (Chapter 2) and a viable room temperature synthesis method was presented (Chapter 3). Additionally, a variety of functionalized DMOF materials were synthesized at room temperature using the following ligands: 1,2,4,5-tetramethyl-dicarboxylic acid (TM), 9,10-anthracene-dicarboxylic acid (ADC), naphthalene-dicarboxylic acid (NDC), and dimethyl-dicarboxylic acid (DM) (Figure E.1 shows the structure of the linkers). This chapter continues researching DMOF as the platform material, but further assesses the stability and adsorption characteristics of DMOF in the presence of humidity, dry SO₂, and humid SO₂.

This chapter utilizes DMOF as a platform material to develop structure property relationships upon exposure to SO₂ in dry and humid environments. These structure property relationships were explored using: 1) metal substitution and 2) linker functionalization. Metal substitution was explored using the following metals centers: zinc,

nickel, cobalt, and copper. All of the metal substitutions were performed on DMOF containing functionalized TM linkers, as previous experiments had shown that the TM linkers provided additional stability towards water vapor and it was theorized that a similar impact could be had on the SO₂ stability of the material.¹ These metal substituted samples will be referenced using the following notation: M-DMOF-TM (M = Zn, Ni, Co, Cu). The linker functionalized samples were synthesized with zinc as the metal center and the following functionalized BDC linkers: TM, ADC, NDC, and DM. These linker functionalizations will be referenced using the following notation: Zn-DMOF-X (X = TM, ADC, NDC, DM).

Previous work by Tan et. al.² reported the adsorption properties of zinc and nickel DMOF in dry SO₂. The authors' work combined FTIR and molecular modeling to probe the adsorption sites of SO₂ in these two M-DMOF structures. It was discovered that Ni-DMOF was more stable than Zn-DMOF when exposed to dry SO₂ as was observed in post exposure PXRD patterns. This trend follows the prediction of metal-ligand bond strength in the Irving-Williams series such that the metal center obeys the following stability relationship: Co < Ni < Cu > Zn.³ The trend established in the Irving-Williams series can be attributed to three factors. 1) The strength of the metal-ligand bond decreases with increasing size of the metal atom. 2) The metal-ligand bond strength is increased by the crystallization field energy, nickel has the highest crystallization field energy and zinc has no crystallization field energy.^{4,5} The crystallization field energy is the stabilizing energy associated with placing a metal atom into a ligand field. Ranking the metal atoms used in this chapter would follow this trend: Co < Zn < Cu < Ni. 3) The final factor that contributes to the stability of the framework is Jahn-Teller distortion.⁶ Jahn-Teller distortion is an

electronic property of the material. Jahn-Teller distortion occurs due to the degeneracy of the copper atoms which contains nine electrons in its outer d-orbital. This electronic degeneracy changes the molecular orbitals of octahedrally coordinated copper compounds such that they fall to a lower energy state, thereby increases the stability of those compounds. Due to these factors we predicted that incorporating copper into the structure of DMOF-TM should provide enhanced stabilization over the other metals.

In this work, substitution of the metal node in DMOF-TM with zinc, nickel, copper, and cobalt, and substitution of the organic linker in Zn-DMOF with DM, NDC, TM, and ADC were examined to determine stability towards SO₂ in both dry and humid environments. The purpose of this study is to gain a fundamental understanding of these interactions while maintaining constant topology. Future chapters will explore how other MOFs can be designed with greater chemical stability towards acid gases, as well as expanding stability considerations to include H₂S as an acid gas.

4.2 Experimental

4.2.1 Materials

All of the chemicals utilized in this study were used as received without further purification from the following sources: zinc (II) nitrate hexahydrate (Zn(NO₃)₂·6H₂O), nickel (II) nitrate hexahydrate (Ni(NO₃)₂·6H₂O), cobalt (II) nitrate hexahydrate (Co(NO₃)₂·6H₂O), copper (II) nitrate trihydrate (Cu(NO₃)₂·3H₂O), and 1,4-Diazabicyclo[2.2.2]octane (DABCO) from Sigma Aldrich; tetramethyl-1,4-benzenedicarboxylic acid (TMBDC) from Oakwood Products Inc.; N,N-dimethylformamide (DMF) and methanol (MeOH) from VWR; 1,4-

naphthalenedicarboxylic acid (NDC), 2,5-dimethylterephthalic acid (DM), and 9,10-anthracenedicarboxylic acid (ADC) from TCI.

4.2.1.1 Metal Substitution Synthetic Procedures.

Functionalized M-DMOF samples with TMBDC are referred to as M-DMOF-TM and were prepared separately with four metal ions ($M = \text{Zn, Ni, Co, Cu}$) in a one pot synthesis to produce a series of isorecticular products following the procedures contained in the literature.⁷ See Figure E.1 and E.2 for a schematic of the DMOF structure and ligands. General Procedure: The following materials were added to 15 mL of DMF and allowed to stir for 3 hours at 350 rpm: 0.63 mol of the chosen metal node's nitrate-based metal salt [$\text{Zn}(\text{NO}_3)_2 \cdot 6\text{H}_2\text{O}$ or $\text{Ni}(\text{NO}_3)_2 \cdot 6\text{H}_2\text{O}$ or $\text{Cu}(\text{NO}_3)_2 \cdot 3\text{H}_2\text{O}$ or $\text{Co}(\text{NO}_3)_2 \cdot 6\text{H}_2\text{O}$], 0.63 mmol TMBDC (0.140g), and 0.31 mmol DABCO (0.035 g). The resulting solution was filtered three times through filter paper (size P8), transferred into 22 mL vials, and placed in a sand bath. The samples were then heated for 48 h at 120 °C in an isothermal oven. The samples were then cooled, filtered (size P8), and washed with DMF.

4.2.1.2 Ligand Substitution Synthetic Procedures.

Functionalized Zn-DMOF samples with different ligands are referred to as Zn-DMOF-X, where X corresponds to: TM, DM, NDC, and ADC ligands. Their synthetic procedures are further outlined below.

Zn-DMOF functionalized with ADC (Zn-DMOF-ADC) was prepared following the procedures outlined in the literature.⁸ In a glass beaker, 1 mmol of $\text{Zn}(\text{NO}_3)_2 \cdot 6\text{H}_2\text{O}$ and 1 mmol of ADC were added to 5 mL of DMF at room temperature. To this solution, 0.5 mmol of DABCO was added along with 5 mL of methanol. The solution was then allowed to stir for 18 hours at 350 rpm. The solution was then filtered (size P8) and poured into a

Teflon autoclave and heated for 48 hours at 120 °C in an isothermal oven. The samples were then cooled, filtered (size P8), and washed with DMF.

Zn-DMOF functionalized with NDC (Zn-DMOF-NDC) was prepared following the procedures contained in the literature.⁹ In a glass beaker 0.6 mmol of $\text{Zn}(\text{NO}_3)_2 \cdot 6\text{H}_2\text{O}$, 0.6 mmol NDC, and 0.3 mmol of DABCO were added to 9 mL of DMF at room temperature. The solution was stirred for three hours and then filtered (size P8) and poured into a Teflon autoclave and heated for 48 hours at 120 °C in an isothermal oven. The samples were then cooled, filtered (size P8), and washed with DMF.

Zn-DMOF functionalized with DM (Zn-DMOF-DM) was prepared following the procedures contained in the literature.¹⁰ In a glass beaker 0.6 mmol of $\text{Zn}(\text{NO}_3)_2 \cdot 6\text{H}_2\text{O}$, 0.6 mmol DMBDC, and 0.3 mmol of DABCO were added to 15 mL of DMF at room temperature. The solution was stirred for three hours and then filtered (size P8) and poured into a Teflon autoclave and heated for 48 hours at 120°C in an isothermal oven. The samples were then cooled, filtered (size P8), and washed with DMF.

4.2.2 Characterization

4.2.2.1 Powder X-ray Diffraction

Powder X-ray diffraction (PXRD) patterns were collected on a PANalytical X'Pert X-ray diffractometer containing an X'Celerator detector using Cu K α ($\lambda = 1.5418 \text{ \AA}$) radiation at room temperature. The results were compared to simulated patterns as well as those found in the literature, to confirm that the expected materials had been properly synthesized.

4.2.2.2 Surface Area Analysis

Nitrogen physisorption isotherms at 77 K were measured using a Quadrasorb from Quantachrome Instruments. Brunauer-Emmett-Teller (BET) surface areas were determined over the pressure range $0.003 \leq P/P_0 \leq 0.05$.¹¹ Prior to the experiment the materials were outgassed at 110 °C for 18 hours under vacuum using a Quantachrome FloVac Degasser.

4.2.2.3 Thermogravimetric Analysis

Thermogravimetric Analysis (TGA) of the as-synthesized M-DMOF-TM samples was performed on a NETZSCH STA 449 F1 Jupiter® system under helium flow at 20 cc/min in the temperature range of 25 – 800 °C with a heating rate of 5 °C/min. The sample temperature was maintained at 800 °C for 20 minutes before cooling back down to room temperature.

4.2.2.4 In-Situ Infrared (IR) Spectroscopy

The M-DMOF-TM materials were activated ex-situ under vacuum at 110 °C for 18 hours prior to spectroscopic measurements. The samples were then loaded into a Thermo Nicolet Nexus 670 spectrometer in Diffuse Reflectance mode (DRIFTs), and the outlet gases from the DRIFTs cell (Pike Technologies HC-900) were analyzed using a quadrupole mass spectrometer (Omnistar GSD-301 O₂, Pfeiffer Vacuum) similar to what was described by Mounfield III et. al.¹²

The samples were pretreated by heating to 150 °C under a 50 cc/min He stream for 1 hour and cooled back down to 25 °C before exposure to a 50 cc/min SO₂/He mixed stream during which IR spectra were collected continuously for one-half hour every 12 seconds. Runs were conducted in this manner for SO₂ concentrations of 50, 150, and 260 ppm (max

SO₂ concentration) with the balance being He. Following exposure, the sample chamber was switched back to the pure helium flow until the mass spectrometer reading for SO₂ returned to baseline (approximately 15 minutes). At this time the sample was heated to 150 °C at a ramp rate of 10 °C/min, allowing for complete desorption of SO₂, which was confirmed by monitoring the SO₂ concentration using the output of the quadrupole mass spectrometer. The temperature was held at 150 °C for 5 minutes before cooling to 25 °C. Absorbance spectra during SO₂ adsorption were calculated as $Abs = -\log(I/I_0)$, where I is the single beam spectrum after adsorption and I₀ is the single beam spectrum before adsorption.

4.2.2.5 Water Vapor Adsorption Isotherms

Water vapor isotherms were collected at room temperature using a 3Flex Surface Characterization Analyzer from Micromeritics. Samples were activated on the Micromeritics Smart VacPrep using an activation temperature of 110 °C for 18 hours under vacuum. Samples were measured from 0 to 0.9 P/P₀ water vapor pressure to prevent capillary condensation.

4.2.2.6 Dry SO₂ Pressure Decay and Stability Determination

SO₂ adsorption was measured using a lab-built volumetric system contained within a fume hood. Samples (20 – 30 mg) were first loaded into the unit and activated under vacuum at 110 °C for 18 hours. Adsorption isotherms were then collected between 0 and 2.5 bar at 25 °C using pure SO₂. After adsorption experiments were completed the sample chamber was subject to vacuum overnight to ensure complete removal of SO₂ from the apparatus.

4.2.2.7 Humid SO₂ Exposure

Humid SO₂ exposure was conducted using an in-house exposure unit consisting of a sealed sample chamber and a NaHSO₃ solution kept in a water bath, through which a stream of air was bubbled to generate the desired concentrations of SO₂ and humidity. The sealed sample chamber was equipped with humidity and SO₂ sensors and monitored continuously throughout the exposure time. The SO₂ concentration was adjusted by changing the concentration and pH of the NaHSO₃ solution. A diagram of the setup is located in the supplemental information Figure E.3 and described in detail by Bhattacharyya et. al.¹³

4.2.2.8 Scanning Electron Microscopy

SEM images of the pre- and post-humid SO₂ exposed M-DMOF-TM samples were collected on a Zeiss Ultra60 FE-SEM instrument with a high-efficiency In-lens SE detector at a working distance of 3-4 mm and accelerating voltage of 0.6 kV to prevent charging of the materials. Prior to SEM analysis all samples were dispersed in 2-3 mL of methanol and pipetted onto a flat aluminum sample holder with conductive carbon tape and allowed to dry overnight.

4.3 Results and Discussion

4.3.1 Effects of Water Adsorption

The structure, porosity, and thermal stability of the synthesized Zn-DMOF-X (X = TM, DM, NDC, ADC) were confirmed using a combination of PXRD and nitrogen physisorption at 77K. The PXRD patterns (Figure E.9) were all in good agreement with those found in the literature.¹⁰ The BET surface area analyses are shown in Table 4.1.

Table 4.1: BET Surface Area Measurements of Zn-DMOF-X (X = TM, DM, NDC, and ADC)

	*Zn-DMOF-TM	Zn-DMOF-DM	Zn-DMOF-NDC	Zn-DMOF-ADC
As Synthesized	1002 (0.456)	1092 (0.448)	1414 (0.505)	728 (0.285)
After Water Adsorption	1016 (0.457)	Degrades ⁺	182 (0.007)	730 (0.290)
After 2.5 Bar SO ₂ Adsorption	948 (0.461)	Degrades	137 (0.055)	751 (0.307)
After FTIR Analysis	933 (0.424)	Not Tested	Not Tested	794 (0.331)
250 ppm-days Humid SO ₂ Exposure	Degrades	Not Tested	Not Tested	565 (0.219)

* Surface areas measured in m²/g. Data in parentheses are pore volume in cm³/g

⁺ Degrades signifies a surface area of less than 50 m²/g

The structure, porosity, and thermal stability of the synthesized M-DMOF-TM (M = Zn, Ni, Co, Cu) were confirmed using a combination of PXRD, nitrogen physisorption at 77K, and TGA. The PXRD patterns (Figure 4.4) were all in good agreement with the simulated pattern and resembled that of the parent material signifying that they are all isostructural. The nitrogen physisorption analysis showed that all materials exhibited a type-I isotherm, and only minor deviations in surface area exist among the different metal centers for the as synthesized samples. The results of all BET surface area analyses are shown in Table 4.2. The results of TGA, Figure E.4, show desorption of adsorbed water, DMF, or methanol at temperatures under 150 °C, followed by loss of the ligands beginning around 350-400 °C.

Table 4.2: BET Surface Area Measurements of M-DMOF-TM (M = Zn, Cu, Ni, and Co)

	*Zn-DMOF-TM	Cu-DMOF-TM	Ni-DMOF-TM	Co-DMOF-TM
As Synthesized	1002 (0.426)	1016 (0.457)	940 (0.459)	1003 (0.457)
After Water Adsorption	1016 (0.501)	1136 (0.512)	973 (0.462)	803 (0.372)
After Dry SO ₂ Adsorption	948 (0.461)	861 (0.501)	1066 (0.459)	835 (0.378)
After FTIR	933 (0.424)	952 (0.427)	967 (0.446)	997 (0.490)
50 ppm-days Humid SO ₂ Exposure	Degrades ⁺	750 (0.333)	500 (0.209)	Degrades
100 ppm-days Humid SO ₂ Exposure	Degrades	849 (0.370)	84 (0.005)	Degrades
250 ppm-days Humid SO ₂ Exposure	Degrades	503 (0.233)	Degrades	Degrades

* surface areas measured in m²/g. Data in parentheses are pore volume in cm³/g

⁺ Degrades signifies a surface area of less than 50 m²/g

Water adsorption isotherms were collected for the M-DMOF-TM and Zn-DMOF-X materials to compare to those previously reported in the literature.^{1,14,15} The water adsorption isotherms are shown in Figure 4.1. The M-DMOF-TM materials all have similar total uptake of water vapor across the different metal sites as was expected for materials that do not contain open metal sites. The stability of the samples after water adsorption was also confirmed using nitrogen physisorption measurements at 77K (Table 4.1 and 4.2) and PXRD (Figure 4.4). It was determined that the Zn-DMOF-X materials were unstable for X = DM and NDC and stable for X = TM and ADC, which matches data that were previously published by Jasuja et. al.¹

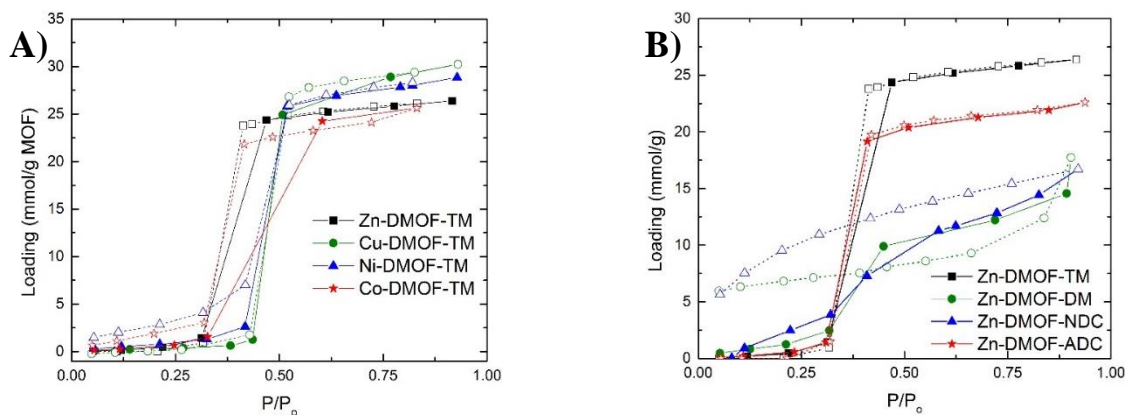


Figure 4.1: Water adsorption isotherms for: A) M-DMOF-TM and B) Zn-DMOF-X, where closed and open symbols represent adsorption and desorption, respectively.

4.3.2 Dry SO_2 Adsorption and FTIR

The results of the SO_2 adsorption experiments for the Zn-DMOF-X and M-DMOF-TM samples are shown in Figure 4.2. Figure 4.2A shows that the Cu and Zn-containing M-DMOF-TM samples exhibit decreased SO_2 uptake compared to the Ni and Co containing materials. Since DMOF-TM does not contain open metal sites this discrepancy could be attributed to two possible factors: (i) the number of defects contained within the material, or (ii) the result of electronic differences between the metal nodes causing differences in adsorption loadings. The BET surface areas of these materials were measured after SO_2 adsorption, and all materials were found to be stable under these exposure conditions (Table 4.2).

Figure 4.2B shows the SO_2 adsorption isotherms for the Zn-DMOF-X materials. While the TM and ADC samples were stable upon exposure, both the NDC and DM samples were unstable, as can be inferred by the large loss in surface area of the materials upon testing (Table 4.1). Zn-DMOF-DM is not shown, as it is evident from the experiment that the material degraded rapidly upon exposure to dry SO_2 . These SO_2 adsorption results

in the DMOF-X materials correlate with those that were seen in the water-exposed samples in which both TM and ADC were stable and NDC and DM were not. This stability can be attributed to a combination of the additional bulk provided by the TM and ADC ligands and their increased hydrophobicity inhibiting attack by SO₂ on the metal-ligand bonds.

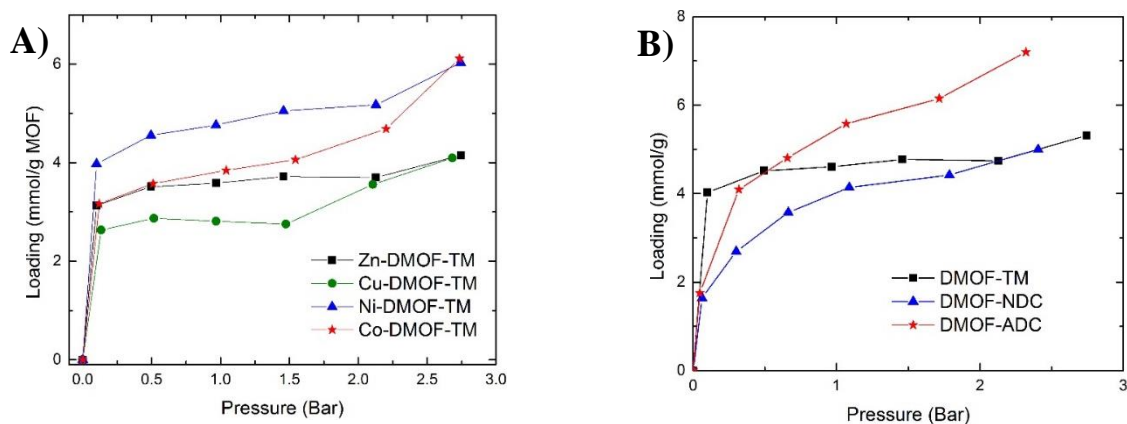


Figure 4.2: Dry SO₂ adsorption measurements for: A) M-DMOF-TM and B) Zn-DMOF-X

In situ FTIR was used to identify possible reasons for the discrepancy in SO₂ adsorption loadings across the metal species as well as offer insight into the effects of ligand substitution. The data were collected at three SO₂ concentrations of 50, 150, and 260 ppm in helium at 25 °C. The data show similar trends across the different concentrations for all of the metal variants. The complete data for the 50, 150, and 260 ppm runs can be found in the supporting information, Figure E.5 and Figure E.6, and the partial difference spectra for experiments performed at 260 ppm SO₂ in helium is shown in Figure 4.3 to emphasize the 700 – 1700 cm⁻¹ region where peaks from SO₂ adsorption sites were expected to occur. Similar peaks can be seen across the 50, 150, and 260 ppm SO₂ concentrations, but the signal to noise ratio was best for the 260 ppm SO₂ trials.

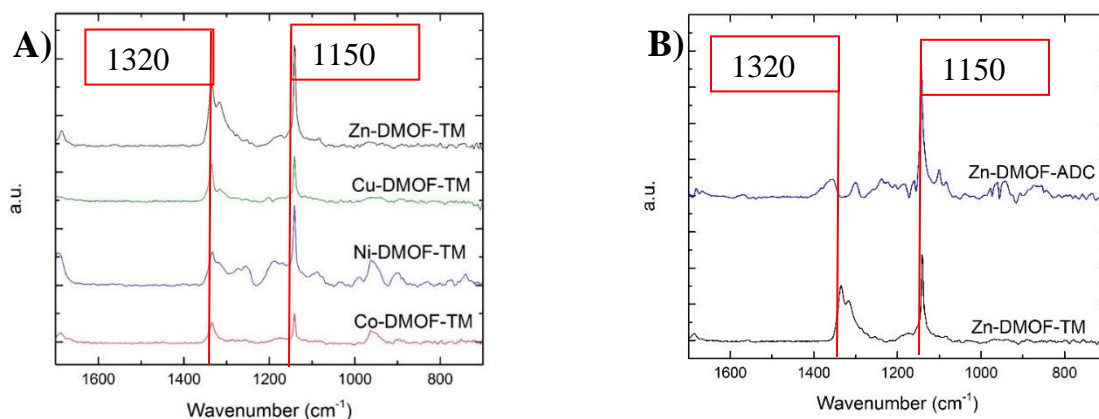


Figure 4.3: FTIR difference spectra of: A) M-DMOF-TM and B) Zn-DMOF-X upon exposure to 260 ppm SO₂ in helium flow

The difference spectra for the M-DMOF-TM (Figure 4.3A) samples show characteristic peaks at 1320 and 1150 cm⁻¹ for all samples tested corresponding to physisorbed SO₂ species similar to what has been observed in non-coordinated DMOF by Tan et al.² Notably, the Ni- and Co-containing DMOF-TM species contain a small additional peak at 950 cm⁻¹, which corresponds to bound sulfite species leading to potential differences across the metal sites. This behavior is unexpected due to the completely coordinated nature of DMOF-TM. Looking back at the water adsorption isotherms, there is very little difference in the relative hydrophobicity of the frameworks. Across the different metals they all show very little adsorption below 30 % RH such that defects may not be able to explain the differences in amount of adsorbed SO₂. Further experimentation would be required to determine the reason for the discrepancy in adsorbed SO₂ across the M-DMOF-TM samples. The additional adsorption sites associated with the band at 950 cm⁻¹ were also observed in the lower SO₂ concentration runs for Ni and Co-DMOF-TM, see Figure E.6 in the supplemental information. The Ni-DMOF-TM spectra also contains

a peak located at 1250 cm^{-1} . This peak has been previously observed in the metal oxide literature and signifies the existence of a more strongly bound SO_2 species within the framework.¹⁶ However, all SO_2 species were readily desorbed upon heating at $150\text{ }^\circ\text{C}$ under He flow as shown in Figure E.8, as was the case for all of the metal containing materials. The ease of desorption indicates that SO_2 adsorption in these DMOF-TM materials is weak. The difference spectra for the Zn-DMOF-X (Figure 4.3B) samples show differences across the two ligands that were tested (TM and ADC). Both Zn-DMOF-TM and Zn-DMOF-ADC have a similar peak located at 1150 cm^{-1} , however, Zn-DMOF-ADC has no peak located at 1320 cm^{-1} . This peak was observed in all of the M-DMOF-TM samples, as well as by Tan et. al., who identified the 1150 and 1320 cm^{-1} peaks as SO_2 physisorption sites.² In particular they identified the 1320 cm^{-1} peak as corresponding to SO_2 interactions with the benzene ring of the terephthalic linker. Since this peak is missing in Zn-DMOF-ADC, it is likely that the additional bulk of that ligand inhibits the physisorption at the central phenyl ring.

The full range FTIR spectra as shown in Figures E.5 and E.6 exhibit a broad feature in the range $3000 - 3700\text{ cm}^{-1}$, corresponds to adsorbed water species that may have been introduced into the setup at low ppm levels; this was also observed by Mounfield III et. al.¹² While the adsorption of water species does not play a role in identifying the SO_2 adsorption sites, it raises stability concerns for the materials due to the combination of acid species and water and was therefore further investigated.

After SO_2 adsorption and FTIR experiments, the stability of the materials was evaluated using the combination of nitrogen physisorption analysis at 77 K and PXRD measurements. BET surface areas are shown in Table 4.1 and Table 4.2, and PXRD

patterns are shown in Figure 4.4 and Figure E.9. All of the M-DMOF-TM samples were found to be stable upon adsorption of SO₂ in the pressure decay apparatus, as was the Zn-DMOF-ADC functionalized material. The materials were also tested for stability after FTIR measurements due to the trace amounts of water that were observed in the FTIR spectra (Figure E.5 and Figure E.6). The small amount of water in the FTIR lines did not play a role in destabilizing the M-DMOF-TM and Zn-DMOF-ADC materials, as they were stable under the conditions of the FTIR analysis. This stability can likely be attributed to the low SO₂ concentration as well as only trace concentrations (ppm levels) of water contained within the gas lines and cylinder.

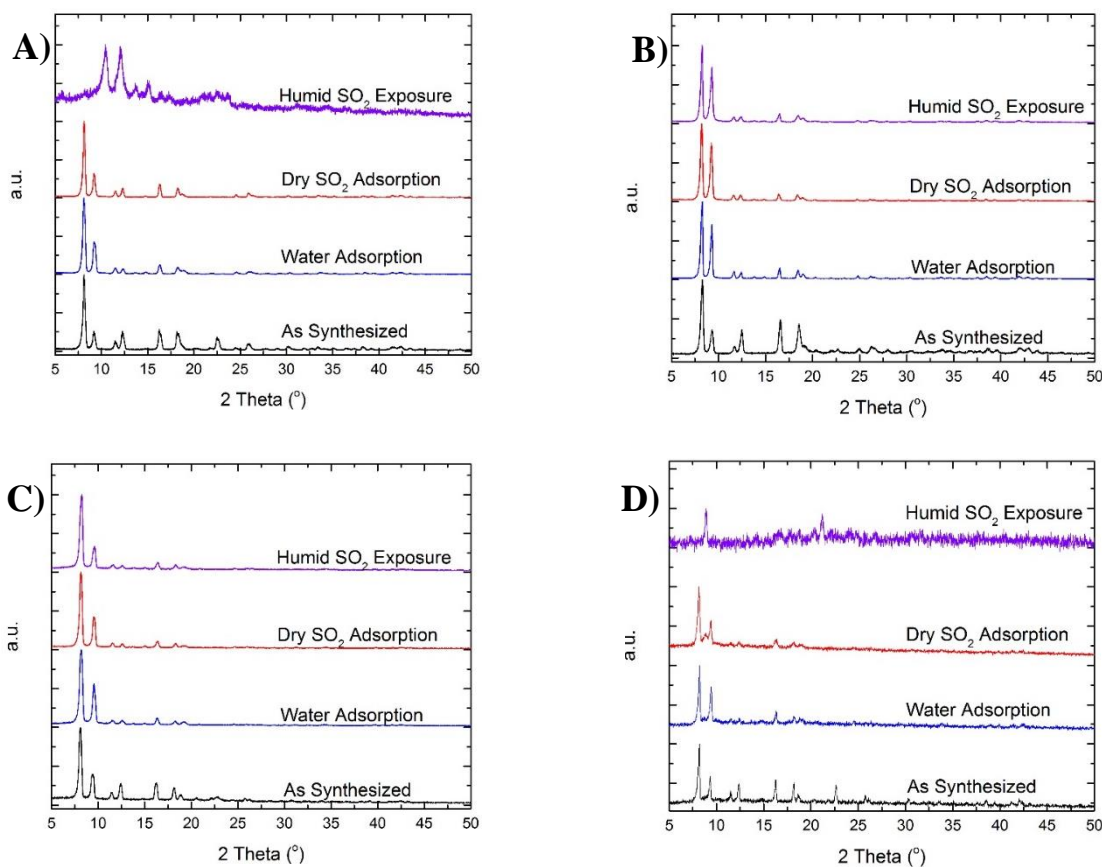


Figure 4.4: PXRD patterns of: A) Zn-DMOF-TM, B) Cu-DMOF-TM, C) Ni-DMOF-TM, and D) Co-DMOF-TM, for as synthesized, after water adsorption, after dry SO₂ adsorption, and after humid SO₂ exposure for 1 day (85% RH and 50 ppm SO₂)

4.3.3 *Humid SO₂ Exposure*

Humid SO₂ exposure tests were conducted on the M-DMOF-TM samples by exposing the materials to 85% RH and 50 ppm SO₂ for varying lengths of time. Initial tests were conducted for 50 ppm-days (1 day exposure at 50 ppm SO₂) day under these conditions, and the materials were then tested to determine the loss in BET surface area and crystallinity. Further testing extended the timeframe to 100 ppm-days and then 250 ppm-days of exposure to humid SO₂. SEM images and digital photographs were also used to assess the degradation of the samples and are shown in the supplemental information, Figure E.11 and Figure E.13, respectively. From the SEM images it can be seen that the humid SO₂ environment is degrading the Co, Zn, and Ni samples as the individual crystals appear to be fusing together and losing overall morphology. The Cu-DMOF-TM sample, however, appears to only undergo slight softening of the crystal edges. Additionally, the drastic color change, (see photographs in the supplemental information Figure E.13) of the Co sample can be identified as the material degrading into cobalt/sulfur species, which was later confirmed by XPS. The PXRD patterns and loss in BET surface areas of the four materials are located in Figure 4.4 and Table 4.2, respectively.

The Co and Zn samples showed a complete loss of BET surface area, and PXRD patterns show no retention of the DMOF-TM crystal structure for all humid SO₂ exposure times. The Ni sample maintained some crystallinity after the 50 ppm-days of exposure, as can be seen through PXRD, and only saw a 50% decrease in surface area after the exposure. In the 100 ppm-days of exposure, Ni-DMOF-TM showed a complete loss in surface area, but some amount of crystallinity remained as was seen through PXRD. However during the 250 ppm-days of exposure both crystallinity of the material and surface area were completely lost. Since all of these materials were stable under exposure to humidity and to

dry SO₂, it appears that the synergistic adsorption of SO₂ and water causes the formation of sulfate/sulfite acid species, and these species are responsible for the MOF degradation. This synergistic degradation has been observed previously in the literature for MIL-125, but to the authors' knowledge it has not been previously reported in DMOF.¹⁷

Cu-DMOF-TM retains its crystallinity (Figure 4.4C), and undergoes only a 15% loss in surface area after 100 ppm-days of exposure to humid SO₂. This signifies that while the porosity of the MOF is being altered due to acid gas attack, the bulk structure maintains its crystalline nature. Bhattacharyya et. al. reported the stability of a variety of ZIF materials after 100 ppm-days of humid SO₂ exposure. ZIF-71 was the only material that was completely stable towards humid SO₂, ZIF-93 had similar humid SO₂ stability when compared to Cu-DMOF-TM from this study, and ZIF-8 had slightly less stability losing roughly 50% of its pore volume upon exposure to 100-ppm days of humid SO₂.¹⁸ MIL-125-NH₂ has also shown stability towards humid SO₂ when exposed for 1000-ppm hours (roughly 42-ppm days) resulting in minimal loss in surface area.¹⁸ For a longer 250 ppm-days humid SO₂ exposure a 50% loss in surface area was observed for the Cu-DMOF-TM material. This result can be explained by the Irving-Williams series, which predicts that the metal ligand bond-strengths will follow the trend: Co < Ni < Cu > Zn.³ The stability of the metal-ligand complex is attributed to three features. First, the strength of the metal-ligand bond increases with decreasing atomic radii. Second, crystal field theory suggests that the stability of the metal complexes should be related to the ionic potential of the metal complex.^{4,5} This would provide the greatest stability for the Ni metal complex and no additional stability for the Zn complex. Lastly, the phenomenon of Jahn-Teller distortion is strongest among octahedral Cu complexes which results in additional stability of the

metal node.⁶ This additional stability is the result of rearrangement of the molecular orbitals of the metal-ligand bonds to minimize the electrostatic interactions of the valence electrons. This distortion is seen in a variety of copper-containing materials such as MOF-74 and CuF₂, and is caused by the electronic degeneracy of the d^9 copper atom.¹⁹⁻²¹ Our results suggest that the combination of these three effects is contributing to the stability of the MOF in humid SO₂ conditions and explain why Cu-DMOF-TM is the most stable and Ni-DMOF-TM the second most stable. The Jahn-Teller distortion has been discussed previously in the literature and is relatively common among copper-based MOFs, but to the best of the authors' knowledge, this is the first time it has been mentioned in the DMOF class.²²⁻²⁵ This may provide insight and promote future research into copper octahedrally-coordinated MOFs to determine whether they are more inherently stable than their other metal-containing counterparts or if this distinction only occurs in the DMOF-TM structure. In either case it appears that changing the metal node was not able to stabilize the structures completely as all of the materials degraded to some degree. Further testing using single crystal XRD would be required to confirm the existence of distortion in the metal-ligand bonds of the Cu-DMOF-TM materials, but all attempts at producing a Cu-DMOF-TM single crystal have been unsuccessful.

Humid SO₂ exposure studies were also conducted on the Zn-DMOF-TM and Zn-DMOF-ADC samples to determine the ligand effects on material stability. Zn-DMOF functionalized with NDC and DM were not tested due to general instability in both pure water and dry SO₂ adsorption, as was observed in previous experiments. As was shown previously, Zn-DMOF-TM completely degraded upon humid SO₂ exposure. Zn-DMOF-ADC, however, only slightly degraded upon 250 ppm-days of humid SO₂ exposure as was

seen by a 23% drop in surface area (Table 4.1), and a retention of crystal structure which was observed in PXRD (Figure E.9). The additional stability of the ADC material over TM can be attributed to the additional bulk and hydrophobicity of the ADC ligand over TM, similar to results in previous studies that compared BDC to TM functionalized DMOF materials.^{1,10}

4.4 Conclusions

We have synthesized and characterized a variety of M-DMOF-TM (M = Zn, Ni, Cu, Co) variants that are isostructural to the parent zinc-containing MOF via a one-pot synthesis. We have confirmed the stability of these materials in the presence of water vapor up to 85 % P/P₀ and proved that the M-DMOF-TM materials were stable after exposure to dry SO₂. The exposure of M-DMOF-TM to SO₂ in the presence of humidity caused a synergistic decomposition of the materials, with the copper containing material exhibiting the greatest stability followed the nickel material as would be predicted by the Irving-Williams series of metal node / ligand stability. The actual mechanism of decomposition remains unknown at this time and future studies will focus on elucidating a better understanding of this process. In addition, a series of Zn-DMOF-X (X = TM, NDC, DM, ADC) samples were also synthesized and functionalization of the materials with TM and ADC resulted in the greatest stability towards both water and dry SO₂, and ADC functionalized materials were most stable to humid SO₂ exposure. The results suggest that ligand functionalization with added bulky side groups enhance the stability of the family of DMOF materials towards water and acid gases as well as the combinations of these substances.

4.5 References

- [1] Jasuja, H.; Huang, Y.; Walton, K. Adjusting the Stability of Metal-organic Frameworks Under Humid Conditions by Ligand Functionalization. *Langmuir* **2012**, 28, 16874-16880.
- [2] Tan, K.; Canepa, P.; Gong, Q.; Liu, J.; Johnson, D.; Dyevoich, A.; Thallapally, P.; Thonhauser, T.; Li, J.; Chabal, Y. Mechanism of Preferential Adsorption of SO₂ into Two Microporous Paddle Wheel Frameworks M(bdc)(ted)_{0.5}. *Chem. Mater.* **2013**, 25, 4653-4662.
- [3] Irving, H.; Williams, R. The Stability of Transition-Metal Complexes. *Journal of the Chemical Society* **1953**, 3192-3210.
- [4] Griffith, J.; Orgel, L. Ligand-Field Theory. *Quarterly Reviews Chemical Society* **1957**, 11, 381-393.
- [5] Figgis, B. In *Comprehensive Coordination Chemistry*. Upton: NY, **1987**; pp. 214 - 276.
- [6] Jahn, H.; Teller, E. Stability of Polyatomic Molecules in Degenerate Electronic States I-Orbital Degeneracy. *Royal Society Publishing*. **1937**, 161, 220-235.
- [7] Chun, H.; Dybtsev, D.; Kim, H.; Kim, K. Synthesis, X-ray Crystal Structures, and Gas Sorption Properties of Pillared Square Grid Nets on Paddle-wheel Motifs: Implications for Hydrogen Storage in Porous Materials. *Chemistry*. **2005**, 11, 3521-3529.
- [8] Tanaka, D.; Horike, S.; Kitagawa, S.; Ohba, M.; Hasegawa, M.; Ozawa, Y.; Toriumi, K. Anthracene Array-Type Porous Coordination Polymer with Host-guest Charge Transfer Interactions in Excited States. *Chem. Comm.* **2007**, 0, 3142-3144.
- [9] Chun, H.; Dybstev, D.; Kim, H.; Kim, K. Synthesis, X-ray Crystal Structures, and Gas Sorption Properties of Pillared Square Grid Nets Based on Paddle-wheel Motifs: Implications for Hydrogen Storage in Porous Materials. *Chem. Eur. J.* **2005**, 11, 3521-3529.
- [10] Jasuja, H.; Burtch, N.; Huang, Y.; Cai, Y.; Walton, K. Kinetic Water Stability of an Isostructural Family of Zinc-Based Pillared Metal-Organic Frameworks. *Langmuir* **2012**, 29, 633-642.
- [11] Walton, K.; Snurr, R. Applicability of the BET Method for Determining Surface Areas of Microporous Metal-organic Frameworks. *J. Am. Chem. Soc.* **2007**, 129, 8552-8556.
- [12] Mounfield III, W.; Tumuluri, U.; Jiao, Y.; Li, M.; Dai, S.; Walton, K. Role of Defects and Metal Coordination on Adsorption of Acid Gases in MOFs and Metal

- Oxides: An In Situ IR Spectroscopic Study. *Microporous Mesoporous Mater.* **2016**, 227, 65-75.
- [13] Bhattacharyya, S.; Pang, S.; Dutzer, M.; Lively, R.; Walton, K.; Sholl, D.; Nair, S. Interactions of SO₂-Containing Acid Gases with ZIF-8: Structural Changes and Mechanistic Investigations. *J. Phys. Chem. C* **2016**, 120, 27221-27229.
- [14] Burtch, N.; Jasuja, H.; Walton, K. Water Stability and Adsorption in Metal-organic Frameworks. *Chem. Rev.* **2014**, 114, 10575-10612.
- [15] Jasuja, H.; Jiao, Y.; Burtch, N.; Huang, Y.; Walton, K. Synthesis of Cobalt-, Nickel-, Copper-, and Zinc-Based, Water-Stable, Pillared Metal-Organic Frameworks. *Langmuir*, **2014**, 30, 14300-14307.
- [16] Schneider, W.; Li, J.; Hass, K. Combined Computational and Experimental Investigation of SO_x Adsorption on MgO. *J. Phys. Chem. B* **2001**, 105, 6972-6979.
- [17] Mounfield III, W.; Han, C.; Pang, S.; Tumuluri, U.; Jiao, Y.; Bhattacharyya, S.; Dutzer, M.; Nair, S.; Wu, Z.; Lively, R.; Sholl, D.; Walton, K. Synergistic Effects of Water and SO₂ on Degradation of MIL-125 in the Presence of Acid Gases. *J. Phys. Chem. C* **2016**, 120, 27230-27240.
- [18] Bhattacharyya, S.; Han, R.; Kim, W.; Chiang, Y.; Jayachandrababu, K.; Hungerford, J.; Dutzer, M.; Ma, C.; Walton, K.; Sholl, D.; Nair, S. Acid Gas Stability of Zeolitic Imidazolate Frameworks: Generalized Kinetic and Thermodynamic Characteristics. *Chem. Mater.* **2018**, 30, 4089-4101.
- [19] Rowsell, J.; Yaghi, O. Effects of Functionalization, Catenation, and Variation of the Metal Oxide and Organic Linking Units on the Low-pressure Hydrogen Adsorption Properties of Metal-organic Frameworks. *J. Am. Chem. Soc.* **2006**, 128, 1304-1315.
- [20] Billy, C.; Haendler, H. The Crystal Structure of Copper(II) Fluoride. *J. Am. Chem. Soc.* **1957**, 79, 1049-1051.
- [21] Rowsell, J.; Yaghi, O. Strategies for Hydrogen Storage in Metal-organic Frameworks. *Angew. Chem. Int. Ed.* **2005**, 44, 4670-7679.
- [22] Orcajo, G.; Villajos, J.; Martos, C.; Botas, J.; Calleja, G. Influence of chemical composition of the open bimetallic sites of MOF-74 on H₂ adsorption. *Adsorption*. **2015**, 21, 589-595.
- [23] Dinca, M.; Han, W.; Liu, Y.; Dailly, A.; Brown, C.; Long, J. Observation of Cu²⁺-H₂ Interactions in a Fully Desolvated Sodalite-Type Metal-Organic Framework. *Angew. Chem.* **2007**, 46, 1419-1422.
- [24] Riascos-Rodriguez, K.; Schroeder, A.; Arend, M.; Evans, P.; Hernandez-Maldonado, A. Hysteretic Adsorption of CO₂ onto a Cu₂(pzdc)₂(bpy) Porous

Coordination Polymer and Concomitant Framework Distortion. *Dalton Trans.* **2014**, 43, 10877-10884.

- [25] Luo, F.; Zheng, J.; Batten, S. Unprecedented (3,4)-connected Metal-organic Frameworks (MOFs) with 3-fold Interpenetration and Considerable Solvent-accessible Void Space. *Chem. Comm.* **2007**, 3744-3746.

CHAPTER 5: THE FEASIBILITY OF CU-BTC AS AN ADSORBENT FOR ACID GASES: H₂S, SO₂, AND NO₂

5.1 Introduction

In the previous chapter, functionalized and metal substituted DMOF was exposed to SO₂ in dry and humid environments in order to develop structure property relationships. Other acid gases, such as H₂S and NO₂ were not considered and developing an understanding of how MOFs interact when exposed to those acid gases is necessary. Cu-BTC was discussed as a complementary material for studying acid gas interaction in chapter 2. The open-metal sites in Cu-BTC have been targeted for a variety of adsorption-based separations.¹⁻³ Peterson et. al.¹ explored using Cu-BTC as a broad-spectrum adsorbent towards ammonia, arsine, and hydrogen sulfide. The authors found that the material outperformed activated carbon for ammonia adsorption but was not an effective adsorbent towards arsine or hydrogen sulfide. Computational studies have predicted that the open-metal sites in Cu-BTC will lead to strong binding interactions with H₂S and SO₂.⁴⁻⁶ Peterson et. al.⁷ also explored SO₂ adsorption in Cu-BTC and could not identify strong interactions between the open-metal sites of Cu-BTC and SO₂ like those that were predicted computationally. Further exploration of SO₂ interactions in open-metal site MOFs, such as Cu-BTC, are necessary to identify the nature of adsorption.

In this chapter, Cu-BTC was exposed to NO₂, SO₂, and H₂S gas in order to develop stability relationships, determine degradation products, and assess adsorption characteristics for Cu-BTC when it is exposed to these acid gases. Cu-BTC degraded upon

exposure to H₂S and NO₂, forming copper sulfide and copper nitrate respectively. Cu-BTC was not only stable when exposed to SO₂, but also displayed excellent SO₂ adsorption performance reaching a capacity of 12.5 mmol/g at 2.5 bar pressure. SO₂ breakthrough testing at 1000 ppm SO₂ in nitrogen showed that Cu-BTC has a strong affinity for SO₂ at low concentrations, reaching a breakthrough capacity of 0.45 mmol/g. This chapter provides a basis for further experiments exploring SO₂ and H₂S interactions in UiO-66 and ZIF-8, which will be discussed in chapter 6.

5.2 Results and Discussion

Cu-BTC was obtained from Imundo Tec LLC, it was pelletized at a pressure of 5000 psi, then sieved to a size of 840 μ m. The samples were first characterized using Brunauer-Emmett-Teller (BET) surface area analysis and powder x-ray diffraction (PXRD), Table 5.1 and Figure 5.1 respectively. Prior to acid gas exposure, roughly 100 mg of sample was loaded into a packed bed and was activated under nitrogen flow while heating to 150 °C for 2 hours. During activation, the sample changed from a light to darker blue color, this color change corresponds to the changing coordination environment of the copper atoms within the material and is similar to what others have observed.⁸ After activation, the samples were allowed to cool to room temperature before acid gas exposure.

Following activation, samples were exposed to H₂S (concentration of 5000 ppm), SO₂ (concentration of 1000 ppm), or NO₂ (concentration of 1000pm), all in a balance of nitrogen. Gases were provided by Airgas. A mass flow controller was used to control the rate of acid gas flow and was set to 50 mL/min for all experiments. When H₂S was passed through the bed, the sample rapidly changed from its original dark blue color to a brownish

gray (see Figure 5.2 for color changes over time). The bed changed color completely over a period of roughly 20 minutes. Before removing the sample, the bed was purged with nitrogen to remove any excess H_2S . A new sample was loaded into the bed and activated before exposing the sample to NO_2 , which was also passed through the bed at 50 mL/min. During the run the sample slowly changed from its initial dark blue to a light blue color (see Figure 5.2) over a period of 8 hours. Once again, a new sample was loaded and SO_2 was passed through the bed at 50 mL/min. During the run no color change was observed in the sample.

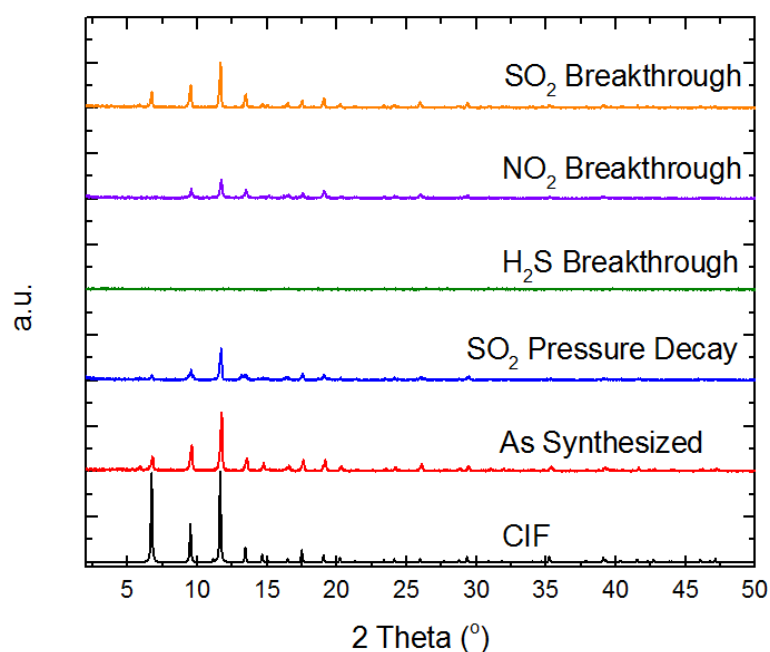


Figure 5.1: PXRD patterns of Cu-BTC exposed to H_2S , SO_2 , and NO_2 , and patterns after SO_2 breakthrough and adsorption experiments

Table 5.1: BET surface area results of nitrogen physisorption analysis for Cu-BTC exposed to H₂S, SO₂, and NO₂ as well as after SO₂ breakthrough and adsorption experiments

Sample	As Synthesized	H ₂ S Exposure	SO ₂ Exposure	NO ₂ Exposure	SO ₂ Breakthrough	SO ₂ Pressure Decay
BET SA (m ² /g)	1513	13	1871	478	1032	1249
Pore Volume (cm ³ /g)	0.646	0.086	0.866	0.413	0.426	0.561

The post exposed Cu-BTC samples were characterized using PXRD and BET surface area analysis and the materials' stability were assessed. The PXRD patterns (Figure 5.1) show that the Cu-BTC degraded upon exposure to NO₂ and H₂S, this is evident from the loss of crystalline peaks compared to the as synthesized material and cif pattern. The results of the nitrogen physisorption analysis confirm degradation of the samples as the surface area of Cu-BTC was diminished upon exposure to NO₂ and H₂S. Cu-BTC exposed to SO₂, however, did not degrade and retained both its crystallinity and BET surface area (See Table 5.1).

X-ray photon spectroscopy (XPS) was also used to assess the degradation species of the Cu-BTC samples. Prior to collecting XPS data the samples were subject to ultra-high vacuum such that any adsorbed sulfur or nitrogen containing molecules within the samples would be removed. The survey and S2p scans of H₂S exposed Cu-BTC show that a significant amount of sulfur has been incorporated into the structure of the material. The peak located at 163 eV corresponds to the formation of copper sulfide and degradation of the MOF structure (Figure F.7). The NO₂ exposed Cu-BTC samples show incorporation of nitrogen into the sample forming copper nitride, this can be seen in the survey and N1s

scans (Figure F.6). Figure F.4 shows the XPS scan of the pristine Cu-BTC sample and one can see that there is no evidence of peaks in either the S2p or N1s spectra. This further supports our claim that sulfur and nitrogen are incorporating into the structure of the H₂S and NO₂ exposed samples and causing the MOF to degrade.

Figure F.5 shows the XPS spectra for the SO₂ exposed Cu-BTC sample. While this sample did not degrade, it is interesting that we observe a small peak at 170 eV in the S2p scan. This signifies that either sulfur has been incorporated into the structure of the MOF or that the SO₂ binding energy is strong such that it cannot be removed under ultra-high vacuum conditions. Interestingly the small peak at 170 eV corresponds to the formation of sulfonic acid and not copper sulfide.⁹ Previously Tan et. al.¹⁰ reported strong binding energies at the metal site in another open-metal site MOF, MOF-74. However, due to peak location in the XPS spectra we cannot confirm the presence of similar interactions in Cu-BTC. It is possible that SO₂ binds to the open-metal site in Cu-BTC, but the binding energy is too weak to be observed under the ultra-high vacuum conditions present in XPS. Further testing is required to gain a better understanding of where SO₂ coordinates within the framework.

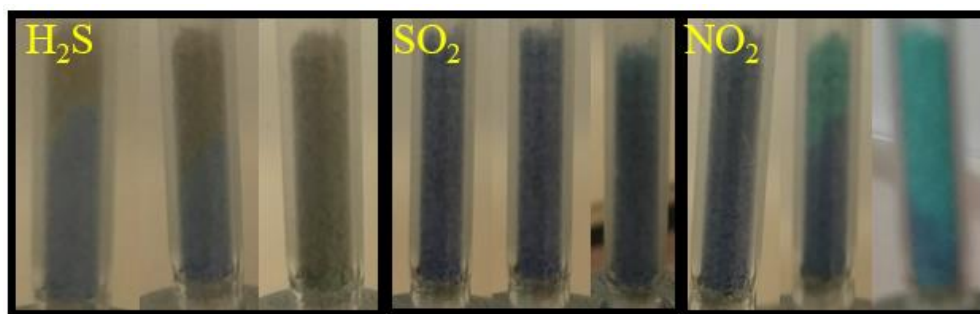


Figure 5.2: Observable color change during the H₂S, SO₂, and NO₂ exposure experiments

The exposure experiments showed that Cu-BTC was not stable when exposed to H₂S or NO₂, therefore SO₂ was the only gas utilized in breakthrough and equilibrium adsorption testing. On the breakthrough apparatus, a sample of roughly 100 mg was loaded into a packed bed and activated in the same manner as was discussed previously for the SO₂ exposure experiments. A mixture of 1000 ppm SO₂ in nitrogen was then passed through the bed at 50 mL/min and the outlet concentration was monitored using a mass spectrometer. Figure F.3 shows the breakthrough curve with the dead volume subtracted out. Once again, the sample did not change color during the length of the breakthrough experiment. From the breakthrough curve we measured a SO₂ adsorption capacity of 0.45 mmol SO₂/g MOF (0.0288 g SO₂/g MOF), breakthrough was determined as the time in which the concentration measured by the mass spectrometer matched the concentration of the SO₂ cylinder. Britt et. al. achieved an adsorption of 0.032 g SO₂/ g MOF, albeit under different breakthrough conditions (10,000 ppm SO₂ in nitrogen, however they calculated breakthrough at a concentration of 100 ppm SO₂).¹¹ Following this experiment PXRD and BET physisorption analysis were conducted and the material was found to be stable, retaining both its crystallinity and surface area.

SO₂ adsorption isotherms were collected on a lab build pressure decay system similar to the one reported by Bhattacharyya et. al.¹² The Peng-Robinson equation of state was used to relate the pressure from the pressure transducers to a molar volume which was used to calculate the amount of adsorbed SO₂. Samples were first activated in situ under vacuum at 150 °C overnight. Pure SO₂ was then dosed into the system from 0 - 2.5 bar while maintaining a constant temperature of 25 °C. The sample was tested three times for repeatability and stability. Between each measurement the sample was subject to vacuum

overnight to remove adsorbed SO₂. The results of this experiment are shown in Figure 5.3. One can see that between the first and second run there was no decrease in SO₂ capacity and both sample runs reached a maximum capacity of 13 mmol SO₂/g MOF. This SO₂ capacity is among the highest reported capacity for SO₂ among MOF materials, just slightly below what was reported for ZIF-65 by Bhattacharyya et. al. at 2.5 bar. Cu-BTC however shows significantly more favorable adsorption in the low-pressure region, below 1 bar, than ZIF-65.¹² The adsorption can be characterized as physisorption as the SO₂ was only weakly bound and easily desorbed in vacuum overnight, no heating was necessary. In the third SO₂ adsorption run we observed a slight decrease in the amount of adsorbed SO₂ and the sample reached a slightly lower maximum capacity of 11 mmol SO₂/g MOF at 2.5 bar. Table 5.1 shows that BET surface area and pore volume of the post SO₂ adsorption experiment. The lower SO₂ capacity after the third run may be due to the slight decrease in the surface area and pore volume that was observed. Additionally, XPS showed incorporation of sulfur into the structure of the material after SO₂ exposure which may result in the lower surface area and pore volume. The PXRD pattern of the Cu-BTC remains unchanged such that degradation is likely minimal.

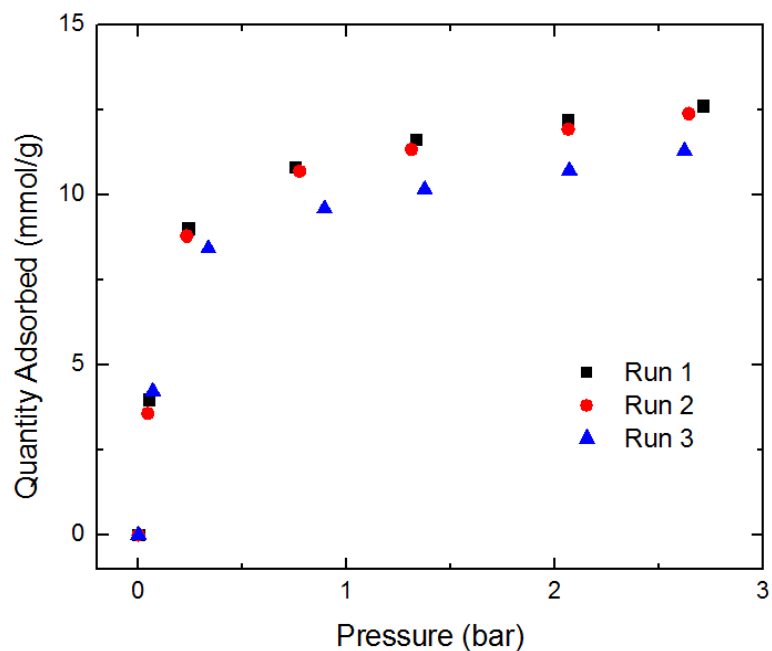


Figure 5.3: SO₂ adsorption isotherms from 0 – 2.5 bar for Cu-BTC

Drifts infrared (IR) spectroscopy was utilized to conduct in situ SO₂ and H₂S exposure on Cu-BTC. IR data was first collected on un-activated sample which was followed by in situ activation under helium gas flow at 150 °C for 2 hours. The sample was then allowed to cool to room temperature under helium flow before a second IR spectra was collected. The helium flow was then switched to 1000 ppm SO₂ or 5000 ppm H₂S in helium and IR spectra were collected every minute for one hour. The results of this experiment are shown in Figure 5.4A, SO₂, and Figure 5.4B, H₂S.

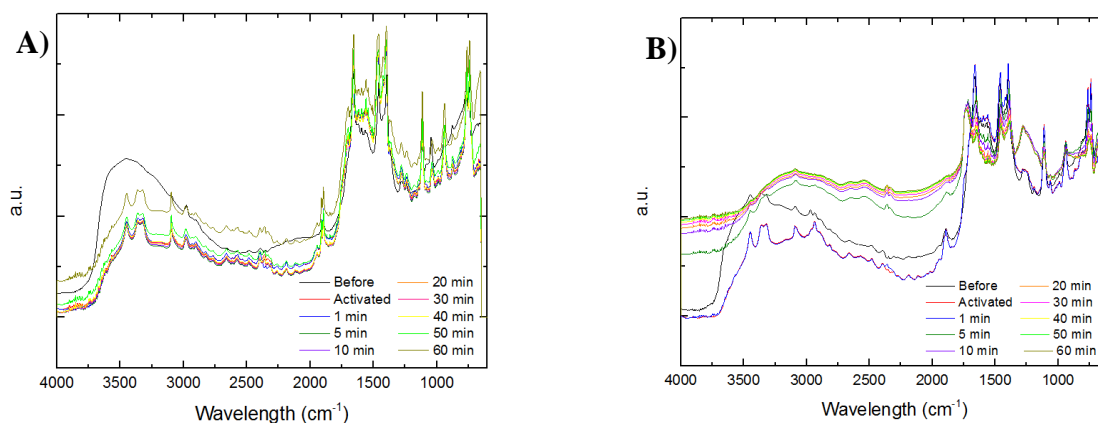


Figure 5.4: A) In Situ IR data collected under 1000 ppm SO₂ in helium flow. B) In Situ IR data collected under 5000 ppm H₂S in helium flow

The IR spectra in Figure 5.4A shows that initially the Cu-BTC samples have a large quantity of adsorbed water prior to activation. This is evident from the broad hump located at 3000 – 3500 cm⁻¹. After activation there is a large drop in intensity in this region signifying that activation is complete and that the initial water in the sample has been desorbed. During the SO₂ data collection we observe little change in the spectra. The asymmetric COO⁻ vibrational peaks at 1650 cm⁻¹ and 1460 cm⁻¹ show little to no change in peak position or intensity such that we can infer that no bonds break and the SO₂ is not cleaving the BTC-metal coordination bond. The vibrational C-C ring peaks located at 1560 cm⁻¹ and 1400 cm⁻¹ do not shift, which would be expected if SO₂ was interacting with the benzene ring. From the IR spectra we see that the general structure of the material is not changed upon exposure to low concentrations of SO₂.

Figure 5.4B shows the IR spectra for Cu-BTC exposed to H₂S, unlike the in situ SO₂ exposure IR studies, the material undergoes rapid changes to its structure after short exposures to H₂S. The peak at 1900 cm⁻¹ is greatly suppressed after only 5 minutes of

exposure to H₂S and has essentially disappeared after 10 minutes. Additionally, there is a substantial left shift of the 1650 cm⁻¹ peak corresponding to the asymmetrical vibration of the COO⁻ functional group. We speculate that the changes in these two peaks is a result of the bond cleavage of the metal-BTC coordination bonds and overall degradation of the framework. After the in situ H₂S IR exposure the Cu-BTC sample was collected and similarly to the original exposure experiments the material turned a light brown color signifying that it had completely degraded.

5.3 Conclusions

In this work we exposed Cu-BTC to three different acid gases, H₂S, SO₂, and NO₂. Cu-BTC was unstable towards H₂S and NO₂ but showed stability towards SO₂. The XPS data confirmed that Cu-BTC degraded when exposed to H₂S and NO₂ into copper sulfide and copper nitrate respectively. SO₂ exposure showed incorporation of sulfur into the material's structure, however this did not significantly impact the BET surface area of the material and it maintained its crystallinity. In the high pressure SO₂ adsorption experiments Cu-BTC showed exceptional performance, reaching a capacity of 13 mmol/g at 2.5 bar. Additionally, the total capacity of Cu-BTC only dropped slightly after 3 cycles.

5.4 References

- [1] Peterson, G.; Britt, D.; Sun, D.; Mahle, J.; Browe, M.; Demasky, T.; Smith, S.; Jenkins, A.; Rossin, J. Multifunctional Purification and Sensing of Toxic Hydride Gases by Cu-BTC Metal-Organic Framework. *Ind. Eng. Chem. Res.* **2015**, 54, 3626-3633.
- [2] Wu, Y.; Lv, Z.; Zhou, X.; Peng, J.; Tang, Y.; Li, Zhong. Tuning Secondary Building Unit of Cu-BTC to Simultaneously Enhance its CO₂ Selective Adsorption and Stability Under Moisture. *Chemical Engineering Journal.* **2019**, 355, 815-821.

- [3] Song, F.; Zhong, Q.; Zhao, Y. A Protophilic Solvent-assisted Solvothermal Approach to Cu-BTC for Enhanced CO₂ Capture. *Appl. Organometal Chem.* **2015**, 29, 612-617.
- [4] DeCoste, J.; Peterson, G. Metal-organic Frameworks for Air Purification of Toxic Chemicals. *Chem. Rev.* **2014**, 114, 5695-5727.
- [5] Supronowicz, B.; Mavrandonakis, A.; Heine, T. Interaction of Small Gases with the Unsaturated Metal Center of the HKUST-1 Metal-organic Framework. *J. Phys. Chem. C.* **2013**, 117, 14570-14578.
- [6] Watanabe, T.; Sholl, D. Molecular Chemisorption on Open Metal Sites in Cu₃(benzenetricarboxylate)₂: A Spatially Periodic Density Functional Theory Study. *J. Chem. Phys.* **2010**, 133.
- [7] Peterson, G.; Rossin, J.; DeCoste, J.; Killops, K.; Browe, M.; Valdes, E.; Jones, P. Zirconium Hydroxide Metal-organic Framework Composites for Toxic Chemical Removal. *Ind. Eng. Chem. Res.* **2013**, 52, 5462-5469.
- [8] Peterson, G.; Britt, D.; Sun, D.; Mahle, J.; Browe, M.; Demasky, T.; Smith, S.; Jenkins, A.; Rossin, J. Multifunctional Purification and Sensing of Toxic Hydride Gases by Cu-BTC Metal-Organic Framework. *Ind. Eng. Chem. Res.* **2015**, 54, 3626-3633.
- [9] Siril, P.; Shiju, N.; Brown, D.; Wilson, K. Optimising Catalytic Properties of Supported Sulfonic Acid Catalysts. *Applied Catalysis A.* **2009**, 364, 95-100.
- [10] Tan, K.; Zuluaga, S.; Wang, H.; Canepa, P.; Soliman, K.; Cure, J.; Li, J.; Thonhauser, T.; Chabal, Y. Interaction of Acid Gases SO₂, and NO₂ with Coordinatively Unsaturated Metal Organic Frameworks: M-MOF-74 (M= Zn, Mg, Ni, Co). *Chem. Mater.* **2017**, 29, 4227-4235.
- [11] Britt, D.; Tranchemontagne, D.; Yaghi, O. Metal-Organic Frameworks with High Capacity and Selectivity for Harmful Gases. *PNAS.* **2008**, 105, 11623-11627.
- [12] Bhattacharyya, S.; Han, R.; Kim, W.; Chiang, Y.; Jayachandrababu, K.; Hungerford, J.; Dutzer, M.; Ma, C.; Walton, K.; Sholl, D.; Nair, S. Acid Gas Stability of Zeolitic Imidazolate Frameworks: Generalized Kinetic and Thermodynamic Characteristics. *Chem. Mater.* **2018**, 30, 4089-4101.

CHAPTER 6: IMPACT OF METAL-ORGANIC FRAMEWORK SYNTHESIS PROCEDURE ON ADSORPTION PERFORMANCE: ROOM TEMPERATURE VERSUS SOLVOTHERMAL

6.1 Introduction

In the previous chapters, DMOF was synthesized at room temperature in only 4 hours (Chapter 3) and the stability of DMOF towards humidity, dry SO₂, and humid SO₂ was assessed in a metal substituted M-DMOF-TM (M = Co, Ni, Cu, Zn) and a ligand substituted Zn-DMOF-X (X = DM, NDC, TM, ADC) system (Chapter 4). Additionally, we determined that DMOF containing bulkier TM and ADC ligands is stable towards dry SO₂ and provides enhanced stability towards humid SO₂ when copper replaces zinc as the metal center. In this chapter we will build upon what was learned in chapters 3 and 4 and expand from the platform material into two additional MOFs, UiO-66 and ZIF-8.

In this chapter, we synthesized UiO-66, DMOF-TM, and ZIF-8 to compare the materials obtained through room temperature synthesis methods to those obtained through traditional solvothermal synthesis techniques. UiO-66 and ZIF-8 were both selected in addition to DMOF-TM for this study due to: 1) increased water and chemical stability over DMOF-TM.^{1,2} 2) UiO-66 is among the most studied MOFs for understanding defect interactions in MOFs and previous work analyzed the formation of defects within the framework as a result of room temperature synthesis.³⁻⁷ 3) A comprehensive study of ZIF materials identified the stability of ZIF-8 in dry SO₂ and instability upon exposure to humid SO₂.⁸ A similar characteristic was observed in DMOF-TM in chapter 4. In addition to these

three factors, this is the first study investigating room temperature synthesis as a feasible route to incorporating defects in MOFs and the impact of defective MOFs on stability towards acid gases.

A recent article by Park et. al.⁹ discussed the reproducibility of adsorption isotherms in MOFs across a variety of different materials. They concluded that approximately 20% of isotherms in the literature were classified as outliers. They also stated that these outliers may have been the result of variations in material properties as a result of different synthesis procedures or degradation of materials during adsorption measurements. In this work we synthesized a series of MOFs: UiO-66, DMOF-TM, and ZIF-8 via traditional solvothermal synthesis methods and room temperature synthesis methods found in the literature. We hypothesized that room temperature synthesis methods would yield MOFs with a greater concentration of defects than materials synthesized solvothermally, similar to the observations made by DeStefano et. al.³ We further hypothesized that these defects would impact the adsorption properties and stability of these materials. In this work we report the CO₂ adsorption capacity, water adsorption capacity, SO₂ adsorption capacity, SO₂ breakthrough capacity, and H₂S breakthrough capacity of UiO-66, DMOF-TM, and ZIF-8 synthesized solvothermally and at room temperature.

6.2 Experimental

6.2.1 Materials

All of the chemicals utilized in this study were used as received without further purification from the following sources: zinc (II) nitrate hexahydrate (Zn(NO₃)₂·6H₂O), zirconium(IV) chloride (ZrCl₄), zirconium(IV) propoxide solution (Zr(OCH₂CH₂CH₃)₄),

benzene-1,4-dicarboxylic acid (BDC), acetic acid ($\text{CH}_3\text{CO}_2\text{H}$), triethylamine ($(\text{C}_2\text{H}_5)_3\text{N}$), and 1,4-Diazabicyclo[2.2.2]octane (DABCO) from Sigma Aldrich; tetramethyl-1,4-benzenedicarboxylic acid (TMBDC) from Oakwood Products Inc.; N,N-dimethylformamide (DMF) and methanol from VWR; 2-methylimidazole ($\text{CH}_3\text{C}_3\text{H}_2\text{N}_2\text{H}$) from TCI America.

6.2.1.1 Solvothermal Synthesis Procedures

UiO-66,¹ DMOF-TM,¹⁰ and ZIF-8² were synthesized solvothermally using the methods available in the literature. This section will briefly describe the synthesis methods that were used to form these materials. A schematic of the MOFs as well as the linkers used in their synthesis are available in the supplemental information (See Figures G.1 and G.2).

ZIF-8 was synthesized solvothermally by preparing a solution containing 0.239 g (0.803 mmol) $\text{Zn}(\text{NO}_3)_2 \cdot 6\text{H}_2\text{O}$ and 0.060 g (0.731 mmol) 2-methylimidazole in 18 mL of DMF. The solution was then stirred until both the $\text{Zn}(\text{NO}_3)_2 \cdot 6\text{H}_2\text{O}$ and 2-methylimidazole had dissolved in solution and the solution was transferred to a Teflon lined autoclave. The autoclave was then heated from room temperature to 140 °C at 5 °C/min and held for 24 hours. The oven was then cooled at a rate of 0.4 °C/min to room temperature. The solution was then filtered and washed three times with DMF. Before sample testing, the sample was activated at 150 °C overnight.

UiO-66 was synthesized solvothermally by preparing a solution containing 0.212 g (0.908 mmol) of ZrCl_4 and 0.136 g (0.820 mmol) of BDC in 25 mL of DMF. The solution was stirred until both the BDC and ZrCl_4 had completely dissolved and the solution was transferred into a Teflon lined autoclave. The autoclave was then heated at 120 °C for 24

hours. The solution was then filtered and the sample was washed three times with DMF. Before sample testing, the sample was activated at 150 °C overnight.

DMOF-TM was synthesized solvothermally by preparing a solution containing 0.187 g (0.63 mmol) of $\text{Zn}(\text{NO}_3)_2 \cdot 6\text{H}_2\text{O}$, 0.140 g (0.63 mmol) of TMBDC, and 0.035 g (0.315 mmol) of DABCO in 15 mL of DMF. The solution was then stirred for 3 hours, filtered and the white precipitate that formed was removed. The filtrate was then transferred to a Teflon lined steel reactor and heated for 48 hours at 120 °C. After synthesis the sample was collected via filtration and washed three times with DMF. Before sample testing, the sample was activated at 150 °C overnight.

6.2.1.2 Room Temperature Synthesis Procedures

UiO-66,³ DMOF-TM,¹¹ and ZIF-8¹² were synthesized at room temperature using the methods present in the literature. All samples were subject to the same activation conditions after synthesis to maintain consistency with the solvothermally synthesized materials. It should be noted that DMOF-TM and ZIF-8 obtained from room temperature synthesis had much smaller particle sizes than those obtained via solvothermal methods such that some material was lost during washing, even when using very fine filter paper.

ZIF-8 was synthesized at room temperature by preparing a solution containing 1.17 g (3.932 mmol) of $\text{Zn}(\text{NO}_3)_2 \cdot 6\text{H}_2\text{O}$ in 8 mL of water. A separate solution of 80 mL of water was prepared and 22.7 g (276.4 mmol) of 2-methylimidazole was dissolved in this solution. The two solutions were then mixed at room temperature and allowed to stir on a stir plate for 5 minutes. The solution was then centrifuged for 20 minutes and the sample was collected via filtration and washed three times with DMF. Before sample testing, the sample was activated at 150 °C overnight.

UiO-66 was synthesized at room temperature by preparing a solution of 7 mL of DMF and 4 mL of acetic acid. To this solution 71 μ L of 70% zirconium propoxide solution was added. The solution was then covered with parafilm and heated on a hot plate for 2 - 4 hours at 130 °C. (It should be noted that the time is only a rough estimate. When the solution turns a yellowish hue, the reaction is complete and the zirconium SBU has been formed.) The solution was then allowed to cool to room temperature and 0.0749 g (0.252 mmol) of BDC was added to the solution. The solution was then allowed to stir for 18 hours at 200 rpm at room temperature. The sample was then collected via filtration and before testing it was activated at 150 °C overnight.

DMOF-TM was synthesized at room temperature by preparing two separate solutions of 7.5 mL of DMF. To the first solution, 0.218 g (0.75 mmol) of $\text{Zn}(\text{NO}_3)_2 \cdot 6\text{H}_2\text{O}$ and 0.166 g (0.75 mmol) of TMBDC were added. To the second solution, 0.07 g (0.625 mmol) of DABCO and 175 μ L of TEA were added. The solutions were then combined and the resulting mixture was stirred for 4 hours. The sample was then centrifuged and washed three times with DMF. Due to stability concerns, the sample was stored in DMF. Before sample testing, the sample was activated at 150 °C overnight.

6.2.2 Characterization

6.2.2.1 Thermogravimetric Analysis

Thermogravimetric analysis (TGA) of the room temperature and solvothermally synthesized samples was performed on a NETZSCH STA 449 F1 Jupiter® system under helium flow at 20 cc/min in the temperature range of 25 – 700 °C. Heating was done in stages: a 5 °C/min ramp rate was used from 25 – 110°C, the temperature was then left at 110 °C for 2 hours, and finally the temperature was ramped from 110 – 700 °C at a rate of

1 °C/min. The sample temperature was maintained at 700 °C for 20 minutes before cooling back down to room temperature at 40 °C/min.

6.2.2.2 Scanning Electron Microscopy

SEM images of the room temperature and solvothermally synthesized samples were collected on a Zeiss Ultra60 FE-SEM instrument. The instrument contains a high-efficiency In-lens SE detector which was operated at a working distance of 3 - 5 mm and an accelerating voltage of 0.6 kV to prevent charging. Prior to SEM analysis all samples were dispersed in a few drops of methanol and pipetted onto an aluminum sample holder covered in carbon tape and allowed to dry overnight.

6.2.2.3 Powder X-ray Diffraction

Powder X-ray diffraction (PXRD) patterns of the room temperature and solvothermally synthesized UiO-66, DMOF-TM, and ZIF-8 were collected on a PANalytical X'Pert X-ray diffractometer containing an X'Celerator detector. Cu K α (λ = 1.5418 Å) radiation was used to collect the powder patterns at room temperature. The results were then compared to simulated patterns as well as those found in the literature.

6.2.2.4 Surface Area Analysis

Nitrogen physisorption isotherms at 77K were measured using a Quadrasorb from Quantachrome Instruments. Brunauer-Emmett-Teller (BET) surface areas were determined over the pressure range $0.003 \leq P/P_0 \leq 0.05$.¹³ Before nitrogen physisorption measurements all samples were outgassed at 150 °C for 18 hours under vacuum using a Quantachrome FloVac Degasser.

6.2.2.5 Infrared (IR) Spectroscopy

Prior to IR spectroscopy measurements, all MOF materials were first activated ex-situ under vacuum at 150 °C for 18 hours in an Isotemp Vacuum Oven Model 281A from Fisher Scientific. The samples were then tested on a Nicolet iS10 spectrometer from Fisher Scientific operating in ATR mode.

6.2.2.6 Dry SO₂ Pressure Decay and Stability Determination

SO₂ adsorption was measured using a lab-built volumetric system. MOF samples (20 – 30 mg) were first loaded into the unit and activated under vacuum at 150 °C for 18 hours. Adsorption isotherms were then collected between 0 and 2.5 bar using pure SO₂ and operating at a constant temperature of 25 °C which was controlled using a recirculating water bath. After adsorption experiments were completed the sample chamber was subject to vacuum overnight to ensure complete removal of SO₂ from the apparatus. See Figure G.29 in the supplemental for a picture of the SO₂ apparatus.

6.2.2.7 H₂S and SO₂ Breakthrough Experiments

H₂S and SO₂ breakthrough experiments were collected on a lab build system. The outlet gases from the breakthrough system were monitored using a Pfeiffer Omni^{Start}™ mass spectrometer. The MOFs were first pelletized using a pressure of 5000 psi (2000 psi for UiO-66 synthesized at room temperature as the MOF degraded when pelletized at 5000 psi) and sieved to 840 microns to prevent pressure drop in the packed bed. The sieved MOF sample was then packed into a quartz tube and activated under helium flow for two hours at 150 °C. The sample was then cooled to 25 °C and the helium flow was switched to either SO₂ (1000 ppm with a balance of nitrogen) or H₂S (5000 ppm with a balance of nitrogen) and the outlet concentration was monitored using the mass spectrometer. Breakthrough

was calculated at the point in which the outlet concentration reached the concentration of the cylinder (1000 ppm for SO₂ and 5000 ppm for H₂S). In all runs, a flowrate of 50 mL/min was used. After testing, the flow was switched back to helium and the system was heated to 100 °C to remove any SO₂ or H₂S that remained adsorbed in the breakthrough bed. For each sample three cyclic runs were collected with heating stages in between each run. After breakthrough testing the samples were characterized using nitrogen physisorption and PXRD to determine their stability to the acid gas exposure.

6.3 Results and Discussion

Three MOFs: UiO-66, DMOF-TM, and ZIF-8 were synthesized using conventional solvothermal methods and recently reported room temperature methods. These materials were then subject to a variety of characterization and adsorption testing to understand how synthesis conditions can affect the material structure and adsorption properties. Specifically, we wanted to investigate whether room temperature and solvothermal synthesis procedures produce materials of equal quality when considering: water adsorption, CO₂ adsorption, SO₂ adsorption, and SO₂ and H₂S breakthrough experiments.

6.3.1 Characterization of Materials

UiO-66, DMOF-TM, and ZIF-8 were synthesized solvothermally and at room temperature. The obtained materials were then characterized using SEM imaging (Figure 6.1), Brunauer-Emmett-Teller (BET) surface area analysis (Table 6.1), powder x-ray diffraction (PXRD) (Figure 6.2), infrared spectroscopy (IR) (supplemental information Figures G.10 – G.13), and thermogravimetric analysis (TGA) (supplemental information Figures G.14 – G.16).

Figure 6.1 shows SEM images of the solvothermally synthesized MOFs (capital letters) and room temperature synthesis (lower case letters). The room temperature synthesized MOFs resulted in a smaller particle size than those that were synthesized solvothermally for all samples. This is likely due to shorter synthesis times in the room temperature synthesis methods which promoted fast growth through: separate formation of zirconium clusters (UiO-66), deprotonation of linkers (DMOF-TM), or extreme excess of linker directing the synthesis to completion (ZIF-8). UiO-66, DMOF-TM, and ZIF-8 have room temperature synthesis times of 18 hours, 4 hours, and 5 minutes respectively while these materials have solvothermal synthesis times of 48 hours, 48 hours, and 24 hours respectively. Examining the SEM images of DMOF-TM we see the formation of plate-like structures in the solvothermally synthesized MOF (Figure 6.1A) and an agglomeration of smaller particles in the room temperature synthesis (Figure 6.1a). ZIF-8 synthesized solvothermally shows the typical well-defined crystallites in sodalite topology that can be expected (Figure 6.1B),¹⁴ however when synthesized at room temperature ZIF-8 did not form into a defined shape and the particle size of the resultant material was very small (Figure 6.1b). Room temperature synthesized ZIF-8 particles agglomerated into large rectangular structures. UiO-66 looks the most similar when comparing solvothermally and room temperature synthesized MOF. In both scenarios UiO-66 had no defined particle shape (Figures 6.1C and 6.1c), however the room temperature synthesized samples are slightly smaller than their solvothermal counterparts.

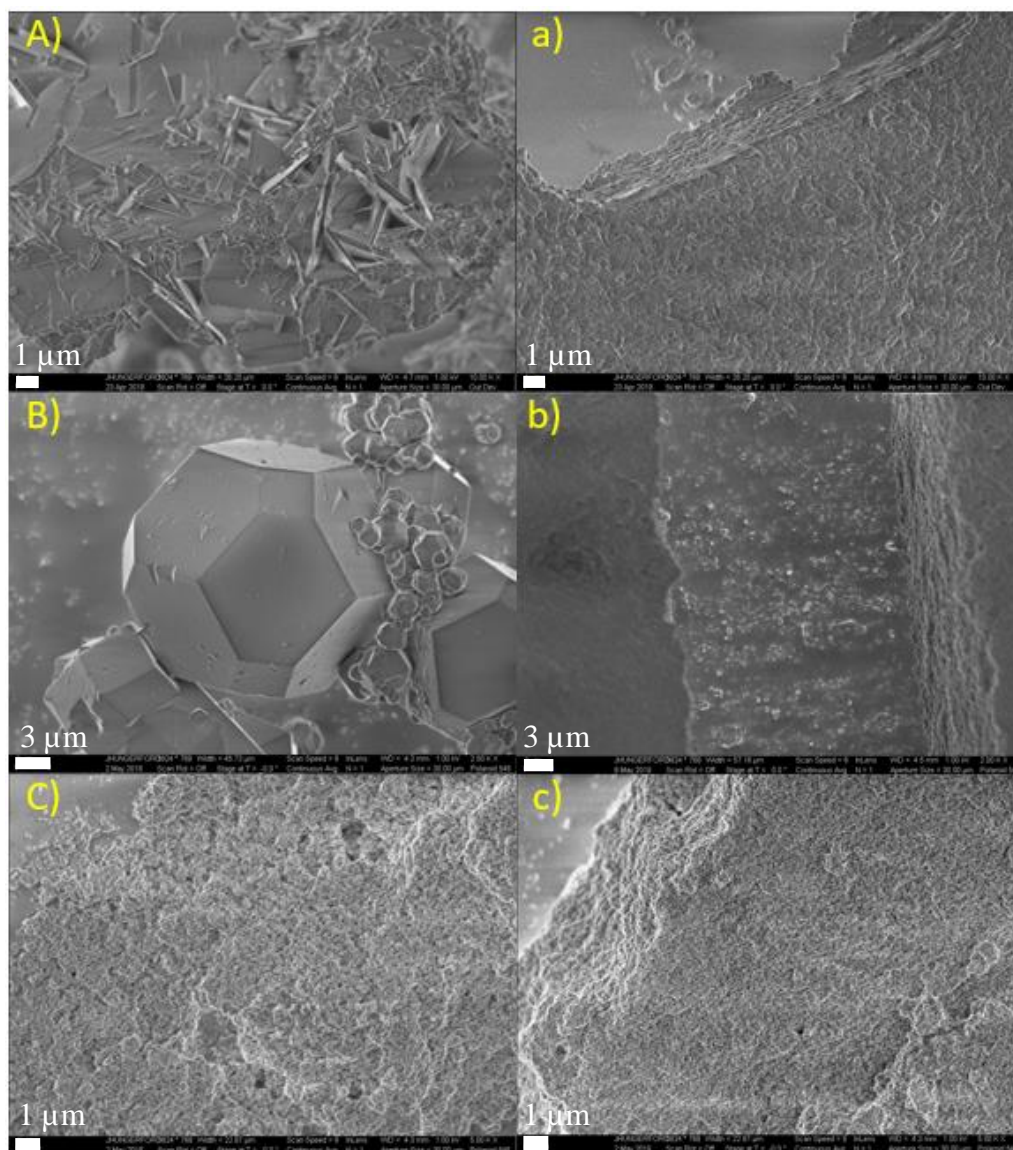


Figure 6.1: SEM images of A) DMOF-TM, B) ZIF-8, and C) UiO-66. Capital letters are material synthesized solvothermally and lower case letters are materials synthesized at room temperature

Nitrogen physisorption was used to assess the surface areas and pore volumes of the obtained MOFs. We hypothesized that the fast room temperature synthesis procedures would lead to a larger concentration of defects in the MOF structure. These defects have been shown to lead to an increase in surface area and adsorption properties; this is

especially true of UiO-66 where defects have been well documented.¹⁵ Table 6.1 shows the BET surface areas and pore volumes of the as synthesized UiO-66, DMOF-TM, and ZIF-8 materials. The obtained surface areas and pore volumes of the solvothermally synthesized samples match those that have been previously reported in the literature.^{1,2,10} UiO-66 and ZIF-8 synthesized at room temperature both show a roughly 50 % increase in BET surface area and pore volume when compared to the materials that were synthesized solvothermally. In the original UiO-66 room temperature synthesis manuscript, the authors attributed a similar increase in surface area to structure defects.³ These defects are likely caused by acetic acid which was used in high concentration during the formation of the zirconium cluster. Acetic acid can act as a modulator in the synthesis, exchanging with the BDC linker in the framework. Interestingly, there have been no reported cases of defects in ZIF-8 to the authors' knowledge, however defects in ZIF-8 have been theorized via computation methods.¹⁶ Figure G.16 shows the TGA data for ZIF-8 and it is evident that missing cluster defects are present in the room temperature synthesized material as the metal content is significantly lower than that of the solvothermally synthesized ZIF-8. The presence of missing cluster defects in ZIF-8 likely results in the increase surface area and pore volume, both of which are reported per unit mass. DMOF-TM displayed similar BET surface area and pore volume regardless of whether it was synthesized solvothermally or at room temperature. This is likely a result of dangling linker defects (See Figures G.11 and G.12) and not missing linker/missing cluster defects which were identified previously in the room temperature synthesis of this material. These defects have been shown to negatively impact the stability of the material when left in humid air for extended periods

of time.¹¹ Therefore, DMOF-TM was stored in DMF after synthesis to limit exposure to humidity in the atmosphere.

Table 6.1: BET surface areas of UiO-66, DMOF-TM, and ZIF-8 synthesized via room temperature (RT) and solvothermal (Solvo) methods

MOF	BET SA (m²/g)	Pore Volume (cm³/g)
DMOF-TM		
Solvo	1050	0.51
RT	1119	0.53
ZIF-8		
Solvo	1468	0.55
RT	2163	0.87
UiO-66		
Solvo	970	0.46
RT	1462	0.67

Figure 6.2 shows the PXRD patterns of the room temperature and solvothermally synthesized UiO-66, DMOF-TM, and ZIF-8 as well as the cifs of those materials. The PXRD patterns of the MOFs match those of the respective cif regardless of the synthesis method, signifying that the proper materials and topologies have been formed. The PXRD patterns of the room temperature synthesized UiO-66 show the presence of amorphous material or disorder in the structure that may be the result of structure defects. The presence of amorphous material is most evident in the low angle region from 5 – 7°. The UiO-66 sample was washed thoroughly before PXRD testing, but it is possible that some BDC or acetic acid may be stuck within the pore space of the MOF. The room temperature synthesis patterns of DMOF-TM and ZIF-8 show significantly more peak broadening compared to the solvothermally synthesized materials, which is consistent with the smaller particle size that was observed in the SEM images (Figure 6.1).

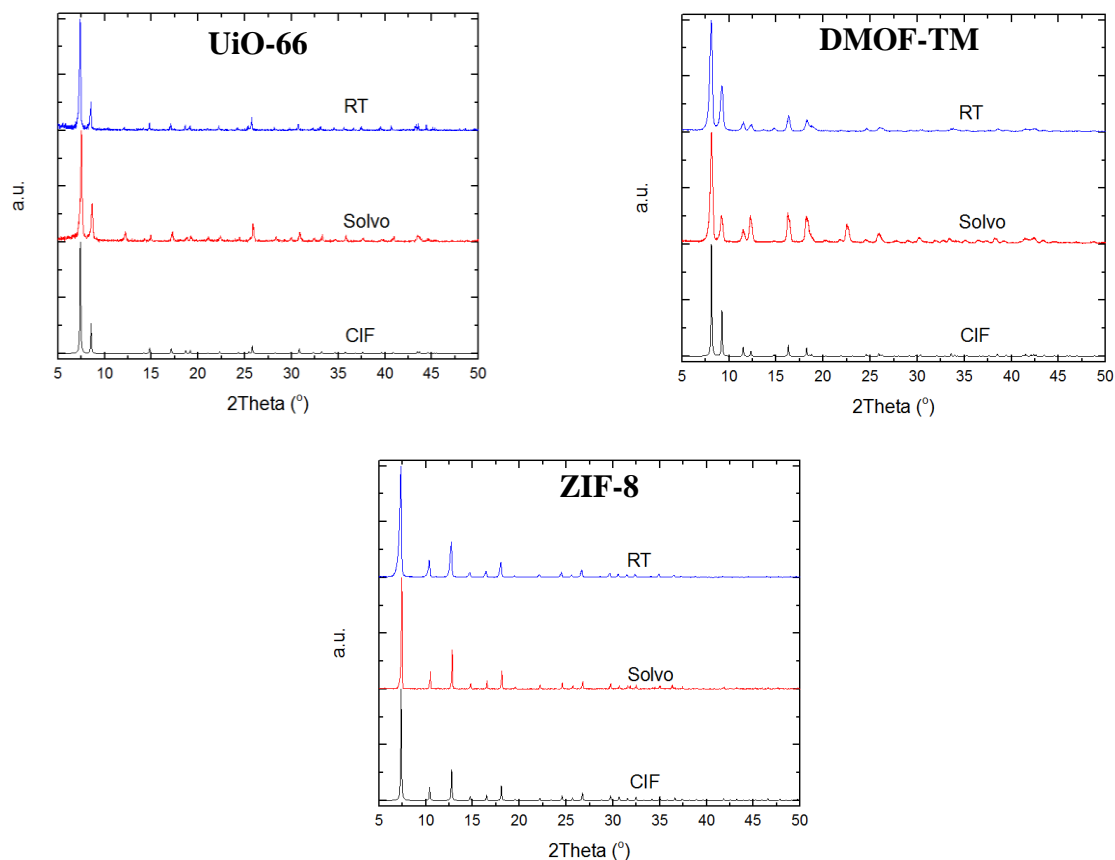


Figure 6.2: PXRD patterns of UiO-66, DMOF-TM, and ZIF-8 synthesized solvothermally (Solvo) and at room temperature (RT)

6.3.2 Water Adsorption Experiments

Water adsorption isotherms were collected for the materials from 0 to 85 % relative humidity (RH). The results of these experiments are shown in Figure 6.3. The UiO-66 water adsorption isotherms display S-shaped curves undergoing a step change in adsorptive uptake at roughly 30 % RH for the solvothermally synthesized sample and 40 % RH for the room temperature synthesis. The room temperature synthesized UiO-66 reached a maximum adsorption of 30 mmol/g which was greater than that of the solvothermally synthesized material (22 mmol/g). Both materials displayed slight hysteresis upon desorption beginning at the step change. The increase in adsorption of the room

temperature material is likely due to structure defects which also increased the material's pore volume and surface area by roughly 50% (Table 6.1). Interestingly, the room temperature synthesized material was slightly more hydrophobic than the solvothermally synthesized sample. The water adsorption isotherms for DMOF-TM also exhibited an S-shaped isotherm, however the two materials reached a similar maximum adsorption capacity of 23 mmol/g. Also similarly to UiO-66, the room temperature synthesized DMOF-TM is slightly more hydrophobic than the solvothermal material. If dangling linkers were present in DMOF-TM it would explain the increased hydrophobicity of the framework. ZIF-8 has previously been shown to be highly hydrophobic and this was also true of our materials regardless of synthesis method.^{17,18} Both the solvothermally and room temperature synthesized ZIF-8 materials adsorbed less than 5 mmol/g at 85% RH.

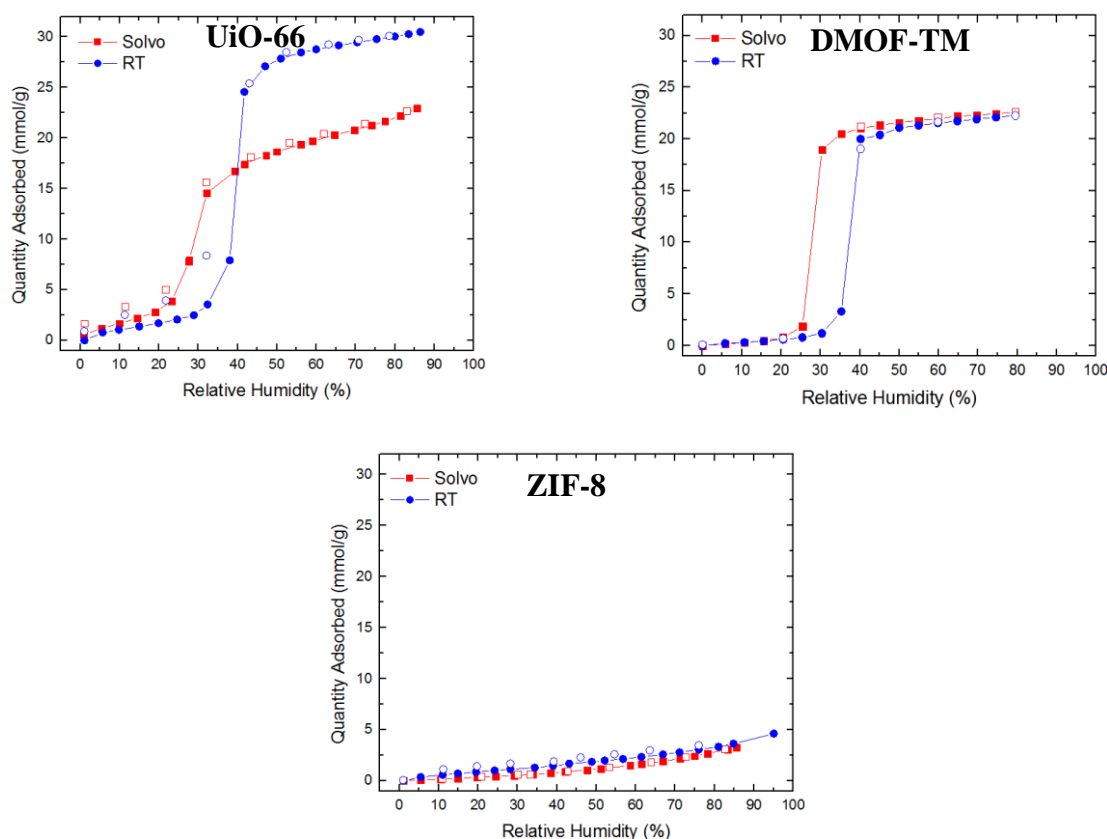


Figure 6.3: Water adsorption isotherms for UiO-66, DMOF-TM, and ZIF-8 synthesized solvothermally (Solvo) and at room temperature (RT)

6.3.3 CO_2 Adsorption Experiments

CO_2 adsorption isotherms were collected on the solvothermally and room temperature synthesized UiO-66, DMOF-TM, and ZIF-8 in the pressure range from 0 to 20 bar. The results of these experiments are shown in Figure 6.4. All materials display type-I isotherms with no hysteresis upon desorption. UiO-66 and DMOF-TM have similar adsorption capacities reaching between 7 to 8 mmol/g for both the solvothermally and room temperature synthesized samples. ZIF-8 synthesized at room temperature showed substantially larger CO_2 adsorption capacity at 20 bar when compared to the material that was synthesized solvothermally. This may be due to the higher surface area and pore

volume of the room temperature synthesized ZIF-8 (See Table 6.1), however we did not observe an increase in the room temperature synthesized UiO-66.

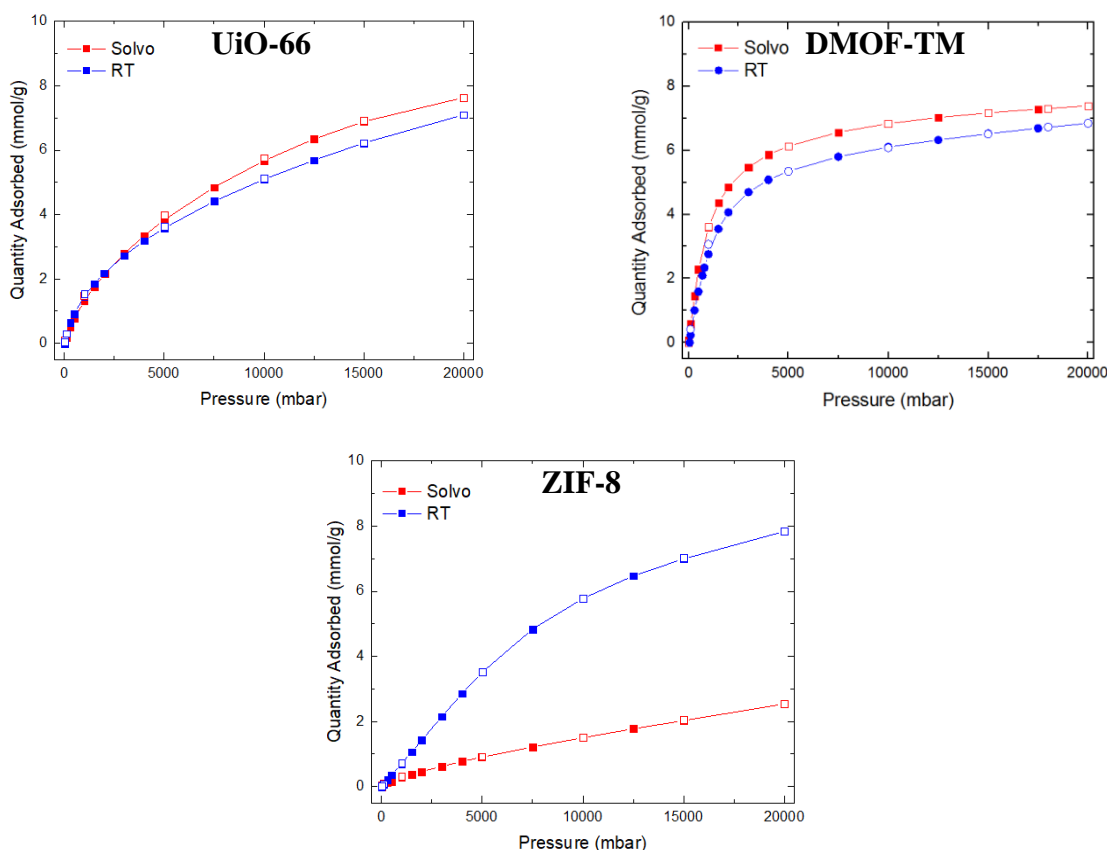


Figure 6.4: CO₂ adsorption isotherms for UiO-66, DMOF-TM, and ZIF-8 synthesized solvothermally (Solvo) and at room temperature (RT)

6.3.4 SO₂ Pressure Decay

SO₂ adsorption isotherms were collected for all of the MOF samples, the results of these experiments are shown in Figure 6.5. Interestingly UiO-66 does not show an increase in the amount of adsorbed SO₂ as was seen by Yang et. al.¹⁹ This may be due to the nature of defects in the room temperature synthesized UiO-66 compared to defects created by Yang et. al. or perhaps our solvothermal UiO-66 contains a greater number of defects than Yang's defect free sample. ZIF-8, however shows a substantial increase in SO₂ adsorption.

This increase in SO₂ adsorption is likely due to the increased surface area and pore volume measured in the material. Figure G.16 shows the TGA data for solvothermally and room temperature synthesized ZIF-8. ZIF-8 synthesized at room temperature contains much less metal species than the ZIF-8 that was synthesized solvothermally. This is evident from the mass percent remaining following TGA experiments and shows the presence of missing cluster defects in the material. DMOF-TM shows roughly no change in the amount of adsorbed SO₂ when comparing the materials that were synthesized solvothermally and at room temperature. However, the adsorption uptake of SO₂ at low pressure is extremely high for both DMOF-TM materials, reaching 3.5 mmol/g at only 0.01 bar (first adsorption point). Further breakthrough studies will examine this material's SO₂ adsorption performance at 1000 ppm SO₂ to better elucidate its potential at concentrations more similar to those that may be seen in industrial applications. We believe that the fantastic low pressure SO₂ adsorption of DMOF-TM is a result of molecular sieving, the pore diameter of DMOF-TM (3.5 Å) is very similar in size to the kinetic diameter of SO₂ (3.6 Å). UiO-66 and ZIF-8 did not show as favorable low pressure SO₂ adsorption compared to DMOF-TM, however both materials adsorbed more SO₂ at high pressures.

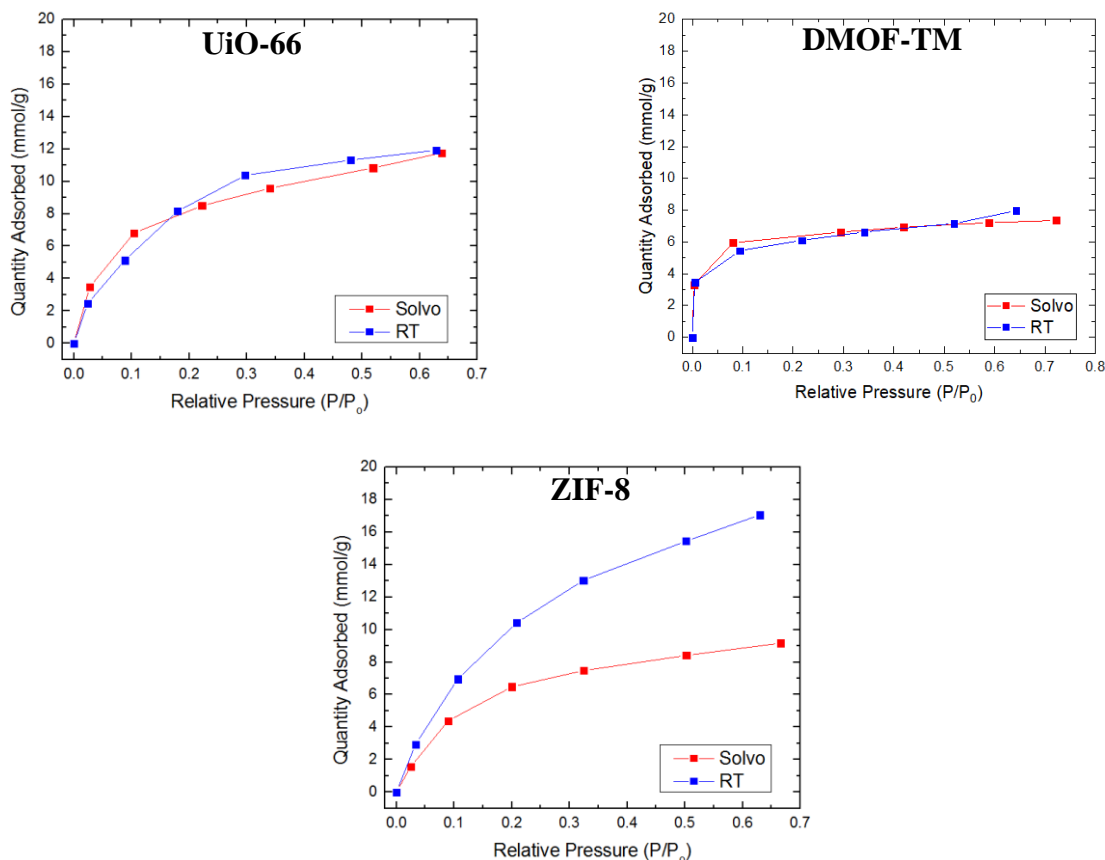


Figure 6.5: SO_2 pressured decay isotherms for UiO-66, ZIF-8, and DMOF-TM synthesized solvothermally (Solvo) and at room temperature (RT)

6.3.5 Acid Gas Breakthrough

H_2S breakthrough measurements were collected for the room temperature and solvothermally synthesized UiO-66, DMOF-TM, and ZIF-8 materials. The results of these experiments are shown in Figures 6.6. In the breakthrough measurements a flowrate of 50 mL/min and an H_2S concentration of 5000 ppm in nitrogen was used. The dead volume was determined using the nitrogen in the H_2S cylinder as a tracer gas. Breakthrough measurements were collected three times in succession for each sample. Between each run the sample was reactivated at 100 °C and the outlet concentration was monitored using a

mass spectrometer to determine when reactivation had finished. The complete breakthrough curves for each run (including the nitrogen tracer gas) can be found in the supplemental information, Figures G.17 – G.19.

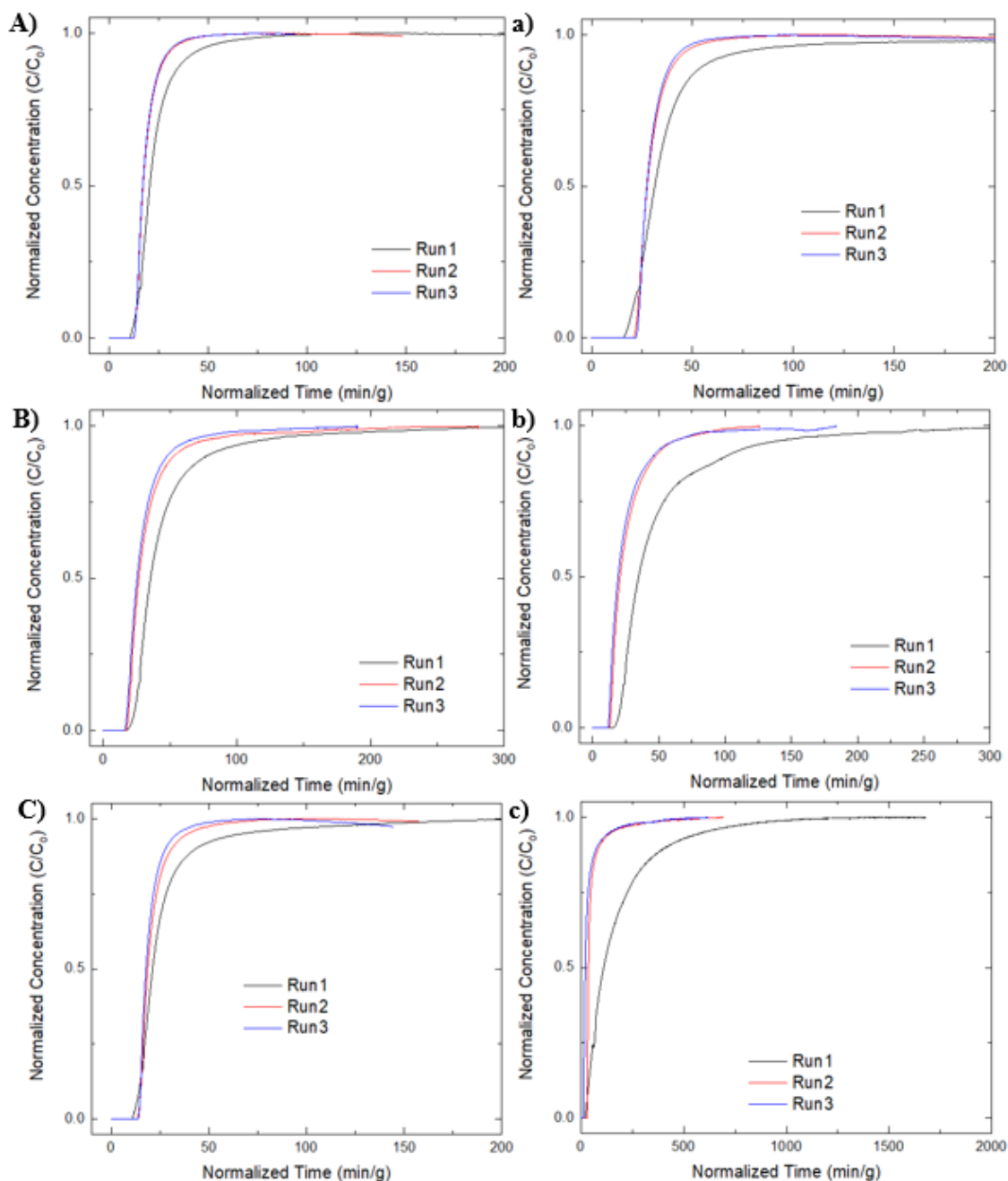


Figure 6.6: H₂S breakthrough curves for solvothermally (upper case) and room temperature (lower case) synthesized A) UiO-66, B) DMOF-TM, and C) ZIF-8. Breakthrough was conducted using a flowrate of 50 mL/min and an H₂S concentration of 5000 ppm in nitrogen.

Figure 6.6 shows that in all samples, regardless of synthesis conditions, we observed a substantial decrease in the H₂S breakthrough capacity between the first run and subsequent second and third runs. Nitrogen physisorption and PXRD patterns were collected after H₂S breakthrough experiments to aid in identifying the cause of the decreased capacity. While sample degradation did occur, it is not the only cause for the decrease in breakthrough capacity in subsequent runs. H₂S is bound strongly in each of the MOF samples such that it cannot be easily removed with only heating and helium flow. ZIF-8 synthesized at room temperature displayed the largest breakthrough capacity of all of the samples, 1.59 mmol/g, however the sample could not be regenerated (run 2 and 3 capacity: 0.24 and 0.26 mmol/g respectively), additionally we observed a 50 % loss in surface area of the material (see Table G.1 and Figures G.4 – G.6 in the supplemental) as well as discoloration of the sample (sample turned a dark tan color).

All room temperature synthesized samples adsorbed more H₂S than their solvothermal counterparts. We hypothesize that this is due to the defects in the structure, which result in additional strong adsorption sites in the materials. Additionally, we observed a greater percent loss in breakthrough capacity for the room temperature synthesized samples between runs 1 and 2 compared to the solvothermally synthesized samples. UiO-66 reached a first pass breakthrough capacity of 0.14 mmol/g and 0.35 mmol/g for solvothermally synthesized and room temperature synthesized samples respectively. All samples were pelletized and sieved prior to breakthrough measurements to prevent pressure drop and this processing had the greatest impact on UiO-66 samples. Room temperature synthesized UiO-66 was pelletized at a lower pressure (2000 psi) than the other samples (5000 psi) due to sample degradation. DMOF-TM adsorbed 0.42 mmol/g

and 0.48 mmol/g for solvothermally synthesized and room temperature synthesized samples respectively. Table 6.2 shows the H₂S and SO₂ breakthrough capacities for all samples collected in this study.

Table 6.2: H₂S (5000 ppm in nitrogen) and SO₂ (1000 ppm in nitrogen) breakthrough capacities (mmol/g) for UiO-66, DMOF-TM, and ZIF-8 synthesized solvothermally and at room temperature.

MOF	H ₂ S Breakthrough Capacity (mmol/g)			SO ₂ Breakthrough Capacity (mmol/g)		
	Run1	Run2	Run3	Run1	Run2	Run3
UiO-66						
Solvo	0.14	0.10	0.10	0.19	0.19	0.18
RT	0.35	0.18	0.15	0.24	0.24	0.21
DMOF-TM						
Solvo	0.42	0.28	0.25	0.90	0.80	0.76
RT	0.48	0.23	0.23	0.94	0.87	0.97
ZIF-8						
Solvo	0.17	0.10	0.09	0.26	0.11	0.08
RT	1.59	0.24	0.26	0.10	0.05	0.04

SO₂ breakthrough measurements were collected for the room temperature and solvothermally synthesized UiO-66, DMOF-TM, and ZIF-8 materials. The results of these experiments are shown in Figure 6.7. The breakthrough measurements were collected at a flowrate of 50 mL/min and an SO₂ concentration of 1000 ppm in nitrogen was used. The dead volume was once again determined using nitrogen tracer gas and measurements were collected three times in succession for each sample. Reactivation of the samples was performed in the same manner as was described for H₂S. The complete breakthrough curves for each run (including the nitrogen tracer gas) can be found in the supplemental information, Figures G.23 – G.25.

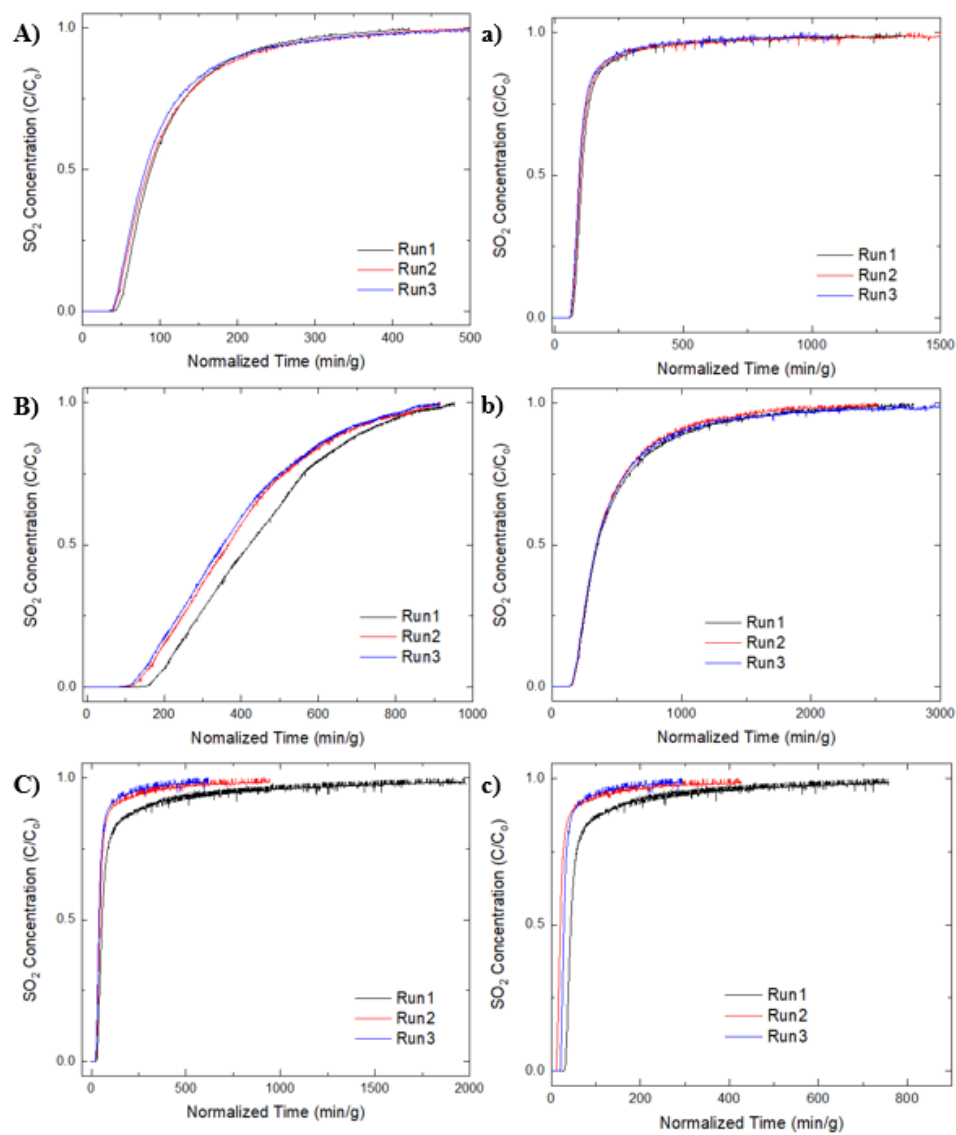


Figure 6.7: SO₂ breakthrough curves for solvothermally (upper case) and room temperature (lower case) synthesized A) UiO-66, B) DMOF-TM, and C) ZIF-8. Breakthrough was conducted using a flowrate of 50 mL/min and concentration of 1000 ppm in nitrogen.

Figure 6.7 shows the SO₂ breakthrough curves for UiO-66, DMOF-TM, and ZIF-8. Unlike the H₂S breakthrough curves, UiO-66 and DMOF-TM displayed more consistent breakthrough capacities between each run. UiO-66 (Figure 6.7A) did not adsorb much SO₂

for both the solvothermally (0.19 mmol/g) and room temperature (0.24 mmol/g) synthesized samples, however we did not observe a significant decrease in breakthrough capacity across consecutive runs. UiO-66 synthesized at room temperature did adsorb more SO₂ than the solvothermally synthesized sample, which is likely due to structure defects. DMOF-TM (Figure 6.7B) displayed the largest SO₂ breakthrough capacity reaching 0.90 mmol/g for the solvothermally synthesized sample and 0.94 mmol/g for the room temperature synthesized MOF. Additionally, both materials were easily reactivated and displayed minimal loss in breakthrough capacity between cycles. Post breakthrough experiments also showed that the materials retained their surface areas and crystallinity (See Table G.1 and Figure G.8). ZIF-8 displayed a small SO₂ breakthrough capacity regardless of synthesis method (0.26 solvothermal and 0.10 room temperature). Additionally, the breakthrough capacity was further decreased between runs and post nitrogen physisorption experiments identified that the material lost most of its BET surface area and pore volume when compared to the as synthesized materials. Breakthrough for ZIF-8 was also very slow due to diffusion limitations, the pore window of ZIF-8 is smaller than the kinetic diameter of SO₂.

6.4 Conclusions

We synthesized three commonly studied MOFs: UiO-66, DMOF-TM, and ZIF-8 via traditional solvothermal synthesis procedures and room temperature synthesis procedures in order to investigate the differences in materials properties from MOFs synthesized using different methods. We proceeded to characterize these materials using nitrogen physisorption, PXRD, infrared spectroscopy, and TGA. We also investigated the

water, CO₂, and SO₂ adsorption performance of these materials and collected SO₂ and H₂S breakthrough capacities.

UiO-66 synthesized at room temperature contained a greater number of defects compared to the solvothermally synthesized material. We showed that this led to increased surface area, water adsorption, H₂S breakthrough capacity, and SO₂ breakthrough capacity. While adsorption properties did tend to increase, the stability of the material was a concern as it was not as mechanically stable when synthesized at room temperature and the sample degraded when pelletized at pressure greater than 2000 psi. We recommend that future studies involving defective UiO-66 consider the ramifications of defects on the structural integrity of the MOF especially when concerning applications where processing of the material is required.

DMOF-TM synthesized at room temperature contained a small concentration of dangling linker defects. These defects have been shown to decrease the water vapor stability of the material. The water adsorption capacity, CO₂ adsorption capacity, SO₂ adsorption capacity, and H₂S and SO₂ breakthrough capacities were largely unaffected by this structure defect. DMOF-TM adsorbed the most SO₂ in breakthrough experiments collected at 1000 ppm reaching an SO₂ capacity of roughly 0.90 mmol/g for both solvothermally and room temperature synthesized materials.

Characterization of ZIF-8 showed differences in the surface area of the material as well as morphology. ZIF-8 synthesized at room temperature did not display the typical crystal morphology that is present in solvothermally synthesized ZIF-8. Additionally, ZIF-8 synthesized at room temperature displayed much higher CO₂ and SO₂ adsorption. ZIF-8 synthesized at room temperature adsorbed the most H₂S in breakthrough experiments

reaching a first run capacity of 1.59 mmol/g, however the material was not able to be reactivated and lost most of its capacity in subsequent breakthrough runs.

In conclusions further experimentation need to be conducted in order to truly understand how synthesis affects MOF structure and how defects can impact the adsorption characteristics and adsorption in MOFs. UiO-66, DMOF-TM, and ZIF-8 all behaved differently when synthesized at room temperature compared to the traditional solvothermal synthesis routes. Other nontraditional synthesis methods such as: microwave, electrochemical, ball mill, and extrusion were not considered, but should be investigated in further studies to validate the quality of materials synthesized using those techniques. PXRD and BET surface area analysis alone may not be enough to ensure the quality of a material. Future studies involving new MOF synthesis methods must rigorously characterize the materials in order to confirm that the materials are of similar quality to those that have been synthesized via traditional means.

6.5 References

- [1] Cavka, J.; Jakobsen, S.; Olsbye, U.; Guillou, N.; Lamberti, C.; Bordiga, S.; Lillerud, K. A New Zirconium Inorganic Building Brick Forming Metal-Organic Frameworks with Exceptional Stability. *J. Am. Chem. Soc.* **2008**, 130, 13850-13851.
- [2] Park, K.; Ni, Z.; Cote, A.; Choi, J.; Huang, R.; Uribe-Romo, F.; Chae, H.; O’Keeffe, M.; Yaghi, O. Exceptional Chemical and Thermal Stability of Zeolitic Imidazolate Frameworks. *PNAS*. **2006**, 103, 10186-10191.
- [3] DeStefano, M.; Islamoglu, T.; Garibay, S.; Hupp, J.; Farha, O. Room-Temperature Synthesis of UiO-66 and Thermal Modulation of Densities of Defect Sites. *Chem. Mater.* **2017**, 29, 1357-1361.
- [4] Gutov, O.; Hevia, M.; Escudero-Adan, E.; Shafir, A. Metal-organic Framework (MOF) Defects under Control: Insights into the Missing Linker Sites and Their Implication in the Reactivity of Zirconium-based Frameworks. *Inorg. Chem.* **2015**, 54, 8396-8400.

- [5] Liang, W.; Coghlan, C.; Ragon, F.; Rubio-Martinez, M.; D'Alessandro, D.; Babarao, R. Defect Engineering of UiO-66 for CO₂ and H₂O Uptake – A combined Experimental and Simulation Study. *Dalton Trans.* **2016**, 45, 4496-4500.
- [6] Bueken, B.; Velthove, N.; Krajnc, A.; Smolders, S.; Taulelle, F.; Mellot-Draznieks, C.; Mali, G.; Bennett, T.; De Vos, D. Tackling the Defect Conundrum in UiO-6: A Mixed-Linker Approach to Engineering Missing Linker Defects. *Chem. Mater.* **2017**, 29, 10478-10486.
- [7] Cliffe, M.; Wan, W.; Zou, X.; Chater, P.; Kleppe, A.; Tucker, M.; Wilhelm, H.; Funnell, N.; Coudert, F.; Goodwin, A. Correlated Defect Nanoregions in a Metal-Organic Framework. *Nature Communications.* **2014**, 5(4176).
- [8] Bhattacharyya, S.; Han, R.; Kim, W.; Chiang, Y.; Jayachandrababu, K.; Hungerford, J.; Dutzer, M.; Ma, C.; Walton, K.; Sholl, D.; Nair, S. Acid Gas Stability of Zeolitic Imidazolate Frameworks: Generalized Kinetic and Thermodynamic Characteristics. *Chem. Mater.* **2018**, 30, 4089-4101.
- [9] Park, J.; Howe, J.; Sholl, D. How Reproducible are Isotherm Measurements in Metal-Organic Frameworks. *Chem. Mater.* **2017**, 29, 10487-10495.
- [10] Jasuja, H.; Huang, Y.; Walton, K. Adjusting the Stability of Metal-Organic Frameworks under Humid Conditions by Ligand Functionalization. *Langmuir.* **2012**, 28, 16874-16880.
- [11] Hungerford, J.; Walton, K. Room Temperature Synthesis of Metal-organic Framework Isomers in the Tetragonal and Kagome Crystal Structure. *Inorganic Chemistry*. Submitted.
- [12] Pan, Y.; Liu, Y.; Zeng, G.; Zhao, L.; Lai, Z. Rapid Synthesis of Zeolitic Imidazolate Framework-8 (ZIF-8) Nanocrystals in an Aqueous System. *Chem. Comm.* **2011**, 47, 2071-2073.
- [13] Walton, K.; Snurr, R. Applicability of the BET Method for Determining Surface Areas of Microporous Metal-organic Frameworks. *J. Am. Chem. Soc.* **2007**, 129, 8552-8556.
- [14] Pang, S.; Han, C.; Sholl, D.; Jones, C.; Lively, R. Facet-Specific Stability of ZIF-8 in the Presence of Acid Gases Dissolved in Aqueous Solutions. *Chem. Mater.* **2016**, 28, 6960-6967.
- [15] Trickett, C.; Gagnon, K.; Lee, S.; Gandara, F.; Burgi, H.; Yaghi, O. Definitive Molecular Level Characterization of Defects in UiO-66 Crystals. *Angew. Chem. Int. Ed.* **2015**, 54, 11162-11167.
- [16] Han, R.; Sholl, D. Computational Model and Characterization of Stacking Faults in ZIF-8 Polymorphs. *J. Phys. Chem. C.* **2016**, 120, 27380-27388.

- [17] Tian, F.; Mosier, A.; Park, A.; Webster, E.; Cerro, A.; Shine, R.; Benz, L. In Situ Measurement of CO₂ and H₂O Adsorption by ZIF-8 Films. *J. Phys. Chem. C*. **2015**, 119, 15248-15253.
- [18] Sun Q.; He, H.; Gao, W.; Aguila, B.; Wojtas, L.; Dai, Z.; Li, J.; Chen, Y.; Xiao, F.; Ma, S. Imparting Amphiphobicity on Single-Crystalline Porous Materials. *Nature Communications*. **2016**, 7, 13300.
- [19] Jiao, Y.; Liu, Y.; Zhu, G.; Hungerford, J.; Bhattacharyya, S.; Lively, R.; Sholl, D.; Walton, K. Heat-Treatment of Defective UiO-66 from Modulated Synthesis: Adsorption and Stability Studies. *J. Phys. Chem. C*. **2017**, 121, 23471-23479.

CHAPTER 7: COMPREHENSIVE STUDY OF SO₂ ADSORPTION IN A SERIES OF METAL-ORGANIC FRAMEWORKS

This chapter contains data that was reproduced from the following manuscripts. 1) “Adapted with permission from Hungerford, J.; Bhattacharyya, S.; Tumuluri, U.; Nair, Z.; Wu, Z.; Walton, K. DMOF-1 as a Representative MOF for SO₂ Adsorption in Both Humid and Dry Conditions. *J. Phys. Chem. C*. 2018, 122, 23493 – 23500. Copyright 2018 American Chemical Society.” 2) “Adapted with permission from Bhattacharyya, S.; Han, R.; Kim, W.; Jayachandrababu, C.; Hungerford, J.; Dutzer, M.; Ma, C.; Walton, K.; Sholl, D.; Nair, S. Acid Gas Stability of Zeolitic Imidazolate Frameworks: Generalized Kinetic and Thermodynamic Characteristics. *Chem. Mater.*, 2018, 30, 4089-4101. Copyright 2018 American Chemical Society.”

7.1 Introduction

This chapter will discuss the dry SO₂ adsorption performance across a variety of MOF materials. This chapter is an extension of chapter 4 in which the platform material DMOF-TM was analyzed to assess its SO₂ adsorption capacity. The work presented in this chapter is a result of collaborations that have been conducted within the Energy Frontiers Research Center (EFRC) UNCAGE-ME. SO₂ adsorption performance will be discussed in for the following materials: DMOF-TM, DMOF-ADC, UiO-66, UiO-66-NH₂, MIL-101(Cr), ZIF-7, ZIF-8, ZIF-11, ZIF-65, Cu-BTC, and MIL-53(Al). These materials provide an assortment of MOF topologies, structures, coordination environments, surface areas,

and ligand functionalities to develop structure property relationships for MOF materials exposed to dry SO₂. Table 7.1 shows the surface areas and pore windows for these materials. It should be noted that the kinetic diameter of SO₂ is 3.6 Å. Due to the flexibility of MOF linkers, we expect SO₂ to diffuse into the pore space of MOFs with pore windows smaller than the kinetic diameter of SO₂.

Table 7.1: Surface areas and pore volumes for select MOF materials

MOF	Surface Area (m ² /g)	Pore Window (Å)
MIL-101(Cr) ¹	2789	16
ZIF-8 ^{2,3}	1679	3.4
Cu-BTC ⁴	1513	6.9
ZIF-65 ^{2,5}	1512	3.4
MIL-53(Al)	1478	8.5
ZIF-11 ^{2,3}	1452*	3.0
UiO-66 ⁶	1080	7.0
DMOF-TM ⁷	1002	3.5
UiO-66-NH ₂ ⁸	977	6.0
DMOF-ADC ⁷	728	4.8 x 3.2
ZIF-7 ^{2,5}	362	2.9

* Surface area was determined computationally

SO₂ adsorption in DMOF-TM and DMOF-ADC have been discussed previously in chapter 4 and I recommend the reader to review the stability and adsorption characteristics for these materials presented there. UiO-66 is among the most stable MOFs reported in the literature,⁹ however it is not among the highest adsorbing MOFs in the literature in its unmodified state due to its low surface area and pore volume as well as lack of strong adsorption sites. UiO-66 is highly tunable through both defect incorporation and linker functionalization, which has resulted in increased adsorption interactions compared to the parent material. Yang et. al. reported a 20 % increase in SO₂ adsorption capacity for defective UiO-66 over the defect free material.¹⁰ UiO-66-NH₂ has shown increased

adsorption characteristics for CO₂ as well as toxic chemicals.^{11,12} UiO-66 and UiO-66-NH₂ are both highly coordinated MOFs that do not contain open-metal sites. The stability of these materials has been attributed to the coordination environment and strong coordination bonds between oxygen and zirconium. MIL-101(Cr) and Cu-BTC both contain open-metal sites such that one may expect these materials to bind SO₂ strongly. This strong adsorption may lead to high SO₂ uptake at low pressures, making these materials good candidates for low pressure applications. Additionally, MIL-101(Cr) has the largest pore volume and surface area of all MOFs tested which was expected to result in a large SO₂ capacity for the material.¹ ZIFs 7, 8, 11, and 65 contain imidazolate linkers. ZIF-7 and 11 have pore windows much smaller than the kinetic diameter of SO₂ such that diffusion into the pore space will be slow or unfeasible in these materials. SO₂ adsorption in ZIF-8 was discussed in chapter 6 and ZIF-65 contains a cobalt metal center unlike the other ZIFs, which all contain zinc secondary building units (SBUs).² Lastly, MIL-53(Al) was selected due to its unique breathing behavior and similar surface area and pore volume compared to Cu-BTC, however it does not contain open-metal sites.

7.2 Materials and Methods

7.2.1 MOF and ZIF Materials

This chapter discusses the results of a numerous SO₂ adsorption isotherms that were collected on a wide variety of materials. These materials were acquired from the following sources: I synthesized and previously discussed the DMOF-TM and DMOF-ADC materials that were also used in this study and for a comprehensive assessment of these materials I recommend revisiting chapter 4 of this dissertation. I also synthesized MIL-

53(Al) and its synthesis route shall be presented below. Cu-BTC and UiO-66-NH₂ were both obtained from Inmondo Tech LLC. UiO-66 was synthesized by Yang Jiao in Dr. Walton's group. MIL-101(Cr) was synthesized by Eli Carter, also in Dr. Walton's group. ZIF-7, ZIF-8, ZIF-11, and ZIF-65 were all synthesized by Souryadeep Bhattacharyya in Dr. Nair's group.

7.2.2 MIL-53(Al) Synthesis Procedure

MIL-53(Al) was synthesized solvothermally by dissolving 3.5 mmol (1.3 g) of Al(NO₃)₃·9H₂O and 1.75 mmol (0.288 g) of BDC in a beaker containing 80 mL of water.^{13,14} The solution was then stirred until the Al(NO₃)₃·9H₂O and BDC had completely dissolved. The solution was then transferred to a Teflon lined autoclave and placed into an isothermal oven for 3 days at 220 °C. Samples were activated prior to testing at 150 °C under vacuum for 18 hours.

7.2.3 Dry SO₂ Pressure Decay and Stability Determination

SO₂ adsorption was measured using a lab-built volumetric system contained within a fume hood. Samples (20 – 30 mg) were first loaded into the unit and activated under vacuum at 150 °C for 18 hours. Adsorption isotherms were then collected between 0 and 2.5 bar at 25 °C using pure SO₂. After adsorption experiments were completed the sample chamber was subject to vacuum overnight to ensure complete removal of SO₂ from the apparatus.

7.3 Results and Discussion

Figure 7.1 shows the SO₂ adsorption isotherms for the following materials: DMOF-TM, DMOF-ADC, UiO-66, UiO-66-NH₂, MIL-101(Cr), ZIF-7, ZIF-8, ZIF-11, ZIF-65,

Cu-BTC, and MIL-53(Al). These MOF materials were selected for this study as they have an assortment of surface areas, pore volumes, metal coordination environments, and ligand groups. This diversity in MOF structure provides an excellent variety for the purpose of establishing a heuristic for structure property relationships of MOFs exposed to SO₂. This section will first focus on the high-pressure region of the SO₂ adsorption isotherm, which would show potential for applications in storage. The focus will then shift to analyzing the low-pressure region where concentrations are closer to those that might be experienced in flue gas or natural gas purification applications.

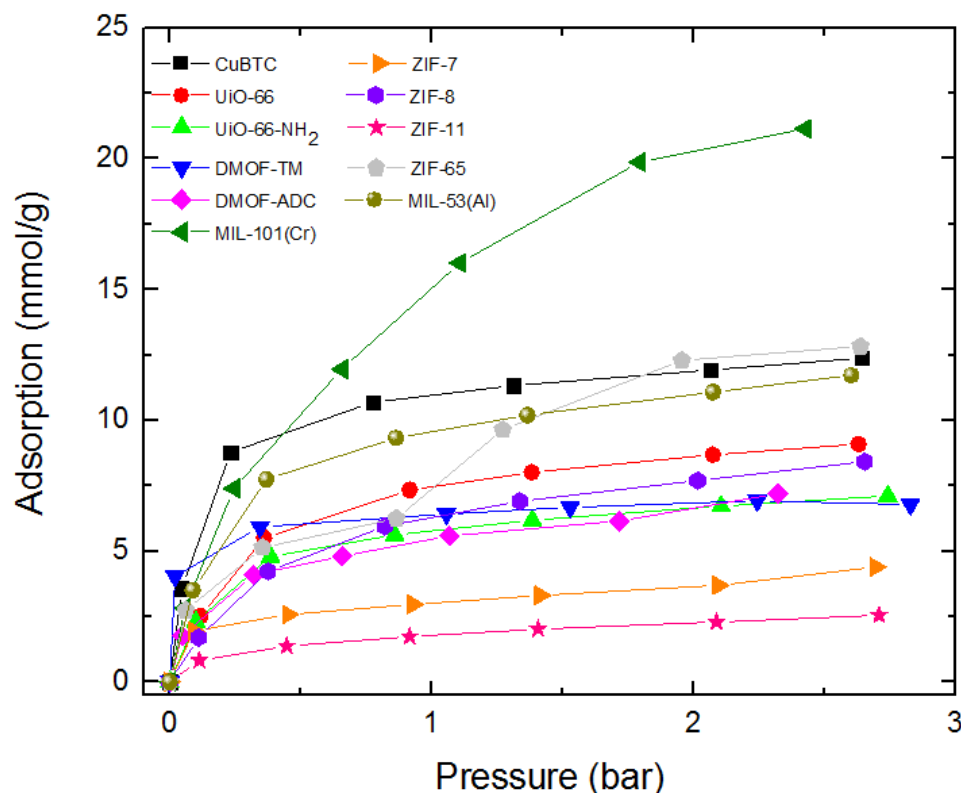


Figure 7.1: SO₂ adsorption isotherms of Cu-BTC, UiO-66, UiO-66-NH₂, DMOF-TM, DMOF-ADC, MIL-101(Cr), ZIF-7, ZIF-8, ZIF-11, ZIF-65, and MIL-53(Al)

Analyzing the high pressure SO₂ loading (greater than 2 bar), MIL-101(Cr) displays the highest adsorption of all materials tested. MIL-101(Cr) reached a loading of over 22 mmol/g at roughly 2.5 bar total pressure, far exceeding that of the other MOFs in this study. Additionally, the storage density of SO₂ in MIL-101(Cr) is close to the liquid density of SO₂ at room temperature, signifying that MIL-101(Cr) can store SO₂ very efficiently.¹⁵ The material's storage capabilities can be attributed to the large surface area and pore volume, which are significantly larger than any of the other materials. ZIF-65, MIL-53(Al), and Cu-BTC all reach a second tier of adsorption around 12 – 13 mmol/g. Notably, these three materials have similar pore volumes and surface areas. UiO-66, UiO-66-NH₂, DMOF-TM, DMOF-ADC, and ZIF-8 all have similar SO₂ adsorption capacities reaching 5 – 8 mmol/g at 2.5 bar. ZIF-7 and ZIF-11 had the lowest SO₂ adsorption and we believe that this is primarily due to the small pore window of both materials limiting diffusion of SO₂ into the structure. ZIF-7 and ZIF-11 each have pore windows much smaller than the kinetic diameter of SO₂ (SO₂ kinetic diameter 3.6 Å).¹⁶ In conclusion, high pressure SO₂ loading shows a direct correlation with the surface area and pore volume of the MOF.

The low-pressure region of the SO₂ adsorption isotherms shows a very different trend than the one identified in the high-pressure region. Cu-BTC shows excellent SO₂ adsorption below 0.25 bar of pressure. Chapter 6 showed that Cu-BTC achieved a breakthrough capacity of 0.45 mmol/g at 1000 ppm SO₂ in nitrogen and is a viable adsorbent for SO₂. In addition to Cu-BTC, DMOF-TM also shows very favorable SO₂ adsorption isotherms. Unlike Cu-BTC, however, DMOF-TM does not contain an open-metal site. The strong adsorption in DMOF-TM at low pressures can be attributed to its narrow pore window and favorable interactions with the MOF ligands. SO₂ has a kinetic

diameter of 3.6 Å and the pore window in DMOF-TM is 3.5 Å. Since the kinetic diameter of SO₂ and the pore window of DMOF-TM are similar in size, low pressure SO₂ adsorption will have a capillary effect resulting in large adsorption at low pressures. In chapter 6, DMOF-TM displayed an SO₂ breakthrough capacity of 0.90 mmol/g which is among the highest reported for all MOF materials at 1000 ppm SO₂ concentration.

7.4 Conclusions

In conclusion, we assessed the SO₂ adsorption performance of 11 MOF materials: DMOF-TM, DMOF-ADC, UiO-66, UiO-66-NH₂, MIL-101(Cr), ZIF-7, ZIF-8, ZIF-11, ZIF-65, Cu-BTC, and MIL-53(Al) and were able to establish structure property relationships for SO₂ adsorption in these materials. High pressure SO₂ adsorption is dominated by MOFs with the highest surface areas and pore volume such that for storage applications a MOF with exceptionally high surface area and pore volume is preferred. In this study MIL-101(Cr) was the best performing MOF in this category. Low pressure SO₂ adsorption is dominated by two facts: 1) strong interactions due to OMS, such as those that exist in Cu-BTC. 2) Molecular sieving which can be achieved in MOFs with pore windows similar in size to that of SO₂, such as DMOF-TM.

7.5 References

- [1] Yan, J.; Yu, Y.; Ma, C.; Xiao, J.; Xia, Q.; Li, Y.; Li, Z. Adsorption Isotherms and Kinetics of Water Vapor on Novel Adsorbents MIL-101(Cr)@GO with Super-high Capacity. *Applied Thermal Engineering*. **2015**, 84, 118-125.
- [2] Bhattacharyya, S.; Han, R.; Kim, W.; Chiang, Y.; Jayachandrababu, K.; Hungerford, J.; Dutzer, M.; Ma, C.; Walton, K.; Sholl, D.; Nair, S. Acid Gas Stability of Zeolitic Imidazolate Frameworks: Generalized Kinetic and Thermodynamic Characteristics. *Chem. Mater.* **2018**, 30, 4089-4101.

- [3] Assfour, B.; Leoni, Stefano, Yurchenko, S.; Seifert, G. Hydrogen Storage in Zeolite Imidazolate Frameworks. A Multiscale Theoretical Investigation. *International Journal of Hydrogen Energy*. **2011**, 36, 6005-6013.
- [4] Schlichte, K.; Kratzke, T.; Kaskel, S. Improved Synthesis, Thermal Stability and Catalytic Properties of the Metal-Organic Framework Compound Cu₃(BTC)₂. *Microporous Mesoporous Mater.* **2004**, 73, 81-88.
- [5] Yuan, Y.; Dong, X.; Chen, Y.; Zhang, M. Computational Screening of Iodine Uptake in Zeolitic Imidazolate Frameworks in a Water-containing System. *Phys. Chem. Chem. Phys.* **2016**, 18, 23246-23256.
- [6] Peterson, G.; DeCoste, J.; Glover, T.; Huang, Y.; Jasuja, H.; Walton, K. Effects of Pelletization Pressure on the Physical and Chemical Properties of the Metal-Organic Frameworks Cu₃(BTC)₂ and UiO-66. *Microporous Mesoporous Mater.* **2013**, 179, 48-53.
- [7] Hungerford, J.; Bhattacharyya, S.; Tumuluri, U.; Nair, S.; Wu, Z.; Walton, K. DMOF-1 as a Representative MOF for SO₂ Adsorption in Both Humid and Dry Conditions. *J. Phys. Chem. C*. **2018**, 122, 23493-23500.
- [8] Zunkovic, E.; Mazaj, M.; Mali, G.; Rangus, M.; Devic, T.; Serre, C.; Logar, N. Structural Study of Ni- or Mg-based Complexes Incorporated within UiO-66-NH₂ Framework and their Impact on Hydrogen Sorption Properties. *Journal of Solid State Chemistry*. **2015**, 225, 209-215.
- [9] Cavka, J.; Jakobsen, S.; Olsbye, U.; Guillou, N.; Lamberti, C.; Bordiga, S.; Lillerud, K. A New Zirconium Inorganic Building Brick Forming Metal-Organic Frameworks with Exceptional Stability. *J. Phys. Chem. C*. **2008**, 130, 13850-13851.
- [10] Jiao, Y.; Liu, Y.; Zhu, G.; Hungerford, J.; Bhattacharyya, S.; Lively, R.; Sholl, D.; Walton, K. Heat-treatment of Defective UiO-66 from Modulated Synthesis: Adsorption and Stability Studies. *J. Phys. Chem. C*. **2017**, 121, 23471-23479.
- [11] Cheng, Y.; Ying, Y.; Zhai, L.; Liu, G.; Dong, J.; Wang, Y.; Christopher, M.; Long, S.; Wang, Y.; Zhao, D. Mixed Matrix Membranes Containing MOF@COF Hybrid Fillers for Efficient CO₂/CH₄ Separation. *Journal of Membrane Science*. **2019**, 573, 97-106.
- [12] Peterson, G.; DeStefano, M.; Garibay, S.; Ploskonka, A.; McEntee, M.; Hall, M.; Karwacki, C.; Hupp, J.; Farha, O. Optimizing Toxic Chemical Removal through Defect-Induced UiO-66-NH₂ Metal-Organic Framework. *Chem. Eur. J.* **2017**, 23, 15913-15916.
- [13] Ferey, G.; Latroche, M.; Serre, C.; Millange, F.; Loiseau, T.; Percheron-Guegan, A. Hydrogen Adsorption in the Nanoporous Metal-benzenedicarboxylate

M(OH)(O₂C-C₆H₄-CO₂)(M=Al³⁺, Cr³⁺), MIL-53. *Chem. Commun.* **2003**, 24, 2976-2977.

- [14] Loiseau, T.; Serre, C.; Huguenard, C.; Fink, G.; Taulelle, F.; Henry, M.; Bataille, T.; Ferey, G. A Rationale for the Large Breathing of the Porous Aluminum Terephthalate (MIL-53) Upon Hydration. *Chem. Eur. J.* **2004**, 10, 1373-1382.
- [15] Air Products. Accessed 3/15/2019.
<http://www.airproducts.com/Products/Gases/gas-facts/physical-properties/physical-properties-sulfur-dioxide.aspx>
- [16] Matteucci, S.; Yampolskii, Y.; Freeman, B.; Pinnau, I. "Transport of Gases and Vapors in Glassy and Rubbery Polymers". *Materials Science of Membranes for Gas and Vapor Separation*. pp. 1-47. John Wiley & Sons, **2006**.

CHAPTER 8: CONCLUSIONS AND RECOMMENDATIONS

8.1 Dissertations Conclusions

This dissertation explored the impact of water and acid gas exposure on the degradation and adsorption properties in a variety of metal-organic frameworks (MOFs). The goal of this dissertation was to develop a better understanding of acid gas interactions in MOFs, which were a relatively unexplored area at the beginning of my dissertation research. Chapter 1 of this dissertation introduced MOFs as porous materials and discussed the many potential applications that have been explored in the literature. Chapter 2 introduced DMOF (DABCO MOF) as a platform material. DMOF was selected as a platform material due to its tailorability through both metal substitution and linker functionalization. Previous studies had shown that the stability of DMOF towards water vapor can be improved via incorporation of bulky side groups onto the BDC linker. We hypothesized that similar linker functionalizations may also improve stability towards acid gases. UiO-66, ZIF-8, and Cu-BTC were also introduced in chapter 2 as complementary materials to explore acid gas interactions in MOFs.

Chapter 3 discussed a new room temperature synthesis procedure for DMOF and a DMOF isomer, ZnBD. Solvent choice was found to play an instrumental role in the formation of one framework topology over the other. Both DMF and DMSO resulted in the formation of ZnBD at room temperature, while acetone, ethanol, and methanol resulted in the formation of DMOF. Additionally, functionalized Zn-DMOF-L (L = 2,5-dimethylterephthalic acid (DM), 2-aminoterephthalic acid (NH₂), 2,3,5,6-

tetramethylterephthalic acid (TM), and 9,10-anthracenedicarboxylic acid (ADC)) were also synthesized at room temperature. Zn-DMOF-TM, however, was found to be unstable towards humidity when synthesized at room temperature, the material degraded after several months when left in air. The decreased stability of room temperature synthesized Zn-DMOF-TM was attributed to an increased concentration of defects in the structure which compromised its water vapor stability.

In chapter 4, experimentation using the platform material continued. Metal substitution with zinc, copper, cobalt, and nickel in M-DMOF-TM was explored to assess SO₂ stability in dry and humid conditions. Cu-DMOF-TM was found to be the most stable material in humid SO₂ conditions which followed the predictions of the Irving-Williams series stability order. Linker substitution in Zn-DMOF was also explored using: DM, NH₂, TM, and ADC linkers. The linkers with the bulkiest side groups: TM and ADC, were stable in dry SO₂ and ADC provided the most stability when exposed to humid SO₂. These experiments showed that while linkers can provide additional stability towards acid gases in dry and humid environments, metal node is also an important factor that can affect stability and adsorption properties.

Chapter 5 analyzed Cu-BTC as an adsorbent for SO₂, H₂S, and NO₂ in dry conditions. Cu-BTC readily degraded when exposed to H₂S and NO₂. The degradation products that formed were copper sulfide and copper nitrate respectively. Cu-BTC, however, was stable towards SO₂ and we observed excellent breakthrough capacity, 0.45 mmol/g at 1000 ppm SO₂ in nitrogen, and high-pressure adsorption performance, 13 mmol/g at 2.5 bar pure SO₂. Cu-BTC proved to be an effective adsorbent for SO₂ at both high and low pressures as long as water, H₂S, and NO₂ are not also present.

In chapter 6, UiO-66, DMOF-TM, and ZIF-8 were synthesized solvothermally and at room temperature to assess how synthesis effects can impact the adsorption and stability of MOFs towards acid gases such as H₂S and SO₂. H₂S breakthrough experiments showed a substantial loss in breakthrough capacity in subsequent trials for all materials such that they could not be completely regenerated. Therefore, none of the MOFs tested could be recommended for H₂S adsorption. In SO₂ breakthrough experiments, DMOF-TM displayed the largest breakthrough capacity of the MOFs testing, reaching a breakthrough capacity of roughly 0.90 mmol/g SO₂ for both solvothermally and room temperature synthesized samples. DMOF-TM was also successfully regenerated between each run such that little to no capacity was lost in subsequent trials. Post PXRD and nitrogen physisorption analysis showed that DMOF-TM had retained its structure.

Chapter 7 discussed the combined SO₂ adsorption experiments that were conducted on the pressure decay apparatus across the following MOFs: UiO-66, UiO-66-NH₂, Cu-BTC, DMOF-TM, DMOF-ADC, MIL-101(Cr), MIL-53(Al), ZIF-7, ZIF-8, ZIF-11, and ZIF-65. MIL-101(Cr) was identified as the best performing MOF for high pressure SO₂ adsorption reaching a capacity of over 20 mmol/g at 2.5 bar. CuBTC and DMOF-TM had the highest low pressure SO₂ adsorption and the most favorable isotherms at low pressure. Two trends were identified from this data, first high pressure SO₂ adsorption is dominated by MOFs with the largest surface areas and pore volumes. Second, low pressure SO₂ adsorption is dominated by MOFs with open metal sites, like CuBTC, or MOFs with pore diameters similar to the kinetic diameter of SO₂.

8.2 Recommendations and Future Work

This section of the dissertation will focus on areas where I believe future research on MOF materials should be directed. The three research thrusts that will be highlighted are: 1) H₂S interactions in MOFs, 2) multicomponent adsorption, and 3) applications for MOFs outside of adsorption-based separations. I believe that simulations and big data will be a vital component for all three areas of research in the future and will be an immense asset in directing future research. The largest asset that MOFs provide is their tailorability to the particular application at hand. Lab scale synthesis of all available MOFs is not feasible and computational studies will be instrumental in supporting experimental studies. This work primarily focused on SO₂ interactions in MOFs with chapters 5 and 6 also investigating H₂S exposure and breakthrough experiments. H₂S is a common contaminant found in natural gas and flue gas streams and initial results from my research have shown that it is more corrosive than SO₂ towards MOFs and binds more strongly. I believe that further experimentation needs to be conducted in order to discover MOFs that are stable to H₂S or determine ways to improve the stability of MOFs towards H₂S.

All of the work presented in this dissertation, and much of the work that exists in the MOF literature only contains single component adsorption or breakthrough data. More recent studies have begun to involve additional gas component, but they are still uncommon in the literature and limited in scope. If MOFs are to be considered for industrial applications, all constituents found in flue gas and natural gas streams must be considered. Natural gas typically contains methane, CO₂, H₂S, SO₂, and NO₂ and while examining how MOFs interact with each component individually is an important first step. Multicomponent adsorption is necessary to advance the field. The EFRC's capabilities to

handle multicomponent adsorption and breakthrough data is growing and will likely be vital to future research.

The two previous paragraphs highlighted areas of future research in the areas of adsorption-based separation for natural gas purification and flue gas capture. While I believe that further research in these areas is necessary, I am concerned with the speed of development of MOFs for these applications and the emergence of new energy policies. Alternative energy sources will likely replace natural gas and flue gas capture, it is unclear when this may happen, but MOF development for these applications is slow and some predictions expect renewables to overtake oil and gas as soon as the early 2030s. MOFs have existed for over 20 years and while they have found use in several niche applications, they are not in widespread use throughout industry, including the area of adsorption-based separations. For this reason I believe that future MOF research should continue to progress into emerging areas of research such as utilizing MOFs for drug delivery or as supports for energy storage systems. The number of articles published each year has increased for these categories and they may prove to be a better topic for future research than adsorption-based separations.

APPENDIX A: MOF SYNTHESIS PROCEDURES

A.1 Solvothermal Synthesis Procedures for M-DMOF-L

This section will contain the solvothermal synthesis procedures for all M-DMOF-L samples synthesized in this dissertation work. For all metal substituted samples a nitrate-based salt was added in the same molar ratio as zinc (II) nitrate hexahydrate, therefore only that synthesis procedure will be provided. Additionally all of the solvothermal synthesis procedures for M-DMOF-L produced roughly equal quantities of material regardless of whether zinc, copper, nickel, or cobalt nitrate based salts were used in the synthesis procedure and all of the materials obtained via these synthesis methods produced isorecticular products. Attempts were made at synthesizing magnesium and iron based M-DMOF-L, however they were all unsuccessful and led to non-crystalline products.

A.1.1 *Solvothermal Synthesis of Parent DMOF*

Parent DMOF was synthesized following the procedures found in the literature.¹ A solution of 150 mL of DMF was prepared and 6 mmol of $\text{Zn}(\text{NO}_3)_2 \cdot 6\text{H}_2\text{O}$ (1.74 g), 6 mmol of BDC (1.02 g), and 9.63 mmol of DABCO (1.08 g) were added to this solution. The resulting solution was filtered three times through filter paper (size P8) to remove the white precipitate that formed. The filtrate was then transferred into 10 22 mL vials and placed into a sand bath. The samples were then heated from 35 °C to 120 °C at a rate of 2.5 °C/min and the temperature was held for 12 hours at 120 °C before cooling back to room temperature. The samples were then cooled, filtered (size P8), and washed 3 times with DMF. Lastly, the samples were activated under vacuum overnight at 110 °C before further testing.

A.1.2 Solvothermal Synthesis of DMOF-TM

The following materials were added to 15 mL of DMF and allowed to stir for 3 hours at 350 rpm: 0.63 mol of $\text{Zn}(\text{NO}_3)_2 \cdot 6\text{H}_2\text{O}$ (0.187 g), 0.63 mmol TMBDC (0.140 g), and 0.31 mmol DABCO (0.035 g). The resulting solution was filtered three times through filter paper (size P8), transferred into 22 mL vials, and placed in a sand bath. The samples were then heated for 48 h at 120 °C in an isothermal oven. The samples were then cooled, filtered (size P8), and washed with DMF.

A.1.3 Solvothermal Synthesis of DMOF-DM

Zn-DMOF functionalized with DM (Zn-DMOF-DM) was prepared following the procedures contained in the literature.² In a glass beaker 0.6 mmol of $\text{Zn}(\text{NO}_3)_2 \cdot 6\text{H}_2\text{O}$ (0.178 g), 0.6 mmol DMBDC (0.116 g), and 0.31 mmol of DABCO (0.035 g) were added to 15 mL of DMF. The solution was stirred for three hours and then filtered (size P8) and poured into a Teflon autoclave and heated for 48 hours at 120 °C in an isothermal oven. The samples were then cooled, filtered (size P8), and washed with DMF.

A.1.4 Solvothermal Synthesis of DMOF-NDC

Zn-DMOF functionalized with NDC (Zn-DMOF-NDC) was prepared following the procedures contained in the literature.³ In a glass beaker 0.6 mmol of $\text{Zn}(\text{NO}_3)_2 \cdot 6\text{H}_2\text{O}$ (0.178 g), 0.6 mmol NDC (0.130 g), and 0.31 mmol of DABCO (0.035) were added to 9 mL of DMF at room temperature. The solution was stirred for three hours and then filtered (size P8) and poured into a Teflon autoclave and heated for 48 hours at 120 °C in an isothermal oven. The samples were then cooled, filtered (size P8), and washed with DMF.

A.1.5 Solvothermal Synthesis of DMOF-ADC

Zn-DMOF functionalized with ADC (Zn-DMOF-ADC) was prepared following the procedures outlined in the literature.⁴ In a glass beaker, 1 mmol of $\text{Zn}(\text{NO}_3)_2 \cdot 6\text{H}_2\text{O}$

(0.297 g) and 1 mmol of ADC (0.266 g) were added to 5 mL of DMF at room temperature. To this solution, 0.5 mmol of DABCO (0.056 g) was added along with 5 mL of methanol. The solution was then allowed to stir for 18 hours at 350 rpm. The solution was then filtered (size P8) and poured into a Teflon autoclave and heated for 48 hours at 120 °C in an isothermal oven. The samples were then cooled, filtered (size P8), and washed with DMF.

A.2 Room Temperature Synthesis Procedures for M-DMOF-L

This section will contain the room temperature synthesis procedures for M-DMOF-L. All of these procedures contain the same molar ratios of metal salts and ligands regardless of metal center or ligand functionalization. Therefore, only the synthesis procedure for Zn-DMOF will be presented. It should be noted, however, that DMF should not be used as a synthesis solvent when forming parent DMOF structures, as it will likely lead to the formation of the MOF isomer with kagome topology (ZnBD). For functionalized ligands, DMF may be used as a solvent as no ZnBD-L samples were ever formed.

A.2.1 Room Temperature Synthesis of Zn-DMOF

Two separate solvent solutions of 15 mL of methanol were first prepared. To the first solution 1.5 mmol $\text{Zn}(\text{NO}_3)_2 \cdot 6\text{H}_2\text{O}$ (0.436 g) and 1.5 mmol BDC (0.249 g) were added, and to the second solution 1.25 mmol DABCO (0.140 g) and 350 μL of TEA were added. The solutions were then separately mixed at room temperature until a uniform solution appeared. Solution 1 and 2 were then mixed and stirred on a stir plate at 200 rpm at room temperature for 4 hours. (Solvent was added as needed to maintain the solution level) The mixture was then poured into a vial and centrifuged until solid samples were observed at the bottom of the vial. The solvent was then exchanged 3 times with DMF to

remove any excess starting materials and then 3 times with methanol. Prior to characterization the samples were all activated at 150 °C for 18 hours.

A.3 Room Temperature Synthesis Procedure of MBD

This section will contain the room temperature synthesis procedures for MBD. All of these procedures contain the same molar ratios regardless of metal center and no ligand functionalizations were obtainable for this material as was discussed in chapter 3. Therefore, only the synthesis procedure for ZnBD will be presented. It should be noted, however, that while the synthesis of ZnBD is straightforward, I observed difficulties when synthesizing NiBD and CoBD, and was never able to synthesize CuBD. Failed synthesis generally resulted in the formation of the DMOF crystal structure instead. No difficulties were ever reported by the original author when synthesizing NiBD or CoBD and CuBD was not attempted.⁵ DMOF is the thermodynamically favorable MOF in this system, so it is understandable that we observed that crystal structure when failing to synthesize MBD.

A.3.1 Room Temperature Synthesis of ZnBD

ZnBD was synthesized at room temperature following the procedures available in the literature.⁵ Two separate solvent solutions of 15 mL of DMF were first prepared. To the first solution 1.5 mmol $\text{Zn}(\text{NO}_3)_2 \cdot 6\text{H}_2\text{O}$ (0.436 g) and 1.5 mmol BDC (0.249 g) were added, and to the second solution 1.25 mmol DABCO (0.140 g) and 350 μL of TEA were added. The solutions were then separately mixed at room temperature until a uniform solution appeared. Solution 1 and 2 were then mixed and stirred on a stir plate at 200 rpm at room temperature for 4 hours. The mixture was then poured into a vial and centrifuged until solid samples were observed at the bottom of the vial. The solvent was then exchanged

3 times with DMF to remove any excess starting materials and then 3 times with methanol. Prior to characterization the samples were all activated at 150 °C for 18 hours.

A.4 Solvothermal Synthesis of UiO-66

UiO-66 was synthesized by using the methods present in the literature.⁶ A solution containing 0.908 mmol of ZrCl₄ (0.212 g) and 0.820 mmol of BDC (0.136 g) in 25 mL of DMF was first prepared. The solution was stirred until both the BDC and ZrCl₄ had completely dissolved and the solution was transferred into a Teflon lined autoclave. The autoclave was then heated at 120 °C for 24 hours. The solution was then filtered and the sample was washed three times with DMF. Before sample testing, the sample was activated at 150 °C overnight.

A.5 Room Temperature Synthesis of UiO-66

UiO-66 was synthesized at room temperature following the procedures found in the literature.⁷ A solution was first prepared containing 7 mL of DMF and 4 mL of acetic acid. To this solution 71 µL of 70% zirconium propoxide solution was added. The solution was then covered with parafilm and heated on a hot plate for 2 - 4 hours at 130 °C. (It should be noted that the time is only a rough estimate. When the solution turns a yellowish hue, the reaction is complete and the zirconium SBU has been formed.) The solution was then allowed to cool to room temperature and 0.252 mmol of BDC (0.0749 g) was added to the solution. The solution was then allowed to stir for 18 hours at 200 rpm at room temperature. The sample was then collected via filtration and before testing it was activated at 150 °C overnight.

A.6 Solvothermal Synthesis of ZIF-8

ZIF-8 was synthesized following the procedures found in the literature.⁸ A solution containing 0.803 mmol of $\text{Zn}(\text{NO}_3)_2 \cdot 6\text{H}_2\text{O}$ (0.239 g) and 0.731 mmol of 2-methylimidazole (0.060 g) in 18 mL of DMF was prepared. The solution was then stirred until both the $\text{Zn}(\text{NO}_3)_2 \cdot 6\text{H}_2\text{O}$ and 2-methylimidazole had dissolved in solution and the solution was transferred to a Teflon lined autoclave. The autoclave was then heated from room temperature to 140 °C at 5 °C/min and held for 24 hours. The oven was then cooled at a rate of 0.4 °C/min to room temperature. The solution was then filtered and washed three times with DMF. Before sample testing, the sample was activated at 150 °C overnight.

A.7 Room Temperature Synthesis of ZIF-8

ZIF-8 was synthesized at room temperature following the procedures found in the literature.⁹ A solution containing 0.983 mmol of $\text{Zn}(\text{NO}_3)_2 \cdot 6\text{H}_2\text{O}$ (0.2925 g) in 2 mL of water was first prepared. A separate solution of 20 mL of water was prepared and 69.1 mmol of 2-methylimidazole (5.675 g) was dissolved in this solution. The two solution were then mixed at room temperature and allowed to stir for 5 minutes. The solution was then centrifuged for 20 minutes and the sample was collected via filtration, where it was washed three times with water. Before sample testing, the sample was activated at 150 °C overnight.

A.8 References

- [1] Chun, H.; Dybtsev, D.; Kim, H.; Kim, K. Synthesis, X-ray Crystal Structures, and Gas Sorption Properties of Pillared Square Grid Nets on Paddle-wheel Motifs: Implications for Hydrogen Storage in Porous Materials. *Chemistry* **2005**, 11, 3521-3529.
- [2] Jasuja, H.; Burtch, N.; Huang, Y.; Cai, Y.; Walton, K. Kinetic Water Stability of an Isostructural Family of Zinc-Based Pillared Metal-Organic Frameworks. *Langmuir* **2012**, 29, 633-642.
- [3] Chun, H.; Dybtsev, D.; Kim, H.; Kim, K. Synthesis, X-ray Crystal Structures, and Gas Sorption Properties of Pillared Square Grid Nets Based on Paddle-wheel Motifs: Implications for Hydrogen Storage in Porous Materials. *Chem. Eur. J.* **2005**, 11, 3521-3529.
- [4] Tanaka, D.; Horike, S.; Kitagawa, S.; Ohba, M.; Hasegawa, M.; Ozawa, Y.; Toriumi, K. Anthracene Array-Type Porous Coordination Polymer with Host-guest Charge Transfer Interactions in Excited States. *Chem. Comm.* **2007**, 0, 3142-3144.
- [5] Zhou, K.; Chaemchuen, S.; Wu, Z.; Verpoort, F. Rapid Room Temperature Synthesis Forming Pillared Metal-Organic Frameworks with Kagome Net Topology. *Microporous Mesoporous Mater.* **2017**, 239, 28-33.
- [6] Cavka, J.; Jakobsen, S.; Olsbye, U.; Guillou, N.; Lamberti, C.; Bordiga, S.; Lillerud, K. A New Zirconium Inorganic Building Brick Forming Metal Organic Frameworks with Exceptional Stability. *J. Am. Chem. Soc.* **2008**, 130, 13850-13851.
- [7] DeStefano, M.; Islamoglu, T.; Garibay, S.; Hupp, J.; Farha, O. Room-temperature Synthesis of UiO-66 and Thermal Modulation of Densities of Defect Sites. *Chem. Mater.* **2017**, 29, 1357-1361.
- [8] Park, K.; Ni, Z.; Cote, A.; Choi, J.; Huang, R.; Uribe-Romo, F.; Chae, H.; O'Keeffe, M.; Yaghi, O. Exceptional Chemical and Thermal Stability of Zeolitic Imidazolate Frameworks. *PNAS*. **2006**, 103, 10186-10191.
- [9] Pan, Y.; Liu, Y.; Zeng, G.; Zhao, L.; Lai, Z. Rapid Synthesis of Zeolitic Imidazolate Framework-8 (ZIF-8) Nanocrystals in an Aqueous System. *Chem. Commun.* **2011**, 47, 2071-2073.

APPENDIX B: CHARACTERIZATION AND EXPERIMENTAL TECHNIQUES

This section will discuss the characterization techniques and experimental methods that were used throughout this dissertation. These techniques have been discussed in some length throughout the previous chapters but will be discussed in greater detail in this section.

B.1 Powder X-ray Diffraction

Powder X-ray diffraction (PXRD) patterns were collected on a PANalytical X'Pert X-ray diffractometer containing an X'Celerator detector using Cu K α ($\lambda = 1.5418 \text{ \AA}$) radiation at room temperature. Data was collected from $2 - 50^\circ 2\theta$ using a mask size of 10 mm and an anti-scattering slit size of 1/8 cm. The results were compared to simulated patterns as well as those found in the literature, to confirm that the expected materials had been properly synthesized.

B.2 Nitrogen Physisorption Analysis

Nitrogen physisorption isotherms were measured at 77K using a Quadrasorb from Quantachrome Instruments. Brunauer-Emmett-Teller (BET) surface areas were determined over the pressure range $0.003 \leq P/P_0 \leq 0.05$.¹ The BET theory is an extension of Langmuir theory, which is a theory for monolayer adsorption. BET theory is based on the following hypothesis: 1) gas molecules physically adsorb on a solid in layers infinitely, 2)

gas molecules only interact with adjacent layers, and 3) each layer can be solved using Langmuir theory. Prior to the experiment the materials were activated overnight at 150 °C under vacuum using a Quantachrome FloVac Degasser.

B.3 Thermogravimetric Analysis (TGA)

Thermogravimetric Analysis (TGA) of the as-synthesized M-DMOF-TM samples was performed on a NETZSCH STA 449 F1 Jupiter® system under helium flow at 20 cc/min in the temperature range of 25 – 700 °C. Samples were first heated at a rate of 5 °C/min from 25 to 110 °C. The temperature was then held at 110 °C for 2 hours to remove any solvent trapped within the pore space of the MOF. The sample was then heated from 110 °C to 700 °C at a rate of 1 °C/min. The sample temperature was then maintained at 700 °C for 20 minutes before cooling back down to room temperature.

B.4 Scanning Electron Microscope (SEM)

SEM images of samples were collected on a Zeiss Ultra60 FE-SEM instrument with a high-efficiency In-lens SE detector at a working distance of 3-4 mm and accelerating voltage of 0.6 kV to prevent charging of the materials. Prior to SEM analysis all samples were dispersed in 2-3 mL of methanol and pipetted onto a flat aluminum sample holder with conductive carbon tape and allowed to dry overnight.

B.5 X-ray Photoelectron Spectroscopy (XPS)

XPS spectra were collected on a Thermo K-Alpha XPS, which was used to assess the degradation species and metal node environment of MOFs materials. Prior to testing,

samples were activated in a vacuum oven overnight at 150 °C to ensure that all weakly adsorbed species had been removed from the framework. Samples were then loaded into the XPS where they were allowed to degas under ultra-high vacuum for one hour prior to instrument testing. Survey and elemental scans were then collected for the samples.

B.6 Infrared Spectroscopy

Infrared spectroscopy measurements of MOF samples were collected on a Nicolet iS10 spectrometer from Fisher Scientific operating in ATR mode. Prior to experiments, samples were activated ex-situ under vacuum at 150 °C for 18 hours in an Isotemp Vacuum Oven Model 281A from Fisher Scientific.

B.7 Water Vapor Adsorption Isotherms

Water vapor isotherms were collected at room temperature using a 3Flex Surface Characterization Analyzer from Micromeritics. Samples were activated on a Micromeritics Smart VacPrep using an activation temperature of 150 °C for 18 hours under vacuum. Samples measurements were taken from 0 to 0.9 P/P₀ water vapor pressure to prevent capillary condensation.

B.8 Dry CO₂ Adsorption Isotherms

CO₂ adsorption isotherms were collected using an Intelligent Gravimetric Adsorption (IGA-1) instrument from Hiden Isochema. Prior to testing, samples were activated in situ under vacuum at 150 °C. Sample weight was tracked using the built-in balance and activation was completed once the sample weight remained constant for an

extended period. Once activation completed CO₂ adsorption isotherms were collected from 0 to 20 bar. Isotherms were typically collected at 25 °C and the temperature was controlled using a recirculation water bath.

B.9 Dry SO₂ Pressure Decay and Stability Determination

SO₂ adsorption was measured using a lab-built volumetric system contained within a fume hood. Samples (20 – 30 mg) were first loaded into the unit and activated under vacuum at 150 °C for 18 hours. Adsorption isotherms were then collected between 0 and 2.5 bar at 25 °C using pure SO₂ using the following reference cell adsorption points: 7 psi, 14 psi, 21 psi, 28 psi, 42 psi, and 48 psi. After adsorption experiments were completed the sample chamber was subject to vacuum overnight to ensure complete removal of SO₂ from the apparatus. The Peng-Robinson equation of state (See equation 9.1) was used to relate the pressure measured by the pressure transducers to the amount of SO₂ adsorbed by the tested MOF materials.

Equation 9.1

$$p = \frac{RT}{V_m - b} - \frac{a\alpha}{V_m^2 + 2bV_m - b^2}$$

$$a = \frac{0.45724R^2T_c^2}{p_c}$$

$$b = \frac{0.07780RT_c}{p_c}$$

$$\alpha = \left[1 + ((0.37464 + 1.54226\omega - 0.26992\omega^2)(1 - T_r^{0.5})) \right]^2$$

B.10 Humid SO₂ Exposure

Humid SO₂ exposure was conducted using an in-house exposure unit consisting of a sealed sample chamber and a NaHSO₃ solution contained in a water bath. The entire system is contained within a fume hood for safety. A stream of air was bubbled through the NaHSO₃ solution to generate the desired concentrations of SO₂ and humidity. The sealed sample chamber was equipped with a humidity sensor and Draeger detector to continuously monitor the concentrations throughout the length of the experiment. The outlet of the sealed chamber flows through a NaOH sink before being vented to the fume hood. The SO₂ concentration was adjusted by changing the concentration and pH of the NaHSO₃ solution. A diagram of the setup is located below and described in detail by Bhattacharyya et. al.² All exposures were conducted at room temperature targeting a humidity of 85 % and an SO₂ concentration of 50 ppm. Exposures will be described using units of ppm-days, such that 50 ppm-days refers to a 1-day exposure at a concentration of 50 ppm SO₂. (100 ppm-days is 2 days at an SO₂ concentration of 50 ppm etc.)

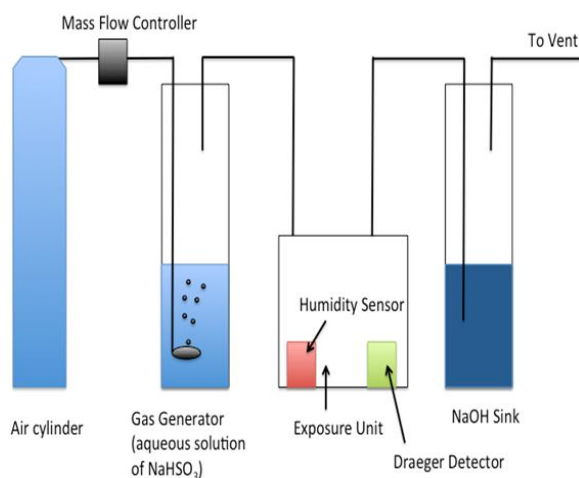


Figure B.1 Diagram of humid exposure unit

B.11 In-Situ SO₂ Exposure Infrared Spectroscopy

In-Situ SO₂ exposure experiments were conducted at Oak Ridge National Laboratories alongside the EFRC collaborator Dr. Zili Wu. Samples were first activated ex-situ at 150 °C for 18 hours prior to spectroscopic measurements. The samples were then loaded into a Thermo Nicolet Nexus 670 spectrometer in Diffuse Reflectance mode (DRIFTs), and the outlet gases from the DRIFTs cell (Pike Technologies HC-900) were analyzed using a quadrupole mass spectrometer (Omnistar GSD-301 O₂, Pfeiffer Vacuum) similar to what was described by Mounfield III et. al.³

The samples were pretreated by heating to 150 °C under a 50 cc/min helium stream for 1 hour and cooled to 25 °C before exposure to a 50 cc/min SO₂/He mixed stream during which IR spectra were collected continuously for one-half hour every 12 seconds. Runs were conducted in this manner for SO₂ concentrations of 50, 150, and 260 ppm (max SO₂ concentration) with the balance being He. Following exposure, the sample chamber was switched back to the pure helium flow until the mass spectrometer reading for SO₂ returned to baseline (approximately 15 minutes). At this time the sample was heated to 150 °C at a ramp rate of 10 °C/min, allowing for complete desorption of SO₂, which was confirmed by monitoring the SO₂ concentration using the output of the quadrupole mass spectrometer. The temperature was held at 150 °C for 5 minutes before cooling to 25 °C. Absorbance spectra during SO₂ adsorption were calculated as $Abs = -\log(I/I_0)$, where I is the single beam spectrum after adsorption and I_0 is the single beam spectrum before adsorption.

B.12 Breakthrough Acid Gas Experiments

Breakthrough experiments were collected using a lab-built system capable of testing the following acid gases: SO_2 , H_2S , and NO_2 . The outlet of the breakthrough system is directed into an OMNI^{Star} mass spectrometer from Pfeiffer Vacuum which measures the outlet gas concentration of the system. In addition to gases, the system can also expose samples to humid SO_2 , H_2S , and NO_2 , however the mass spectrometer is not capable of measuring the outlet concentration of the gases as it is not chemically compatible. Samples were first loaded into the system using a quartz capillary tube packed with quartz wool and activated under nitrogen flow at 150 °C. After activation, the flow was switched to acid gas flow (1000 ppm SO_2 , or 1000 ppm NO_2 , or 5000 ppm H_2S all in nitrogen) and passed through the system. During experiments, the outlet concentration was monitored using the mass spectrometer. Breakthrough was determined when the outlet concentration matched the concentration of the corresponding acid gas cylinder. Figure B.2 shows a typical breakthrough curve that may be collected during a run.

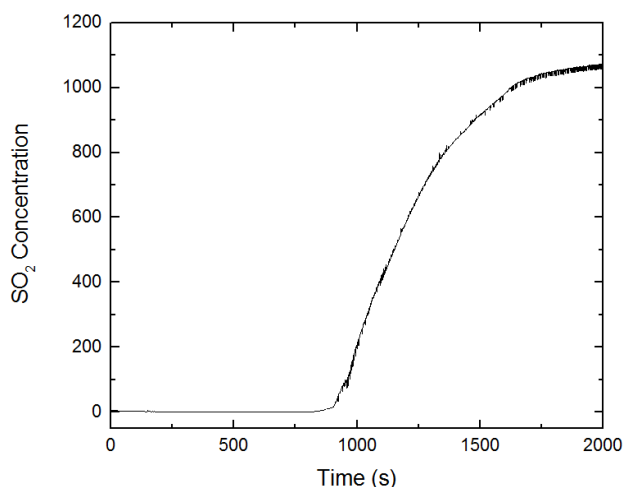


Figure B.2: Typical breakthrough curve. (Cu-BTC breakthrough curve for 1000 ppm SO_2 in nitrogen (Capacity: 0.45 mmol/g MOF))

B.13 References

- [1] Walton, K.; Snurr, R. Applicability of the BET Method for Determining Surface Areas of Microporous Metal-Organic Frameworks. *J. Am. Chem. Soc.* **2007**, 129, 8552-8556.
- [2] Bhattacharyya, S.; Han, R.; Kim, W.; Chiang, Y.; Jayachandrababu, K.; Hungerford, J.; Dutzer, M.; Ma, C.; Walton, K.; Sholl, D.; Nair, S. Acid Gas Stability of Zeolitic Imidazolate Frameworks: Generalized Kinetic and Thermodynamic Characteristics. *Chem. Mater.* **2018**, 30, 4089-4101.
- [3] Mounfield III, W.; Tumuluri, U.; Jiao, Y.; Li, M.; Dai, S.; Walton, K. Role of Defects and Metal Coordination on Adsorption of Acid Gases in MOFs and Metal Oxides: An In Situ IR Spectroscopic Study. *Micropor. Mesopor. Mater.* **2016**, 227, 65-75.

APPENDIX C: WATER ADSORPTION IN DMOF

This appendix contains information and figures from the following sources. 1) “Adapted with permission from Jasuja, H.; Huang, Y.; Walton, K. Adjusting the Stability of Metal-Organic Frameworks under Humid Conditions by Ligand Functionalization. *Langmuir*. 2012, 28, 16874-16880. Copyright 2012 American Chemical Society.” 2) “Adapted with permission from Jasuja, H.; Burtch, N.; Huang, Y.; Walton, K. Kinetic Water Stability of an Isostructural Family of Zinc-Based Pillared Metal-Organic Frameworks. *Langmuir*. 2013, 29, 633-642. Copyright 2012 American Chemical Society.” 3) Adapted with permission from Tan, K.; Nijem, N.; Canepa, P.; Gong, Q.; Li, J.; Thonhauser, T.; Chabal, Y. Stability and Hydrolyzation of Metal Organic Frameworks with Paddle-Wheel SBUs upon Hydration. *Chem. Mater.* 2012, 24, 3153-3167. Copyright 2012 American Chemical Society.”

C.1 Introduction

This section of the appendix will provide a thorough background of the humidity and water adsorption experiments conducted on DMOF and its various functionalized isomers. This section will discuss the work conducted by previous Walton research group members,^{1,2} the Chabal research group,³ as well as recent beamline experiments conducted at Argonne Nation lab by myself and others in the Walton research group.⁴ This appendix will be broken down into the following three sections. Section 1 will cover ligand functionalization and how the stability of DMOF towards water vapor can be improved. Section 2 will discuss metal substitution and how metal node impacts the water degradation

mechanism in DMOF. Section 3 will discuss recent experiments at Argonne National lab and how water vapor interacts with DMOF-TM at different humidity concentrations.

C.2 Ligand Functionalization in DMOF

This section will provide a background of the work that was conducted by Jasuja et. al. related to Zn-DMOF-X (X = functionalized BDC linker). The authors chose a variety of BDC functionalized ligands including: polar groups (-NO₂, -OH, and -Br), methyl groups (DM and TM), and aromatic rings (NDC and ADC) to investigate water adsorption and stability in DMOF. Figure C.1 shows the ligand functionalizations used in these studies.^{1,2} Parent DMOF had previously been shown to be unstable when exposed to humidity above 40% RH, and linker functionalization was hypothesized to increase the humid stability of DMOF.

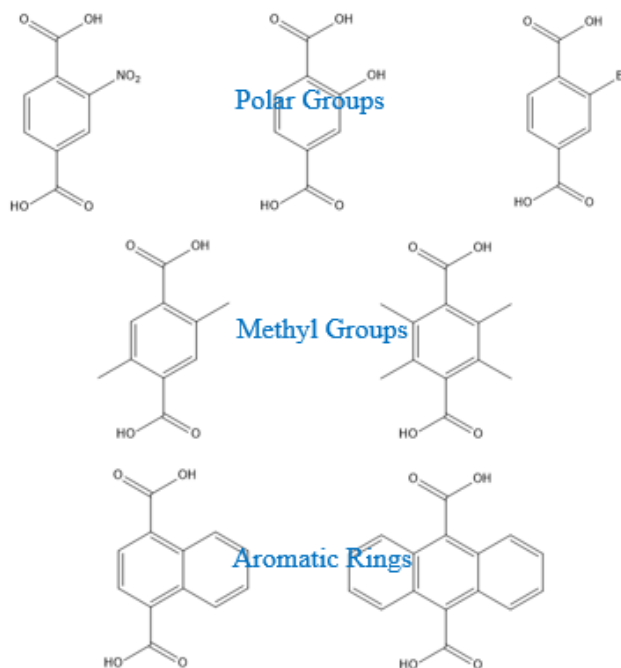


Figure C.1: Ligand functionalization of BDC. (Top left to right) BDC-NO₂, BDC-OH, BDC-Br. (Middle left to right) DM, TM. (Bottom left to right) NDC, ADC.

Parent DMOF displays type-V water adsorption isotherms, such that the material adsorbs very little water from 0 to 40% RH, then undergoes a substantial increase between 40 and 50% RH, which is followed by material degradation. By incorporating polar functional groups, Jasuja et. al.^{1,2} showed that the material became more hydrophilic and underwent the step change and corresponding material degradation at lower humidity levels (See Figure C.2). Thus by incorporating polar functional groups, DMOF became less stable towards humidity. In contrast, the authors showed that incorporation of methyl functional groups onto the BDC ligand resulted in increased framework stability. This was theorized to be a result of the bulkiness of the linkers protecting the Zn-O bond from attack by water molecules as well as increased hydrophobicity due to the added methyl groups. Only DMOF-TM displayed complete humid stability, DMOF-DM and partially substituted TM remained unstable towards water exposure. Lastly, NDC and ADC ligands showed similar stability characteristics when compared to the DM and TM functional groups such that only protecting the Zn-O bond from one side was not enough to completely stabilize the framework towards water vapor. DMOF-ADC proved to be stable when exposed to 90 % RH whereas DMOF-NDC was not. Table C.1 contains the surface areas before and after water exposure for the three systems that have been discussed in this section.

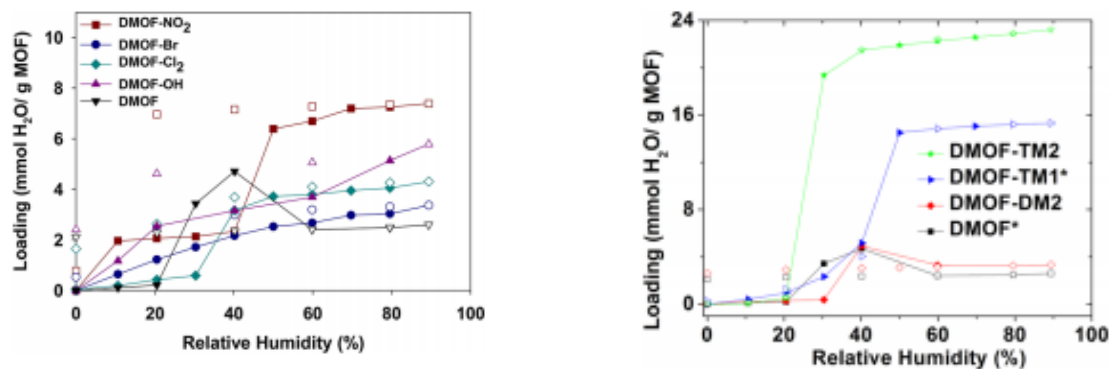


Figure C.2: (Left) Water vapor adsorption/desorption isotherms at 298 K for DMOF-NO₂, DMOF-Br, DMOF-Cl₂, and DMOF-OH. “Reproduced from 1. Copyright 2012, American Chemical Society.” (Right) Water vapor adsorption/desorption isotherms at 298 K for DMOF-TM (Labeled as DMOF-TM2) and DMOF-DM. “Reproduced from 1. Copyright 2012, American Chemical Society.”

Table C.1: BET surface areas before and after water adsorption in functionalized DMOF. “Reproduced from 1 and 2. Copyright 2012, American Chemical Society.”

Material	Pore Volume (cm ³ /g)	Surface Area (m ² /g)		
		Before	After	% Loss
DMOF	0.75	1980	7	100
DMOF-NO ₂	0.53	1310	38	97
DMOF-Br	0.53	1315	1	100
DMOF-OH	0.54	1130	2	100
DMOF-DM	0.51	1115	14	99
DMOF-TM	0.51	1050	1050	0
DMOF-NDC	0.57	1420	1050	26
DMOF-ADC	0.33	760	726	4

C.3 Metal Substitution in DMOF

Tan et. al.³ investigated metal substitution in DMOF by examining nickel, cobalt, and copper, in addition to the parent, zinc, metal nodes. This section will discuss their work and major findings involving metal substitution in parent DMOF. It was previously known that Zn-DMOF was unstable towards water vapor as was shown in Table C.1. Tan et. al. showed that substitution of nickel, cobalt, or copper as the metal node in DMOF produced

materials that were unstable towards high water vapor concentrations, however the water degradation mechanism differed depending on the metal node. The differences in degradation mechanisms was attributed to the differences in electronic structure as a result of the metal node. Figure C.3 shows the degradation pathway for the four different metals used in this study.

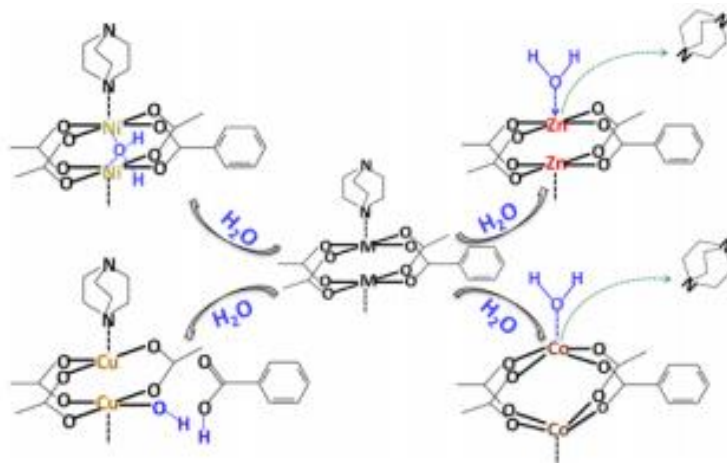


Figure C.3: Schematic illustration of decomposition pathway of $M(bdc)(ted)_{0.5}$ ($M = Cu, Zn, Ni, Co$) reactions with water. “Reproduced from 3. Copyright 2012, American Chemical Society.”

Tan et. al.³ showed that Co-DMOF and Zn-DMOF have similar degradation mechanisms. Water molecules attack the metal-nitrogen bond, displacing the DABCO ligand. After displacement of the DABCO ligand, Zn-DMOF forms MOF-2 sheets which contains a similar square grid Zn-Zn paddlewheel when compared to DMOF, see Figure C.4. MOF-2 can then be regenerated in DMF by adding DABCO and reacting at 110 °C for 2 days.⁵ Co-DMOF does not degrade into MOF-2. After the DABCO ligands are displaced by water molecules in Co-DMOF, Co-Co interactions are removed such that the

entire crystal structure collapses. This destruction of the framework can be seen in the PXRD patterns of the original vs hydrated structures, see Figure C.4.

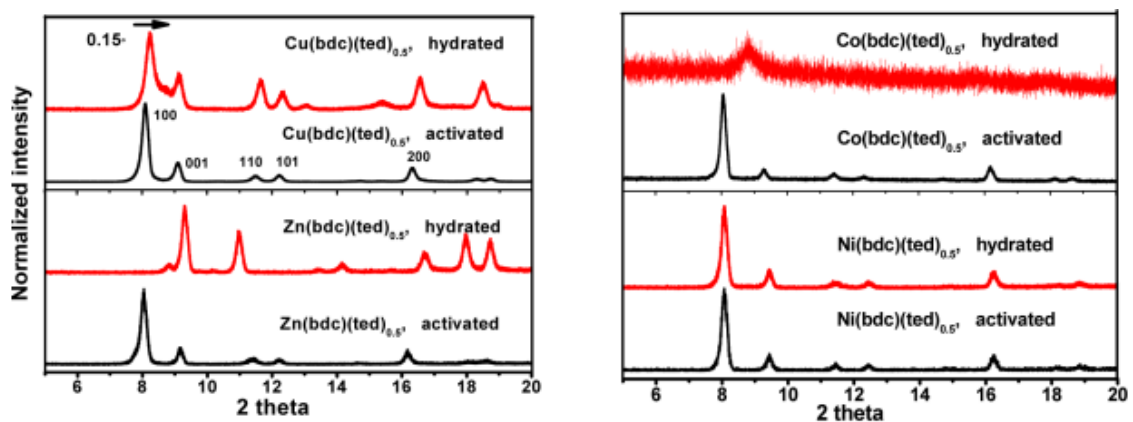


Figure C.4: PXRD pattern of hydrated MOF materials after exposing to 9.5 Torr D₂O vapor and pristine MOF samples. “Reproduced from 3. Copyright 2012, American Chemical Society.”

Cu-DMOF undergoes a different degradation mechanism when compared to Zn and Co-DMOF. Tan et. al.³ showed that Cu-DMOF has improved stability over Zn and Co-DMOF at very low water vapor concentrations of 6 Torr. At higher water vapor concentration, Cu-DMOF undergoes hydrolysis of the Cu-O metal-ligand bond. The authors noted that the Cu-N bond of Cu-DMOF is less susceptible to displacement than in the Zn or Co-DMOF frameworks. They attributed the additional stability of the Cu-N bond to be due to the stability constant of its amine complex being significantly higher than it is for Zn-N. Figure C.4 shows the PXRD patterns of pristine and hydrated Cu-DMOF. One can observe some degradation in the PXRD pattern as there is increased background concentration as well as peak broadening and a few additional peaks that arise in the PXRD pattern.

Ni-DMOF did not degrade upon exposure to low water vapor concentration. This stability can be seen by comparing the pristine and hydrated PXRD patterns in Figure C.4. Tan et. al. used Raman spectroscopy to show that while water does coordinate to the nickel metal site in Ni-DMOF, it does not lead to cleaving of the Ni-O or Ni-N bonds in the framework. Figure C.5 shows the Raman spectra for all of the M-DMOF (M = Ni, Co, Cu, Zn) samples used in this study.

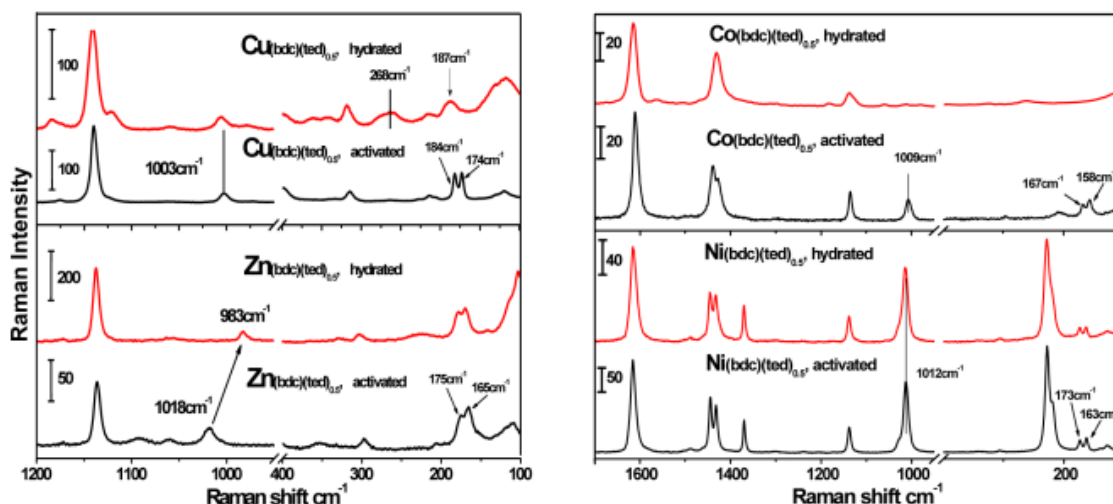


Figure C.5: Raman spectra of activated and hydrated MOF samples after exposure to 9.5 Torr water vapor pressure. “Reproduced from 3. Copyright 2012, American Chemical Society.”

The work by Tan et. al.³ showed that by changing the metal site in DMOF, the framework’s stability towards humidity can be changed even though DMOF does not contain open-metal sites. Additionally, they showed that in low humidity environments Ni-DMOF is stable while Zn and Co-DMOF are not. Cu-DMOF also showed partial stability at the lowest water vapor concentrations tested due to the stability of its corresponding amine complex.

C.4 Experiments at Argonne National Lab

The previous water stability work conducted by Jasuja et. al. and Tan et. al. gave a fundamental understanding of the water stability and degradation mechanisms of DMOF synthesized with a variety of metal nodes and ligand functionalities. However, they did not completely describe why DMOF-TM was stable toward humidity, which prompted further experimentation at Argonne National lab at the synchrotron source. I traveled to Argonne National to conduct two sets of experiments. The first experiment was conducted on the PXRD beamline 17 alongside Nick Burtch (experiment lead), Cody Morelock, and Yang Jiao.⁴ In this experiment we collected in situ PXRD data of DMOF-TM as it was exposed to increasing concentrations of water vapor. The second experiment was collected on the SCXRD beamline, 15BM, alongside Ian Walton. In this experiment we collected in situ SCXRD data on DMOF-TM exposed to the humidity conditions that were identified as the most important during the first visit to Argonne National lab.

C.4.1 Powder X-ray Diffraction Experiments at Argonne National Lab

DMOF-TM samples were synthesized and stored in chloroform for transportation to Argonne National Lab. Samples were prepared at Argonne National Lab for testing by loading into a quartz capillary tube. The samples were then activated in situ while collecting PXRD data under nitrogen flow. Activation was determined to be complete when diffraction peak intensities remained stable for an extended period. Following sample activation, samples were exposed to increasing concentration of humidity including the following: 20, 40, 60, and 70% RH. Between each humidity interval, data was collected for 30 minutes before increasing the humidity further. After humidity testing, the humidity was lower to 0% RH and the capillary tube containing the sample was removed. Previous

water adsorption experiments confirmed the stability of DMOF-TM such that it was not a concern during testing at Argonne National Lab.

Figure C.6 shows the change in diffraction peak intensities of the first two Bragg peaks in the DMOF-TM pattern (Figure C.6A) as well as the water adsorption isotherm corresponding to the different humidity concentrations (Figure C.6B). The water adsorption isotherm can be broken into three regimes: 1) low water adsorption and framework hydrophobicity. 2) Step change in water adsorption and strong adsorption, and 3) saturation of water loading capacity.

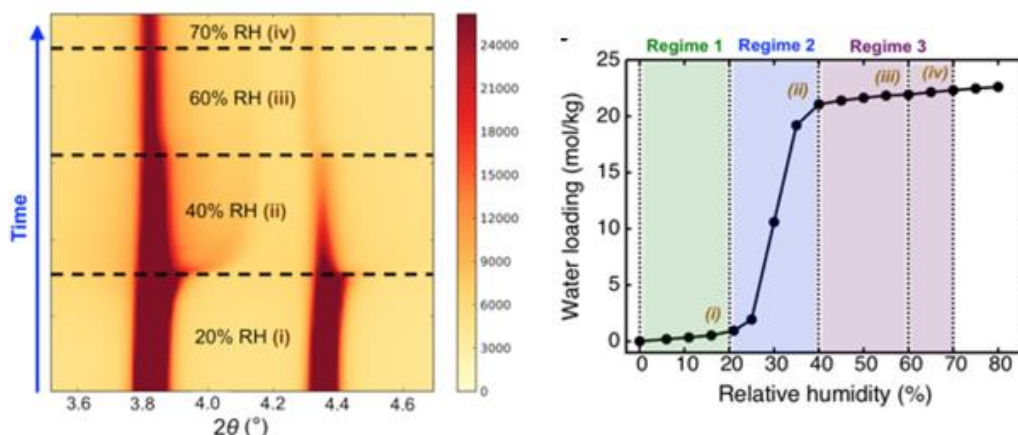


Figure C.6: A) Change in the (1 1 0) and (0 0 1) Bragg peaks collected at Argonne National Lab. B) DMOF-TM water adsorption isotherm in the humidity range from 0 to 80% RH, i – iv correspond to the four humidity levels that we used in the in situ PXRD experiment. “Reproduced from 4. Copyright 2019, Nature Materials.”

The PXRD results in Figure C.6A show decreasing intensity across the (1 1 0) and (0 0 1) Bragg peaks as well as a right shift of the (1 1 0) peak upon increasing humidity from 20 to 40%. This change signifies the creation of a defect structure where a water molecule reversibly binds to the metal node of Zn-DMOF-TM and displaces the TMBDC

ligand. Follow up studies involving SCXRD would confirm these results and the formation of the defect structure upon hydration.

C.4.2 Single Crystal X-ray Diffraction Experiments at Argonne National Lab

Single crystals of DMOF-TM were synthesized and examined under a microscope to confirm that they were large enough for diffraction measurements. Samples measuring 20 μm x 20 μm with a thickness of 5 – 10 μm were of sufficient size and were stored in chloroform for transportation to Argonne National Lab. At Argonne, single crystals were selected using a microscope, and epoxy was used to mount samples onto a quartz fiber that was then placed into the SCXRD detector for testing. Nitrogen gas was passed over the single crystals in order to activate them. No heat was required to remove chloroform from the pore space of the MOF. Additionally, we found that the DMOF-TM single crystals degraded after roughly 30 minutes of exposure to the x-ray beam such that samples would become useless for future measurements. Therefore, several crystals were used to test the humidity regions that were identified in previous PXRD experiments. Separate crystals were chosen to collect SCXRD measurements at 20, 40, 60, and 70% RH and SCXRD data was collected every minute for 30 minutes at which time the sample degraded beyond usefulness.

The software package Olex2 was used to solve the structure of DMOF-TM at 0% RH as well as resolve the location of water molecules within the structure at increasing humidity concentrations from 20 to 70% RH. We first noticed during structure refinement that the originally obtained structure for DMOF-TM was incorrect and the proper space group was determined to be P4/nbm. Figure C.7 shows the solved structure of DMOF-TM as well as the identified defect structures as a result of water adsorption in DMOF-TM.

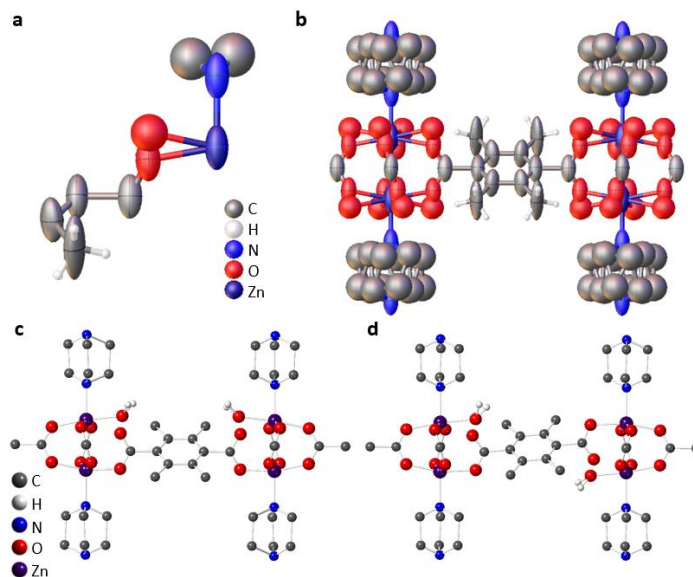


Figure C.7: a) Asymmetric unit of DMOF-TM obtained from SCXRD measurements. b) Expanded structure of DMOF-TM. Proposed c) cis and d) trans defect formation in upon water adsorption in DMOF-TM. “Reproduced from 4. Copyright 2019, Nature Research.”

The combination of SCXRD and PXRD experiments allow us to propose the following mechanism for water adsorption in DMOF-TM. In regime 1, the water induced defect structure forms, dislocating the Zn-O bond between the metal node and carboxylate group of the TMBDC ligand (See Figure C.7 c and d). In regime 2, the majority of water loading occurs filling the pore space of the MOF. In regime 3, a slight expansion of the framework is observed as loading saturation is reached. Figure C.8 shows the proposed water adsorption mechanism in DMOF-TM and the location of water molecules within the structure obtained by SCXRD.

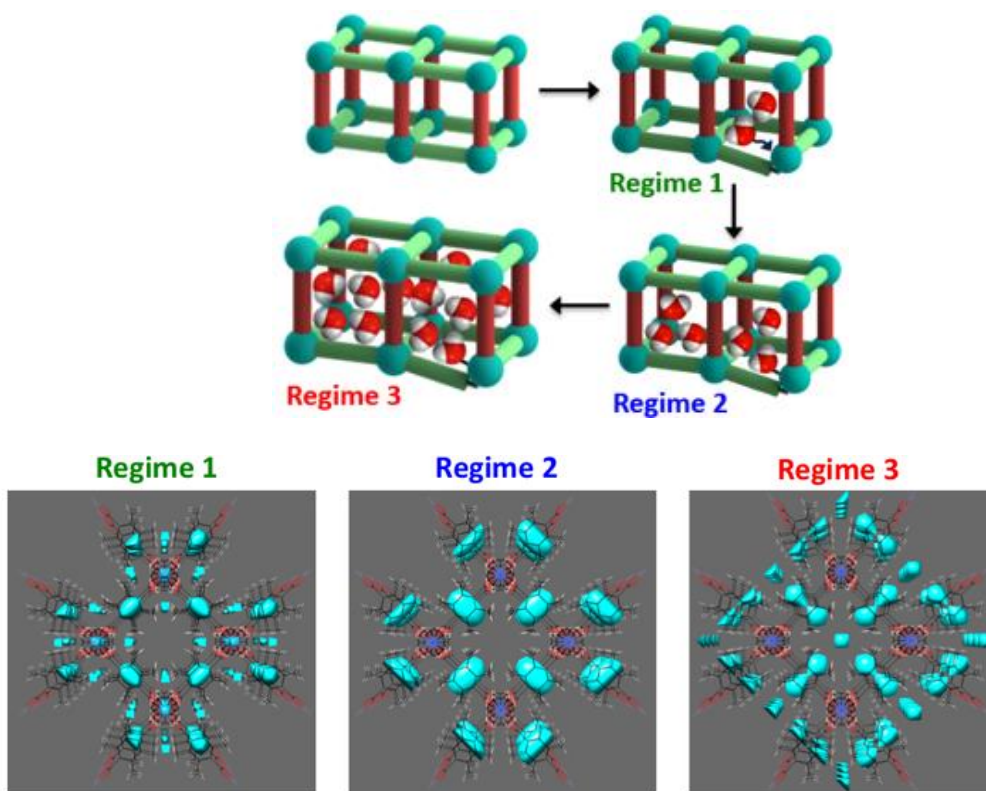


Figure C.8: (Top) Water loading in DMOF-TM corresponding to the 3 regimes identified during PXRD measurements. (Bottom) SCXRD measurements showing the location of water molecules at increasing levels of water loading within the structure. “Reproduced from 4. Copyright 2019, Nature Research.”

C.5 Conclusion

In section C.2, the impact of ligand functionalization on the stability of Zn-DMOF was discussed. Jasuja et. al.^{1,2} identified that the incorporation of bulkier TM and ADC ligands improved the stability of DMOF towards humidity in the air, allowing the materials to be stored in air for years without observable degradation. In section C.3 Tan et. al.³ showed that M-DMOF (M = Zn, Co, Cu, Ni) degrades differently depending on metal center when exposed to low concentrations of water vapor. Zn and Co-DMOF, degrade similarly when water coordinates to the metal center and displaces the DABCO ligand. In

Cu-DMOF, the water molecules instead displace the carboxylate group of the BDC ligand and Ni-DMOF showed no water degradation at very low concentrations of water vapor. In section C.4 I worked alongside Nick Burtch (experiment lead), Yang Jiao, Ian Walton, and Cody Morelock to perform PXRD and SCXRD experiments at Argonne National Lab in order to determine the water loading mechanism in DMOF-TM as well as identify the defect structure formed upon water loading. These were the first of this type of experiment at Argonne National Lab and the first that directly analyzed a water induced defect structure using PXRD and SCXRD experiments in a MOF material. These experiments have laid the groundwork for future studies involving water adsorption and degradation in MOFs and will be useful in future studies that may expand to acid gases. A recent article published by Carter et. al.⁶ examined in situ SO₂ and CO₂ adsorption in MFM-601 at the Diamond Light Source in the UK and hopefully similar in situ studies using acid gases may soon be run at Argonne National lab.

C.6 References

- [1] Jasuja, H.; Huang, Y.; Walton, K. Adjusting the Stability of Metal-Organic Frameworks under Humid Conditions by Ligand Functionalization. *Langmuir*. **2012**, 28, 16874-16880.
- [2] Jasuja, H.; Burtch, N.; Huang, Y.; Cai, Y.; Walton, K. Kinetic Water Stability of an Isostructural Family of Zinc-Based Pillared Metal-Organic Frameworks. *Langmuir*. **2013**, 29, 633-642.
- [3] Tan, K.; Nijem, N.; Canepa, P.; Gong, Q.; Li, J.; Thonhauser, T.; Chabal, Y. Stability and Hydrolyzation of Metal Organic Frameworks with Paddle-Wheel SBUs upon Hydration. *Chem. Mater.* **2012**, 24, 3153-3167.
- [4] Burtch, N.; Walton, I.; Hungerford, J.; Morelock, C.; Jiao, Y.; Heinen, J.; Chen, Y.; Yakovenko, A.; Xu, W.; Dubbeldam, D.; Walton, K. In Situ Visualization of Loading-dependent Water Effects in a Stable Metal-organic Framework. *Nature Materials*. Submitted.

- [5] Chen, Z.; Xiang, S.; Zhao, D.; Chen, B. Reversible Two-Dimensional-Three Dimensional Framework Transformation within a Prototype Metal-Organic Framework. *Cryst. Growth Des.* **2009**, 9, 5293-5296.
- [6] Carter, J.; Han, X.; Moreau, F.; Silva, I.; Nevin, A.; Godfrey, H.; Tang, C.; Yang, S.; Schroder, M. Exceptional Adsorption and Binding of Sulfur Dioxide in a Robust Zirconium-based Metal-organic Framework. *J. Am. Chem. Soc.* **2018**, 140, 15564-15567.

APPENDIX D: SUPPLEMENTAL INFORMATION FOR ROOM TEMPERATURE SYNTHESIS OF METAL-ORGANIC FRAMEWORK ISOMERS IN THE TETRAGONAL AND KAGOME CRYSTAL STRUCTURE

This appendix was reproduced from Hungerford, J.; Walton, K., “Room Temperature Synthesis of Metal-Organic Framework Isomers in the Tetragonal and Kagome Crystal Structure” *Inorganic Chemistry*, Submitted.

D.1 Materials and Crystal Structure

A series of functionalized DMOF-1 materials were synthesized via a fast room temperature synthesis procedure. The parent ligand for DMOF-1, terephthalic acid (BDC), is shown below. The other ligands used in this study are also shown below: dimethyl terephthalic acid (DM), 2-aminoterephthalic acid (NH₂), 2,3,5,6-tetramethyl terephthalic acid (TM), and anthracene dicarboxylic acid (ADC). The formed materials will be referred to as DMOF-DM, DMOF-NH₂, DMOF-TM, and DMOF-ADC respectively. A solvents property table for the solvents used in the synthesis of DMOF and ZnBD is also provided in Table D.1.

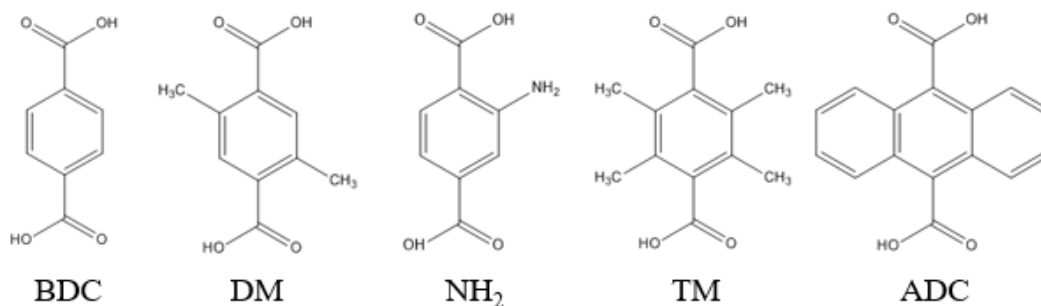


Figure D.1: Ligands in DMOF and ZnBD Room Temperature Synthesis

The structures of DMOF-1 and ZnBD are shown in Figure D.2. DMOF-1 has tetragonal crystal structure and has a 7.5 Å x 7.5 Å pore window in the BDC ligand plane. ZnBD has a Kagome crystal structure and has two pore windows in the BDC ligand plane. The smaller pore is triangular in shape and can fit a circle of diameter 4.5 Å within this pore. The larger pore is hexagonal and measures 15 Å from one end to the other. Table D.2 summarizes the BET surface areas, pore sizes, and pore volumes of the DMOF-1 (including functionalized forms with DM, TM, and ADC) and ZnBD MOFs.¹⁻⁵



Figure D.2: Crystal structure of DMOF-1 (left) and ZnBD (right). “Reproduced from 5. Copyright 2017, Elsevier.”

Table D.1: Solvent Properties.^{6,7,8}

Solvent	Dielectric Constant	Density (g/ml)	Dipole Moment (D)	Boiling Point (°C)	MOF Formed
Acetone	20.7	0.788	2.85	56	DMOF-1
Acetonitrile	37.5	0.782	3.45	82	DMOF-1
DEF	29.02	0.910	3.93	176	DMOF-1
DMF	36.7	0.945	3.86	152	ZnBD
DMSO	46.7	1.096	3.9	189	ZnBD
Ethanol	24.5	0.789	1.69	78	DMOF-1
Methanol	32.7	0.791	1.7	65	DMOF-1

Table D.2: BET SA, pore volume, and pore sizes for the DMOF-1 and ZnBD MOFs.¹⁻⁵

MOF	BET SA (m ² /g)	Pore Volume (cm ³ /g)	Pore Size(s) (Å)
DMOF-1	1980	0.75	7.5 x 7.5
DMOF-TM	1050	0.5	3.5 x 3.5
DMOF-DM	1115	0.51	5.8 x 5.8
DMOF-ADC	760	0.33	3.75 x 3.75
ZnBD	2000-2400	0.8	4.5; 15 (diameter)

D.2 Brunauer-Emmett-Teller (BET) Surface Area Analysis

Nitrogen physisorption analysis was used to assess the pore volumes and surface areas of the synthesized materials. Table 3.1 in the main text shows the results of those experiments and Figures D.3 – D.5 show the nitrogen physisorption isotherms that were collected at 77 K.

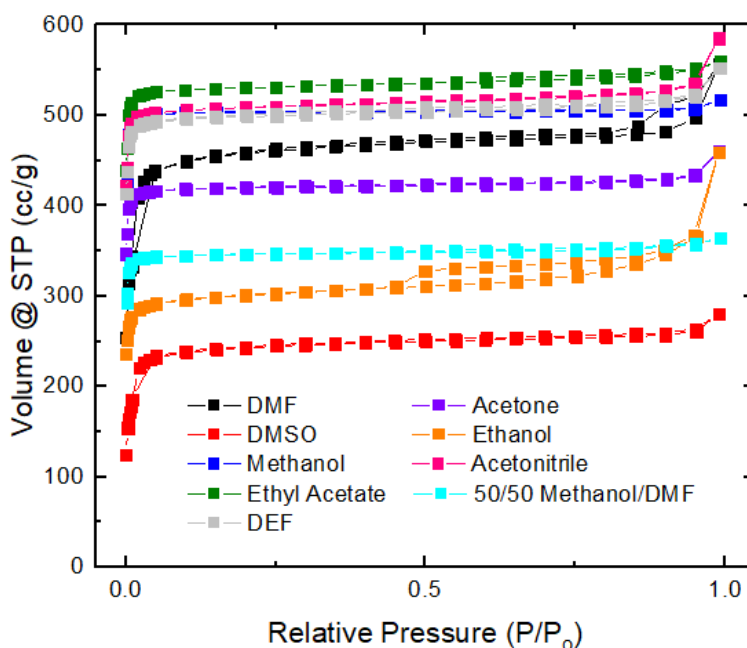


Figure D.3: Nitrogen physisorption isotherms for ZnBD and DMOF samples synthesized using a variety of solvents (DMF = N,N-dimethylformamide, DMSO = dimethyl sulfoxide, methanol, ethyl acetate, DEF = N,N-diethylformamide, acetone, ethanol, acetonitrile, 50/50 methanol/DMF)

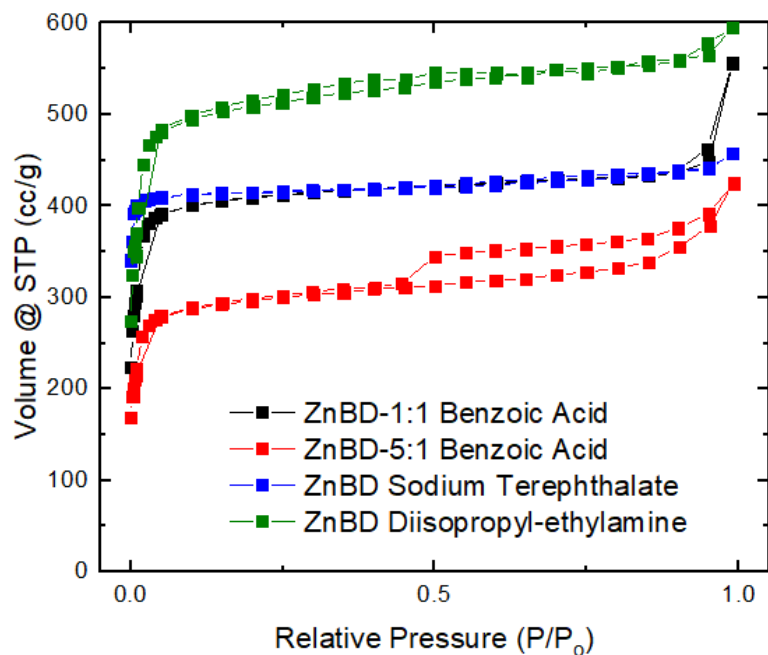


Figure D.4: Nitrogen physisorption isotherms for ZnBD samples synthesized using a variety of acid and base modulators (1:1 Benzoic acid/BDC, 5:1 Benzoic acid/BDC, Sodium terephthalate, diisopropyl-ethylamine)

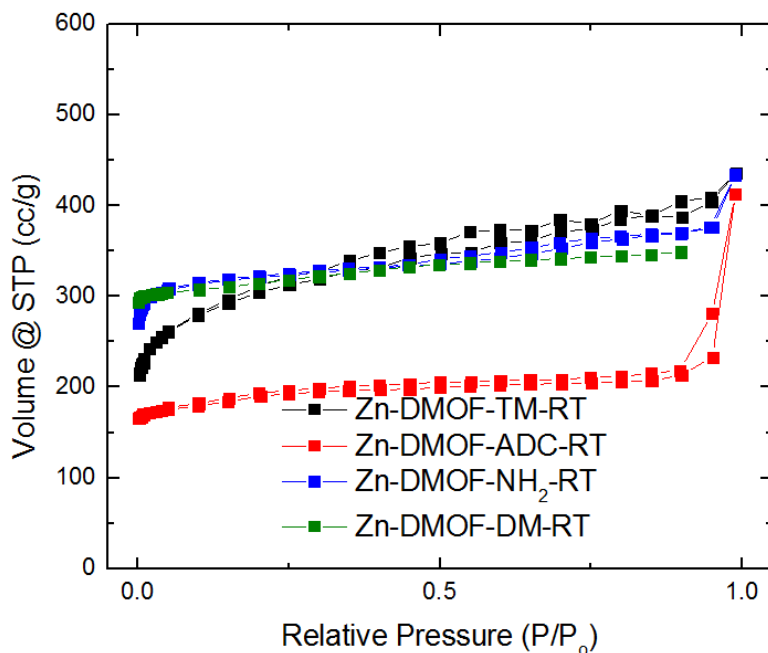


Figure D.5: Nitrogen physisorption isotherms for Zn-DMOF-X samples synthesized at room temperature in DMF. (DM = 2,5-dimethylterephthalic acid, NH₂ = 2-aminoterephthalic acid, TM = 2,3,5,6-tetramethylterephthalic acid, and ADC = 9,10-anthracenedicarboxylic acid)

D.3 CO₂ Adsorption Comparison

Figure D.6 shows a comparison of the CO₂ adsorption isotherms between the ZnBD-DMF, Zn-DMOF-Methanol, Zn-DMOF-Ethanol, and Zn-DMOF synthesized by Liang et. al.⁹ There is essentially complete overlap between the Zn-DMOF-Liang et. al. synthesized DMOF-1 and the DMOF-1 that we synthesized in methanol at room temperature. When ethanol was used as a solvent we see a slight decrease in the CO₂ adsorption, likely due to the decreased surface area and pore volume present in the material.

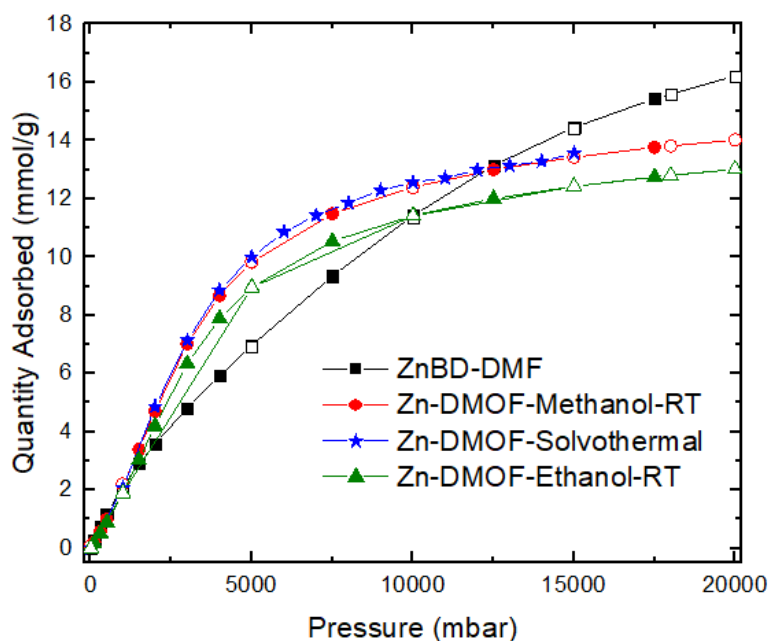


Figure D.6: Comparison of the CO₂ adsorption isotherms for ZnBD-DMF, Zn-DMOF-Methanol-RT, Zn-DMOF-Ethanol-RT, and Zn-DMOF-Solvothermal. “Reproduced from 9. Copyright 2010, *Elsevier*.”

D.4 Zn-DMOF-TM Stability

Zn-DMOF-TM has previously been reported as an air stable MOF for periods of up to one year.^{1,2} However, when synthesizing the material via room temperature synthesis methods we noted that the material broke down after a period of roughly 1 month as was

evident by a loss in crystal structure, measured using PXRD and BET surface area analysis (Figure D.7 and Table D.3 respectively). We have been unable to identify the cause of this degradation and will be investigating it further in follow-up research.

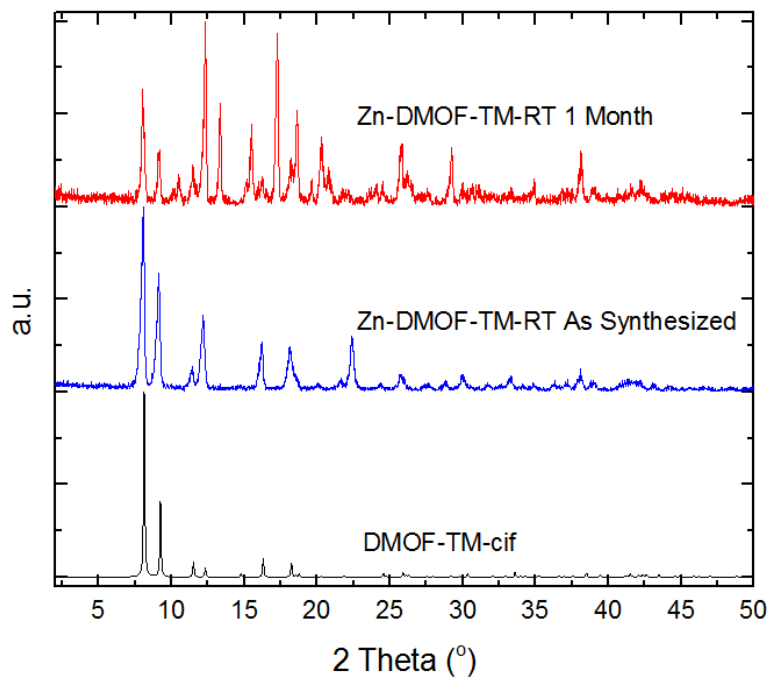


Figure D.7: Zn-DMOF-TM PXRD patterns showing degradation after 1 month in air.

Table D.3: BET surface area and pore volume of Zn-DMOF-TM-RT over time

MOF	BET SA (m ² /g)	Pore Volume (cm ³ /g)
Zn-DMOF-TM		
As Synthesized	950	0.434
1 month	265	0.122

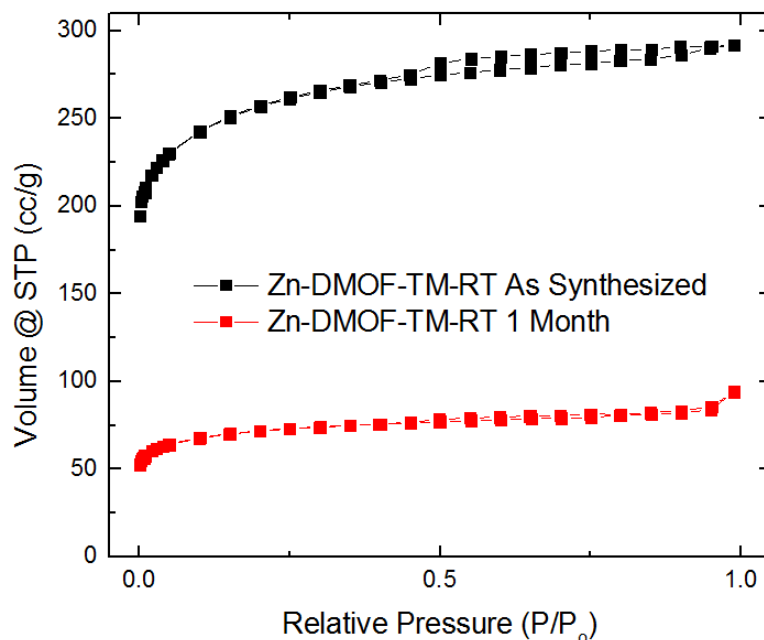


Figure D.8: Nitrogen physisorption isotherms for Zn-DMOF-TM-RT over time

D.5 Metal Substitution Room Temperature Synthesis

Metal substitution in DMOF-1 has been successful for the following metal centers: zinc, cobalt, nickel, and copper.^{3,10,11} In this work we attempted to synthesize ZnBD, CoBD, NiBD, and CuBD using the room temperature synthesis procedure that was discussed in the main text of the manuscript. For all metal substitutions, metal nitrate salts were used as precursor materials and DMF was used as a solvent. Figure D.9 shows the PXRD patterns of the resulting materials.

Figure D.9 shows that we were successfully able to synthesize both ZnBD and CoBD, however after numerous trials we were unable to produce NiBD or CuBD. When conducting the room temperature synthesis using nickel salts we generally achieved an unidentified power pattern that does not match either the DMOF-1 or Kagome ZnBD lattice. It is also highly likely that the formed structure contains many phase impurities

such that determination of its structure would be difficult. When using copper salts in the room temperature synthesis, a DMOF-1 phase persisted across multiple trials such that we were never able to produce a Kagome CuBD lattice. Table D.4 shows the BET surface areas and pore volumes for the metal substituted $M_2(BDC)_2(DABCO)$ (Nitrogen physisorption isotherms are located in Figure D.10). ZnBD-DMF and CoBD-DMF displayed similar surface areas (2100-2300 m^2/g) and pore volumes (0.80 - 0.87 cm^3/g) and Cu-DMOF-DMF had a slightly lower surface area (1871 m^2/g) and pore volume (0.71 cm^3/g).

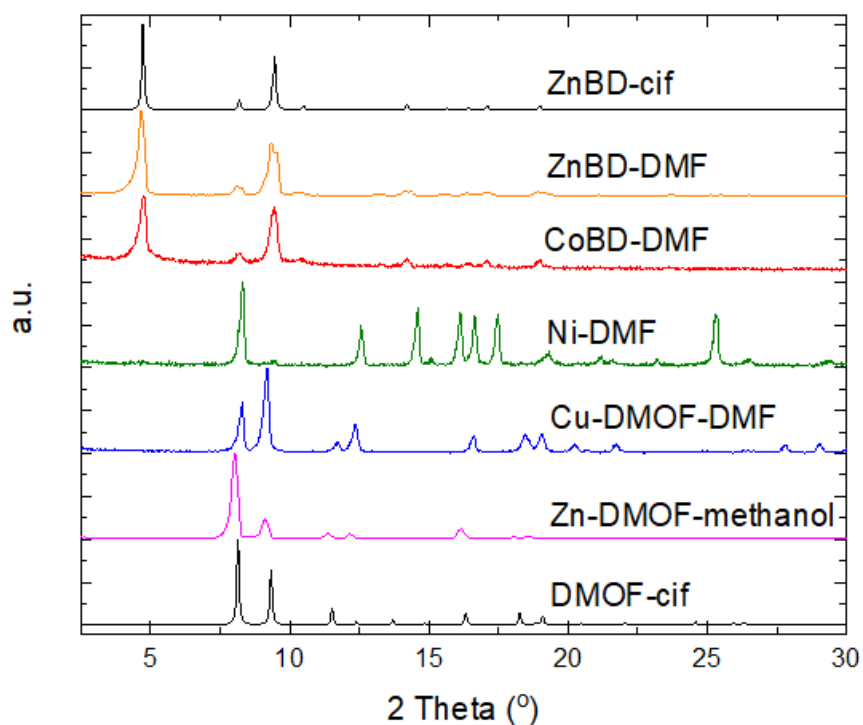


Figure D.9: PXRD patterns of $M_2(BDC)_2(DABCO)$ where $M = Zn, Co, Ni, Cu$ all synthesized at room temperature in DMF.

Table D.4: BET surface area and pore volume of $M_2(BDC)_2(DABCO)$ where $M = Zn, Co, Ni, Cu$ synthesized solvothermally in DMF.

MOF	BET SA (m^2/g)	Pore Volume cm^3/g
ZnBD-DMF	2104	0.80
CoBD-DMF	2281	0.86
Ni-DMF	NA	NA
Cu-DMOF-DMF	1871	0.71

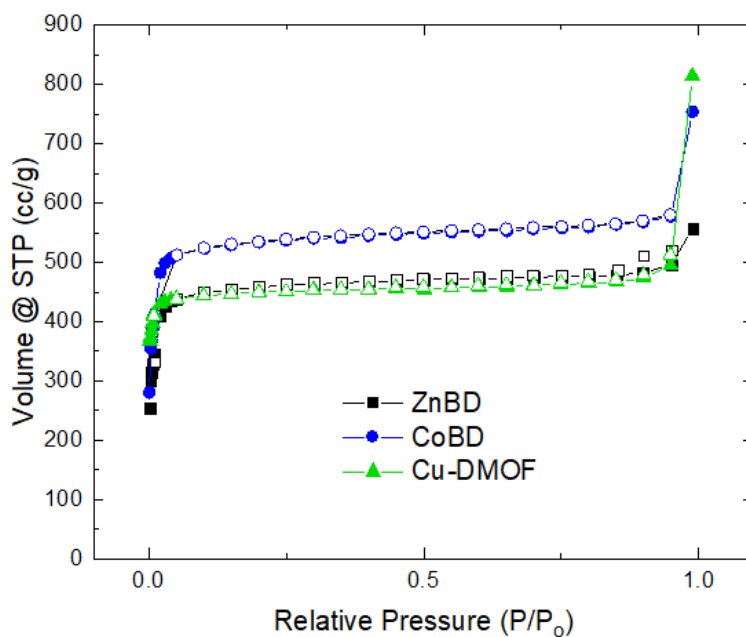


Figure D.10: Nitrogen physisorption isotherms for ZnBD-DMF, CoBD-DMF, and Cu-DMOF-DMF synthesized at room temperature.

D.6 Investigation of Zinc Precursors in the Room Temperature

Synthesis Procedure

In addition to $Zn(NO_3)_2 \cdot 6H_2O$, which was used as the metal precursor throughout the main text, zinc acetate ($Zn(CH_3CO_2)_2 \cdot 2H_2O$) and zinc chloride ($ZnCl_2$) were also explored as metal precursors. The PXRD patterns (Figure D.11) and BET surface areas

(Table D.5 and nitrogen physisorption isotherms included in Figure D.12) of the resultant materials are shown below.

DMOF-1 was formed in methanol for both metal precursors, zinc acetate and ZnCl_2 , see PXRD patterns in Figure D.10. The surface areas of these materials were smaller than those obtained from the $\text{Zn}(\text{NO}_3)_2 \cdot 6\text{H}_2\text{O}$ metal precursor used throughout the main text. The ZnCl_2 metal precursor in DMF did not form either of the expected structures and also resulted in a material with a very low surface area. Zinc acetate in DMF produced a combination of both frameworks, DMOF-1 and ZnBD, which can be observed in the PXRD patterns in Figure D.11. This result suggests that the formation of the metal secondary building unit may also influence MOF topology and further experimentation would be required to completely understand the impact that metal salts have on directing MOF topology. We therefore recommend that when conducting room temperature synthesis of DMOF-1 or ZnBD that $\text{Zn}(\text{NO}_3)_2 \cdot 6\text{H}_2\text{O}$ be used as the preferred metal precursor.

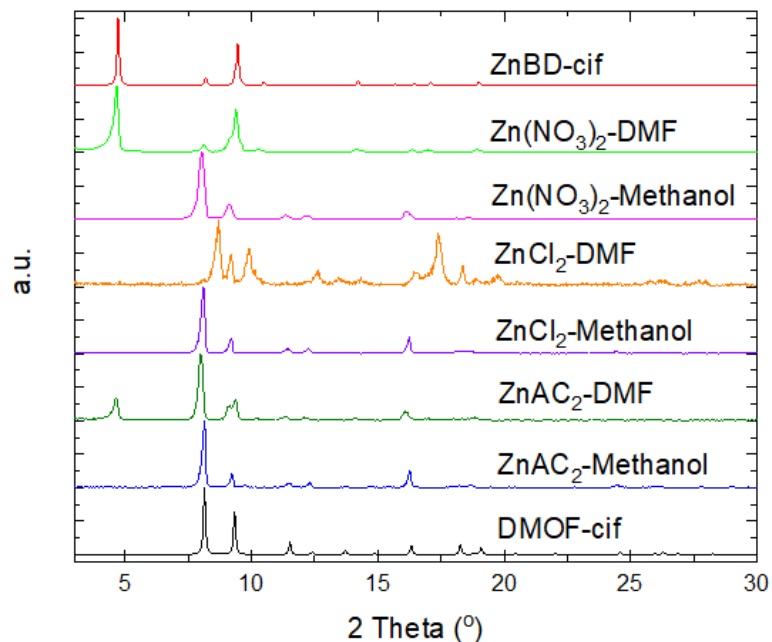


Figure D.11: PXRD patterns of $\text{Zn}_2(\text{BDC})_2(\text{DABCO})$ synthesized from different metal precursors (zinc nitrate = $\text{Zn}(\text{NO}_3)_2 \cdot 6\text{H}_2\text{O}$, zinc chloride = ZnCl_2 , and zinc acetate = $\text{Zn}(\text{CH}_3\text{CO}_2)_2 \cdot 2\text{H}_2\text{O}$ (AC_2)) using methanol and DMF as solvents

Table D.5: BET surface area and pore volume of $\text{Zn}_2(\text{BDC})_2(\text{DABCO})$ synthesized from different metal precursors ($\text{Zn}(\text{NO}_3)_2 \cdot 6\text{H}_2\text{O}$, ZnCl_2 , and $\text{Zn}(\text{CH}_3\text{CO}_2)_2 \cdot 2\text{H}_2\text{O}$) using methanol and DMF as solvents

MOF	BET SA (m^2/g)	Pore Volume cm^3/g
$\text{Zn}(\text{NO}_3)_2$ -DMF	2104	0.80
$\text{Zn}(\text{NO}_3)_2$ -Methanol	2113	0.78
ZnCl_2 -DMF	50	0.03
ZnCl_2 -Methanol	1519	0.57
ZnAC_2 -DMF	1481	0.57
ZnAC_2 -Methanol	1704	0.64

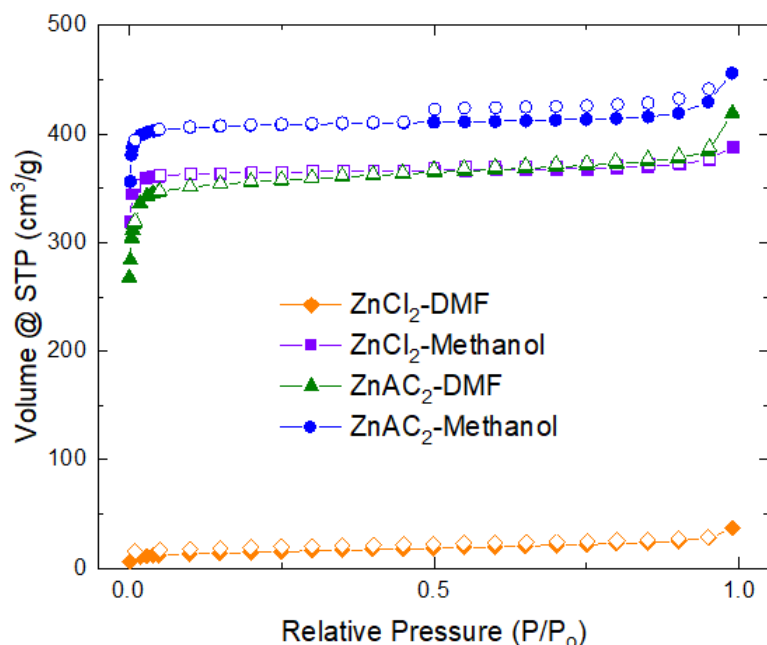


Figure D.12: Nitrogen physisorption isotherms of $\text{Zn}_2(\text{BDC})_2(\text{DABCO})$ synthesized from different metal precursors ($\text{Zn}(\text{NO}_3)_2 \cdot 6\text{H}_2\text{O}$, ZnCl_2 , and $\text{Zn}(\text{CH}_3\text{CO}_2)_2 \cdot 2\text{H}_2\text{O}$) using methanol and DMF as solvents. Closed circles correspond to adsorption and open circles correspond to desorption.

D.7 References

- [1] Jasuja, H.; Burtch, N.; Huang, Y.; Cai, Y.; Walton, K. Kinetic Water Stability of an Isostructural Family of Zinc-Based Pillared Metal–Organic Frameworks. *Langmuir*. **2012**, 29, 633-642.
- [2] Jasuja, H.; Huang, Y.; Walton, K. Adjusting the Stability of Metal–Organic Frameworks under Humid Conditions by Ligand Functionalization. *Langmuir*. **2012**, 28, 16874-16880.
- [3] Chun, H.; Dybtsev, D.; Kim, H.; Kim, K. Synthesis, X-ray Crystal Structures, and Gas Sorption Properties of Pillared Square Grid Nets Based on Paddle-Wheel Motifs: Implications for Hydrogen Storage in Porous Materials. *Chem. Eur. J.* **2005**, 11, 3521-3529.
- [4] Chun, H.; Moon, J. Discovery, Synthesis, and Characterization of an Isomeric Coordination Polymer with Pillared Kagome Net Topology. *Inorg. Chem.* **2007**, 46, 4371-4373.

- [5] Zhou, K.; Chaemchuen, S.; Wu, Z.; Verpoort, F. Rapid Room Temperature Synthesis Forming Pillared Metal-Organic Frameworks with Kagome Net Topology. *Microporous Mesoporous Mater.* **2017**, 239, 28-33.
- [6] University of California Berkley Department of Chemistry. <http://www.cchem.berkeley.edu/rsgp/solventproperties.pdf>. (Accessed 8/2/2018)
- [7] Sigma-Aldrich. <https://www.sigmaaldrich.com/catalog/product/aldrich/186317?lang=en®ion=US>. (Accessed 8/2/2018)
- [8] R. Stenutz. <http://www.stenutz.eu/chem/solv6.php?name=N,N-diethylformamide>. (Accessed 8/2/2018)
- [9] Liang, Z.; Marshall, M.; Chaffee, A. CO₂ Adsorption, Selectivity and Water Tolerance of Pillared-layer Metal-Organic Frameworks. *Microporous Mesoporous Mater.* **2010**, 132, 305-310.
- [10] Tan, K.; Nijem, N.; Canepa, P.; Gong, Q.; Li, J.; Thonhauser, T.; Chabal, Y. Stability and Hydrolyzation of Metal Organic Frameworks with Paddle-Wheel SBUs upon Hydration. *Chem. Mater.* **2012**, 24, 3153-3167.
- [11] Lee, J.; Olson, D.; Pan, L.; Emge, T.; Li, J. Microporous Metal-Organic Frameworks with High Gas Sorption and Separation Capacity. *Adv. Funct. Mater.* **2007**, 17, 1255-1262.

APPENDIX E: SUPPLEMENTAL INFORMATION FOR DMOF-1 AS A REPRESENTATIVE MOF FOR SO₂ ADSORPTION IN BOTH HUMID AND DRY CONDITIONS

This appendix was reproduced from a previous manuscript. “Reprinted with permission from Hungerford, J.; Bhattacharyya, S.; Tumuluri, U.; Nair, Z.; Wu, Z.; Walton, K. DMOF-1 as a Representative MOF for SO₂ Adsorption in Both Humid and Dry Conditions. *J. Phys. Chem. C*. 2018, 122, 23493 – 23500. Copyright 2018 American Chemical Society.”

E.1 Materials

Functionalized DMOF-1 was synthesized using a variety of different linkers for this study including terephthalic acid (BDC), 2,5-dimethyl-terephthalic acid (DM), 1,4-naphthalenedicarboxylic acid (NDC), 2,3,5,6-tetramethylterephthalic acid (TM), 9,10-anthracenedicarboxylic acid (ADC). These linkers are shown in Figure E1 below and the structure of nonfunctionalized DMOF-1 is shown in Figure E.2.¹

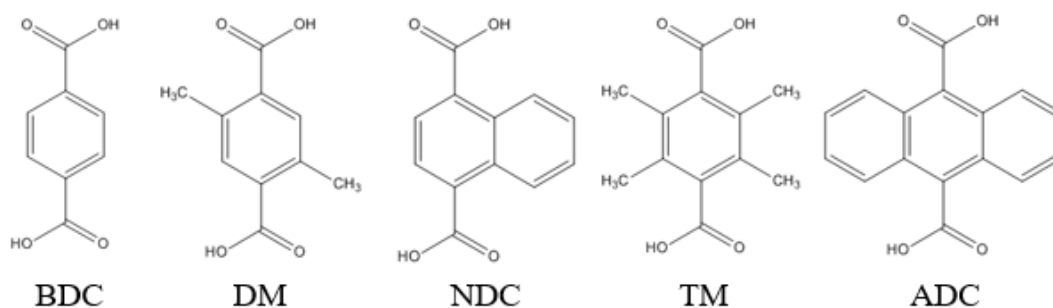


Figure E.1: DMOF substituting ligands (BDC, DM, NDC, TM, and ADC)

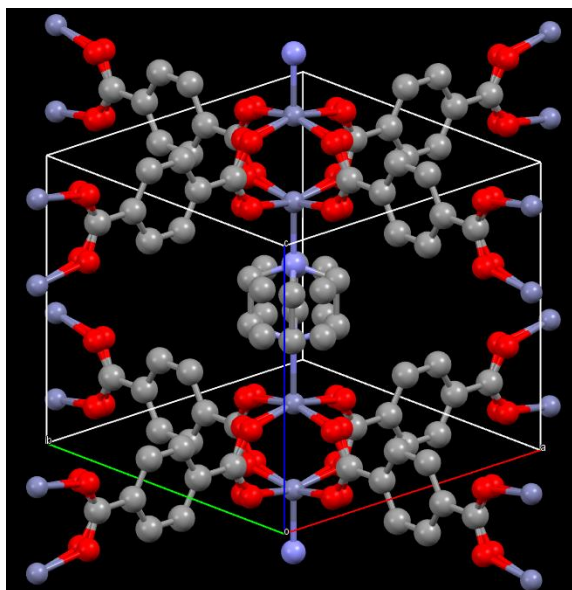


Figure E.2: Structure of DMOF (hydrogen atoms omitted)

E.2 Humid SO₂ Exposure Unit

Humid SO₂ exposure tests were conducted in a lab build system. A schematic of this system is shown in Figure E.3. The humid SO₂ is generated by flowing air through an aqueous NaHSO₃ solution into an exposure unit equipped with a humidity sensor and Draeger detector. The exhaust flows through a NaOH sink before being vented to the fume hood. All exposures were conducted at room temperature, 85% RH +/- 5% RH, and ~50 ppm SO₂ +/- 10 ppm for the 3 trials of 50, 100, and 250 ppm-days (1, 2, and 5 day exposures at 50 ppm SO₂).

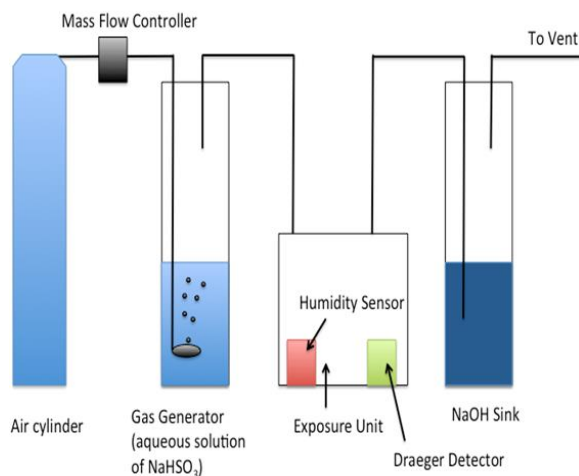


Figure E.3: Diagram of humid exposure unit setup

E.3 Thermal Gravimetric Analysis (TGA)

Figure E.4 shows the TGA curves for the M-DMOF-TM ($M = \text{Zn}, \text{Cu}, \text{Ni}, \text{Co}$) samples. The data was collected under helium flow using a ramp rate of $5^\circ\text{C}/\text{min}$ from room temperature up to 700°C .

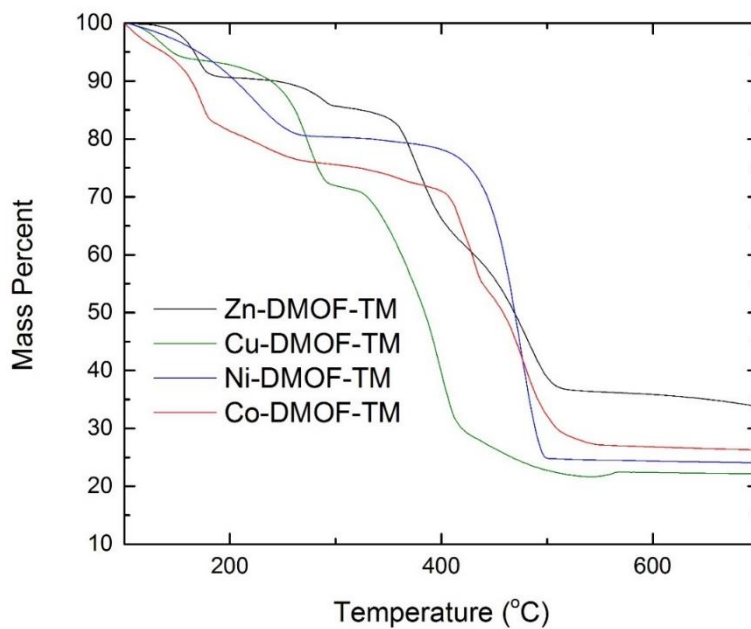


Figure E.4: TGA curves for M-DMOF-TM conducted from room temperature to 700°C using a ramp rate of $5^\circ\text{C}/\text{min}$

E.4 In Situ FTIR Difference Spectra

The difference spectra for the in situ SO₂ FTIR are shown in Figures E5 through E8. Figure E.5 shows the spectra from 700 – 4000 cm⁻¹ for the M-DMOF-TM samples and the Zn-DMOF-ADC sample. Zn-DMOF-NDC and Zn-DMOF-DM were not tested as these materials are not water stable and there are trace concentrations of water in the 260 ppm SO₂ in helium cylinder as well as the FTIR apparatus. For this reason these materials were not tested. Figures E6A and E6B show the difference spectra for the other two SO₂ concentrations that were tested in this study, 50 and 150 ppm.

Figure E.7 shows how the difference spectra change with exposure time for the M-DMOF-TM and Zn-DMOF-ADC samples collected at 260 ppm SO₂ in helium. In all of the samples tested there is trace water present, this is evident by the broad peaks that evolve over time from 3000 – 3500 cm⁻¹. The peaks, however are largest for the Ni and Co samples, which is interesting since all materials were activated using the same procedures. Figure E.8 shows the desorption profile for the post activation of the M-DMOF-TM (M = Zn, Ni, Co, Cu) and Zn-DMOF-ADC samples. In all samples the SO₂ desorbed quickly as can be seen by the loss in SO₂ interaction peaks upon heating to 40 °C.

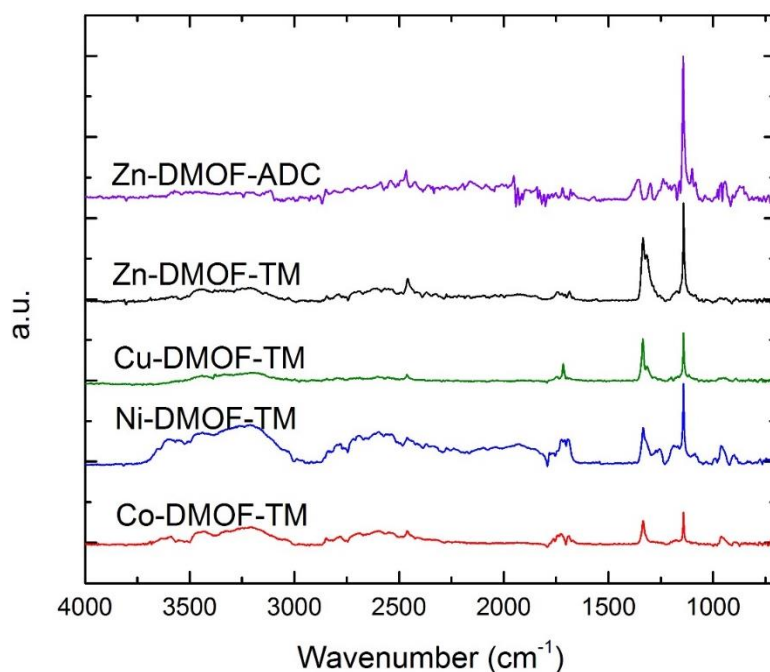


Figure E.5: Complete FTIR difference spectra of M-DMOF-TM and Zn-DMOF-ADC at 260 ppm SO_2 concentration

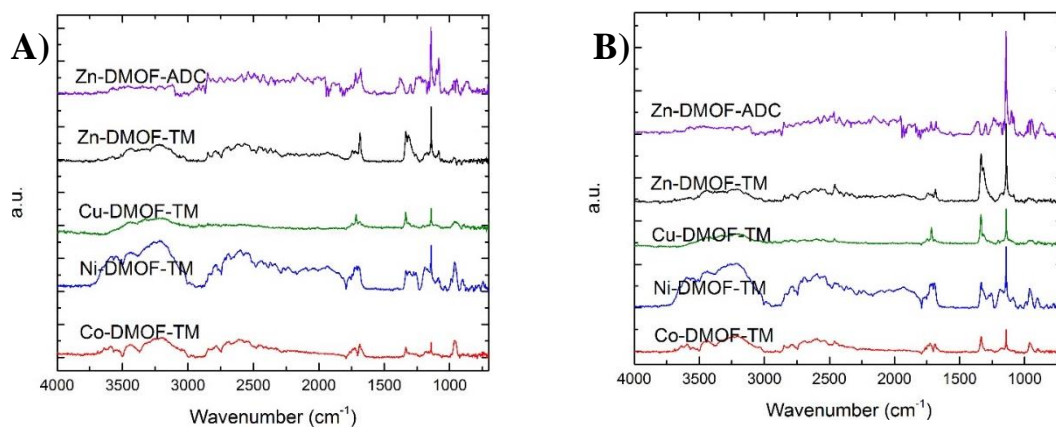


Figure E.6: Complete FTIR difference spectra of M-DMOF-TM and Zn-DMOF-ADC at A) 50 ppm SO_2 concentration and B) 150 ppm SO_2 concentration in helium carrier gas

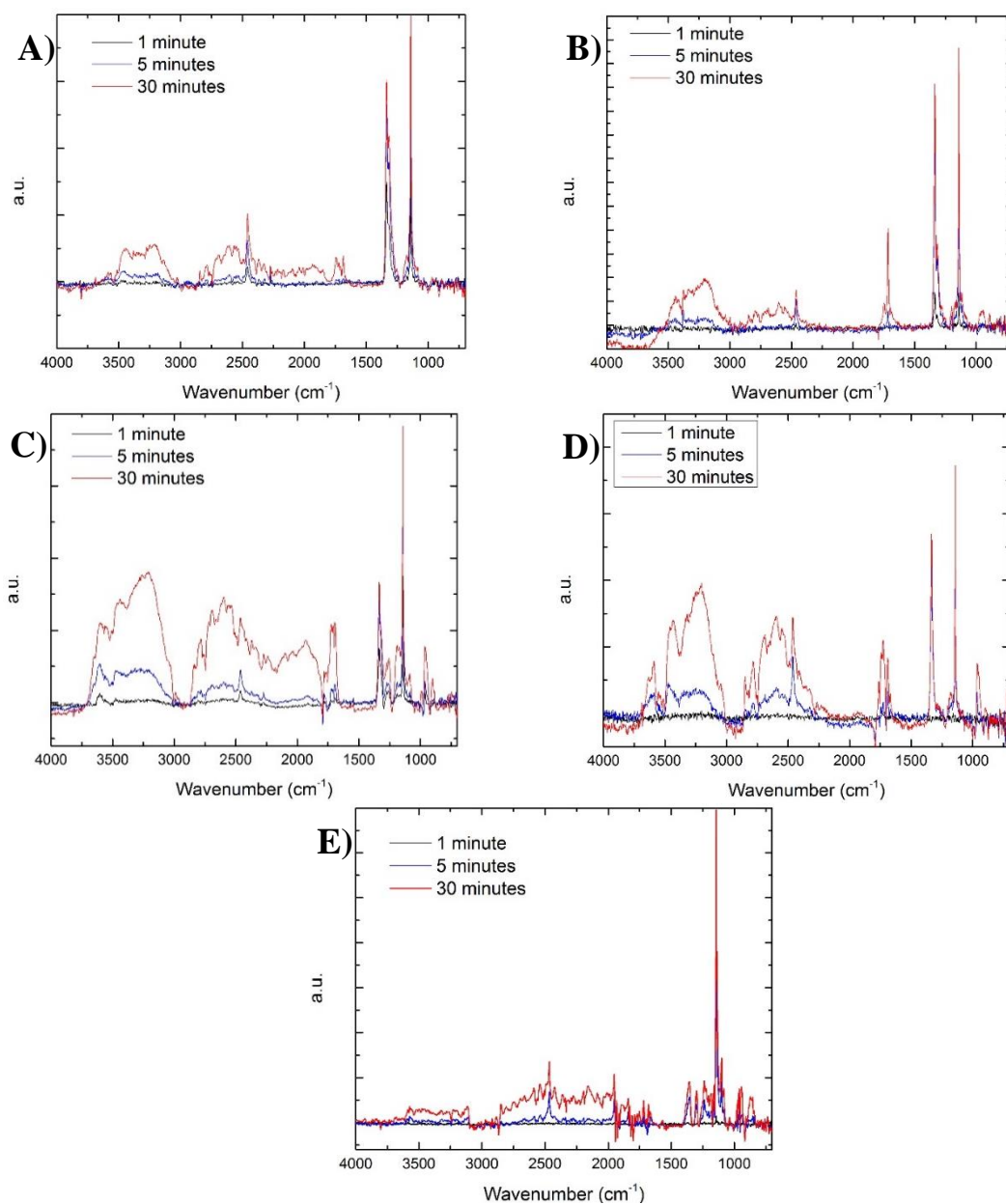


Figure E.7: FTIR difference spectra variation with exposure time for: A) Zn-DMOF-TM B) Cu-DMOF-TM C) Ni-DMOF-TM D) Co-DMOF-TM E) Zn-DMOF-ADC

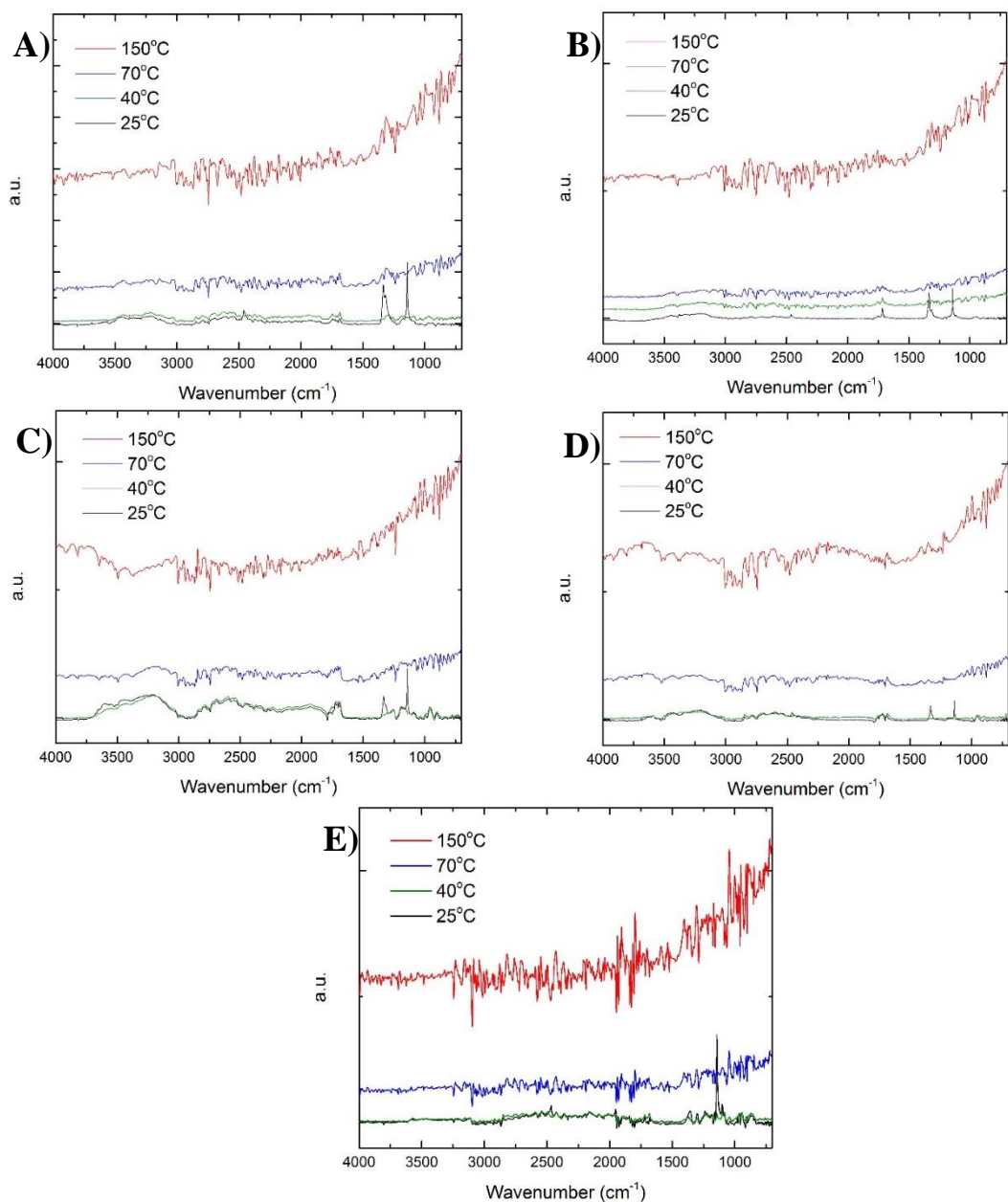


Figure E.8: FTIR Difference Spectra for Desorption Profile of: A) Zn-DMOF-TM B) Cu-DMOF-TM C) Ni-DMOF-TM D) Co-DMOF-TM E) Zn-DMOF-ADC

E.5 Powder X-ray Diffraction Data (PXRD)

PXRD patterns for the Zn-DMOF-X materials are shown in Figure E.9 for the as synthesized, after water adsorption, after dry SO₂ adsorption, and humid SO₂ exposed

samples (where applicable). Zn-DMOF-NDC and Zn-DMOF-DM both degraded upon humidity exposure as was expected from previous results, additionally these samples also degraded upon dry SO₂ adsorption experiments and therefore were not further tested in the humid SO₂ experiments.² Zn-DMOF-TM and Zn-DMOF-ADC were both shown to be stable towards humidity and dry SO₂ testing. Zn-DMOF-ADC was the only functionalized form of Zn-DMOF that retained some of its crystallinity when exposed to 250 ppm-days of humid SO₂.

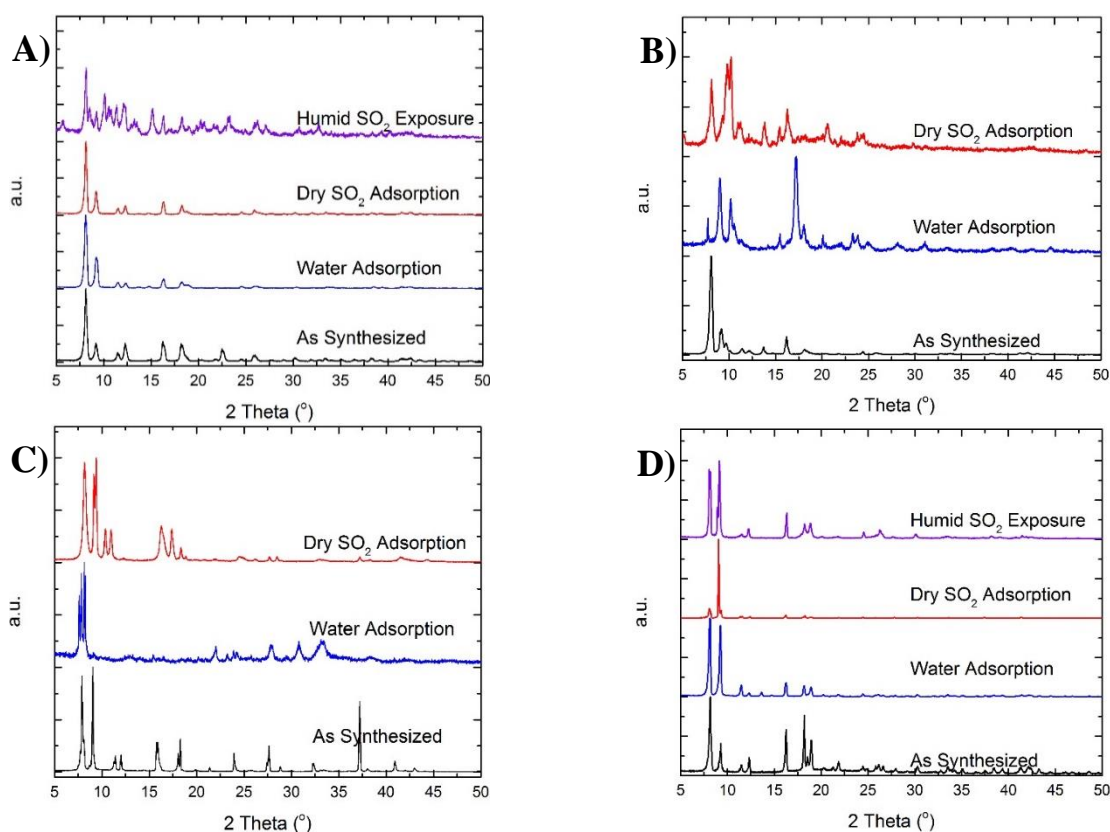


Figure E.9: PXRD patterns of: A) Zn-DMOF-TM B) Zn-DMOF-DM C) Zn-DMOF-NDC D) Zn-DMOF-ADC, for as synthesized, after water adsorption, after dry SO₂ adsorption, and after 250 ppm-days humid SO₂ exposure (when applicable) (50ppm SO₂ and 85% RH)

Figure E.10 shows PXRD patterns for the as synthesized, after FTIR analysis, and after 100 and 250 ppm-days of humid SO₂ exposed samples. All samples retained their crystallinity after the FTIR analysis studies. This shows that the small amounts of water contained in the apparatus were not able to negatively impact the samples to the degree that was observed in the humid SO₂ exposure trials. After 100 ppm-days of humid SO₂ exposure we can see that Zn and Co-DMOF-TM show a loss in their original crystal structure whereas Cu and Ni-DMOF-TM show the retention of their crystal structures. After 250 ppm-days of humid SO₂ exposure only Cu-DMOF-TM retained any of its crystal structure and all of the other M-DMOF-TM samples degraded.

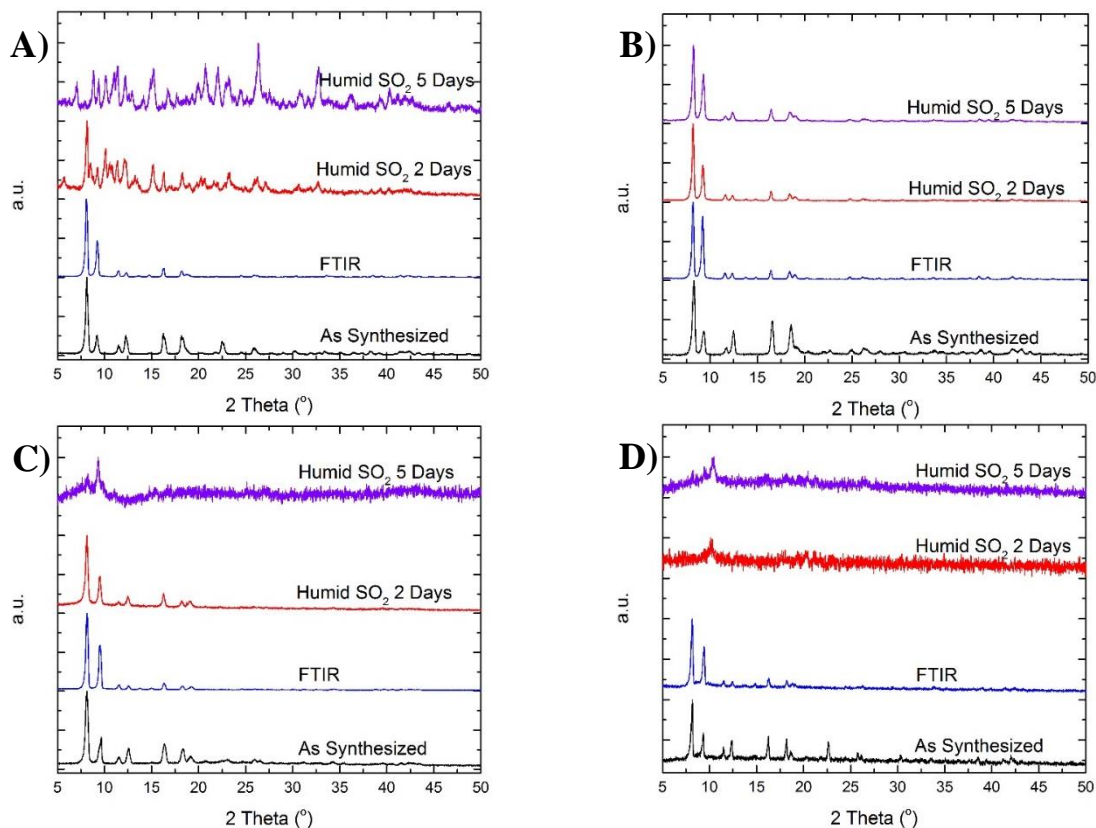


Figure E.10: PXRD Patterns of humid SO₂ exposed samples for 100 and 250 ppm-days, after in situ FTIR, and as synthesized materials for: A) Zn-DMOF-TM B) Cu-DMOF-TM C) Ni-DMOF-TM D) Co-DMOF-TM

E.6 Scanning Electron Microscopy (SEM) and Photographs of Samples

Scanning electron microscopy images were taken of the M-DMOF-TM, Figure E.11, (M = Zn, Cu, Co, Ni) and Zn-DMOF-X, Figure E12, (X = TM, ADC) samples before and after exposure to humid SO₂ (85% RH and 50 ppm SO₂). The samples were prepared for SEM by first activating overnight at 110 °C to remove any remaining DMF or SO₂ in the pores. The samples were then dispersed in a small amount of methanol and transferred using a pipette onto SEM mounts containing carbon tape. The samples were then allowed to dry overnight. Samples were tested on the SEM as is using a low voltage of 0.6 kV to prevent charging.

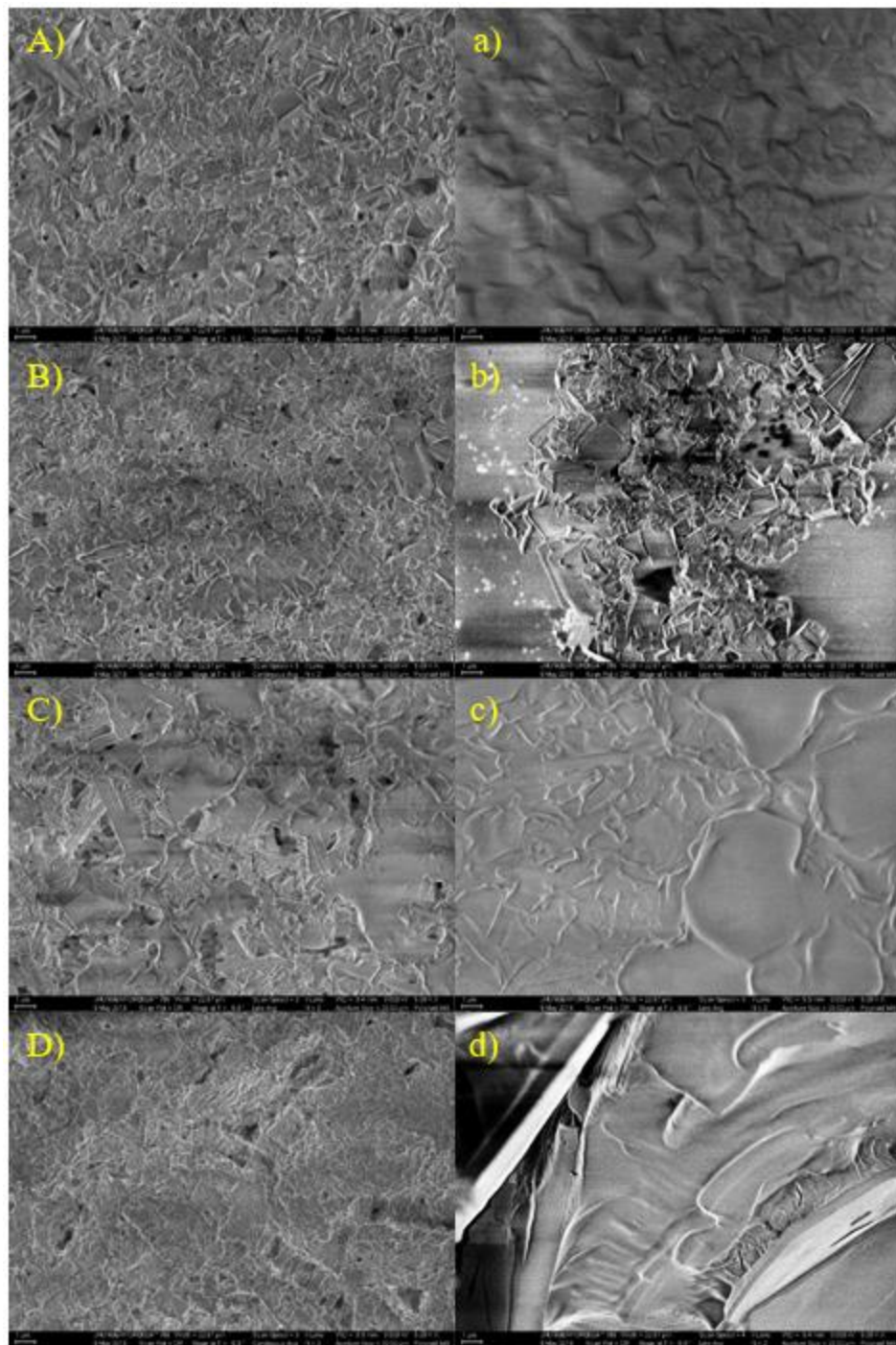


Figure E.11: SEM images of M-DMOF-TM materials taken before and after exposure to humid SO_2 . A) Zn-DMOF-TM before a) after B) Cu-DMOF-TM before b) after C) Ni-DMOF-TM before c) after D) Co-DMOF-TM before d) after

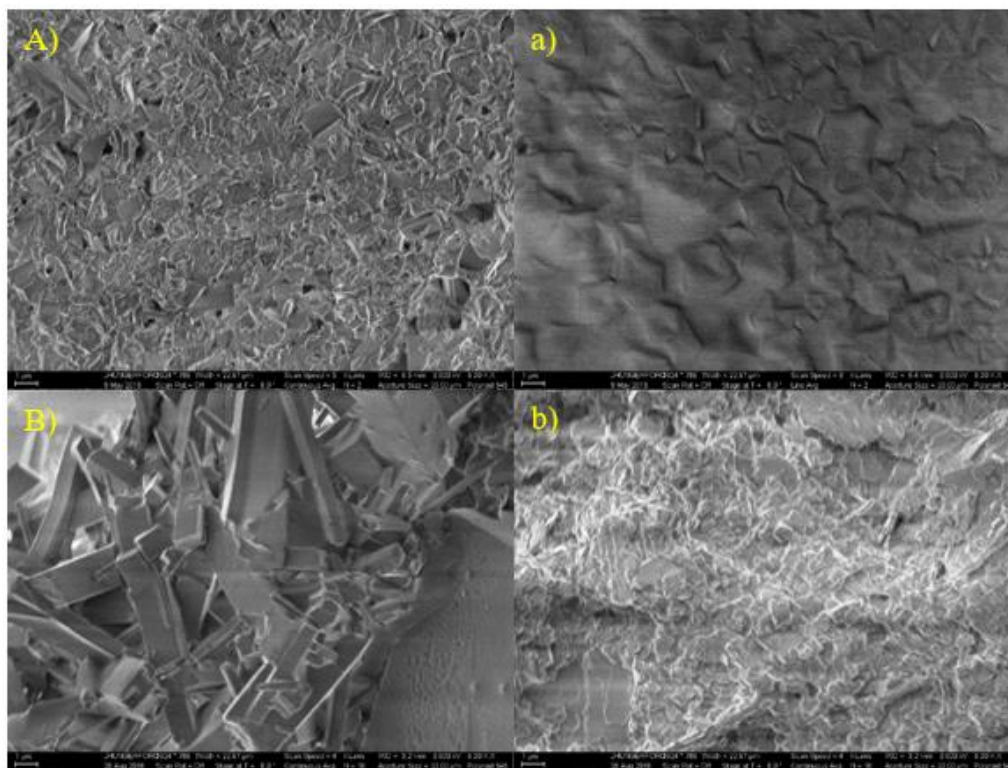


Figure E.12: SEM images of Zn-DMOF-X materials taken before and after exposure to humid SO_2 . A) Zn-DMOF-TM before a) after B) Zn-DMOF-ADC before b) after

Figure E.13 shows pictures of the M-DMOF-TM ($M = \text{Co}, \text{Zn}, \text{Ni}, \text{Cu}$) samples pre exposure to humid SO_2 as well as post exposure, and reactivated samples after exposure to humid SO_2 . The Zn, Ni, and Cu-DMOF-TM all have similar color and physical characteristics as the starting materials, whereas Co-DMOF-TM has undergone a change as is evident by the color change from dark blue to light purple.



Figure E.13: Pictures of Pre Exposed, Post Exposed, and Post Exposure Reactivated Samples of M-DMOF-TM for Humid SO_2 Exposure. Samples are Co, Zn, Ni, Cu from Left to Right.

E.7 Cobalt XPS Data

A large color change was observed in the observed in the Co-DMOF-TM pre and post humid SO_2 exposed samples and a Thermo K-Alpha X-ray photoelectron spectrometer was utilized to detect the incorporation of sulfur into the structure of the material. Figure E.14 shows the location of an S2p peak located at a binding energy of roughly 170 eV.

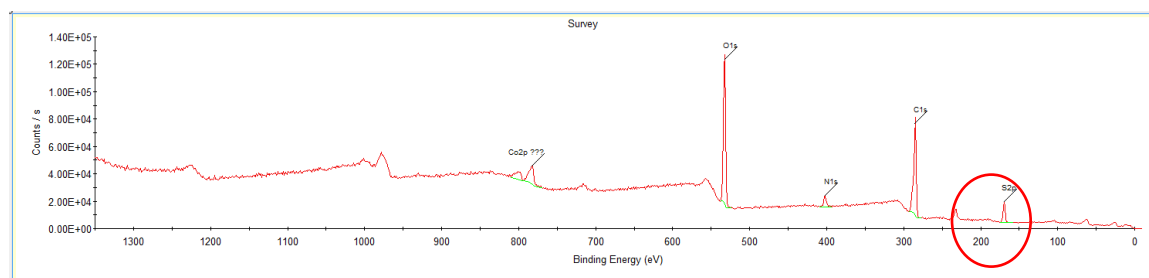


Figure E.14: XPS survey scan of Co-DMOF-TM after 5-day humid SO_2 exposure

E.8 Nitrogen Physisorption Data

The nitrogen physisorption isotherms that were collected for all of the samples (Zn-DMOF-X and M-DMOF-TM) are shown in Figures E.15 – E.21.

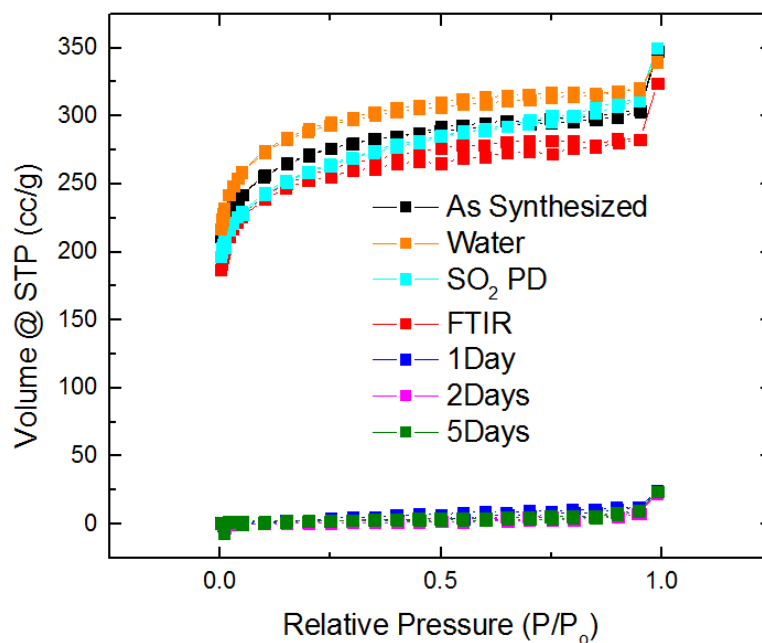


Figure E.15: Nitrogen Physisorption Isotherm of Zn-DMOF-TM collected for as synthesized, water adsorbed, SO₂ pressure decay, FTIR, and 50, 100, and 250 ppm-days humid SO₂ exposed samples

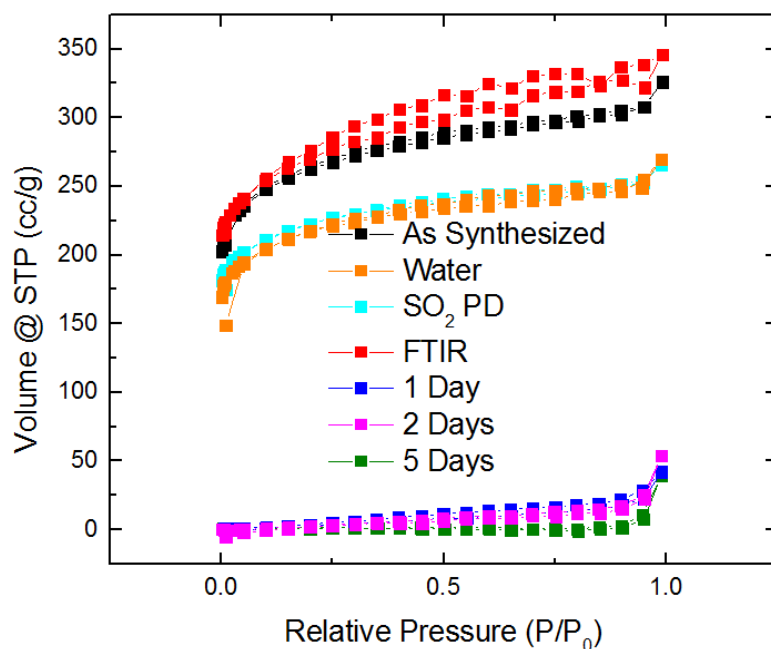


Figure E.16: Nitrogen Physisorption Isotherm of Co-DMOF-TM collected for as synthesized, water adsorbed, SO₂ pressure decay, FTIR, and 50, 100, and 250 ppm-days humid SO₂ exposed samples

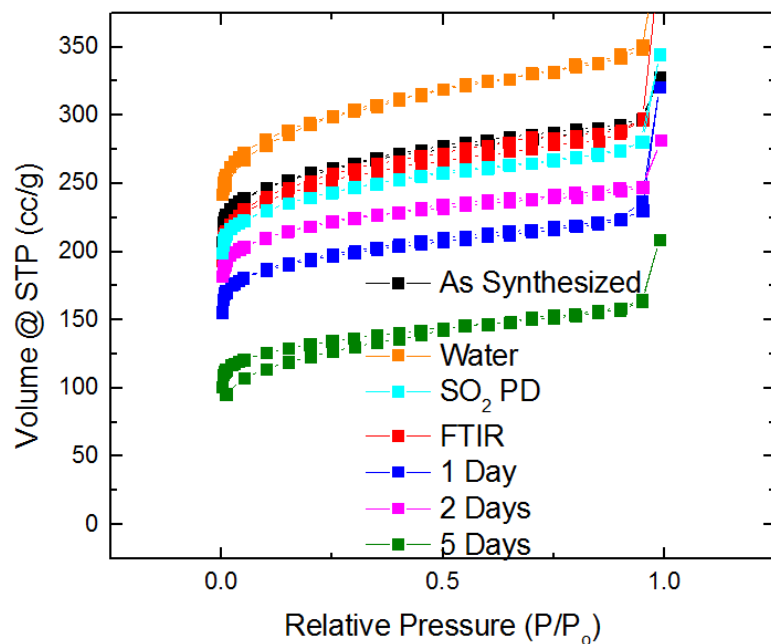


Figure E.17: Nitrogen Physisorption Isotherm of Cu-DMOF-TM collected for as synthesized, water adsorbed, SO₂ pressure decay, FTIR, and 50, 100, and 250 ppm-days humid SO₂ exposed samples

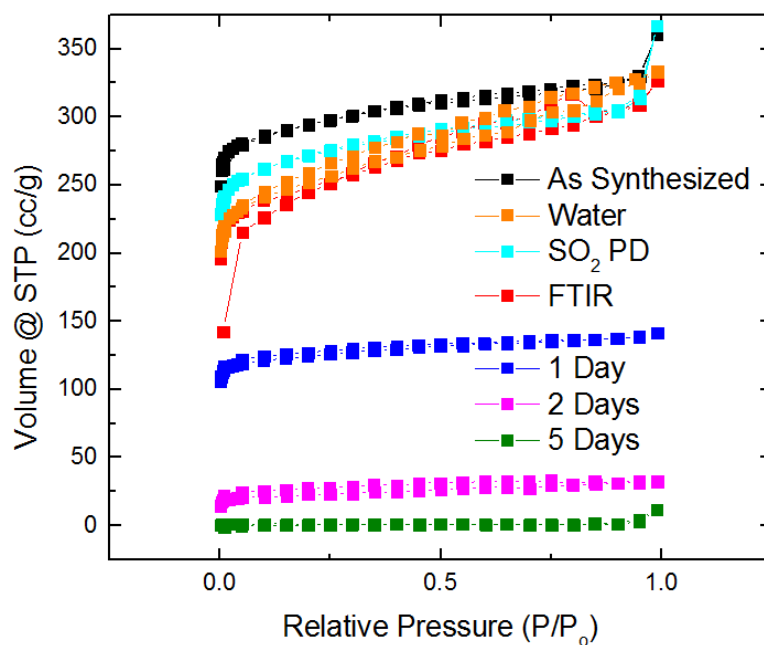


Figure E.18: Nitrogen Physisorption Isotherm of Ni-DMOF-TM collected for as synthesized, water adsorbed, SO₂ pressure decay, FTIR, and 50, 100, and 250 ppm-days humid SO₂ exposed samples

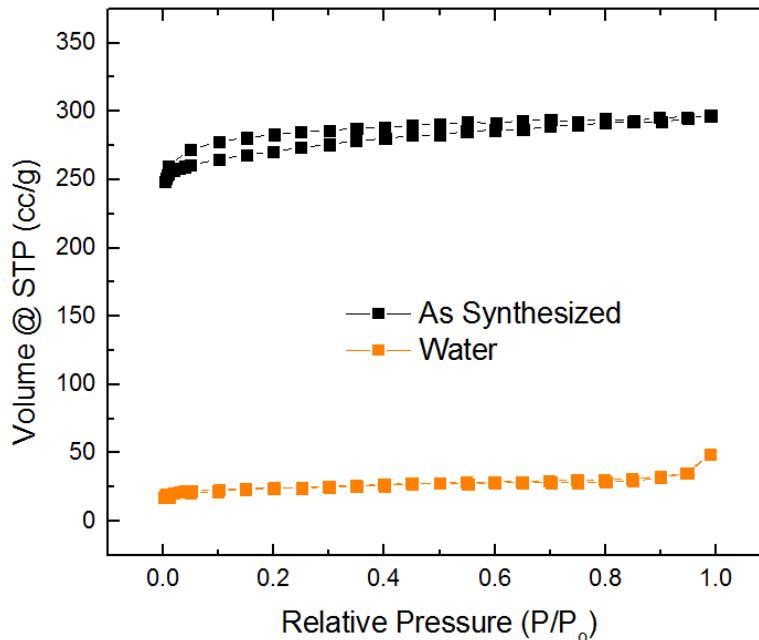


Figure E.19: Nitrogen Physisorption Isotherm of Zn-DMOF-DM collected for as synthesized and water adsorbed samples

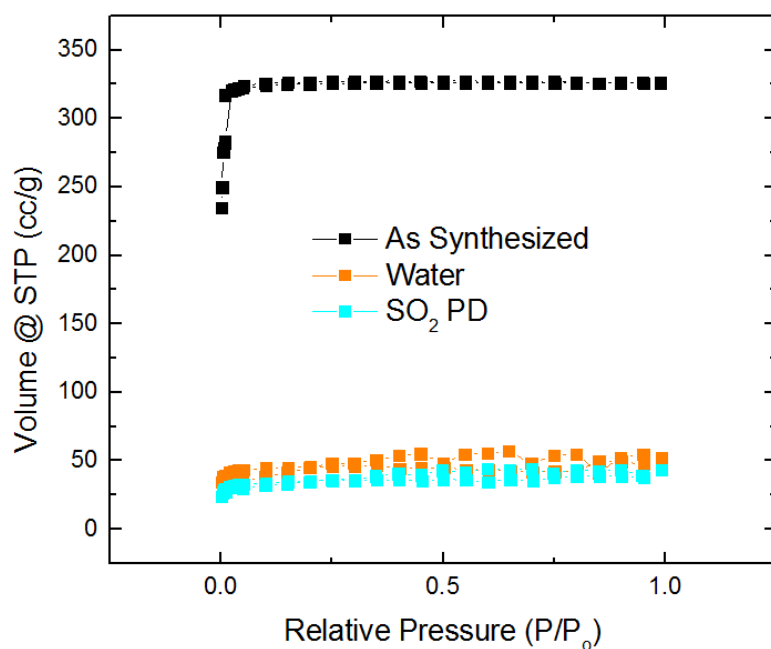


Figure E.20: Nitrogen Physisorption Isotherm of Zn-DMOF-NDC collected for as synthesized, water adsorbed, and SO₂ pressure decay samples

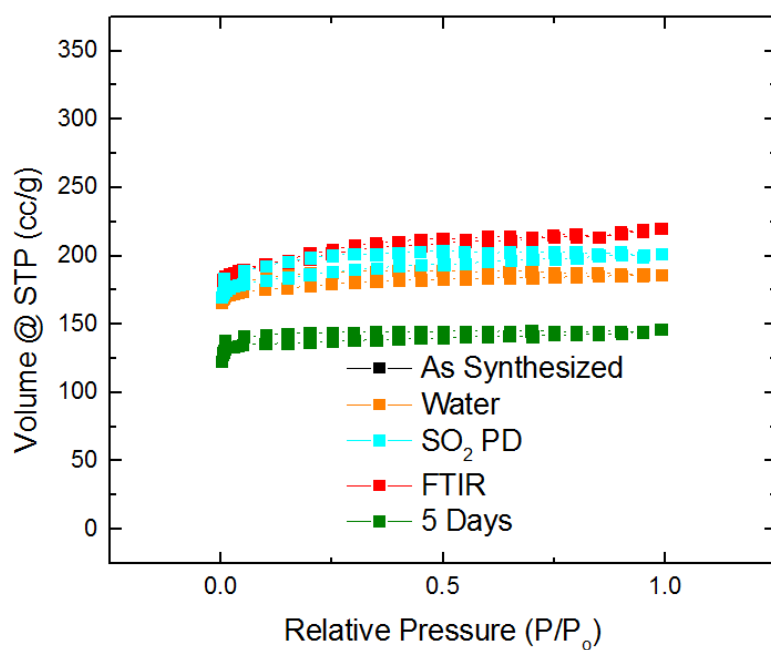


Figure E.21: Nitrogen Physisorption Isotherm of Zn-DMOF-ADC collected for as synthesized, water adsorbed, SO₂ pressure decay, FTIR, and 250 ppm-days humid SO₂ exposed samples

E.9 Previous Water and SO₂ Adsorption Studies

The water adsorption isotherms from Jasuja et. al. (Figure E.22A) show a small irreversible water uptake and degradation of the initial DMOF structure (black triangles).² Figure E.22B displays the SO₂ adsorption isotherms for Zn-DMOF and Ni-DMOF from Tan et. al.³ The authors' noted that the discrepancy between the metal centers is likely the result of stability differences between the zinc and nickel metal centers. These experiments were not repeated and added to this study as there was concern with regards to the materials stability.

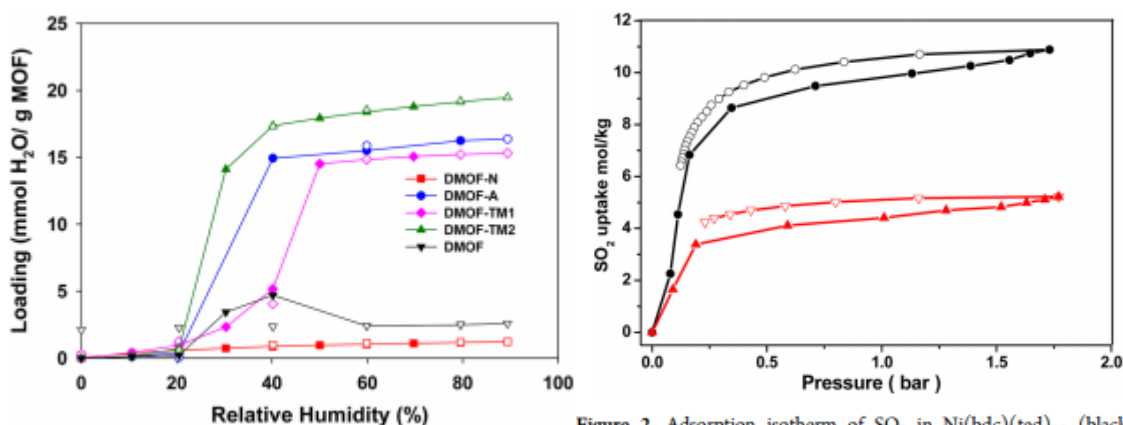


Figure 2. Adsorption isotherm of SO₂ in Ni(bdc)(ted)_{0.5} (black), Zn(bdc)(ted)_{0.5} (red) at room temperature for pressures up to ~1.8 bar. Solid symbol: adsorption. Empty symbol: desorption.

Figure E.22: A) Water adsorption data for DMOF. (Reproduced from 2. Copyright 2012 American Chemical Society) B) SO₂ adsorption data for Ni-DMOF and Zn-DMOF. (Reproduced from 3. Copyright 2013 American Chemical Society)

E.10 References

- [1] Dybtsev, D.; Chun, H.; Kim, K. Rigid and Flexible: A Highly Porous Metal-organic Framework with Unusual Guest-dependent Dynamic Behavior. *Angew. Chem.* **2004**, 116, 5143-5146.
- [2] Jasuja, H.; Huang, Y.; Walton, K. Adjusting the Stability of Metal-organic Frameworks Under Humid Conditions by Ligand Functionalization. *Langmuir* **2012**, 28(49), 16874-16880.

- [3] Tan, K.; Canepa, P.; Gong, Q.; Liu, J.; Johnson, D.; Dyevoich, A.; Thallapally, P.; Thonhauser, T.; Li, J.; Chabal, Y. Mechanism of Preferential Adsorption of SO₂ into Two Microporous Paddle Wheel Frameworks M(bdc)(ted)_{0.5}. *Chem. Mater.* **2013**, 25, 4653-4662.

APPENDIX F: THE FEASIBILITY OF CU-BTC AS AN ADSORBENT FOR ACID GASES: H₂S, SO₂, AND NO₂

F.1 Materials and Crystal Structure

Figure F.1 shows the crystal structure of Cu-BTC as well as the linker used in its synthesis (trimesic acid)

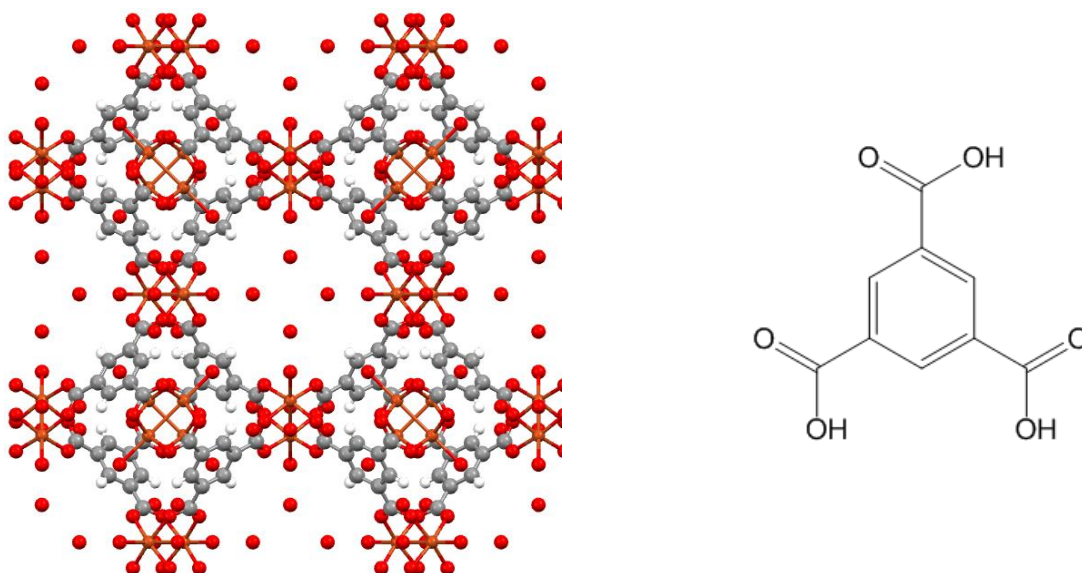


Figure F.1: Crystal structure of Cu-BTC (Left) and Trimesic acid (right)

F.2 Brunauer-Emmett-Teller (BET) Surface Area Analysis

Nitrogen physisorption isotherms were collected using a Quadrasorb instrument from Quantichrome. The surface area of the materials was determined using the Brunauer-Emmett-Teller (BET) method. Figure F.2 shows the nitrogen physisorption isotherms for

the following samples: pristine Cu-BTC, NO₂, SO₂, and H₂S exposed Cu-BTC, and SO₂ pressure decay and breakthrough experiments.

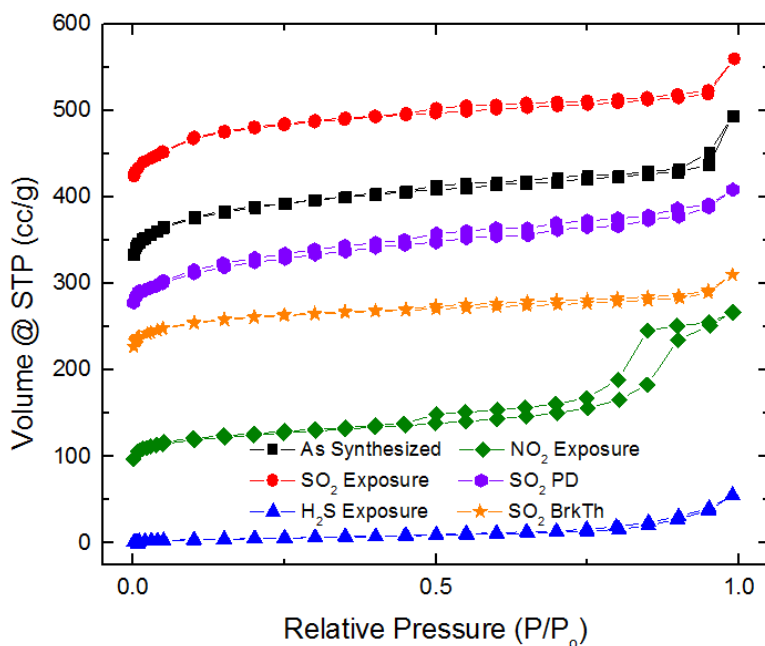


Figure F.2: Nitrogen physisorption isotherms of Cu-BTC samples after acid gas testing

F.3 Breakthrough Experiment

SO₂ breakthrough was collected using a lab-built system. The outlet of the breakthrough system is directed into an OMNI^{Star} mass spectrometer from Pfeiffer Vacuum which measures the outlet concentration of the system. A sample of Cu-BTC was first loaded into the system and activated under nitrogen flow at 150 °C. After activation, the flow was switched to 1000 ppm SO₂ in nitrogen and passed through the system. Breakthrough capacity was determined when the measured SO₂ concentration reached 1000 ppm. Figure F.3 shows the breakthrough curve for Cu-BTC. The breakthrough capacity of Cu-BTC in SO₂ was 0.45 mmol/g MOF.

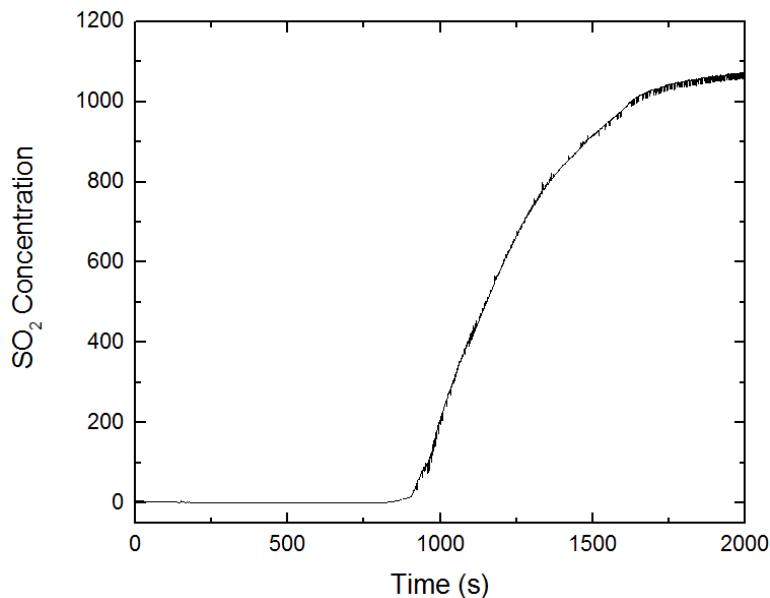


Figure F.3: Cu-BTC breakthrough curve for 1000 ppm SO₂ in nitrogen (Capacity: 0.45 mmol/g MOF)

F.4 X-ray Photoelectron Spectroscopy (XPS)

A Thermo K-Alpha XPS was used to assess the degradation of the Cu-BTC materials after exposure to H₂S, SO₂, and NO₂. Figure F.4 shows the XPS spectra of pristine Cu-BTC. In Figure F.4 we see the absence of any sulfur or nitrogen containing species, as was expected of a pristine sample. Figure F.5 shows the XPS spectra for the SO₂ exposed Cu-BTC. We observe a small peak in the S2p spectra at 169 eV which signifies the presence of sulfur in the sample. Prior to the collection of XPS spectra, the samples were subject to reactivation under vacuum and heating to 150 °C. During XPS collection, samples were further subject to ultra-high vacuum, thus the presence of SO₂ in the spectra infers that sulfur binds strongly to the framework. This bound sulfur is likely the reason for the depression in the surface area of the material that was measured during

BET analysis. Figure F.6 shows the XPS spectra of NO₂ exposed Cu-BTC. In this sample we see nitrogen incorporated into the structure at 407 eV. Lastly, Figure F.7 shows the XPS spectra after H₂S exposure of Cu-BTC. Here we observe a very large peak at 163 eV and a smaller peak at 169 eV. The small peak at 169 eV is at the same binding energy as the SO₂ exposure sample and corresponds to the presence of sulfonic acid, whereas the peak at 163 eV is representative of copper sulfide species.¹ Unlike the SO₂ exposed sample, the H₂S exposed sample completely degraded as was seen in the loss in surface area and crystal structure of the material.

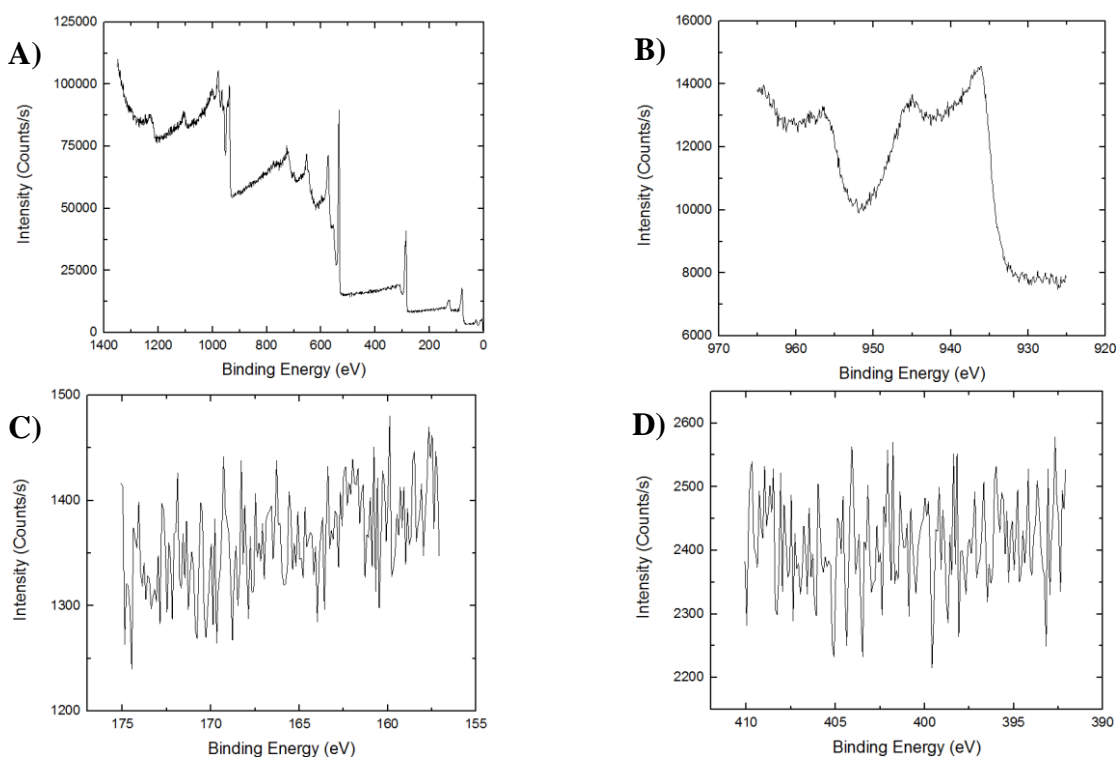


Figure F.4: XPS of Pristine Cu-BTC. A) survey scan B) Cu2p scan C) S2p scan D) N1s scan

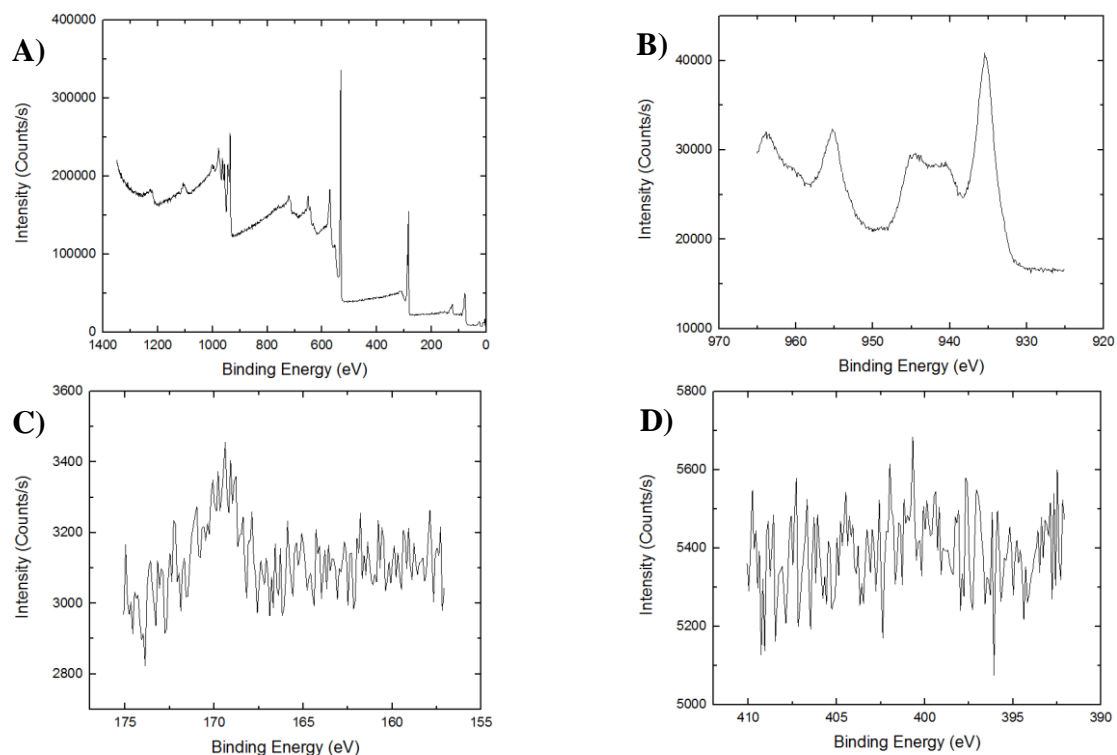


Figure F.5: XPS of SO₂ exposed Cu-BTC. A) survey scan B) Cu₂p scan C) S₂p scan D) N₁s scan

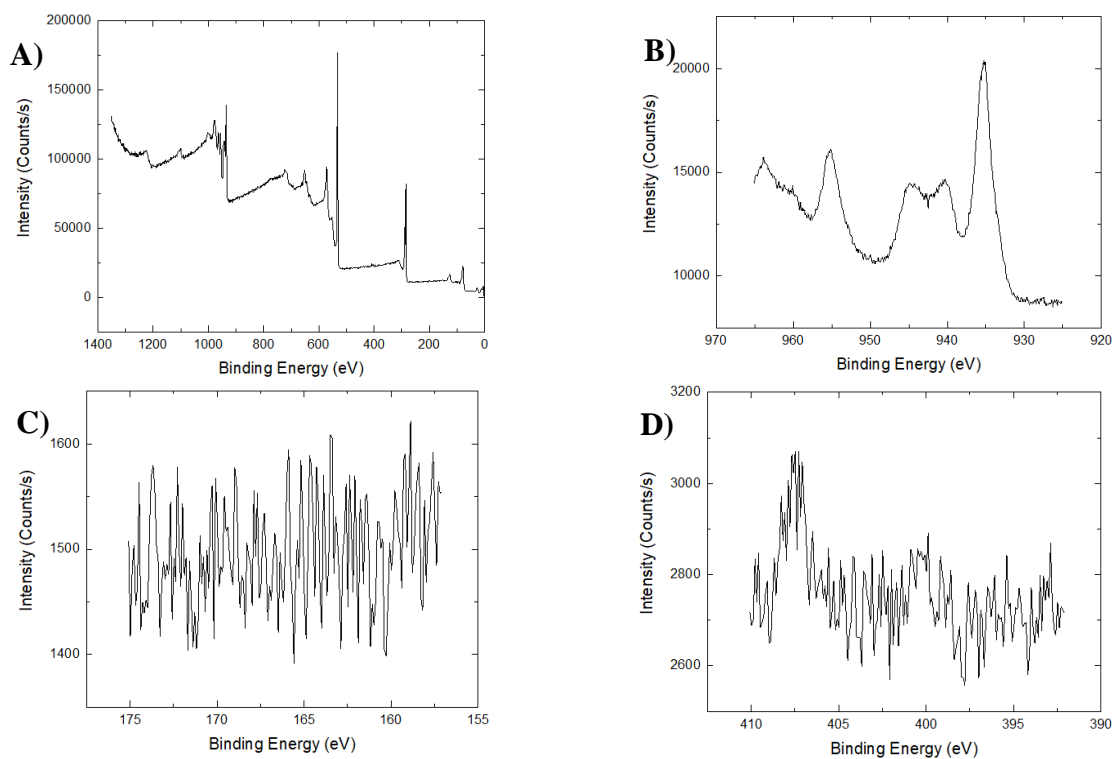


Figure F.6: XPS of NO₂ exposed Cu-BTC. A) survey scan B) Cu₂p scan C) S₂p scan D) N₁s scan

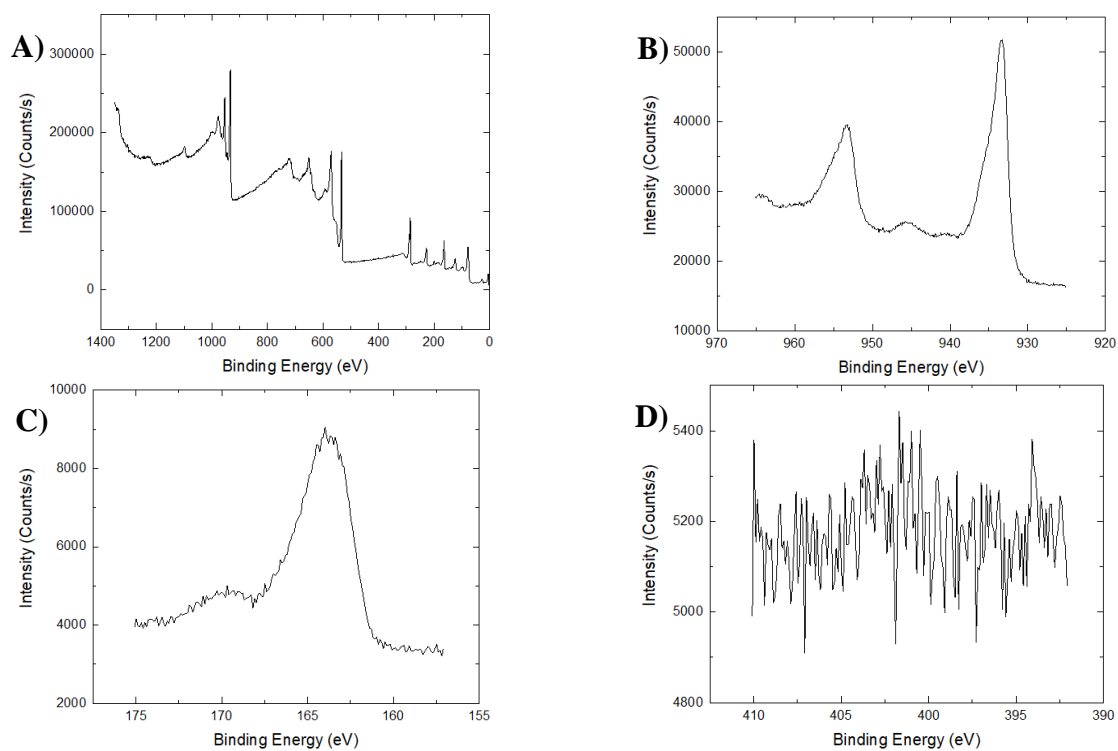


Figure F.7: XPS of H_2S exposed Cu-BTC. A) survey scan B) $\text{Cu}2\text{p}$ scan C) $\text{S}2\text{p}$ scan D) $\text{N}1\text{s}$ scan

F.5 References

- [1] Thermo Scientific XPS. Sulfur. <https://xpssimplified.com/elements/sulfur.php>. (Accessed 3/22/2019)

APPENDIX G: IMPACT OF METAL-ORGANIC FRAMEWORK SYNTHESIS PROCEDURE ON ADSORPTION PERFORMANCE: ROOM TEMPERATURE VERSUS SOLVOTHERMAL

G.1 Materials and Crystal Structure

DMOF-TM, UiO-66, and ZIF-8 were synthesized both solvothermally and via room temperature synthesis methods. The ligands used in the synthesis of these materials is shown in Figure G.1 (DMOF-TM is a pillared MOF containing 2,3,5,6-tetramethylterephthalic acid (TMBCD) and 1,4-diazabicyclo[2.2.2]octane (DABCO), UiO-66 contains the terephthalic acid (BDC) ligand, and ZIF-8 contains the 2-methylimidazole ligand). The structures of the synthesized MOFs are shown in Figure G.2.

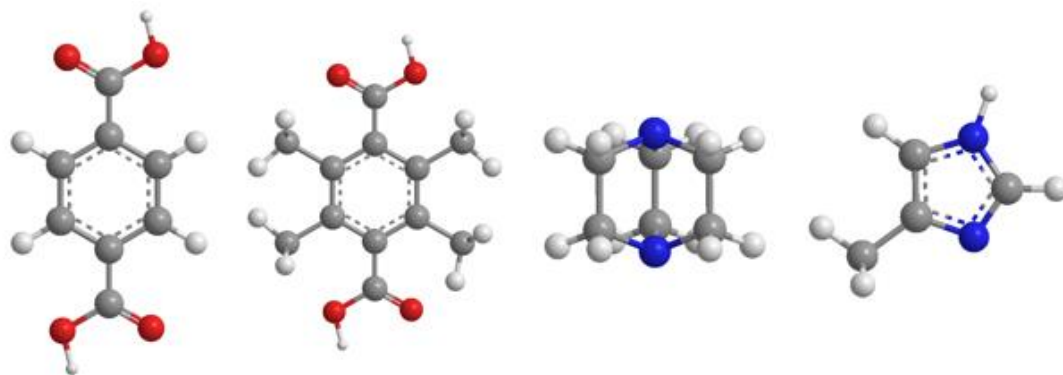


Figure G.1: Ligands used in MOF synthesis from left to right: BDC, TMBC, DABCO, 2-methylimidazole

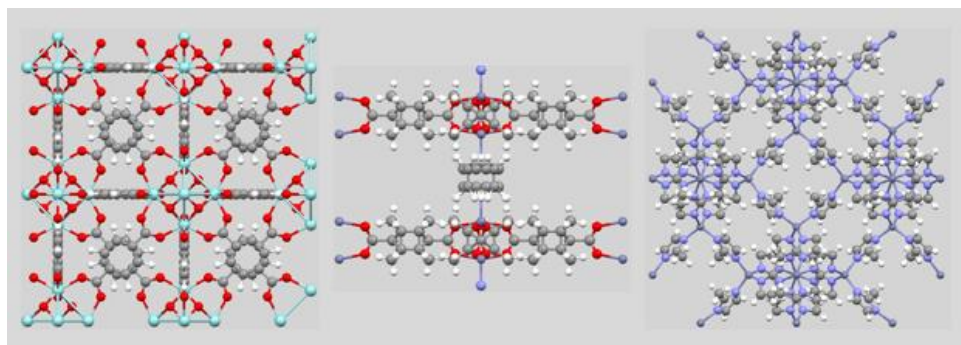


Figure G.2: Structures of UiO-66 (left),¹ DMOF-TM (center),² and ZIF-8 (right)³

G.2 Brunauer-Emmett-Teller (BET) Surface Area Analysis

Nitrogen physisorption measurements were taken to determine the pore volumes and surface areas of the synthesized MOF materials using the BET method. Figure G.3 shows the nitrogen physisorption isotherms for the as synthesized UiO-66, DMOF-TM, and ZIF-8 samples presented in the main text of the manuscript. Table G.1 shows the BET surface areas and pore volumes of the materials after acid gas testing (SO_2 pressure decay, SO_2 breakthrough, and H_2S breakthrough experiments). Figures G.4 – G.6 show the nitrogen physisorption isotherms for the samples from Table G.1.

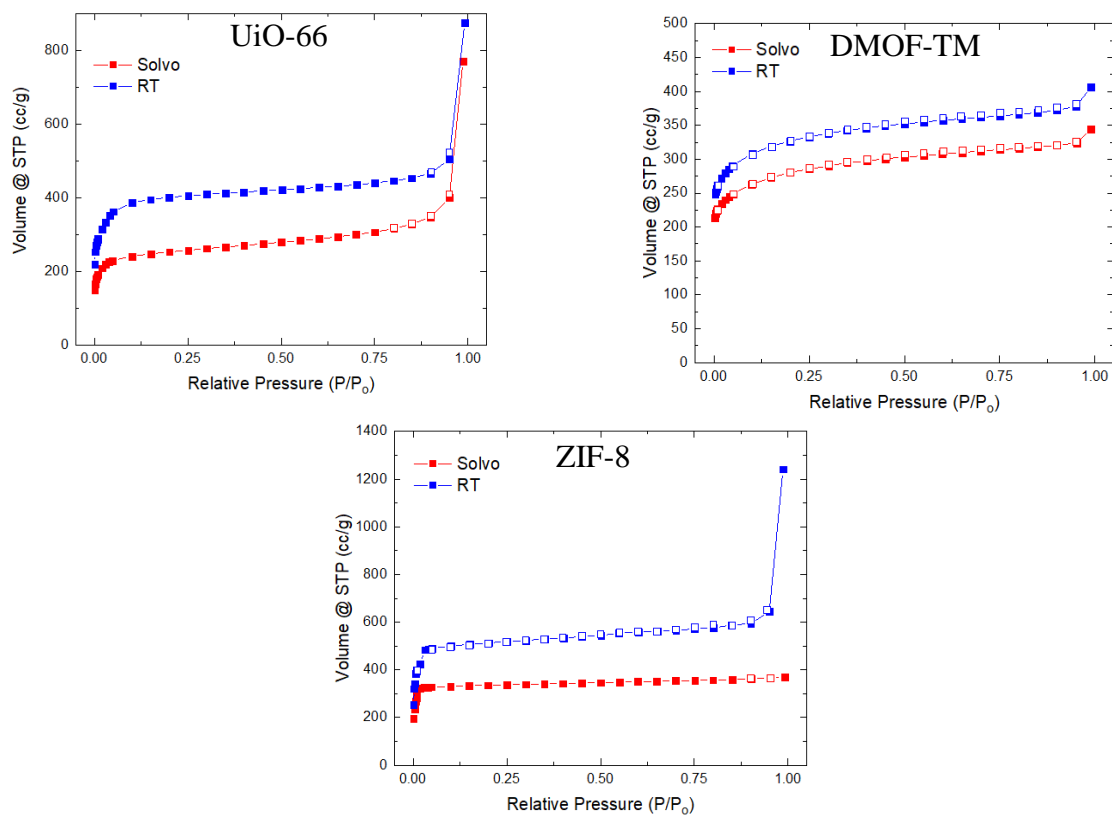


Figure G.3: Nitrogen physisorption isotherms of UiO-66, DMOF-TM, and ZIF-8 synthesized solvothermally and at room temperature corresponding to the BET surface areas reported in the main text

Table G.1: BET surface areas and pore volumes of UiO-66, DMOF-TM, and ZIF-8 synthesized solvothermally and at room temperature for samples after SO₂ pressure decay, SO₂ breakthrough, and H₂S breakthrough analysis.

Sample	BET SA (m ² /g)	Pore Volume (cm ³ /g)
UiO-66-Solvo		
SO ₂ Pressure Decay	1052	0.57
SO ₂ Breakthrough	734	0.34
H ₂ S Breakthrough	918	0.41
H ₂ O Adsorption	942	0.41
UiO-66-RT		
SO ₂ Pressure Decay	535	0.26
SO ₂ Breakthrough	1199	0.53
H ₂ S Breakthrough	1241	0.53
H ₂ O Adsorption	980	0.45
DMOF-TM-Solvo		
SO ₂ Pressure Decay	948	0.46
SO ₂ Breakthrough	998	0.46
H ₂ S Breakthrough	961	0.53
H ₂ O Adsorption	951	0.46
DMOF-TM-RT		
SO ₂ Pressure Decay	1142	0.54
SO ₂ Breakthrough	1344	0.67
H ₂ S Breakthrough	898	0.40
H ₂ O Adsorption	951	0.46
ZIF-8-Solvo		
SO ₂ Pressure Decay	948	0.46
SO ₂ Breakthrough	1059	0.43
H ₂ S Breakthrough	1553	0.57
H ₂ O Adsorption	1084	0.85
ZIF-8-RT		
SO ₂ Pressure Decay	1149	0.53
SO ₂ Breakthrough	1398	0.57
H ₂ S Breakthrough	1058	0.45
H ₂ O Adsorption	1323	0.60

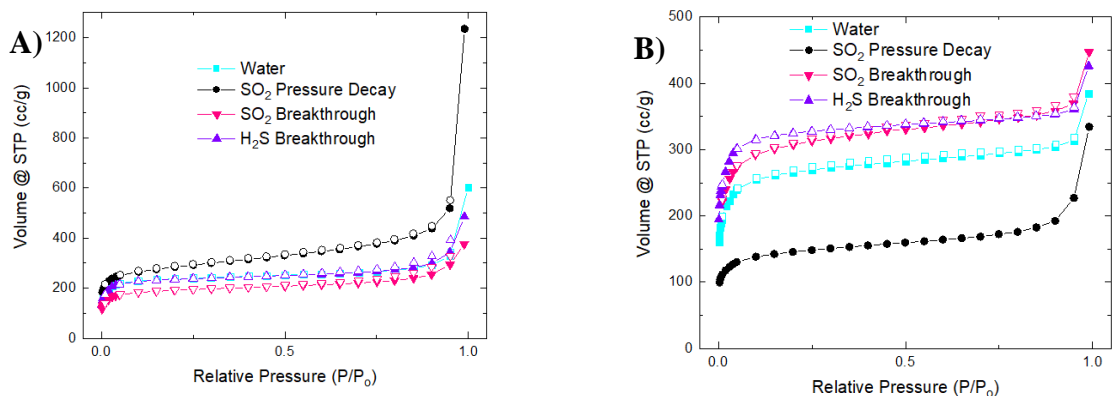


Figure G.4: Nitrogen physisorption isotherms of UiO-66 synthesized A) solvothermally and B) at room temperature after SO_2 pressure decay, SO_2 breakthrough, H_2S breakthrough, and H_2O adsorption experiments.

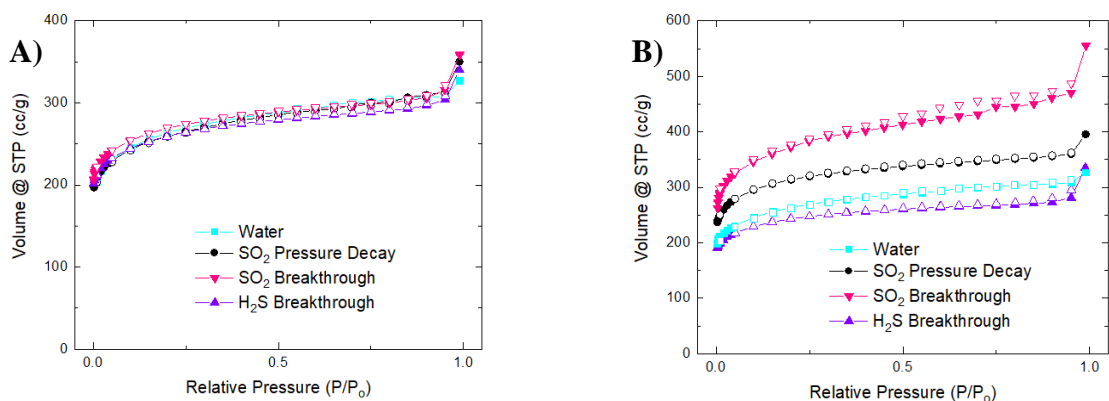


Figure G.5: Nitrogen physisorption isotherms of DMOF-TM synthesized A) solvothermally and B) at room temperature after SO_2 pressure decay, SO_2 breakthrough, H_2S breakthrough, and H_2O adsorption experiments.

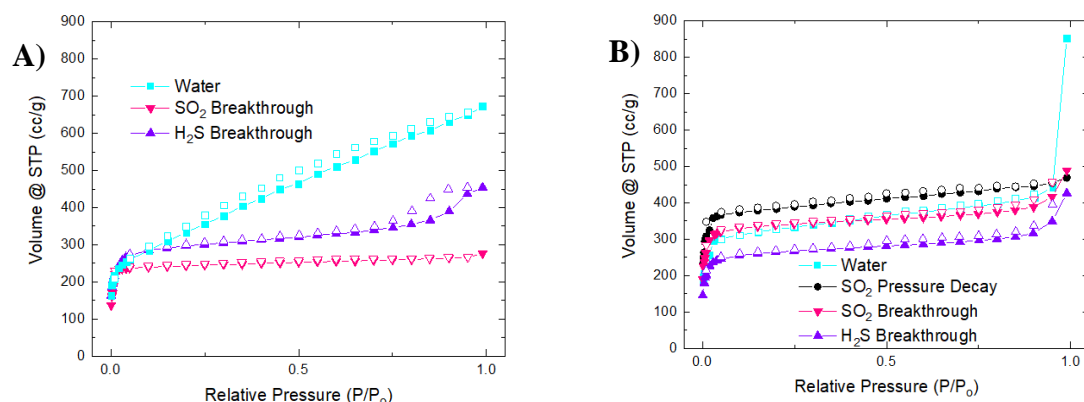


Figure G.6: Nitrogen physisorption isotherms of ZIF-8 synthesized A) solvothermally and B) at room temperature after SO₂ pressure decay, SO₂ breakthrough, H₂S breakthrough, and H₂O adsorption experiments.

G.3 Powder X-ray Diffraction (PXRD)

PXRD patterns of the as synthesized UiO-66, DMOF-TM, and ZIF-8 can be found in the main text (both room temperature and solvothermal synthesis). The PXRD patterns of the post SO₂ pressure decay, SO₂ breakthrough, and H₂S breakthrough samples are shown in Figures G.7 – G.9.

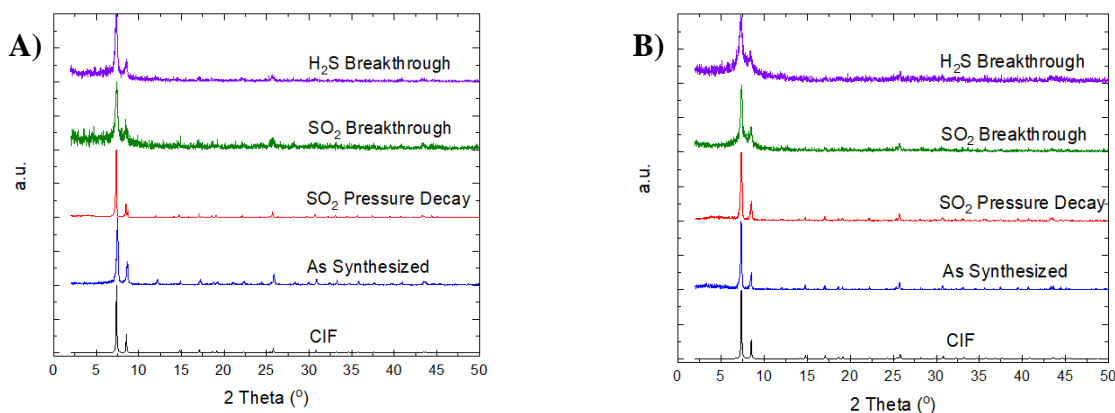


Figure G.7: PXRD patterns of UiO-66 synthesized A) solvothermally and B) at room temperature (right) after SO₂ pressure decay, SO₂ breakthrough, and H₂S breakthrough experiments.

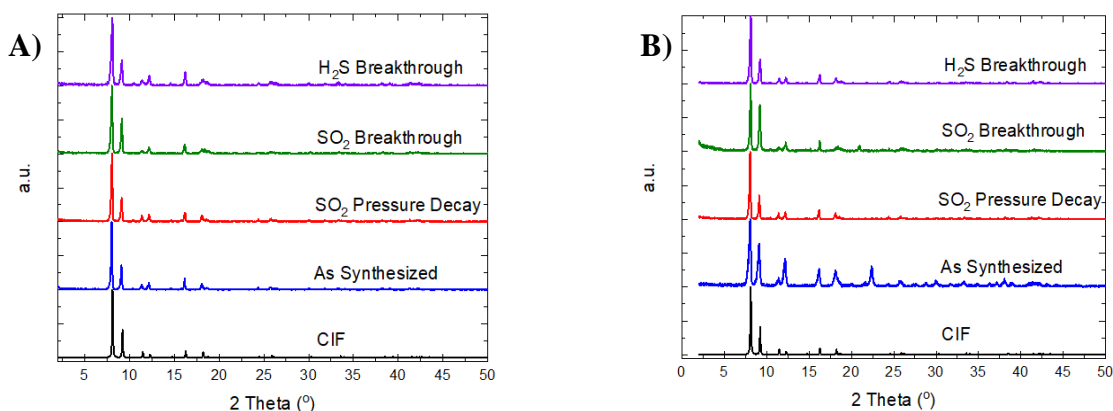


Figure F.8: PXRD patterns of DMOF-TM synthesized A) solvothermally and B) at room temperature after SO₂ pressure decay, SO₂ breakthrough, and H₂S breakthrough experiments.

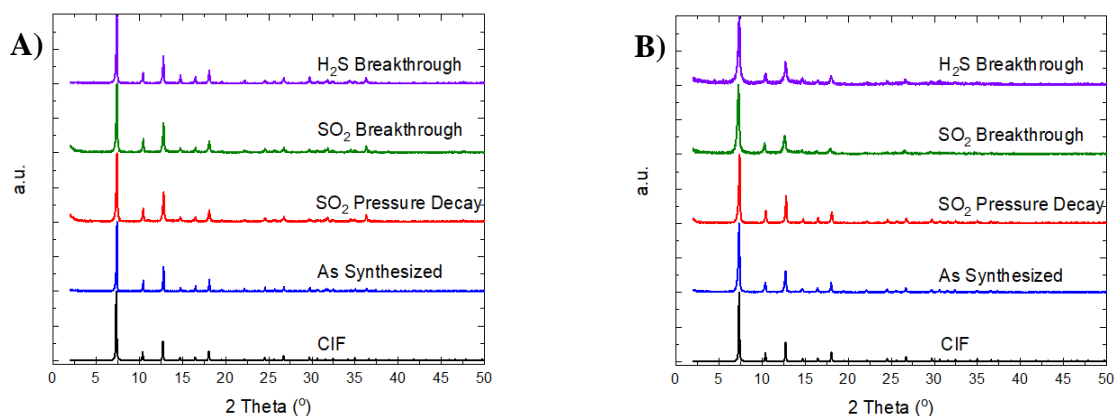


Figure G.9: PXRD patterns of ZIF-8 synthesized A) solvothermally and B) at room temperature after SO₂ pressure decay, SO₂ breakthrough, and H₂S breakthrough experiments.

G.4 Infrared Spectroscopy (IR)

The infrared spectra of UiO-66 (Figure G.10), DMOF-TM (Figures G.11 and G.12), and ZIF-8 (Figure G.13) synthesized solvothermally and at room temperature were collected in ATR mode. Prior to testing, the samples were activated at 150 °C overnight

under vacuum. The samples were then transferred to the IR for testing, during which time they may have adsorbed some water from the air.

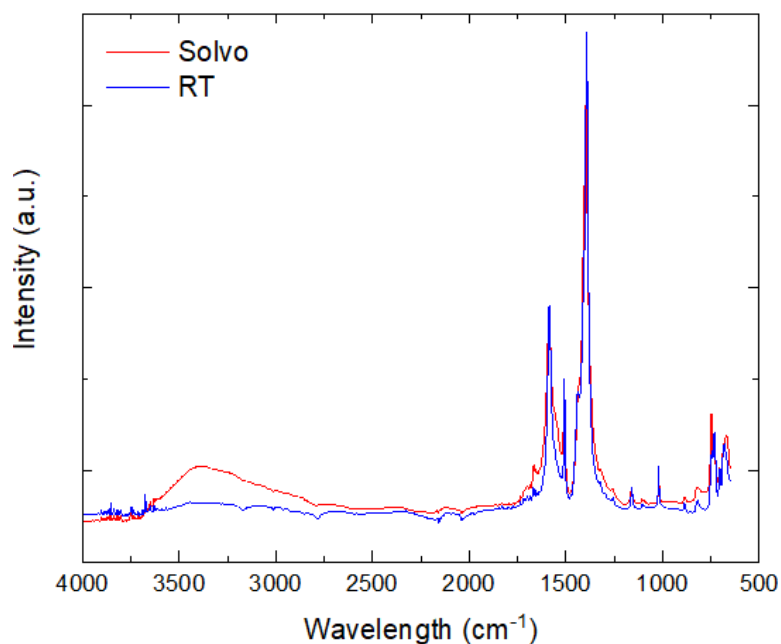


Figure G.10: IR spectra of UiO-66 synthesized solvothermally and at room temperature

Figure G.10 shows the IR spectra for room temperature and solvothermally synthesized UiO-66. The location of IR peaks match between the two samples, however it is evident that the solvothermally synthesized material contains a greater amount of adsorbed water. The two materials were activated overnight under vacuum prior to testing such that any adsorbed water should have been removed from the structure. It is possible that the materials adsorbed water during transport from activation to sample testing. Previously we discussed the water adsorption isotherms of UiO-66 and found that the solvothermally synthesized material was more hydrophilic than the room temperature synthesis material. The IR results are in agreement with the earlier water adsorption results, as the solvothermal material adsorbed more water. The lab thermometer constantly

monitors both temperature and humidity and at the time of testing the room temperature was 19 – 20 °C and the relative humidity was between 40 – 50 %.

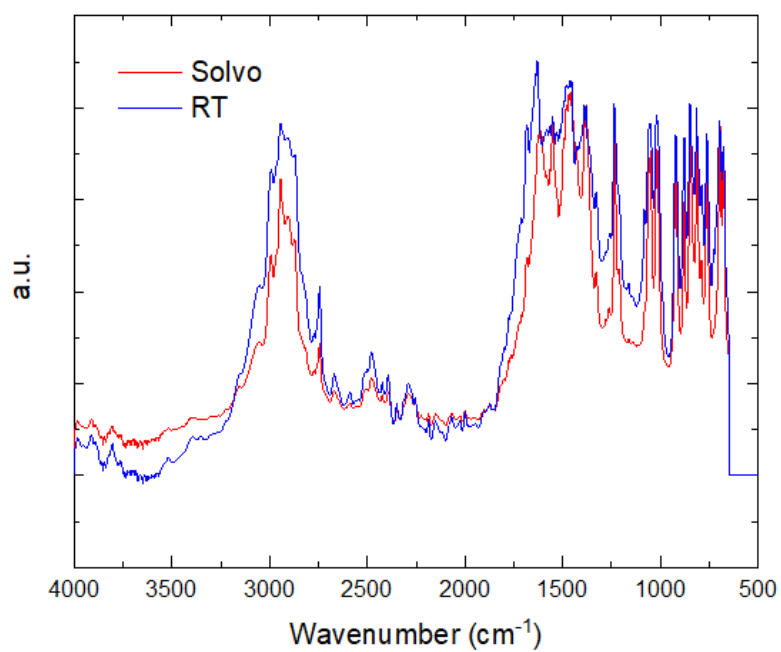


Figure G.11: IR spectra of DMOF-TM synthesized solvothermally and at room temperature

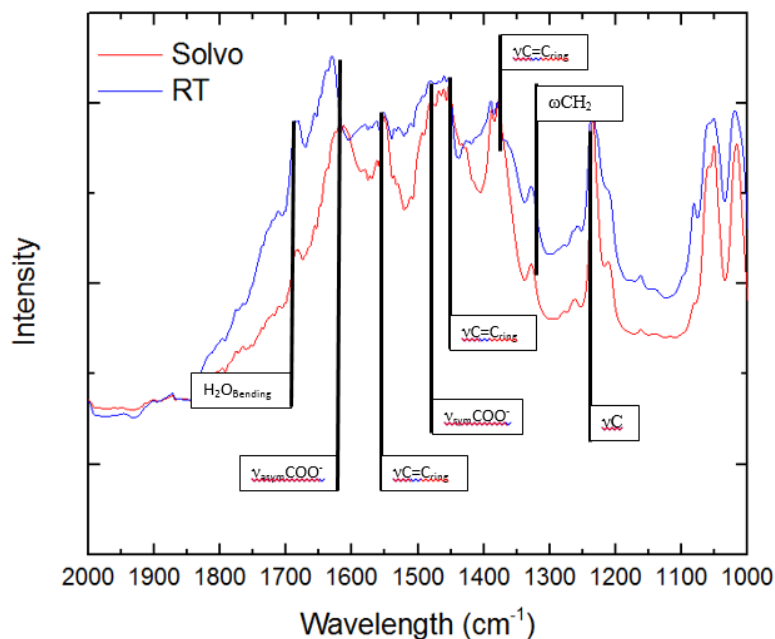


Figure G.12: IR drifts spectra of DMOF-TM synthesized solvothermally and at room temperature focusing on 1000 – 2000 cm^{-1}

Figures G.11 and G.12 show the spectra for DMOF-TM, the majority of peaks match between the two spectra, however there are a few subtle differences. In Figure G.12 we observe that the peak at ~ 1670 associated with a coordinated water molecules is higher for the room temperature synthesized material compared to the solvothermally synthesized one. Additionally, the peak associated with COO^- asymmetric vibrations is slightly left shifted in the room temperature material. Similar reports have also been shown previously by our group and we observed sample degradation over a period of several months when leaving room temperature synthesized DMOF-TM in the air.⁴

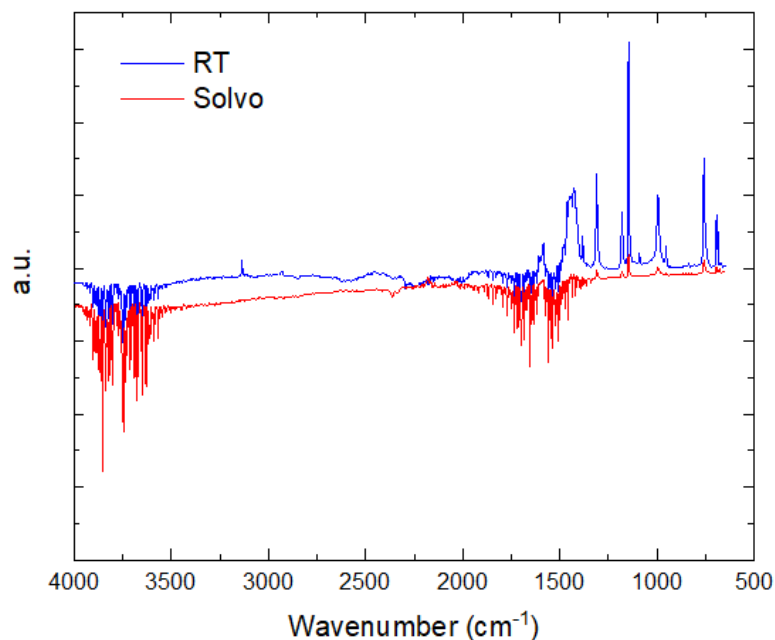


Figure G.13: IR spectra of ZIF-8 synthesized solvothermally and at room temperature

Figure G.13 shows the IR spectra for ZIF-8 synthesized solvothermally and at room temperature. Prior to testing, both samples were activated overnight under vacuum to remove any adsorbed water or solvent molecules. As these materials are highly hydrophobic, we did not expect them to adsorb much water while being transferred to the IR apparatus. We observed a broad set of peaks from $1380 - 1500 \text{ cm}^{-1}$ that all correspond to C-N stretching vibrations in the five-membered ring. We observe numerous C-H bending vibrations corresponding to the hydrogens in the five-member ring and CH_3 group in the range of $1000 - 1100 \text{ cm}^{-1}$ as well as the presence of C-H stretching at 3130 cm^{-1} .⁵ Overall, we observe consistent peak positions between the solvothermally and room temperatures synthesized sample.

G.5 Thermogravimetric Analysis (TGA)

TGA data was collected for UiO-66, DMOF-TM, and ZIF-8 synthesized both solvothermally and at room temperature, Figures G.14, G.15, and G.16 respectively. The temperature was ramped from 25 to 700 °C for all samples. The thermal stability of all materials was consistent between the room temperature and solvothermally synthesized samples. UiO-66 showed substantial mass loss beginning around 400 – 450 °C for both solvothermally and room temperature synthesized materials. Mass loss before 400 °C could be attributed to the loss of DMF that was trapped within the pore space of the MOF. DMOF-TM displayed thermal stability up to roughly 300 °C for both solvothermally and room temperature synthesized materials. Lastly, ZIF-8 began degrading around 400 °C for both solvothermally and room temperature synthesized samples. We observed a much greater mass loss in the room temperature synthesized ZIF-8 which may be a result of missing cluster defects and this offers an explanation as to why we observed a much larger surface area in this material compared to the solvothermally synthesized ZIF-8.

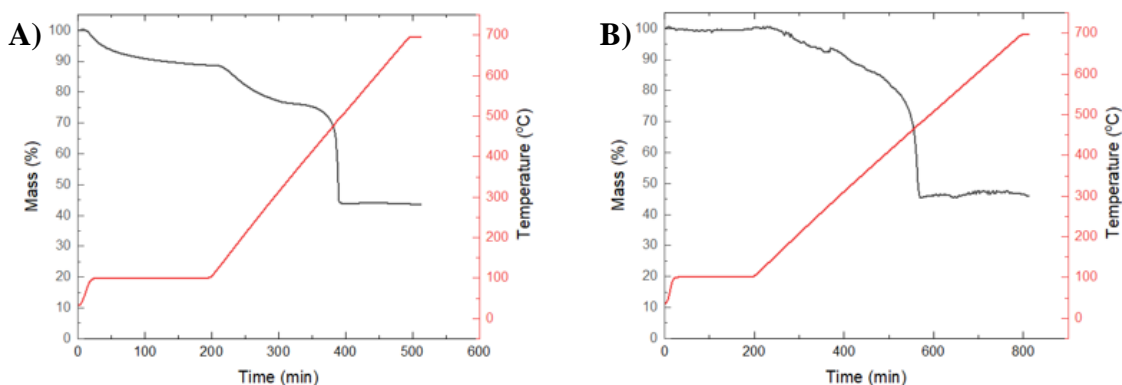


Figure G.14: TGA data for UiO-66 synthesized A) solvothermally and B) at room temperature

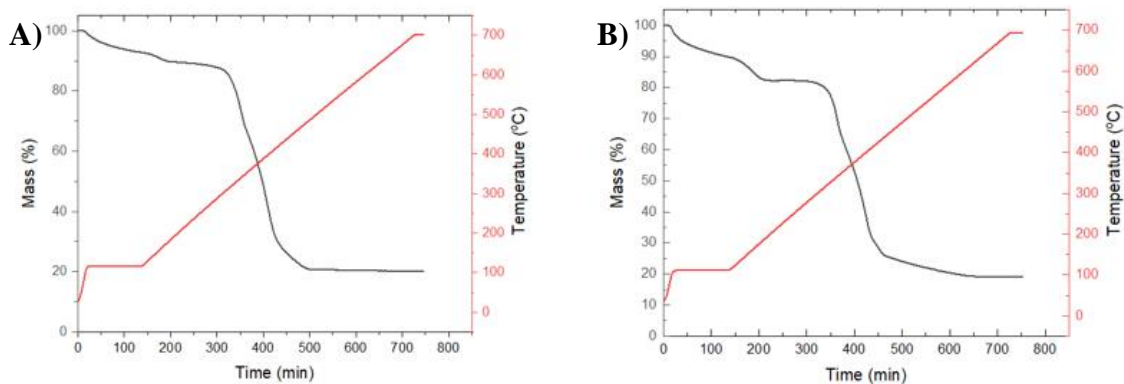


Figure G.15: TGA data for DMOF-TM synthesized A) solvothermally and B) at room temperature

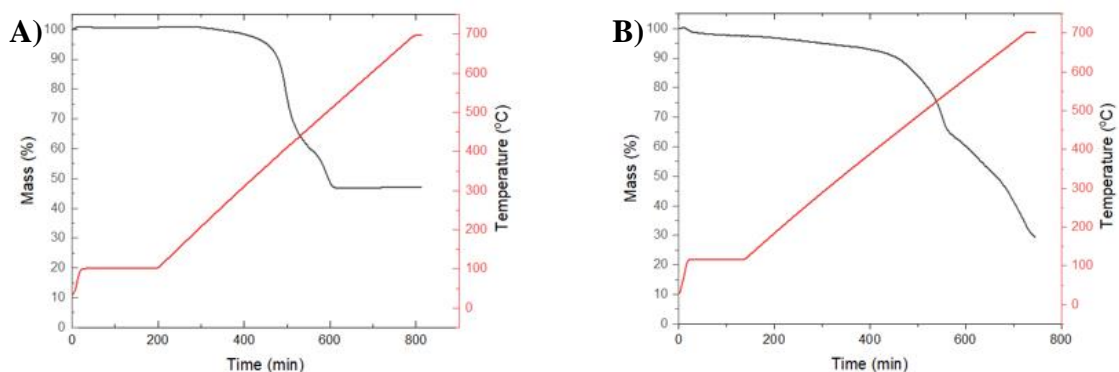


Figure G.16: TGA data for ZIF-8 synthesized A) solvothermally and B) at room temperature

G.6 H₂S Breakthrough

H₂S breakthrough was collected using 5000 ppm H₂S in nitrogen at a flowrate of 50 mL/min. Nitrogen was used as a tracer gas for determining the dead time of the breakthrough bed. Prior to breakthrough measurements, samples were sieved to size 400 microns and the sample was loaded into a quartz tube and activated in situ under helium flow at 150 °C for all MOF samples. After activation, the sample was cooled to 25 °C

before switching to H₂S in nitrogen flow. Breakthrough measurements were collected in 3 runs for each sample. Between breakthrough runs, the samples were re-activated at 100 °C in helium before cooling to 25 °C and beginning the next run. Figures G.17 – G.19 show the breakthrough curve for each sample run for the solvothermally and room temperature synthesized UiO-66, DMOF-TM, and ZIF-8 respectively. The complete H₂S breakthrough experiments for each sample, including desorption, are shown in Figures G.20 – G.22.

The H₂S and SO₂ breakthrough capacity of all samples tested in this study can be found in Table G.2 below.

Table G.2: H₂S (5000 ppm in nitrogen) and SO₂ (1000 ppm in nitrogen) breakthrough capacities (mmol/g) for UiO-66, DMOF-TM, and ZIF-8 synthesized solvothermally and at room temperature.

MOF	H ₂ S Breakthrough Capacity (mmol/g)			SO ₂ Breakthrough Capacity (mmol/g)		
	Run1	Run2	Run3	Run1	Run2	Run3
UiO-66						
Solvo	0.14	0.10	0.10	0.19	0.19	0.18
RT	0.35	0.18	0.15	0.24	0.24	0.21
DMOF-TM						
Solvo	0.42	0.28	0.25	0.90	0.80	0.76
RT	0.48	0.23	0.23	0.94	0.87	0.97
ZIF-8						
Solvo	0.17	0.10	0.09	0.26	0.11	0.08
RT	1.59	0.24	0.26	0.10	0.05	0.04

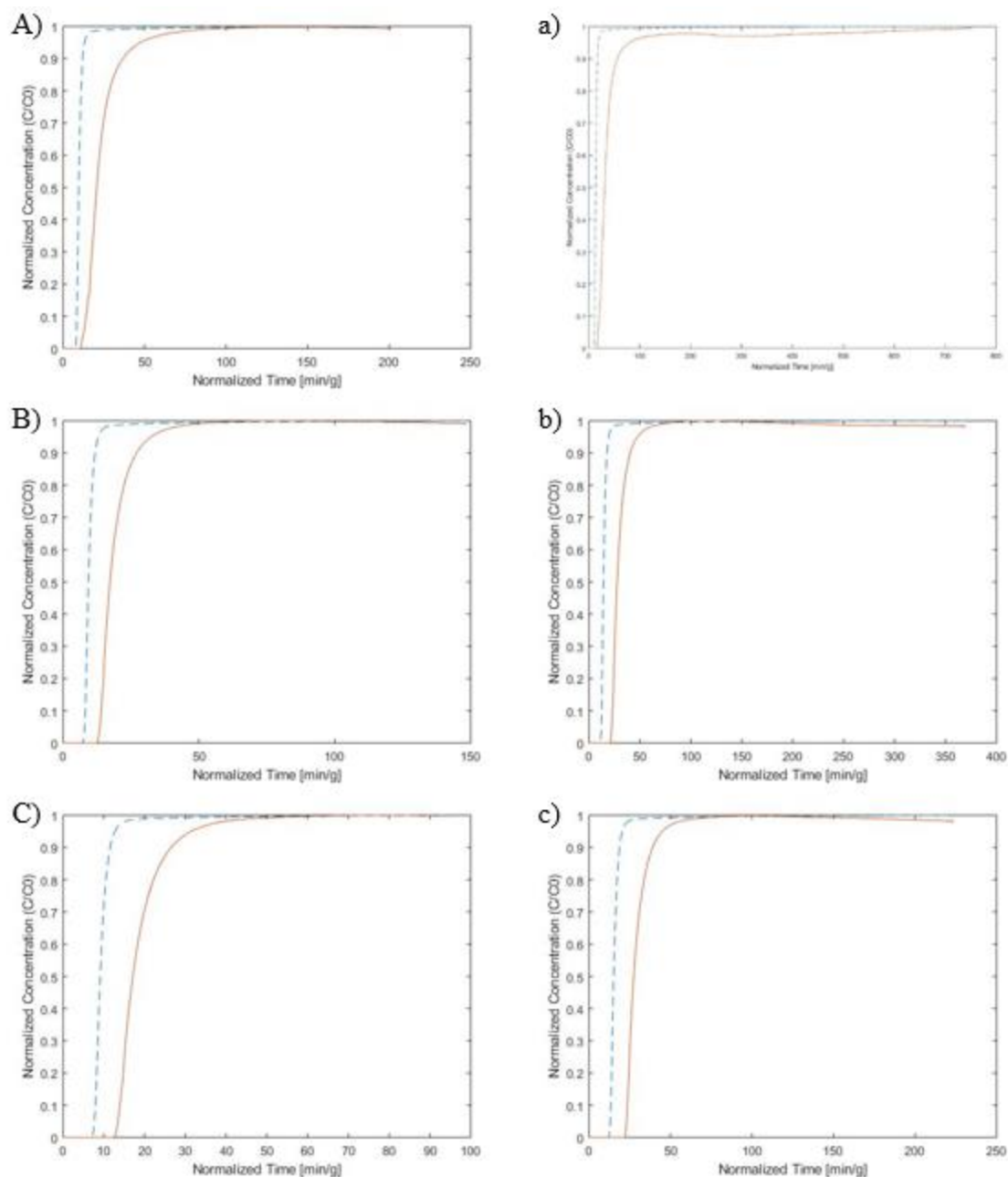


Figure G.17: H₂S breakthrough curves for solvothermally (upper case) and room temperature (lower case) synthesized UiO-66 A) Run 1 B) Run 2 C) Run 3. Solid orange line corresponds to H₂S concentration (C/C_0) and dotted blue line corresponds to the nitrogen concentration (C/C_0).

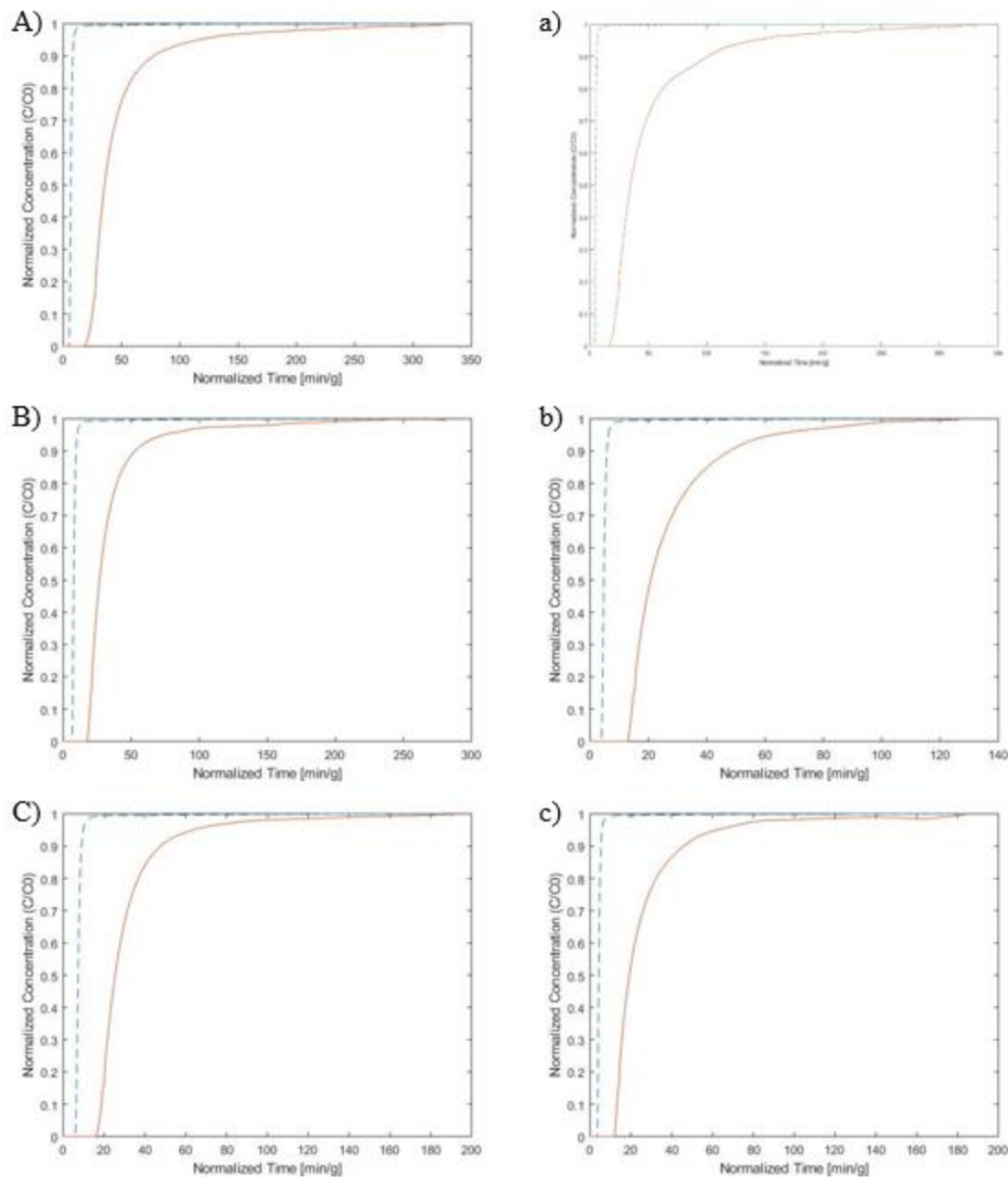


Figure G.18: H₂S breakthrough curves for solvothermally (upper case) and room temperature (lower case) synthesized DMOF-TM A) Run 1 B) Run 2 C) Run 3. Solid orange line corresponds to H₂S concentration (C/C_0) and dotted blue line corresponds to the nitrogen concentration (C/C_0).

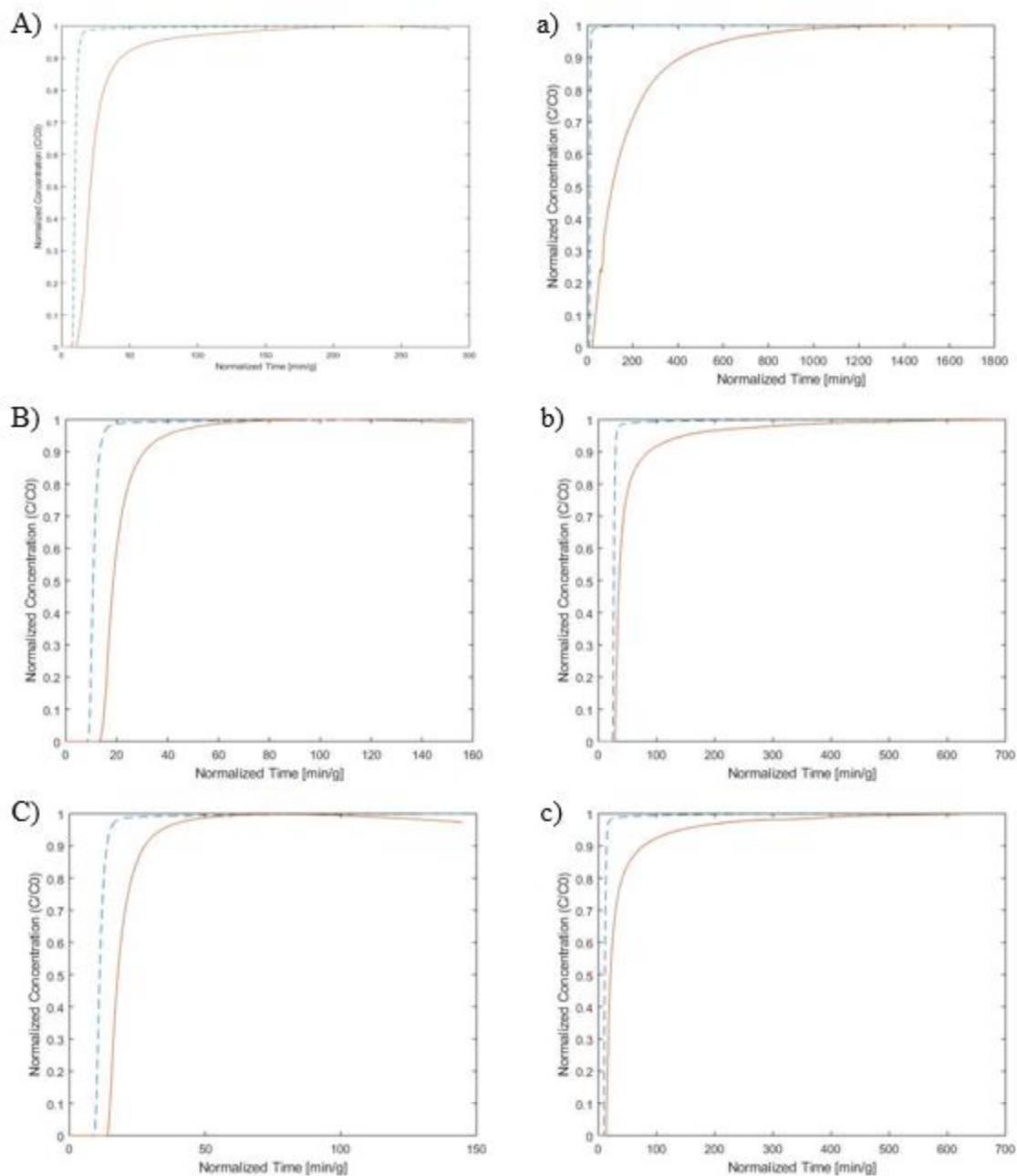


Figure G.19: H₂S breakthrough curves for solvothermally (upper case) and room temperature (lower case) synthesized ZIF-8 A) Run 1 B) Run 2 C) Run 3. Solid orange line corresponds to H₂S concentration (C/C_0) and dotted blue line corresponds to the nitrogen concentration (C/C_0).

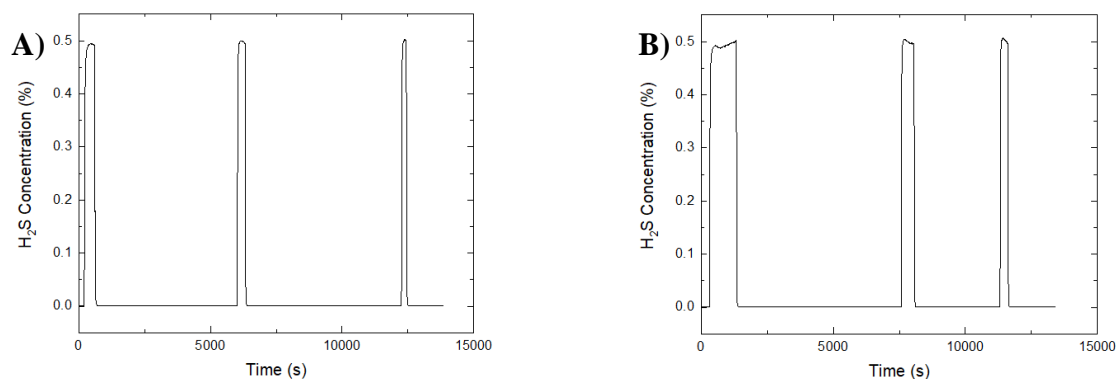


Figure G.20: Complete H₂S breakthrough curve for A) solvothermally and B) room synthesized UiO-66

Figure G.20 shows the complete breakthrough curves for UiO-66 synthesized solvothermally and at room temperature. Interestingly we observe no desorption of H₂S upon reactivation of the sample, all H₂S that was desorbed required only helium flow. The breakthrough capacity between runs 1 and 2 decreased and then remained roughly constant between runs 2 and 3 for both the solvothermally and room temperature synthesized materials. We believe that H₂S is binding strongly in UiO-66 such that it cannot be removed using a simple temperature swing. The capacity loss in UiO-66 synthesized at room temperature was most drastic decreasing from 0.35 mmol/g in run 1 to 0.18 and 0.15 mmol/g in runs 2 and 3 respectively.

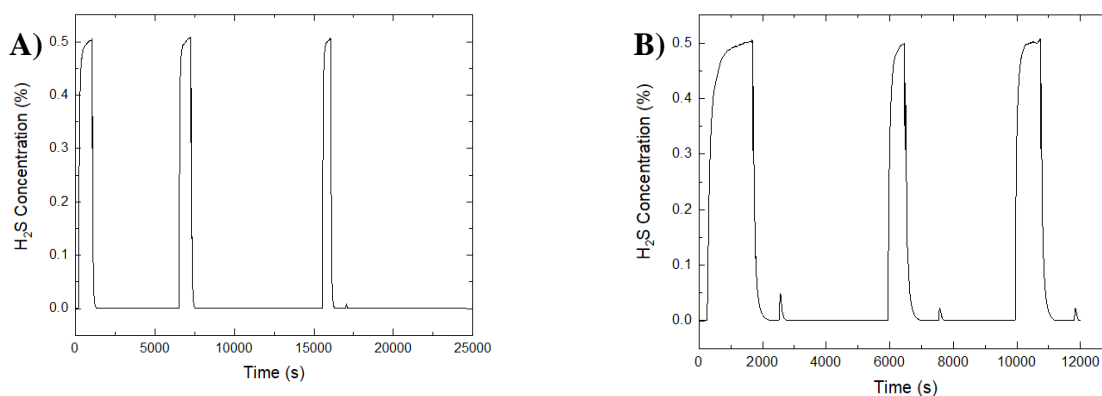


Figure G.21: Complete H₂S breakthrough curve for A) solvothermally and B) room synthesized DMOF-TM

Figure G.21 shows the complete breakthrough curves for DMOF-TM synthesized solvothermally and at room temperature. Similarly, to UiO-66, there is a decrease in H₂S breakthrough capacity from run 1 to run 2 in both the room temperature and solvothermally synthesized samples. Interestingly, the desorption behavior of the two DMOF-TM samples is different. DMOF-TM synthesized solvothermally shows no desorption of H₂S upon heating the sample, whereas there are sharp peaks in the H₂S concentration for the room temperature synthesized DMOF-TM. We hypothesize that the defects in room temperature synthesized DMOF-TM provide an additional adsorption site for H₂S that is tightly bound and requires this heating stage to be desorbed.

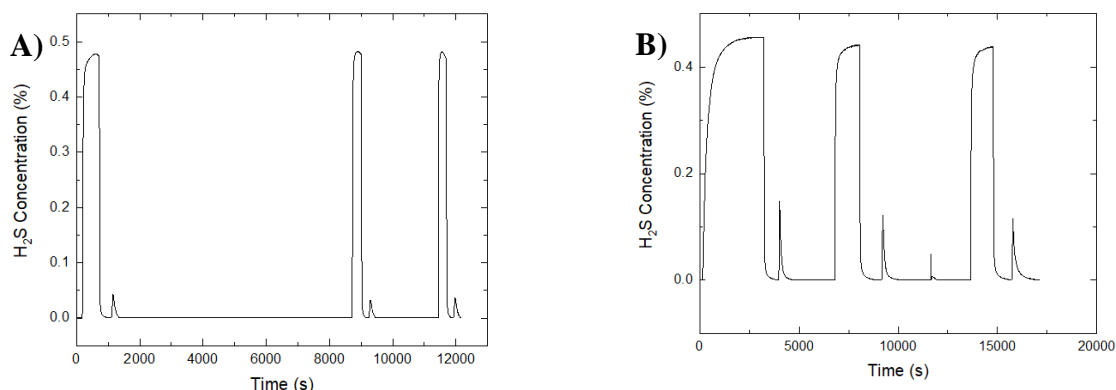


Figure G.22: Complete H₂S breakthrough curve for A) solvothermally and B) room synthesized ZIF-8

Figure G.22 shows the complete breakthrough curves for ZIF-8 synthesized solvothermally and at room temperature. The kinetic diameter of hydrogen sulfide is larger than the pore window of ZIF-8 resulting in diffusion limitations during breakthrough measurements. Desorption of H₂S between runs was also slow and was aided by heating to 100 °C, as can be seen in the small sharp peaks following the breakthrough measurements. ZIF-8 synthesized at room temperature adsorbed a large amount of H₂S, however it could not be regenerated by heating cycles alone. Post PXRD and BET surface area measurement showed that the material lost roughly 50 % of its surface area and PXRD measurements show the presence of amorphous material. Therefore, ZIF-8 does not make a good candidate for adsorbing H₂S due to the combination of diffusion limitation, low capacity in solvothermally synthesized ZIF-8, and instability of the room temperature synthesized ZIF-8.

G.7 SO₂ Breakthrough

SO₂ breakthrough was collected using 1000 ppm SO₂ in nitrogen at a flowrate of 50 mL/min. Nitrogen was used as a tracer gas for determining the dead time of the breakthrough bed. Prior to breakthrough measurements, samples were sieved to size 400 microns and the sample was loaded into a quartz tube and activated in situ under helium flow at 150 °C for all MOF samples. After activation, the sample was cooled to 25 °C before switching to SO₂ in nitrogen flow. Breakthrough measurements were collected in 3 runs for each sample. Between breakthrough runs, the samples were re-activated at 100 °C in helium before cooling to 25 °C and beginning the next run. Figures G.23 – G.25 show the breakthrough curves for each run of the solvothermally and room temperature synthesized UiO-66, DMOF-TM, and ZIF-8 respectively. Figures G.26 to G.28 show the complete breakthrough curves for all runs for the solvothermally and room temperature synthesized UiO-66, DMOF-TM, and ZIF-8 respectively.

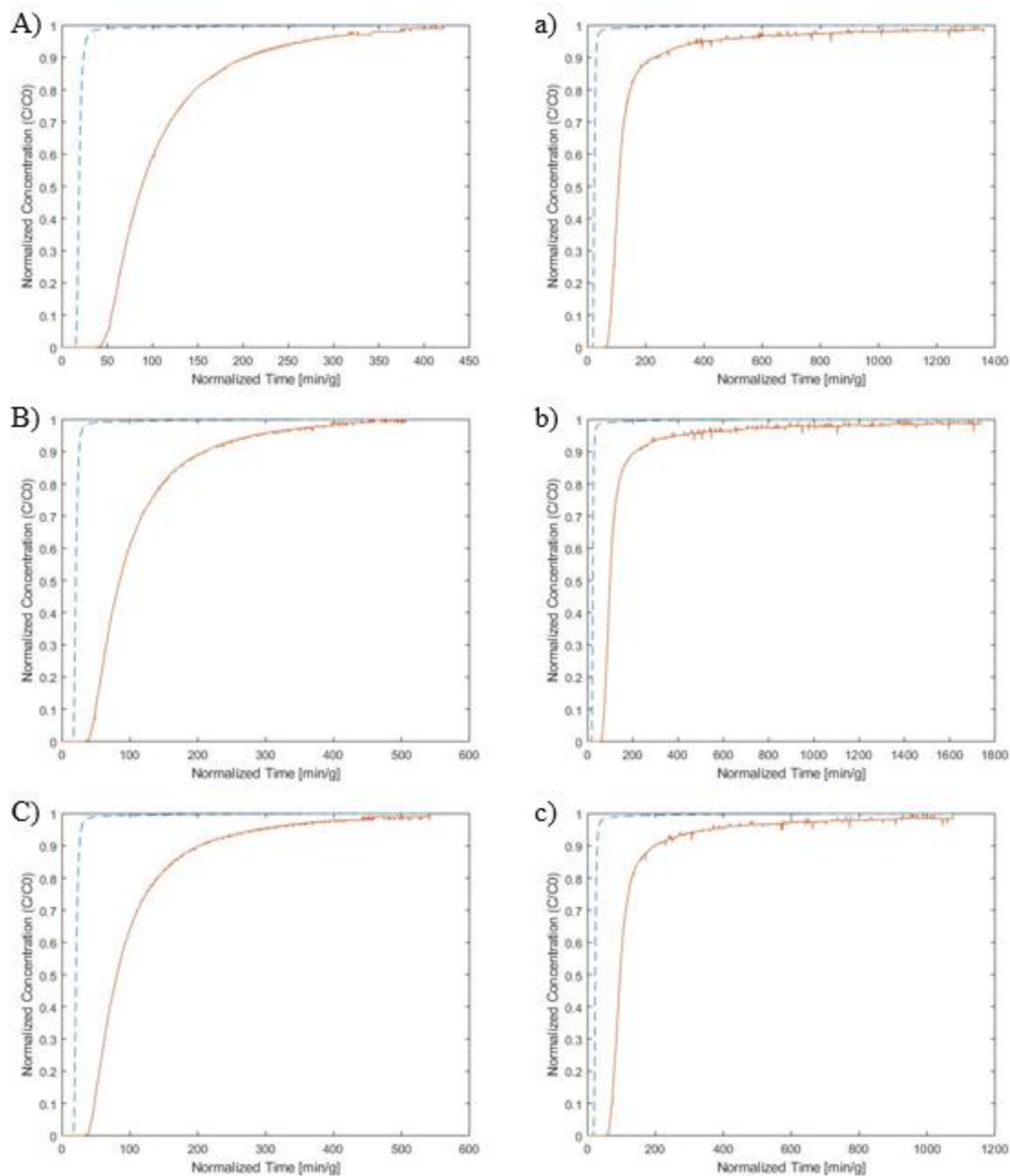


Figure G.23: SO₂ breakthrough curves for solvothermally (upper case) and room temperature (lower case) synthesized UiO-66 A) Run 1 B) Run 2 C) Run 3

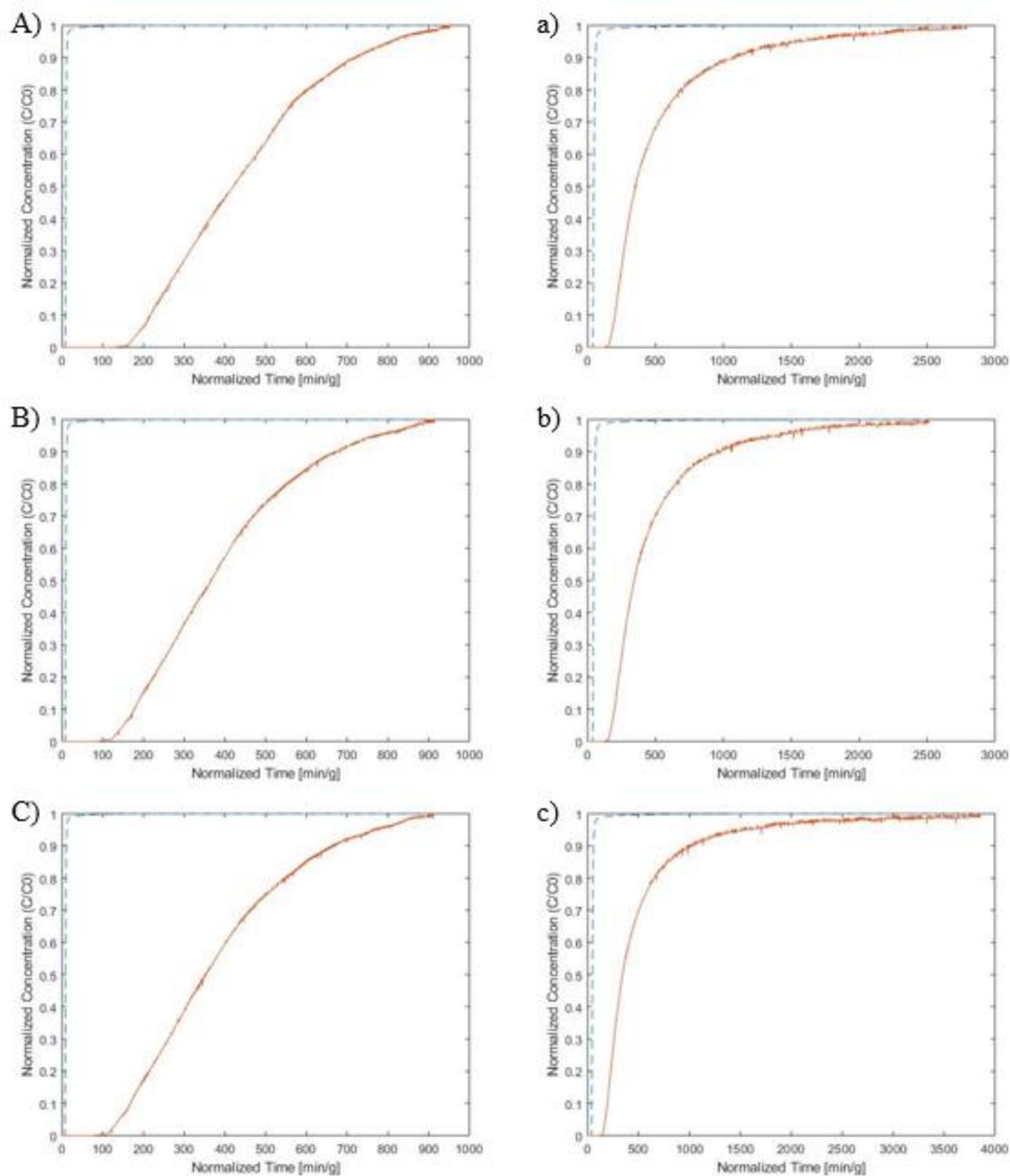


Figure G.24: SO₂ breakthrough curves for solvothermally (upper case) and room temperature (lower case) synthesized DMOF-TM A) Run 1 B) Run 2 C) Run 3

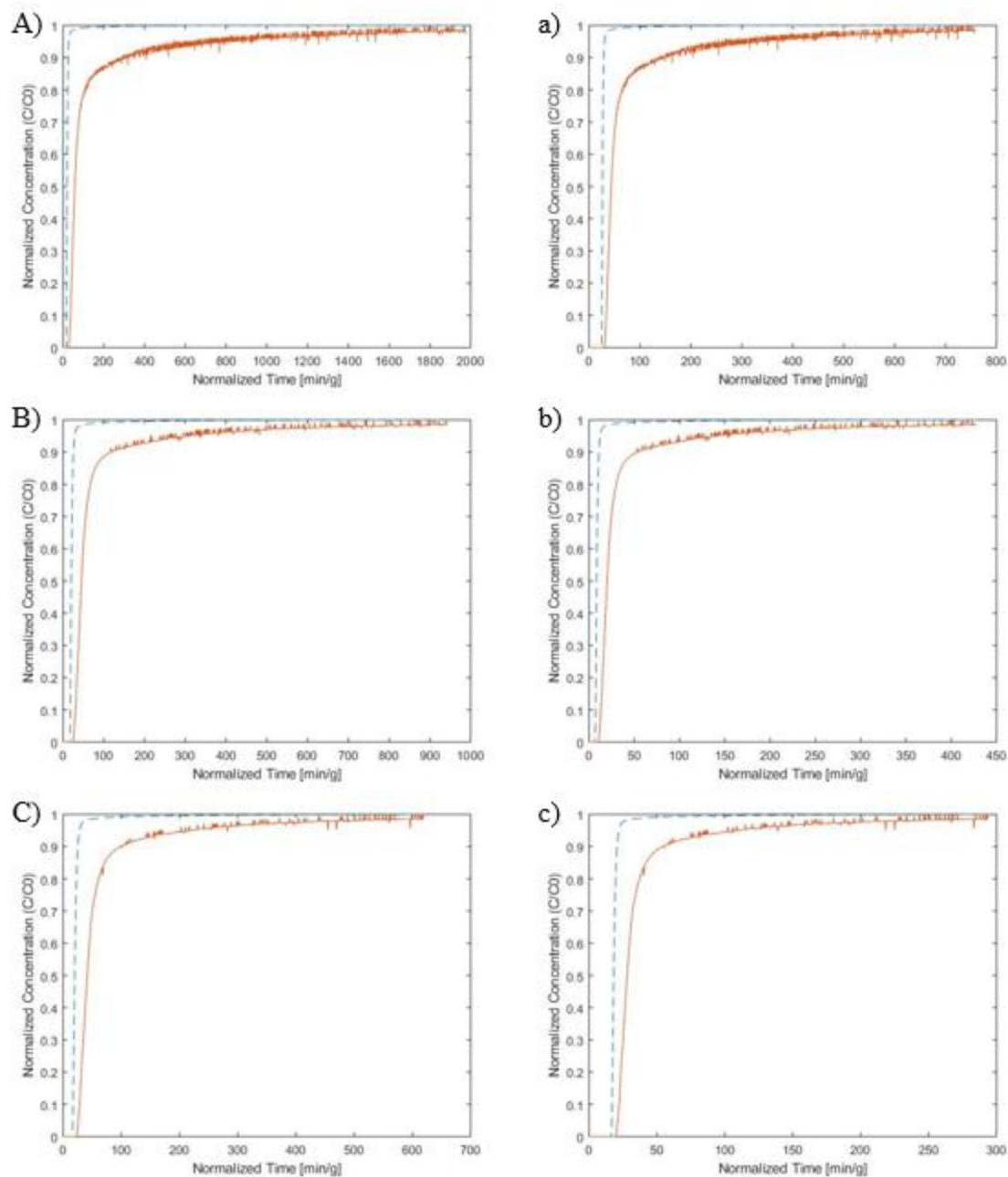


Figure G.25: SO₂ breakthrough curves for solvothermally (upper case) and room temperature (lower case) synthesized ZIF-8 A) Run 1 B) Run 2 C) Run 3

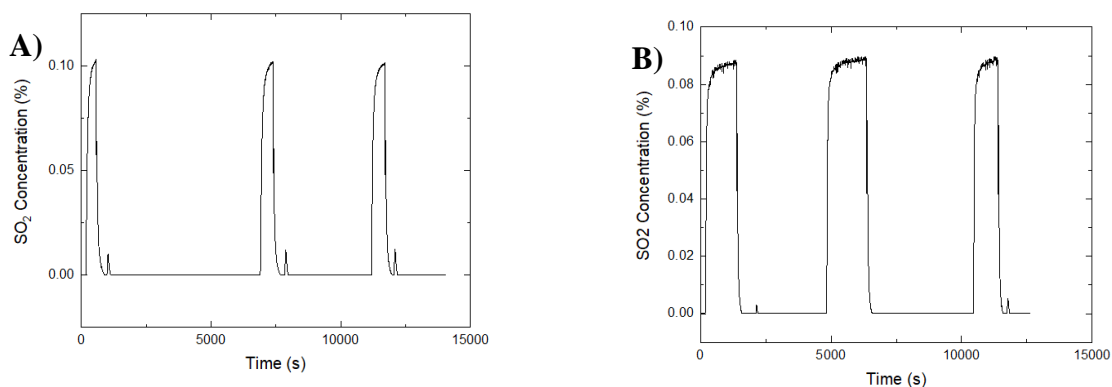


Figure G.26: Complete SO₂ breakthrough curve for A) solvothermally and B) room synthesized UiO-66

Figure G.26 shows the complete SO₂ breakthrough curves for the solvothermally and room temperature synthesized UiO-66. For both samples the breakthrough capacity remained constant across the three trial runs, see Table G.2. The breakthrough capacity of the solvothermally synthesized UiO-66 was 0.19 mmol/g and 0.24 mmol/g for the room temperature synthesized UiO-66. For the solvothermally synthesized UiO-66 we observed that some SO₂ required heating to be desorbed from the material, however it did not appear to be strongly bound, and the material was successfully regenerated for subsequent runs.

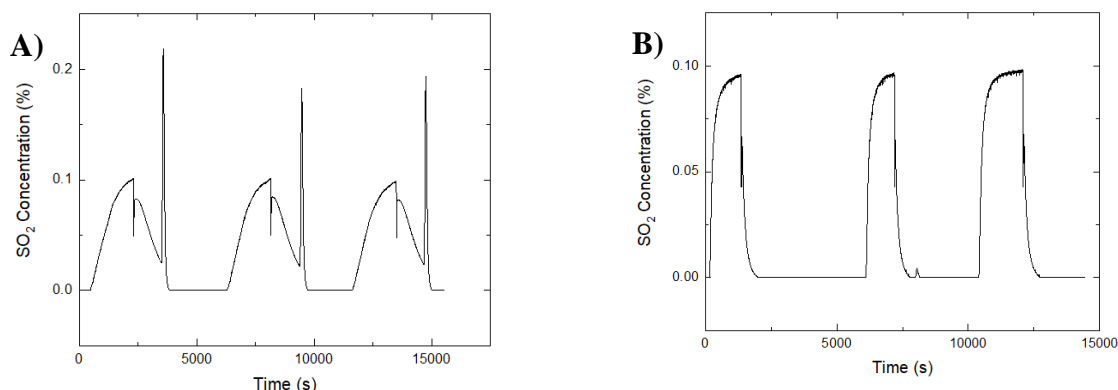


Figure G.27: Complete SO₂ breakthrough curve for A) solvothermally and B) room synthesized DMOF-TM

Figure G.27 shows the SO₂ breakthrough curves for solvothermally and room temperature synthesized DMOF-TM. Both materials adsorbed a large amount of SO₂ reaching capacities of 0.90 mmol/g (solvothermal) and 0.94 (room temperature) mmol/g. While both materials adsorbed similar quantities of SO₂, the adsorption and desorption curves of these materials were very different. Solvothermally synthesized DMOF-TM had much slower adsorption and desorption profiles due to diffusion limitations, the pore window of DMOF-TM is smaller than the kinetic diameter of SO₂. Additionally, heating the sample was required in order to regenerate the material whereas DMOF-TM synthesized at room temperature readily desorbed SO₂ without the aid of heat. We hypothesize that room temperature synthesized DMOF-TM has a larger pore window than solvothermally synthesized DMOF-TM such that we did not observe the same diffusion limitations that were present in the room temperature sample.

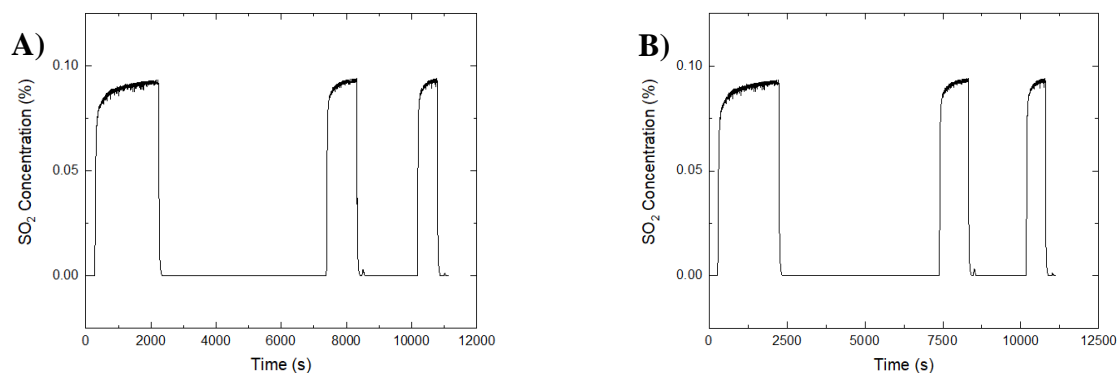


Figure G.28: Complete SO₂ breakthrough curve for A) solvothermally and B) room synthesized ZIF-8

Figure G.28 shows the SO₂ breakthrough curves of solvothermally and room temperature synthesized ZIF-8. Much like the H₂S breakthrough curves diffusion limitations also led to slow adsorption and neither sample adsorbed much SO₂.

G.8 SO₂ Pressure Decay Apparatus

Pure SO₂ adsorption isotherms were collected using a lab build pressure decay apparatus that is shown in Figure G.29. This apparatus is the same one that was previously described in the literature.^{4,5} Prior to isotherm collection samples were activated in situ at 150 °C under vacuum overnight. For adsorption isotherm collection a water bath was used to maintain a constant temperature of 25 °C and pure SO₂ was dosed into the system from 0 to roughly 2.5 bar. The following reference cell pressures were used to collect the equilibrium adsorption points for all materials: 7 psi, 14 psi, 21 psi, 28 psi, 42 psi, and 48 psi. SO₂ was then dosed into the sample cell and it was allowed to equilibrate. The Peng-Robinson equation of state was used to calculate the amount of SO₂ adsorbed by each MOF.

Equation G.1

$$p = \frac{RT}{V_m - b} - \frac{a\alpha}{V_m^2 + 2bV_m - b^2}$$

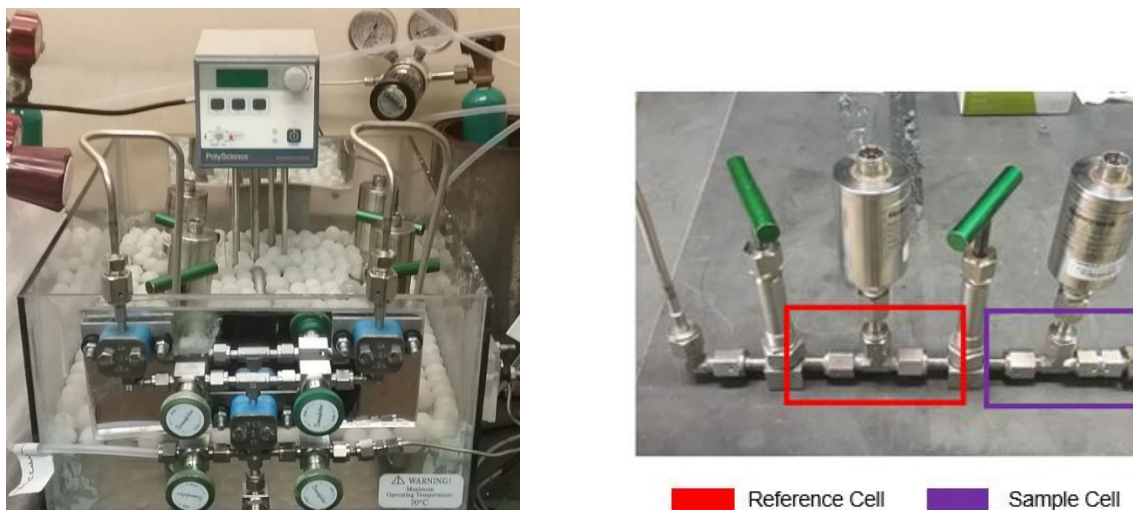


Figure G.29: (left) SO₂ pressure decay apparatus. (right) Close-up of reference cell and sample cell.

G.8 Acid Gas Breakthrough Apparatus

H₂S and SO₂ breakthrough experiments were conducted using the apparatus displayed in Figure G.30. Prior to breakthrough experiments all samples were sieved to size 400 microns, loaded into a quartz tube, and activated in situ under helium flow at 150 °C. After activation, the packed bed was allowed to cool to 25 °C and breakthrough measurements were collected using a mass spectrometer to analyze the outlet gas concentration from the breakthrough bed. Nitrogen was used as a tracer gas for both H₂S and SO₂ breakthrough experiments and was used to calculate the dead time of the packed bed. H₂S was passed through the breakthrough bed using a concentration of 5000 ppm in nitrogen and SO₂ was passed through the bed at a concentration of 1000 ppm in nitrogen.

Three runs were collected in succession with 100 °C in helium reactivation between each run.

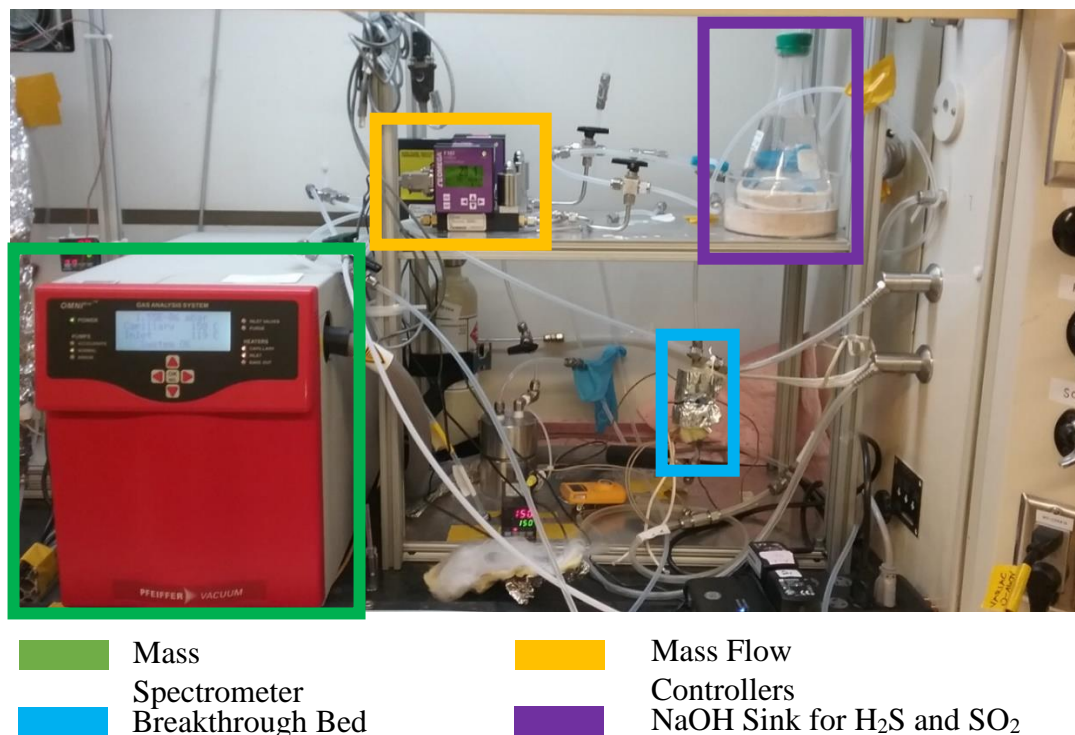


Figure G.30: Photograph of acid gas breakthrough apparatus

G.9 References

- [1] Cavka, J.; Jakobsen, S.; Olsbye, U.; Guillou, N.; Lamberti, C.; Bordiga, S.; Lillerud, K. A New Zirconium Inorganic Building Brick Forming Metal-Organic Frameworks with Exceptional Stability. *J. Am. Chem. Soc.* **2008**, 130, 13850-13851.
- [2] Jasuja, H.; Huang, Y.; Walton, K. Adjusting the Stability of Metal-Organic Frameworks under Humid Conditions by Ligand Functionalization. *Langmuir*. **2012**, 28, 16874-16880.
- [3] Park, K.; Ni, Z.; Cote, A.; Choi, J.; Huang, R.; Uribe-Romo, F.; Chae, H.; O’Keeffe, M.; Yaghi, O. Exceptional Chemical and Thermal Stability of Zeolitic Imidazolate Frameworks. *PNAS*, **2006**, 103, 10186-10191.
- [4] Bhattacharyya, S.; Han, R.; Kim, W.; Chiang, Y.; Jayachandrababu, K.; Hungerford, J.; Dutzer, M.; Ma, C.; Walton, K.; Sholl, D.; Nair, S. Acid Gas

Stability of Zeolitic Imidazolate Frameworks: Generalized Kinetic and Thermodynamic Characteristics. *Chem. Mater.* **2018**, 30, 4089-4101.

- [5] Hungerford, J.; Bhattacharyya, S.; Tumuluri, U.; Nair, S.; Wu, Z.; Walton, K. DMOF-1 as a Representative MOF for SO₂ Adsorption in Both Humid and Dry Conditions. *J. Phys. Chem. C* **2018**, 122, 23493-23500.

APPENDIX H: SUPPLEMENTAL INFORMATION FOR COMPREHENSIVE STUDY OF SO₂ ADSORPTION IN A SERIES OF METAL-ORGANIC FRAMEWORKS

H.1 SO₂ Adsorption Isotherms

SO₂ Adsorption isotherms were collected using a lab build system. Figure H.1 shows a photograph of the system and a close-up picture of the sample and reference cells. Adsorption isotherms were collected from 0 to 2.5 bar (0 – 0.6 P/P_o) using pure SO₂ gas. Prior to testing, samples were activated in situ under vacuum and heat. After activation, samples were dosed to the following reference cell pressures: 7, 14, 21, 28, 42, and 48 psi. The sample cell pressure was then allowed to equilibrate until proceeding to the next point. The Peng-Robinson equation of state (see equation H.1) was used to relate the pressure to molar volume and calculate the amount of SO₂ adsorbed by the sample at each point. After testing the entire setup was subject to vacuum overnight to ensure complete desorption and removal of SO₂ from the apparatus.

Equation H. 1:

$$p = \frac{RT}{V_m - b} - \frac{a\alpha}{V_m^2 + 2bV_m - b^2}$$

$$V_m = \frac{V}{n}$$

$$a = \frac{0.45724R^2T_c^2}{p_c}$$

$$b = \frac{0.07780RT_c}{p_c}$$

$$\alpha = [1 + ((0.37464 + 1.54226\omega - 0.26992\omega^2)(1 - T_r^{0.5}))^2]$$

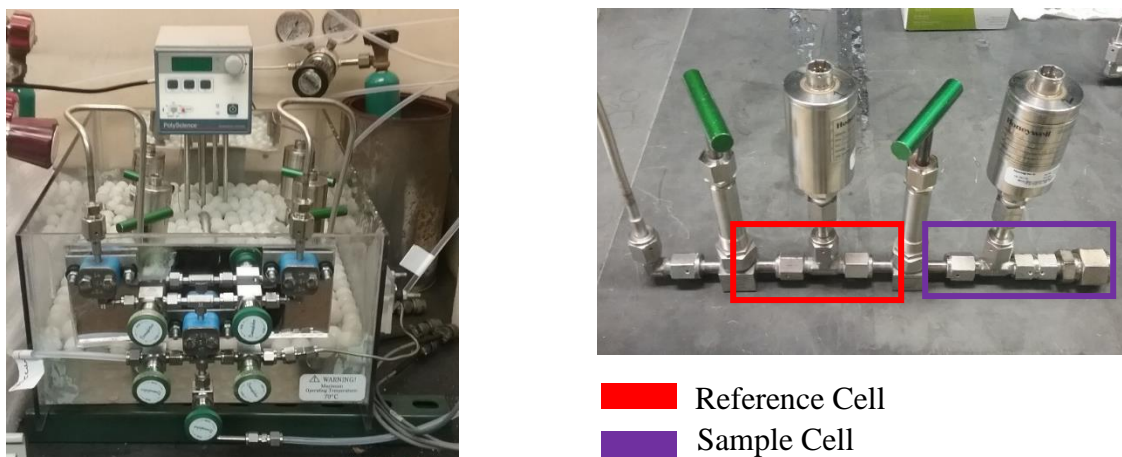


Figure H.1: (Left) SO₂ pressure decay apparatus (Right) Reference and sample cells

The SO₂ adsorption isotherms for: Cu-BTC, UiO-66, UiO-66-NH₂, DMOF-TM, DMOF-ADC, MIL-101, ZIF-7, ZIF-8, ZIF-11, ZIF-65, and MIL-53 were presented in chapter 7, Figure 7.1 in the main text. Table H.1 contains the isothermal points collected to produce that data.

Table H.1: SO₂ adsorption isothermal points

Cu-BTC	
Pressure (bar)	Adsorption (mmol/g)
0.00	0.00
0.05	3.57
0.23	8.78
0.77	10.69
1.31	11.33
2.06	11.92
2.64	12.38

Table H.1: Continued

UiO-66	
Pressure (bar)	Adsorption (mmol/g)
0.00	0.00
0.12	2.51
0.36	5.50
0.92	7.34
1.38	8.01
2.07	8.68
2.63	9.09
UiO-66-NH₂	
Pressure (bar)	Adsorption (mmol/g)
0.00	0.00
0.10	2.30
0.38	4.80
0.86	5.61
1.38	6.18
2.10	6.71
2.74	7.11
DMOF-TM	
Pressure (bar)	Adsorption (mmol/g)
0.00	0.00
0.02	4.04
0.34	5.93
1.06	6.42
1.53	6.67
2.24	6.93
2.83	6.78
DMOF-ADC	
Pressure (bar)	Adsorption (mmol/g)
0.00	0.00
0.05	1.76
0.32	4.09
0.66	4.81
1.07	5.58
1.72	6.15
2.32	7.20

Table H.1: Continued

MIL-101	
Pressure (bar)	Adsorption (mmol/g)
0.00	0.00
0.06	2.82
0.24	7.40
0.66	11.95
1.11	16.01
1.79	19.86
2.42	21.14
MIL-53	
Pressure (bar)	Adsorption (mmol/g)
0.00	0.00
0.09	3.50
0.37	7.74
0.86	9.33
1.37	10.19
2.07	11.07
2.60	11.72
ZIF-7	
Pressure (bar)	Adsorption (mmol/g)
0.00	0.00
0.09	1.95
0.45	2.57
0.93	2.96
1.41	3.30
2.09	3.69
2.69	4.39
ZIF-8	
Pressure (bar)	Adsorption (mmol/g)
0.00	0.00
0.11	1.69
0.38	4.23
0.82	5.95
1.34	6.90
2.01	7.70
2.65	8.42

Table H.1: Continued

ZIF-11	
Pressure (bar)	Adsorption (mmol/g)
0.00	0.00
0.11	0.82
0.45	1.37
0.92	1.73
1.41	2.02
2.09	2.29
2.71	2.54
ZIF-65	
Pressure (bar)	Adsorption (mmol/g)
0.00	0.00
0.06	2.74
0.35	5.13
0.86	6.25
1.27	9.64
1.95	12.29
2.64	12.83